Oxygen, Carbon, Heat: explorations in atmosphere-ocean interaction

Allison Hogikyan

A Dissertation
Presented to the Faculty
of Princeton University
in Candidacy for the Degree
of Doctor of Philosophy

Recommended for Acceptance
by the Program in
Atmospheric and Oceanic Sciences
Adviser: Laure Resplandy

May 2023

© Copyright by Allison Hogikyan, 2023.

All Rights Reserved

Abstract

This thesis describes three novel mechanisms of air-sea interaction. The first two chapters focus on the amplification of the hydrological (water) cycle as the climate system warms in response to a CO_2 increase, which is realized as an amplification of freshwater flux (precipitation - evaporation) patterns. We find that this freshwater flux pattern leads to a redistribution of oxygen and carbon in the ocean, which modifies the previously recognized changes due to the atmospheric CO_2 increase, warming, and circulation changes. The change in oxygen concentrations results from the change in sea surface salinity patterns which modifies the ocean circulation and heat uptake. The change in carbon concentrations results from the dilution or concentration of carbonate species (in parallel to salinity), and the same changes in heat uptake. The redistributions of oxygen and carbonate species in response to hydrological cycle amplification are comparable to the effect of global warming, which decreases both oxygen and carbon concentrations throughout the ocean.

The third chapter provides a causal mechanism, for the first time, to link the change in sea surface temperature that develops during El Niño events to the change in temperature of the tropical free troposphere. The temperature of the free troposphere is primarily determined by the temperature profile followed by moist convection over the ocean (rising air above high sea surface temperatures). We isolate the part of the sea surface associated with convection (which is determined on thermodynamic rather than geographic grounds) and demonstrate that the El Niño surface temperature increase is driven by a decrease in surface wind speed which damps the evaporation rate. This result suggests a possible relationship between the zonal symmetry of the tropical atmospheric circulation, temperature of the free troposphere, and top-of-atmosphere energy budget.

Contents

Abstract iii

0 Introduction **1**

0.1 Atmosphere-ocean coupled system 1

0.2 Freshwater flux pattern amplification accompanies global warming 4

0.3 Why are the warmest SSTs critical for understanding the temperature increase in the free troposphere during El Niño? 6

0.4 Approach to separating forcing from feedbacks in the coupled system 9

1 Oxygen: Hydrological cycle amplification overwhelms warming-driven oxygen loss in subsurface Atlantic Ocean **11**

1.1 Abstract 11

1.2 Introduction 12

1.3 Methods 15

1.3.1 Model and Experimental Setup 15

1.3.2 Atlantic Water Mass Definition 17

1.3.3 Drivers of O_2 changes 18

1.4 Salinity and oxygen track Atlantic ventilation changes 19

1.5 Stronger deoxygenation in fresher water masses 20

1.6 Influence of hydrological cycle amplification on ocean circulation and ventilation 22

1.7 Direct and indirect effects of the hydrological cycle amplification on ocean deoxygenation . . . 25
1.8 Conclusion . . . 27
1.9 Supplemental information . . . 29
1.9.1 Temperature trend in the Atlantic Ocean at 25°W . . . 29
1.9.2 Contribution of precipitation, evaporation, ice melt to sea surface salinity trends . . . 31
1.9.3 Ventilation changes in climate effect largely attributed to hydrological effect . . . 33
1.9.4 Masks for SSS restoring setup and Atlantic Ocean analysis . . . 33

2 Carbon: Influence of hydrological cycle amplification on ocean pH and carbonate chemistry 36

2.1 Abstract . . . 36
2.2 Introduction . . . 37
2.3 Methods . . . 39
2.3.1 Earth System Model and experiments to isolate hydrological and climate effects . . . 39
2.3.2 Freshwater and thermal contributions to DIC and Alkalinity changes 41
2.3.3 Attribution of surface pH changes to hydrological and climate effects 44
2.3.4 Quantifying DIC changes in subsurface water masses . . . 45
2.4 DIC and Alkalinity increase in 'fresh-get-fresher' and decrease in 'salty-get-saltier' regions apparent in total climate effect . . . 46
2.5 Acidification weakened in 'salty-get-saltier' regions and exacerbated in 'fresh-get-fresher' regions . . . 52
2.6 Freshwater fluxes and ocean heat redistribution enhance subsurface carbon storage . . . 55
2.7 Summary . . . 56

2.8 Supplemental Figures 60

3 Heat: Cause of the intense tropics-wide tropospheric warming in response to El Niño 65

4 Conclusions 78

A Appendix: A Synthesis of Global Coastal Ocean Greenhouse Gas Air-sea Fluxes 81

0

Introduction

0.1 Atmosphere-ocean coupled system

Humans live in the surface atmosphere, but the climate we experience is largely determined by flows of energy, momentum, and mass between the global ocean and atmosphere. Each and every interaction exchanging heat, water, carbon, and other quantities between these two reservoirs occurs at the surface, leaving behind information about the exchange (e.g. temperature, salinity, or change in chemistry). This thesis follows flows of mass and energy across the sea surface to enhance understanding of the mechanisms driving changes in oceanic oxygen and dissolved carbon concentrations with global warming in Chapters 1 and 2, and driving changes in sea surface temperature (SST) in response to natural variability in Chapter 3. Flows of heat and momentum are tightly coupled, especially through the surface wind field. Surface winds enhance local evaporation and drive transport of seawater, which may then release its heat to the atmosphere in a remote location. Heat fluxes can modify the

surface pressure field and thereby affect the surface wind field. Surface winds also drive upwelling of water from the deep ocean to the surface, allowing this tremendous store of energy to interact with the atmosphere. As a result, small changes in the surface wind field, even if insignificant to the local surface energy budget, can lead to tremendous perturbations in the global energy budget by modulating these exchanges between the ocean and the atmosphere. Mass fluxes are also coupled to flows of heat and momentum, for example, through freshwater fluxes (precipitation and evaporation) which alter seawater buoyancy and the ocean circulation responsible for transporting heat, carbon, oxygen and other tracers either to the deep ocean, where they can be stored for hundreds of years, or to the surface where they interact with the atmosphere. Notably, carbon dioxide in the atmosphere is a greenhouse gas which warms the climate system, and the partitioning of carbon between the ocean and atmosphere strongly affects Earth's energy budget. Air-sea exchanges of carbon and oxygen vary with temperature, and feedbacks between temperature, circulation, and biogeochemistry modulate the partitioning of heat, carbon, and oxygen between the ocean and atmosphere.

The next two chapters of this thesis are closely related and describe the response of seawater chemistry (oxygen and carbon) to atmospheric forcing. While the response to the atmospheric CO_2 increase and warming have been previously described [1], we consider the effect of an amplification of the hydrological (water) cycle, a robustly simulated response to CO_2-forced atmospheric warming. Hydrological cycle amplification is seen by the ocean in the form of large scale freshwater flux (precipitation - evaporation) patterns, which dilute or concentrate sea surface salinity along with other tracers including carbonate species. In Chapter 1, we demonstrate that this sea surface salinity pattern amplification leads to a redistribution of oxygen in the ocean through modifications to ocean circulation and heat uptake. In Chapter 2, we demonstrate that hydrological cycle amplification also leads to a redistribution of carbon in the ocean, via a direct dilution or concentration of carbonate species by freshwater addition or removal, and change in ocean heat uptake. This redis-

tribution of oxygen and carbon strongly modulates the total oxygen loss associated with ocean warming and circulation weakening, and the global decrease in carbon uptake due to warming.

Chapter 3 considers how a surface temperature anomaly is produced by the near-surface coupled atmosphere-ocean system. We focus on the part of the tropical sea surface that is tightly linked to the temperature of the tropical free troposphere, and find that the rearrangement of the tropical atmospheric circulation leads to a decrease in surface wind speed which damps evaporation, and explains the surface temperature increase.

The Appendix contains a synthesis report on the carbon cycle in the global coastal oceans which I did not lead, but to which I contributed much of the data analysis. This synthesis report comprises the 'Global Coastal Oceans' chapter of the second decadal REgional Carbon Cycle Assessment and Processes (RECCAP-2) report, part of the Global Carbon Project [2]. In this report, we confirm in ocean biogeochemical models and pCO_2-observation-based data products that the coastal ocean has on average lower surface pCO_2 and stronger CO_2 uptake from the atmosphere than the open ocean, as had been previously suggested but not tested globally. However, this may be due to the fact that much of the global coastal area is at high latitudes where low temperatures and biological productivity decrease the surface pCO_2, and not generalizable to any coast- open ocean cross section. Whether this coast- open ocean contrast has strengthened or weakened over recent decades is uncertain due to disagreement among models and products. We also assess seasonality, and find the models underestimate the influence of ocean dynamics and biology in the seasonal cycle of surface pCO_2 in many places, relative to the pCO_2 observation-based products. A follow-up study focusing on case studies of particular coastal regions is also in preparation for publication.

Although the introduction in each chapter is intended to be sufficient to understand that chapter, we provide some additional context for the underlying theory in each case of (a) freshwater flux amplification, which is foundational for Chapters 1 and 2, and (b) the link between the surface and tropical free troposphere in the Pacific Ocean, foundational for

Chapter 3. We also provide a brief perspective on the commonalities in approach among the three chapters.

0.2 Freshwater flux pattern amplification accompanies global warming

Air-sea freshwater fluxes come in the form of precipitation and evaporation. While constrained globally by the atmospheric energy budget [3, 4], the regional occurrence and amount of precipitation and evaporation depend on the local atmospheric and surface conditions, respectively. Patterns of precipitation - evaporation at a given location, or net surface freshwater flux, must balance the horizontal convergence of moisture in the overlying column of the free troposphere to satisfy mass conservation. Here, the hydrological cycle refers to this flow of freshwater via evaporation, transport, and precipitation, and we do not discuss interactions with land.

General circulation models of the atmosphere agree that this hydrological cycle is enhanced as the atmosphere warms. A warmer atmosphere hold more moisture in these simulations, retaining a similar relative humidity but increasing absolute humidity (concentration of water vapor in air). In addition, important features of the large scale flow, notably the Hadley circulation, remain. Although there is a poleward expansion, it is small (around 1° latitude, [5]) relative to the scale of the circulation (30° latitude north and south of the equator). As a result, there is a relatively steady pattern of horizontal convergence of air, but greater horizontal convergence of water vapor. This enhanced convergence of moisture requires enhanced surface freshwater fluxes, termed a 'wet-get-wetter, dry-get-drier' pattern [6, 7]. This amplified pattern of surface freshwater fluxes implies an amplified pattern of sea surface salinity (SSS), which is indeed observed, and termed a 'fresh-get-fresher, salty-get-saltier' pattern [8, 9]. Figure 1 demonstrates this effect in a model simulation, where the regions with highest SSS in the mean state (green and yellow in panel a) also experience

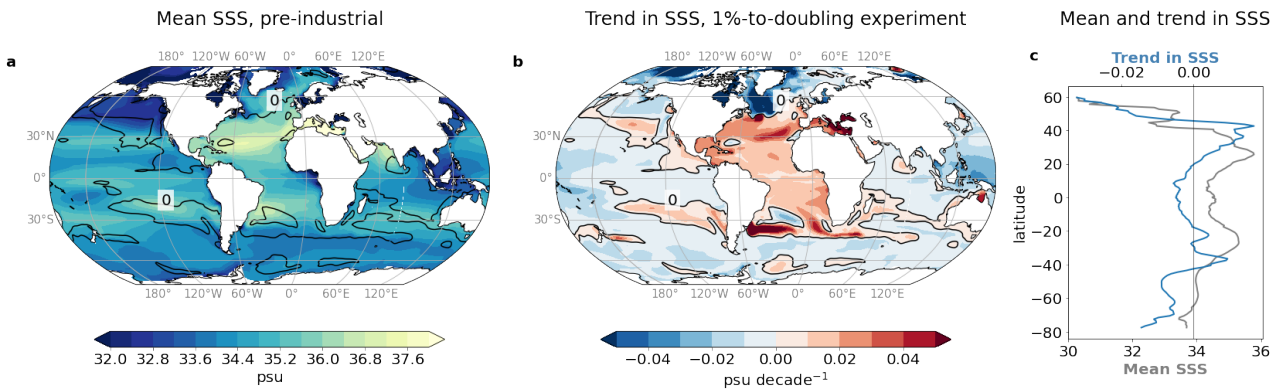


Figure 1: **Sea surface salinity mean (pre-industrial CO_2) and trend (with CO_2 increase)in GFDL-ESM2M.** Maps in (a) and (b) are both overlaid with the zero trend contour from (b). (c) Zonal mean from 80S to 60N, with the mean in grey plotted against the lower x axis, and the trend in blue against the upper x axis. Simulations are (a) pre-industrial control and (b) 1%-to-doubling CO_2 trajectory, as described in Chapters 1 and 2.

an increase in SSS (red in panel b), while those with low mean SSS (blue in panel a) tend to experience a decrease (blue in panel b). A global zonal average reveals that the high mean SSS of the subtropics (15° - 30°) is generally enhanced with warming and the lower mean SSS of the tropics (10°S - 10°N) and higher latitudes is diminished with warming (30° - 50°) (Figure 1c). By this logic, SSS patterns could be expected to strictly amplify, conditional upon steady atmospheric and oceanic circulation. However, the atmospheric and oceanic circulation is not perfectly steady: the descending branch of the Hadley cell and the subtropical gyres tend to widen poleward, expanding 'dry' and 'salty' regions [10, 11]. In ESM2M, for example, this shift in subtropical gyre circulation leads to the poleward offset of the maximum subtropical salinity increase, relative to the mean SSS (Figure 2c). The Atlantic Meridional Overturning Circulation also slows down within the first century, diminishing the transport of warm and salty water from the subtropical gyres into subpolar regions where deep water is formed, further amplifying SSS patterns in the Atlantic Ocean [12, 13].

The amplification of the hydrological cycle is one of several physical changes that result from increasing CO_2 concentrations in the atmosphere in addition to, most notably, warming, which modify ocean biogeochemistry. While the total effect of climate change on ocean

biogeochemistry (including warming, circulation changes, hydrological cycle amplification, and feedbacks in biological activity all together) has been examined before [1, 14, 15], we perform model experiments which isolate the response to hydrological cycle amplification for the first time here (note that the influence of freshwater fluxes was discussed in [16]). Chapters 1 and 2 split the ocean into spatial (3-dimensional) regimes according to whether they become fresher or saltier with global warming, then identify the influence of freshening and salinification on dissolved oxygen and carbon. These freshwater fluxes lead to temperature and circulation changes which affect both oxygen and carbon. Carbon is further affected by freshwater fluxes via the direct dilution of dissolved carbonate and bicarbonate ions by the freshwater fluxes.

0.3 Why are the warmest SSTs critical for understanding the temperature increase in the free troposphere during El Niño?

El Niño-Southern Oscillation (ENSO) events are observed every 5-7 years on average, and oscillate between El Niño events, associated with a weakening of the equatorial upwelling, migration of the tall atmospheric convective storms (atmospheric deep convection) from the west to the central Pacific, and warming of the free troposphere ('free' indicating above the planetary boundary layer), and La Niña events, associated with a strengthening of the equatorial upwelling, migration of atmospheric convection slightly further west and off-equator, and cooling of the free troposphere (Figure 2). There is a strong temperature change in the equatorial upwelling region during El Niño and La Niña, which is well understood to be the result of the change in upwelling strength [17]. The sea surface in the tropics receives steady heating from the sun, and it is only the supply of cold water from below this warm surface layer that maintains the relatively low temperatures in the equatorial east Pacific

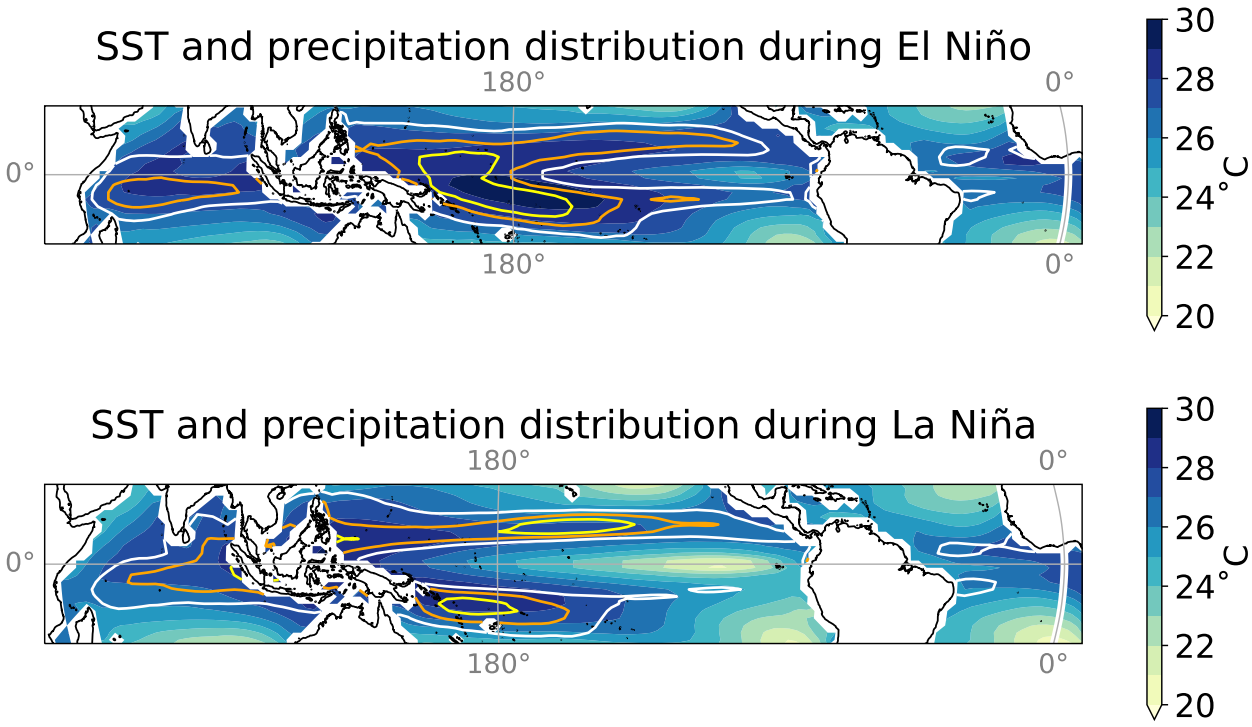


Figure 2: **Mean tropical SST and rainfall rate during simulated El Niño and La Niña events.** Shading of SST and contours of rainfall rate. Composite when simulated Niño3.4 index [23] exceeds 1°C for an El Niño, and falls below -1 °C for La Niña. Rainfall contours at 5.1, 7.8, 10.4 kg m^{-2} day^{-1}. GFDL-ESM2M pre-industrial control simulation described in Chapter 1, 2.

(≈5°C colder than the rest of the equatorial Pacific; Figure 2). A change in supply of cold water therefore leads to strong changes in surface temperature. For this reason, as well as the marine ecosystem impacts of changes in upwelling strength [18], the eastern equatorial upwelling region has been the focus of past research on SST variability and change in the tropical pacific [19, 20, 21, 22]. However, this temperature change does not explain the observed temperature increase in the free troposphere; the free troposphere is only strongly coupled to the surface where atmospheric deep convection occurs.

Deep convection relaxes the atmospheric temperature profile towards a moist adiabatic profile which is determined by the temperature of the surface air. Since the Coriolis effect is weak in the tropics, temperature perturbations are smoothed by gravity waves (which travel around the equator in approximately on month) and the entire tropical free tropo-

sphere lies on the moist adiabat of deep convection [24, 25, 26]. As a result, the surface temperature underlying atmospheric deep convection strongly influences the temperature of the entire tropical free troposphere on monthly-mean or longer timescales. Deep convection is generally co-located with the highest SSTs, where near-surface air is buoyant relative to the overlying free troposphere. We focus on SST since near-surface humidity, which also affects buoyancy, only slightly varies over the tropical oceans (mixing ratio 17-18 g kg^{-1}, relative humidity of 75-80%, [27]). The location of deep convection is thus more directly related to thermodynamics than geography, and we will take advantage of this fact to define a 'convective regime', where SSTs are tightly coupled to the temperature of the free troposphere.

As is illustrated by Figure 2, atmospheric deep convection and the highest (open-ocean) SSTs migrate and deform together over time. In this figure, a high rain rate, denoted by the yellow and orange contours, can be interpreted to represent the mean location of atmospheric deep convection during the El Niño and La Niña events in this model simulation (as moist air rises and cools, condensation forms clouds and, when the cloud droplets are sufficiently large, leads to convective rainfall). The dark blue colors represent high SSTs, and are co-located with the orange outline of deep convection in both El Niño and La Niña situations: this characterizes the 'convective regime' we follow in Chapter 3. We note that, even though SSTs in the equatorial eastern Pacific are warmer than average during El Niño events, they are still not the warmest SSTs in the tropical Pacific and do not host atmospheric deep convection.

Although it has been known for some time that the surface and free troposphere are only coupled in the convective regime, it has remained unclear what mechanisms control the inter-annual variability and long-term change of these high SSTs; ours is the first to isolate the convective regime with a thermodynamic criterion and study the surface energy budget in this physical regime. ENSO events are not the only application of these new findings; it is still unknown what controls the rate of warming in the convective regime, relative to the

tropical or global mean, under global warming. The study of ENSO in Chapter 3 suggests that the spatial structure of the atmospheric circulation might be relevant to long-term changes in the surface energy budget of the convective regime, as will be discussed briefly in the Conclusions (Chapter 4).

0.4 Approach to separating forcing from feedbacks in the coupled system

The tight coupling between exchanges of heat, momentum, and mass makes causality in the coupled atmosphere-ocean system challenging to disentangle. We use numerical simulations of the global ocean and atmosphere to test mechanistic links between the forcing and change of interest, although interpretation of the results is not always obvious. For example, the balanced surface energy budget may suggest two candidate forcings for an SST change, but if only one is independent of the SST change on the timescale considered, then that is interpreted as the forcing while the other is interpreted as a feedback.

Theory describing the behavior of the fluid atmosphere and ocean is often related to physical regimes (e.g. overturning circulations or regions with deep convection, in the ocean or atmosphere) rather than geographical domain. By relating our results to these regimes, we link the novel aspects of our work to pre-existing theory. We explain changes both upstream and downstream of previously established theory, where upstream and downstream do not refer to the literal flow of mass, but to the chain of events. Results in Chapters 1 and 2 explore the downstream impact of the (previously established) amplification of the hydrological cycle on ocean biogeochemistry, and physical regimes are defined in terms of 'salty-get-saltier' and 'fresh-get-fresher' signals, which are linked to the interior ocean with water masses that follow the mean circulation. Results in Chapter 3 identify the source of the sea surface temperature increase which precedes a temperature increase in the troposphere (where the link between the surface and tropospheric temperatures was previously established). In this

case, a 'convective regime' is identified in terms of the warmest sea surface temperatures, which are generally co-located with frequent atmospheric convection. To understand what is driving the changes in each regime, however, we also need to quantitatively attribute the change to a mechanism (ocean stratification, air-sea heat flux, etc.).

Conservation of mass and energy limit the possible mechanisms that could explain the changes in mass concentration and temperature we consider, and allow us to quantify the contribution of each mechanism. From this budget, we infer the forcing for the change, and describe the behavior of primary feedbacks on the change. This identification of a forcing, which is the key to making an argument about causality, will rely on prior knowledge of which drivers can be considered independent of the change on the timescale considered, and independent of the other drivers. In Chapter 1, this is trivial, as only one driver agrees with the sign of change in oxygen concentration; the others are considered to modulate the magnitude of the change. In Chapter 2, we interpret all changes in carbonate species due to dilution/concentration by freshwater flux addition/removal as one mechanism since a freshwater flux must affect the concentrations of all dissolved species. By the same logic, we also interpret all concentration changes associated with temperature changes as one mechanism. Freshwater fluxes and temperature changes are not always coupled, so this separation of freshwater and thermal effects retains relevance for understanding the response to hydrological cycle amplification in a broader context of variability and change in the atmosphere-ocean system. In Chapter 3, we interpret the surface wind change, which leads to the change in latent heat flux (cooling by evaporation), as independent of the local SST change in the sub-monthly timescale, in contrast to the change in surface longwave radiative cooling which immediately responds to the local SST anomaly and is therefore better considered a feedback.

It is our hope that this simple approach helps build intuition in the reader's mind for the interactions between the atmosphere and ocean considered here.

1

Oxygen: Hydrological cycle amplification overwhelms warming-driven oxygen loss in subsurface Atlantic Ocean

1.1 Abstract

The global ocean is losing oxygen due to warming, which is expected to significantly increase production of nitrous oxide, a greenhouse gas, and decrease the habitat of many megafauna. In the subtropical Atlantic Ocean, however, there is an observed oxygen gain that cannot be accounted for by observed warming. We show that the amplification of the hydrological cycle, a response to climate change which results in a 'salty-get-saltier, fresh-get-fresher' sea surface salinity pattern, influences deoxygenation patterns in an Earth System Model, and can explain the observed oxygenation. In the Atlantic Ocean, this hydrological cycle

amplification leads to enhanced ventilation and oxygenation of 'salty-get-saltier' subtropical water masses, while reducing ventilation and oxygen content in 'fresh-get-fresher' water masses formed at higher latitudes. The oxygenation of subtropical Atlantic waters is thus shown to be a regional consequence of climate change (through surface salinity changes) even as the global consequence of climate change (directly through warming) is deoxygenation.

1.2 Introduction

The oceans lose oxygen in response to global warming. This loss is attributed to the rise in ocean temperature, which decreases oxygen solubility and increases upper ocean stratification, thereby weakening the subduction and transport of well oxygenated surface waters into the ocean interior - a process called ocean ventilation [28, 29, 30, 15, 31]. This ocean deoxygenation has the potential to enhance the production of nitrous oxide, a potent greenhouse gas [32, 33, 34], and compress the habitat of macro-organisms, raising concern for the sustainability of fisheries including highly valuable species such as tuna [35, 30]. Observations and modeling studies suggest that the globally integrated ocean oxygen content has already declined by up to 2% over the last five decades [15, 36], and future projections indicate that this oxygen loss could reach up to 6% in 2100 if emissions are not curtailed [28, 37, 38]. The regional patterns of deoxygenation, however, remain highly uncertain and the mechanisms that control them are not well understood [28, 39, 40, 41, 42]. For example, observations in the Atlantic Ocean over the last six decades show a strong oxygen loss at high northern latitudes (north of 50°N), consistent with the temperature-driven decrease in solubility and ventilation, but also a counter-intuitive oxygen gain in parts of the subtropical subsurface Atlantic (10-30° latitude, 200-1000 m depth) which remains unexplained [43, 44, 41]. In this study, we show that the hydrological cycle amplification, a response to global warming that reinforces evaporation and precipitation patterns [6], contributes to the observed oxygen changes in the Atlantic Ocean. Specifically, we find that the changes in sea surface

salinity associated with these evaporation and precipitation changes alter the oceanic supply of oxygen by ventilation, and can explain the oxygen gain observed in the subtropics (about 20-40°N and 100-1000m depth) and the intensification of oxygen loss further north (about 40-60°N and 100-1000m depth).

Observations (in-situ and satellite) and observation-based reanalyses show that mean sea surface salinity (SSS) patterns have intensified globally in recent decades [9, 46]. In the Atlantic Ocean, latitudinal SSS gradients have amplified. The already salty surface waters in the subtropics (∼10-35°) have become saltier, while the fresher surface waters at higher latitudes (poleward of ∼40°) have experienced a decrease or near-zero change in SSS (Figure 1.1a,c). These SSS changes have been attributed to the hydrological cycle amplification, i.e., the amplification of the precipitation minus evaporation pattern (see schematic over Figure 1.1a,b). Climate models robustly project this amplification of the hydrological cycle with global warming [specifically, amplified moisture convergence in the atmosphere requires an amplification of surface moisture flux; 6]. This mechanism explains the SSS changes observed in the Atlantic Ocean as it causes salty regions, where climatological evaporation exceeds climatological precipitation, to become saltier, and fresh regions, where precipitation exceeds evaporation, to become fresher [e.g. 47, Figure 1.1a]. As evidenced by the observation-based Ocean ReAnalysis System 5 (ORAS5, [48]), this surface freshwater forcing propagates into the ocean interior and imprints on the four main water masses that ventilate the Atlantic Ocean interior (water masses shown by black contours and arrows in Figure 1.1). The salty Tropical and Mode Waters, which are formed in the tropics and subtropics and supply oxygen to the surface and subsurface down to 500-1000 m depth, have become saltier (Figure 1.1 a,c). In contrast, the fresher Intermediate and Deep Waters, which are formed at higher latitudes and supply oxygen to the deep ocean underneath Tropical and Mode Waters, have become fresher or not changed salinity (Figure 1.1 a,c).

These changes in salinity influence water masses' density, and therefore their formation rate, subduction and transport into the ocean interior. In particular, the strong increase

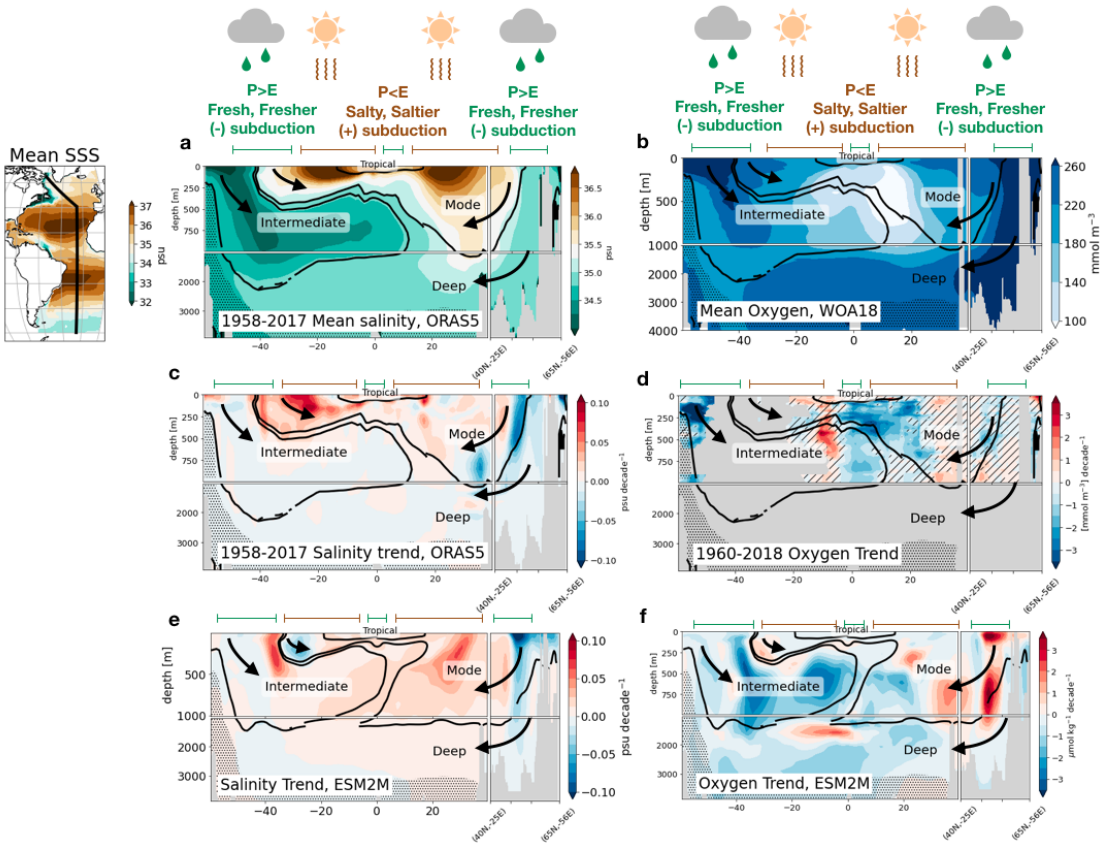


Figure 1.1: **Salinity and oxygen concentration along a mid-Atlantic Ocean depth-section derived from observations and in the ESM2M model.** (a) Mean salinity from observation-based reanalysis ORAS5. (b) Mean oxygen concentration from the World Ocean Atlas 2018 [45]. Schematic above (a, b) identifies 'salty-get-saltier' and 'fresh-get-fresher' regions. (c, e) Salinity trends from ORAS5 (1958-2017) and ESM2M Standard 1% experiment (200-year trend, five-member ensemble mean). (d, f) Oxygen trends from the observation-based product of [43] (1950-2016 trend where at least 20 points are available; hatched where significance does not exceed 25%), and ESM2M Standard 1% experiment (200-year trend, five-member ensemble mean). Section is at 25°W and extends into the Labrador Sea (see inset map next to a). Black lines water masses, defined in Methods; stippled region indicates Bottom Waters which we exclude from this study's analysis.

in salinity in the subtropical Atlantic was shown to efficiently de-stratify the surface layer despite the warming-driven stratification in a global climate model [49], which could potentially lead to deeper mixed layers and enhanced ventilation of the subsurface ocean by Mode Waters. At higher latitudes, the surface freshens [50, 51, 9, 52, 53, 54], enhancing warming-driven stratification and potentially weakening the ventilation of deeper layers by Intermediate and Deep Waters [55, 56, 57, 13, 58]. The amplification of the hydrological cycle and the associated surface salinity changes could therefore alleviate the warming-driven deoxygenation in salty water masses but reinforce it in fresher water masses.

Here, we use a global Earth System model (ESM2M) to quantify the effect of amplified SSS patterns on Atlantic Ocean deoxygenation. We compare a 'Standard' warming experiment in which the model evolves freely and SSS patterns amplify in response to atmospheric CO_2 increase (1% yr^{-1} CO_2 increase until doubling, then held constant for a total of 200 simulation years), to a 'Fix-SSS' experiment in which the same CO_2 increase is prescribed but SSS patterns do not respond and are instead restored to their pre-industrial climatological values [similarly to 49, see details in Methods]. While warming occurs in both experiments, the influence of the hydrological cycle amplification on the ocean only occurs in the Standard experiment (and not in Fix-SSS). In this comparison, we emphasize the contrast between the two saltier Atlantic water masses (Tropical and Mode) and the two fresher water masses (Intermediate and Deep), and establish a mechanistic link between hydrological cycle amplification, salinity changes, and pattern of ocean deoxygenation.

1.3 Methods

1.3.1 Model and Experimental Setup

We isolate the effect of hydrological cycle and SSS pattern amplification using two idealized ensemble experiments in the Geophysical Fluid Dynamics Laboratory (GFDL) Earth System Model, version 2M (ESM2M; source code is based on public release 5.0.2 and can be down-

loaded at github.com/mom-ocean/MOM5) [59, 60]. This version uses the Modular Ocean Model 5 (MOM5) with nominal 1 degree resolution (telescoping to 1/3 degree at the equator), Atmospheric Model 2 (AM2) with 2x2.5 degree resolution, Land Model 3 (LM3.0), and the Tracers of Ocean Phytoplankton with Allometric Zooplankton (TOPAZ) biogeochemical module [full description in the supplemental material of 60]. The model is initialized with a multicentury run from the same model, then spun up for approximately 200 model years with constant pre-industrial atmospheric CO_2 of 286 ppm. Drift in both physical and biogeochemical variables, estimated from the pre-industrial control run, are within the targets outlined in [60]. Specifically, global mean SST and SSS have no apparent drift (variability is within +/- 0.2 K and +/-0.02 psu), the global mean ocean temperature drifts by about 0.01 °C per century, and globally integrated oxygen content drifts by less than 1% per century. Linear drifts derived from the control run are removed from our results at each grid point.

Two transient ensemble climate change experiments are initialized from the spin-up: Standard and fixed sea surface salinity (Fix-SSS). In the Standard experiment, the atmospheric CO_2 concentration is increased at 1% per year until the CO_2 concentration doubles at year 70, after which the concentration is held fixed for 130 years, so the model run is 200 years long. The 'Fix-SSS' experiment is similar to the Standard run but SSS is nudged towards the pre-industrial climatology with a freshwater restoring flux (linear in time, with a 30-day timescale). Since the focus here is on changes in precipitation-evaporation tied to the hydrological cycle amplification, SSS is not restored at locations with seasonal sea ice (Figure 5 and supplemental text). Freshwater from sea ice melt that has been transported and led to freshening outside of the region of seasonal sea ice would be restored and attributed to the hydrological cycle amplification in our setup. This could slightly exaggerate the freshening and consequent impacts in the high latitude North Atlantic. However, our results suggest that the freshening in this region is due to a decrease in evaporation (Figure 2) associated with the cooling due to AMOC slowdown and that freshwater flux trends due to ice melt are relatively small.

The Standard experiment is used to quantify the total effect of climate change on ocean oxygen, which includes the effect of warming, the amplification of the hydrological cycle, as well as other forced changes in the earth system (e.g. sea ice melt, winds, circulation changes). Note that the freshening as a function of warming at polar latitudes may be underestimated (relative to reality) since ESM2M does not incorporate an interactive ice sheet model and therefore is missing the freshening due to ice melt. The effect of hydrological cycle amplification is quantified by the difference between the Standard and Fix-SSS experiments. The total climate effect and hydrological effect are designated as ΔX_{Clim} and ΔX_{Hydro} for any variable X. For example, ΔS_{Hydro} is positive where the ocean gets saltier as the climate system warms, and negative where the ocean gets fresher. To reduce the impact of internal variability in the model solutions, we run five ensemble members for each experiment branched from different years in the pre-industrial control spinup experiment (branched from spinup years 190, 191, 192, 194 and 196). Results are shown for the Atlantic Ocean using the mask shown in Figure 5. Model trends are computed over 200 model years (including the 70 years of CO_2 increase and another 130 years of constant CO_2 at 586ppm) in each member (after removing drift), and then averaged over the five members.

1.3.2 Atlantic Water Mass Definition

We define Atlantic water masses with density and salinity thresholds based on [61] but slightly adjusted for mean model bias (Figure 1.1e,f). Tropical Waters are defined as all waters lighter than $\rho_0 = 1025$ kg m^{-3}. Mode Waters are further delimited as saltier than 35 psu and lighter than $\rho_0 = 1027.7$ kg m^{-3}, while Intermediate Waters are fresher than 34.4 psu and lighter than $\rho_0 = 1027.7$ kg m^{-3}. Mode Waters here include northern and southern subtropical Mode Waters, as well as subpolar Mode Waters in the north Atlantic. Deep Waters include Upper Deep Waters, which are relatively light and can be found between Intermediate and Mode Waters, as well as waters denser than $\rho_0 = 1027.7$ kg m^{-3}. Finally, we remove Bottom Waters based on a threshold of potential density referenced to 2000 dbar

(ρ_2) of 1036.82 kg m^{-3}. The water mass definitions are stationary in time, determined by the time-mean physical sea state in the 200 year pre-industrial control run. See Figure 1.1e, f for a visualization of these water masses at 25°W.

In the observation-based data products, the relevant thresholds in salinity and density are not the same as in the model (which is, for example, biased slightly fresh relative to observations throughout the Atlantic Ocean) but match the observation-based definitions given by [61] (Figure 1.1a-d). Tropical Waters are, again, all waters lighter than 1025 kg m^{-3}. Mode Waters in the reanalysis, however, are defined to be saltier than 36.1psu, warmer than 8°C, and lighter than 1027.7 kg m^{-3}, while Intermediate Waters are fresher than 34.25 psu and lighter than 1027.7 kg m^{-3}. Deep Waters include the remaining volume between and denser than Mode and Intermediate Waters, but lighter than $\rho_2 = 1037$ kg m^{-3}. Water denser than this is considered Bottom Water. See Figure 1.1c, d for a visualization of these water masses at 25°W.

1.3.3 Drivers of O_2 changes

We attribute the changes in oxygen to changes in the saturated oxygen concentration ($O_{2,sat}$), which is primarily reflective of warming, changes in biological consumption or production of oxygen ($O_{2,bio}$), and changes in ventilation ($O_{2,vent}$).

$$\Delta O_2 = \Delta O_{2,sat} + \Delta O_{2,bio} + \Delta O_{2,vent}$$

$O_{2,sat}$ is estimated from monthly-mean conservative temperature and salinity using the Python implementation of the Gibbs Seawater Oceanographic Toolbox (gsw) for the Thermodynamics Equation of Seawater - 10 (TEOS-10) [62]. This calculation assumes saturation at the surface, which is a good assumption for the open ocean, although surface waters may be up to 30% below saturation in coastal waters and highly productive upwelling regions [Fig. 5d, e of 63]. $O_{2,bio}$ is provided by the biogeochemical module of ESM2M (TOPAZ), and

$O_{2,vent}$ is derived as the residual. This is very similar to the 'Apparent Oxygen Utilization' methodology [38, 64, 65], which groups the effects of biology and circulation together for applications where the impact of biology is unknown.

1.4 Salinity and oxygen track Atlantic ventilation changes

We compare the response to climate change (or 'climate effect') in ESM2M (200-year trend averaged across five ensemble members of the Standard experiment, with drift from the pre-industrial control removed) and the observation-based products (1950s-2010s trends) along a mid-Atlantic section that extends into the Labrador Sea and captures the pathways of the four main Atlantic water masses (Tropical, Mode, Intermediate, Deep; Figure 1.1). ESM2M reproduces the propagation of the surface salty-get-saltier and fresh-get-fresher signal into the ocean interior seen in the ORAS5 reanalysis, including the increase in salinity of Mode and Tropical Waters formed at tropical and subtropical latitudes where evaporation increases, and the strong freshening of Deep Waters that outcrop at higher northern latitudes where evaporation decreases (Figure 1.1c,e, see precipitation and evaporation changes in Figure 2). Differences exist, however, between the model and reanalysis. Notably, as the south Atlantic subtropical gyre expands and the boundary between Mode and Intermediate waters moves poleward [a feature supported by satellite and in-situ observations, 66, 10], it redistributes salt meridionally in the model (dipole of salinity change at $\sim$35°S, Figure 1.1e), but has no apparent effect on salinity in the reanalysis (Figure 1.1c).

Oxygen trends derived from the observation-based oxygen product of [43] are limited to parts of the upper 1000 m due to sparse data coverage and are often not statistically significant (Figure 1.1d). Yet, we find encouraging agreement between this dataset and the model. Both suggest a widespread oxygen loss along the mid-Atlantic section, but also pockets of oxygen gain in Mode and Deep Waters despite a general warming of these water masses (Figure 1.1d,f, see warming trends in Supplementary Material and Figure

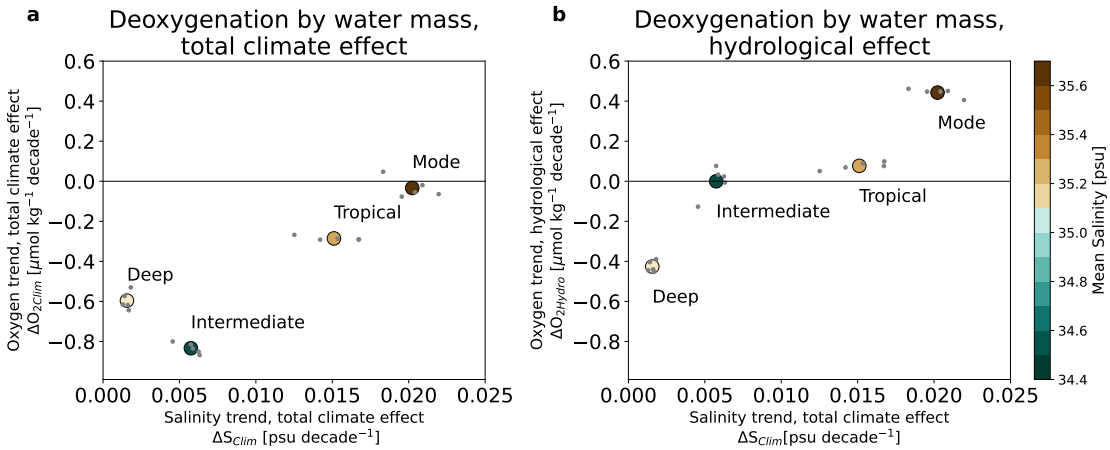


Figure 1.2: **Salty-get-saltier waters lose less oxygen than fresher waters experiencing near-zero salinity changes.** (a) Oxygen change vs. salinity change due to total climate effect (ΔS_{Clim}, and ΔO_{2Clim} corresponding to trends in Standard experiment) and (b) oxygen change due to hydrological effect alone (ΔO_{2Hydro}, difference between trends in Standard and Fix-SSS experiments) vs salinity change due to total climate effect (ΔS_{Clim}). Colors represent the mean salinity in the pre-industrial control experiment. Both panels show ΔS_{Clim} for consistency but note that the salinity trend due to the hydrological effect (ΔS_{hydro}) is nearly identical to ΔS_{Clim}. Colored dots represent 200-year trends, averaged within each water mass and across five ensemble members; grey dots represent the result from each ensemble member.

1). The patchiness of the observed and simulated oxygen changes shows that competing mechanisms are at play, and highlights the challenges associated with the quantification of ocean deoxygenation at each individual point in space. In the following, we employ the water mass framework that follows the ventilation pathways of the four main Atlantic water masses to link changes in hydrological cycle amplification, salinity, and oxygen.

1.5 Stronger deoxygenation in fresher water masses

When averaged over the full Atlantic basin, fresher water masses (Intermediate and Deep Waters) experience stronger deoxygenation and weaker salinity increase than saltier water masses (Tropical and Mode Waters) in response to climate change in the ESM2M model ('climate effect' ΔS_{Clim} and ΔO_{2Clim}, Figure 1.2 a). Salty Mode Waters become saltier and avoid deoxygenation (ΔS_{Clim} = +0.020 [0.015 to 0.022] psu decade^{-1}, ΔO_{2Clim} = -0.03 [-

0.08 to +0.05] μmol kg^{-1} decade^{-1}; mean and range of five ensemble members, see Figure 1.2a and Methods). This small simulated net change in oxygen is due to the opposing oxygenation and deoxygenation trends within the water mass, a result consistent with the observation-based product of ito2017upper and prior studies [Figure 1.1 d,f 41, 44]. Tropical Waters also become saltier but at a lower rate than Mode Waters (ΔS_{Clim} = 0.015 [0.013 to 0.017] psu decade^{-1}) and slightly lose oxygen (ΔO_{2Clim} = -0.28 [-0.29 to -0.27] μmol kg^{-1} decade^{-1}, Figure 1.2a). In contrast, fresh Intermediate and Deep waters are characterized by the weakest salinity changes ($\Delta S_{Clim} < 0.007$ psu decade^{-1}, Figure 1.2a), and the strongest deoxygenation rates (ΔO_{2Clim} = -0.83 [-0.87 to -0.80] and -0.60 [-0.64 to -0.53] μmol kg^{-1} decade^{-1}). The lack of a strict 'fresh-get-fresher' salinity change in Intermediate and Deep Waters in the model is consistent with the ORAS5 reanalysis (Figure 1.1c,e) as well as prior observation-based studies [8]. The Atlantic Ocean as a whole becomes saltier in contrast to the Pacific Ocean becoming fresher, which pushes surface salinity trends towards higher values across the Atlantic (although it still yields higher trends in saltier waters than fresher waters). In addition, the freshening of Intermediate Waters associated with the precipitation increase at the outcrop surface is offset by significant cross-isopycnal mixing with salty Mode Waters in the ocean interior - a process known to contribute significantly to the mean state and changes in this water mass [61, 67] - as well as the southward advection of Mode Waters into Intermediate Waters as the subtropical gyre expands polewards (Figures 1.1e and 1.3a).

We isolate the effect of salinity and oxygen changes associated with the hydrological cycle amplification or 'hydrological effect' from the total 'climate effect' using the difference between the Standard warming experiment and the Fix-SSS experiment in which sea surface salinity is restored towards its pre-industrial values (see Methods). The salinity trends associated with the hydrological cycle amplification (ΔS_{Hydro} in Figure 1.3a) closely match the salinity trends simulated in response to the full climate effect (ΔS_{Clim} in Figure 1.1e). This is consistent with the understanding that salinity trends under climate change are largely attributable to hydrological cycle amplification [9]. Oxygen changes due to the hydrological

effect scale with these salinity changes (Fig 1.2 b). This effect yields a strong oxygen gain in Mode Waters that experience rapid salinification (ΔO_{2Hydro} = +0.44 [+0.40 to +0.46] μmol kg^{-1} decade^{-1}), a near-zero change in Intermediate and Tropical Waters that experience milder salinification ($\Delta O_{2Hydro} < +0.10$ μmol kg^{-1} decade^{-1}), and a strong oxygen loss in Deep Waters that experience a near-zero salinification (ΔO_{2Hydro} = -0.43 [-0.45 to -0.39] μmol kg^{-1} decade^{-1}, Figure 1.2b). The hydrological cycle amplification therefore contributes to the net pattern of deoxygenation due to climate change, by modulating the amplitude of the oxygen loss due to the direct effect of rising ocean temperature (i.e., stratification increase and solubility decrease). Its impact is strongest in salty Mode Waters, where the oxygen gain due to the hydrological effect counteracts the warming-driven deoxygenation yielding a marginal net change in response to the full climate effect, as well as in fresh Deep Waters, where it accounts for more than half of the net simulated deoxygenation (Figure 1.2 a-b).

1.6 Influence of hydrological cycle amplification on ocean circulation and ventilation

The amplification of surface salinity patterns due to the hydrological effect enhances the ventilation of Mode Waters and weakens the ventilation of Deep Waters, by influencing both the depth of winter mixing in outcrop regions, and the strength of the shallow and deep overturning circulations carrying these water masses into the ocean interior. At northern mid-latitudes, where North Atlantic Mode Waters are formed, winter mixed layer depths (MLDs) during the last 50 years of simulation are deeper in the Standard warming experiment than in the Fix-SSS experiment ($\sim$50m deeper along mid-Atlantic section, solid grey line below dashed grey line in Figure 1.3a,b). This indicates that in these regions the effect of salinification (increases density and destabilizes upper ocean) exceeds the effect of warming [reduces density and stratifies upper ocean, see also 49]. In addition, we find that the

transport by the shallow overturning subtropical cells during the last 50 years of simulation is stronger in the Standard warming experiment (15.3 Sv) than in the Fix-SSS experiment (14.1, shallow overturning index calculated as the difference between the maximum of the Atlantic meridional overturning streamfunction between 12°N and 16°N and the minimum between 12°N and 16°S above 200 m depth; adapted from [68]). Together, these results suggest that both the formation and transport into the ocean's interior of Mode Waters is enhanced by the low- to mid-latitude 'salty-get-saltier' pattern.

In contrast, winter MLDs shoal as the surface freshens in regions of Deep Water formation, (solid grey line above dashed grey line in Figure 1.3a,b). In the Labrador Sea (above 55°N), winter MLDs shoal from 2000 m in the pre-industrial control to 500 m at the end of the Standard warming experiment in response to freshening and warming. This shoaling is less pronounced at the end of the Fix-SSS experiment in which the surface warms but does not freshen, shoaling to only 1000 m (Figure 1.3a,b), twice as deep as at the end of the Standard warming experiment. This result suggests that the 'fresh-get-fresher' effect weakens the formation rate of Deep Waters in the Labrador Sea. We also find that the strength of the deep Atlantic meridional overturning circulation (AMOC) is slightly weaker in the last 50 years of the Standard experiment than in the Fix-SSS experiment (by 0.6 Sv, AMOC strength estimated as the maximum of the streamfunction between 10 and 60°N over all depths, e.g. [59]). This slowing down of AMOC is consistent with idealized model 'hosing' experiments in which freshwater is added in large volumes to regions of Deep Water formation [58, 69]. The difference in AMOC between the two experiments presented here is small, but together with the changes in winter MLDs, it suggests that hydrological cycle amplification slightly reduces the formation rate of Deep Waters in the Atlantic Ocean on centennial timescale.

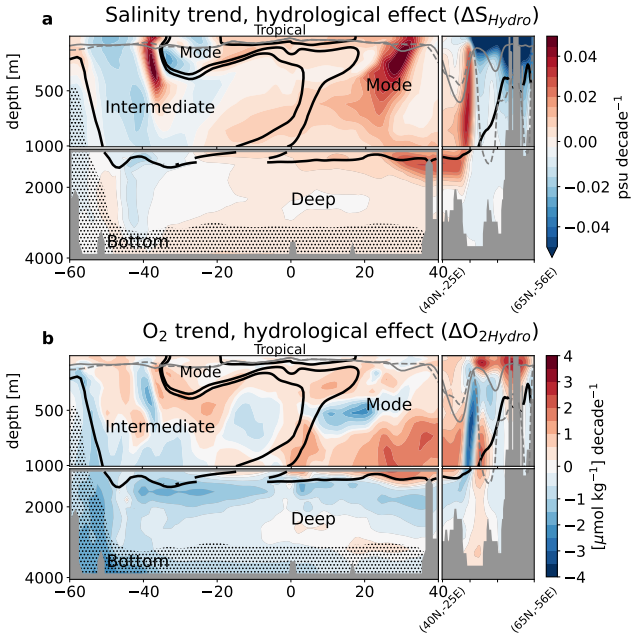


Figure 1.3: **Salinity and oxygen changes in response to hydrological effect along mid-Atlantic Ocean depth section.** Trends in (a) salinity and (b) oxygen from the hydrological effect (ΔO_{2Hydro}, ΔS_{Hydro}; 200-year trend in 'Standard' warming experiment minus 200-year trend in 'Fix-SSS' experiment, each averaged over five ensemble members). Water masses are outlined by black contours (see Methods). Grey lines represent annual maximum mixed layer depths in the last 50 years of each model experiment, with solid representing the Standard experiment and dashed representing the Fix-SSS experiment in both panels. Stippling represents Bottom Waters which we exclude from our analysis. Section is indicated by the black line in inset of Figure 1.1. Contributions from ventilation ($\Delta O_{2Clim,vent}$) and solubility ($\Delta O_{2Clim,sat}$) changes are shown in Figure 4.

1.7 Direct and indirect effects of the hydrological cycle amplification on ocean deoxygenation

Salinity-driven changes in ocean ventilation have a direct impact on ocean oxygen content by modulating the rate at which oxygenated waters are subducted and transported by each water mass, but also indirect effects via oxygen solubility and biological demand. Because hydrological changes slightly alter the ocean circulation, they influence the ocean heat uptake and temperature of the different water masses [49], and consequently the oxygen solubility. These changes in circulation and temperature can also modulate biological production and respiration. We can attribute the simulated changes in oxygen in response to the hydrological effect to these three factors, i.e. changes in ventilation ($\Delta O_{2Hydro,vent}$, dark blue bars in Figure 1.4b), solubility ($\Delta O_{2Hydro,sat}$, light blue bars in Figure 1.4b), and changes in biological activity which we find have a negligible effect here except in Tropical Waters ($\Delta O_{2Hydro,bio}$, green bars in Figure 1.4).

The salinity-driven increase in ventilation in Mode Waters (deeper winter mixed layers and stronger shallow overturning circulation; Figure 1.3b and section 1.6) also enhances their heat uptake and temperature (Figure 1). The oxygen gain associated with the hydrological effect in Mode Waters (ΔO_{2Hydro} = +0.44 [+0.4 to +0.46] umol kg^{-1} decade^{-1}) therefore arises from the partial compensation between a strong gain tied to enhanced ventilation ($\Delta O_{2Hydro,vent}$ = +0.68 [+0.65 to +0.71] μmol kg^{-1} decade^{-1}) and a weaker loss tied to solubility changes ($\Delta O_{2Hydro,sat}$ = -0.23 [-0.25 to -0.20] μmol kg^{-1} decade^{-1}, Figures 1.2b and 1.4). In contrast, the hydrological effect weakens the ventilation of Deep Waters (shallower winter mixed layer and slightly weaker AMOC, Figure 1.3b and section 1.6) and reduces the temperature of the Labrador Sea (north of 40N in Figure 1). Yet, weakened mixing with very cold Bottom Waters in the Standard experiment (relative to the Fix-SSS) leads to a weak warming of most of the Deep Waters volume, which exceeds the more localized cooling in the formation regions (Figure 1). As a result, these two hydrological effects (ventilation

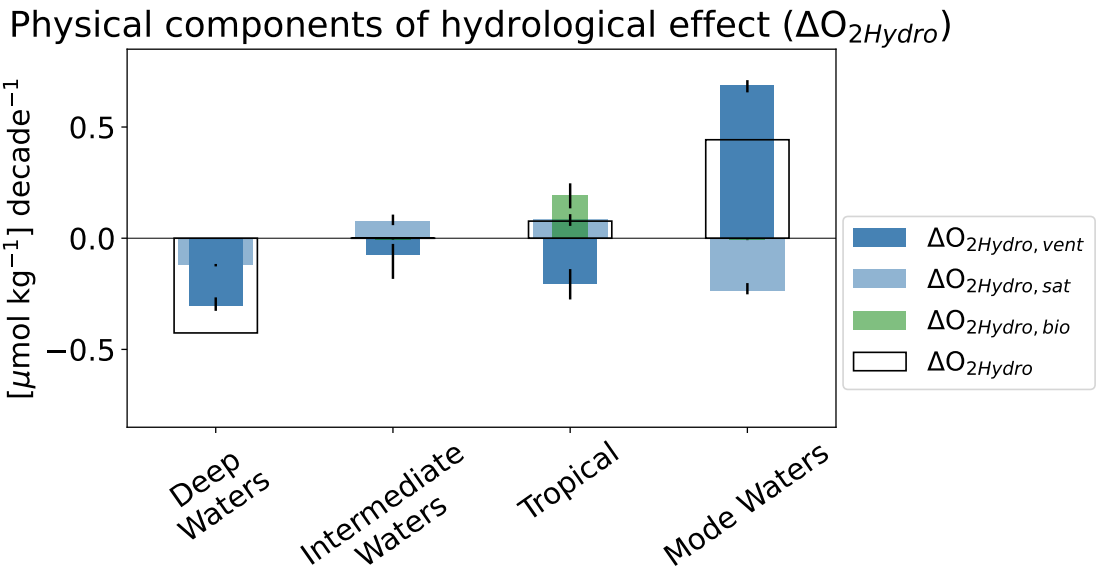


Figure 1.4: **Drivers of (de)oxygenation in Atlantic water masses due to the hydrological effect.** Oxygen trends attributed to the hydrological effect (ΔO_{2Hydro}, black outlined box, the same values as in Figure 1.2b), separated into contributions from ventilation ($\Delta O_{2Hydro,vent}$, dark blue), solubility ($\Delta O_{2Hydro,sat}$, light blue) and biological activity ($\Delta O_{2Hydro,bio}$, green). $\Delta O_{2Hydro,bio}$ is only significant in Tropical Waters (2-4 orders of magnitude smaller than the other terms in other water masses). Bars represent 200-year trends, averaged within each water mass and across five ensemble members; black error bars show the range across the ensemble. The components of $\Delta O_{2,Clim}$ are shown in Figure 3 ($\Delta O_{2Clim,sat}$, $\Delta O_{2Clim,vent}$, and $\Delta O_{2Clim,bio}$).

and solubility) yield a loss of oxygen in Deep Waters, with ventilation contributing about 60% ($\Delta O_{2Hydro,vent}$ = -0.3 [-0.33 to -0.27] μmol kg^{-1} decade^{-1}, $\Delta O_{2Hydro,sat}$ = -0.12 [-0.13 to -0.12] μmol kg^{-1} decade^{-1}, Figure 1.4). This compensation in oxygen solubility changes between the deep interior ocean and formation region might be specific to the ESM2M model and should be interpreted with caution, since the pre-industrial drift we remove in Bottom Waters is greater than half the magnitude of the hydrological effect itself. Despite this uncertainty in net solubility changes, ventilation changes control the oxygenation changes due to the hydrological effect in both Mode and Deep Waters.

In the model, the hydrological effect has little or no influence on the oxygenation of Intermediate and Tropical Waters, due to the near complete compensation between the different contributions (ventilation, solubility and biology, Figure 1.4). In Intermediate Wa-

ters, a small decrease in oxygen supply by ventilation ($\Delta O_{2Hydro,vent}$ = -0.07 [-0.18 to -0.03] umol kg^{-1} decade^{-1}) is entirely opposed by an equally small increase in oxygen solubility ($\Delta O_{2Hydro,sat}$ = +0.08 [+0.06 to +0.11] umol kg^{-1} decade^{-1}). The small ventilation change simulated here (despite a clear surface freshening, Figure 2) is due to the offsetting effects of the surface freshening, which causes a mild ventilation decrease and oxygen loss over much of the volume of Intermediate Waters, and a smaller volume of strong salinification and oxygenation caused by the poleward advection of, and mixing with, Mode Waters (see section 2, Figure 1.3e). Similarly, the small solubility change is tied to the surface freshening, which causes a decrease in ocean heat uptake and cooling (but is partly offset by the intruding and rapidly warming Mode Waters, Figure 1c). In Tropical Waters, the hydrological effect weakens the supply of oxygen by ventilation ($\Delta O_{2Hydro,vent}$ = -0.20 [-0.28 to -0.14] umol kg^{-1} decade^{-1}), but also slightly increases oxygen solubility ($\Delta O_{2Hydro,sat}$ = +0.08 [+0.05 to +0.11] umol kg^{-1} decade^{-1}) and lowers the biological consumption of oxygen (cooling slows respiration, $\Delta O_{2Hydro,bio}$ = +0.19 [+0.13 to +0.25] umol kg^{-1} decade^{-1}). The decrease in ventilation is inconsistent with the stratification change, and is likely due to a slight difference in surface winds. The slight cooling and consequent increase in oxygen solubility at the surface in response to the hydrological effect (i.e. the Standard experiment with hydrological amplification warms less than the Fix-SSS experiment) is balanced by a global increase in ocean heat uptake in subducted water masses [see also 49, 70].

1.8 Conclusion

The patterned change in oxygen in response to the hydrological cycle amplification identified here adds important nuance to the baseline expectation that warming-driven decreases in both solubility and ventilation cause widespread deoxygenation [71, 72, 28, 29, 15]. The oxygenation of Atlantic Mode Waters in response to climate change observed in nature, and previously unexplained [41], can be accounted for by the increase in ventilation of 'salty-

get-saltier' water masses. In contrast, 'fresh-get-fresher' Deep Waters experience weakening ventilation and enhanced deoxygenation.

The exact magnitude of this oxygen redistribution due to hydrological cycle amplification is subject to uncertainty. The increase in salinity in Mode Waters simulated in the model is lower than in the observation-based products (Figure 1.1c,e). This underestimation of the hydrological cycle amplification and associated low latitude salinification in the model is partly due to the slower warming simulated in the 200-year Standard 1% experiment (global surface warming of 0.1K per decade) relative to the historical period (global surface warming of 0.2K per decade for 1960-2018, [73]). As a result, the increase in ventilation and oxygenation associated with the hydrological effect in Mode Waters might be even stronger in nature. In contrast, the simulated freshening of Deep Waters attributed to hydrological cycle amplification in the model might be overestimated, because part of the signal might be associated with the transport of freshwater originating from sea ice melt in the Arctic (poleward of 80°N; see details on surface salinity restoring in Methods).

In the Indo-Pacific ocean basins, SSS changes will also affect surface seawater density, and impact ocean stratification and ventilation. Projected SSS changes in the Pacific and Indian Oceans are, however, weaker than in the Atlantic [8], so the contribution to oxygen changes is expected to be weaker in those basins. On the century timescales considered here, the hydrological cycle amplification is the main driver of salinity changes. In the coming century, ice sheet melt can be expected to reinforce high-latitude freshening [74] and potentially further weaken the ventilation and oxygenation of the deep water masses formed at high latitudes.

1.9 Supplemental information

1.9.1 Temperature trend in the Atlantic Ocean at 25°W

The Atlantic Ocean warms in both the observation-based reanalysis ORAS5 (1958-2017) and the ESM2M model (200-year trend in Standard experiments) (Figure 1.5a, b), with the exception of the North Atlantic around 50°N, which cools in ESM2M and has no temperature change in ORAS5. This lack of warming is consistent with the slight weakening of the Atlantic Meridional Overturning Circulation and associated decrease in northward heat transport and local cooling ['warming hole,' 55]. The hydrological effect alone in ESM2M (difference between Standard and Fix-SSS experiments) acts to enhance ocean warming below about 500-700m depth but weaken warming above (Figure 1.5c), consistent with prior studies [49, 70]. This surface cooling explains the increased $\Delta O_{2Hydro,sat}$ in Tropical Waters (see Figure 4 and Section 4 in main text).

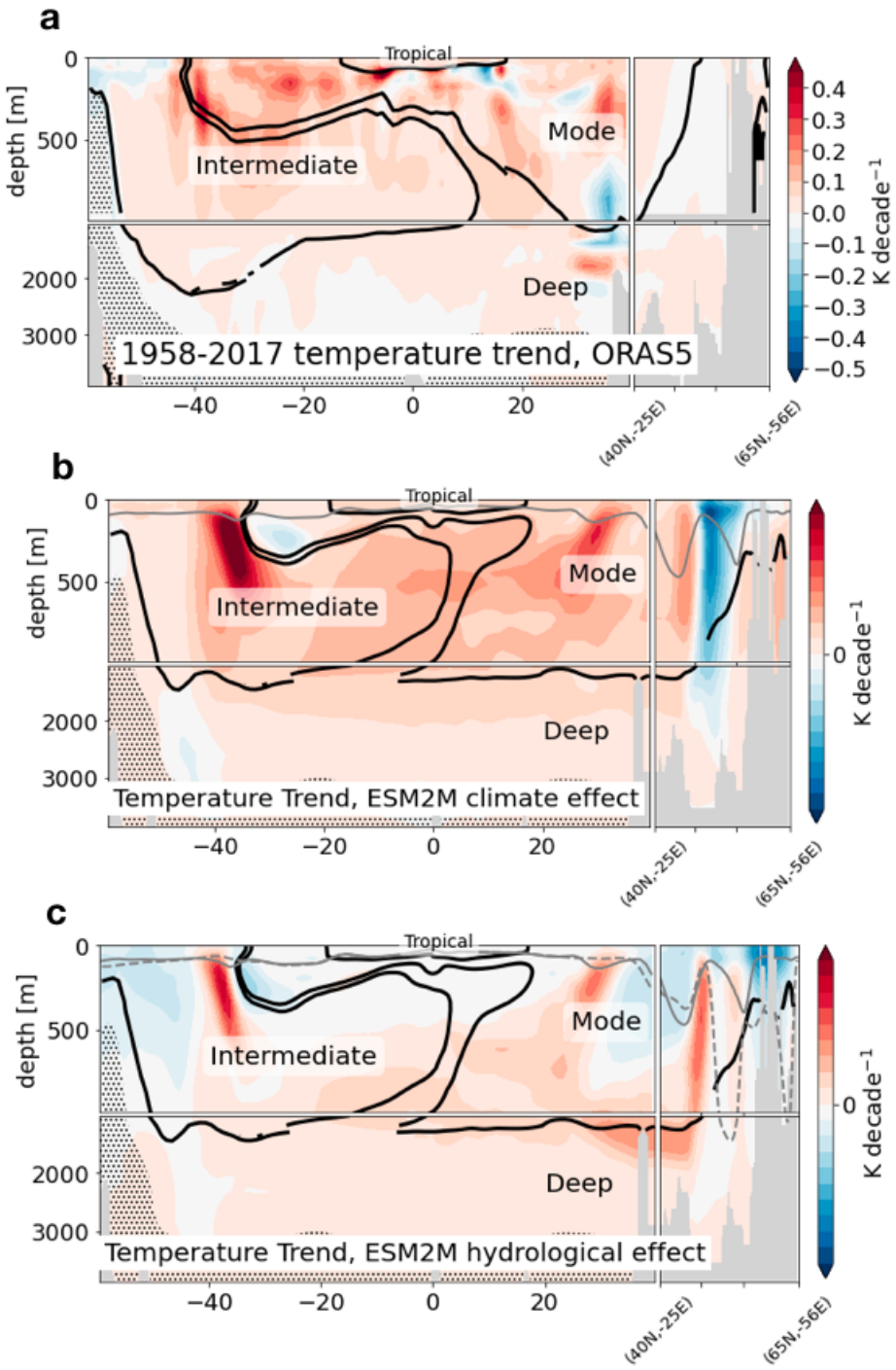


Figure 1.5: **Warming along mid-Atlantic Ocean section.** (a) ORAS5 historical temperature trend (1958-2017), (b) ESM2M temperature trend due to total climate effect (200-year trend in the Standard experiment, averaged across 5 members), (c) ESM2M temperature trend due to hydrological effect (Difference in 200-year trends between the Standard and Fix-SSS experiments, averaged over 5 members for each experiment).

1.9.2 Contribution of precipitation, evaporation, ice melt to sea surface salinity trends

The future projection of a 'salty-get-saltier and fresh-get-fresher' SSS trend is based on the expected evolution of the net air-sea freshwater flux [47] but does not specify the relative contribution of changes in evaporation vs. changes in precipitation. We qualitatively assess trends in evaporation and precipitation (liquid and frozen) as well as the contribution of sea ice melt and freshwater input from land (calving+runoff) which can reinforce or offset the amplification of SSS patterns expected from evaporation and precipitation (Figure 1.6a-d). The strong subtropical SSS increase which increases the ventilation of Mode Waters (Figure 1) is driven by an increase in evaporation and partly opposed by an increase in precipitation (Figure 1.6a-c). We note that the clear increase in precipitation in the equatorial band (which is expected from the evaporation-precipitation amplification argument) does not yield a significant freshening (Figure 1), most likely due to the advection of saltier water from the subtropics by the mean circulation. At higher latitudes, the freshening is driven by a decrease in evaporation in the northern hemisphere where Deep Waters outcrop (although precipitation changes modulate the the zonal pattern of SSS change). In contrast, the surface freshening in the southern hemisphere where Intermediate Waters outcrop is associated with a precipitation increase.

Long-term trends in ice melt, runoff, and calving do not strongly affect the modeled SSS trends, since they are dominated by the retreat of the sea ice edge (i.e. change in location of freshwater input) rather than a secular increase or decrease in freshwater input (brown/green dipole in the Labrador and Irminger Seas, and Weddell Gyre, Figure 1.6d). In fact, the North Atlantic freshening is locally opposed by a decrease in freshwater input from ice melt, calving, and runoff (>50°N; grey in Supplemental Figure 1.6e). However, melt water from long-term sea ice loss in the Arctic (>70°N) could be transported south and enhance the North Atlantic freshening. Similarly, in the South Atlantic, the sea ice edge

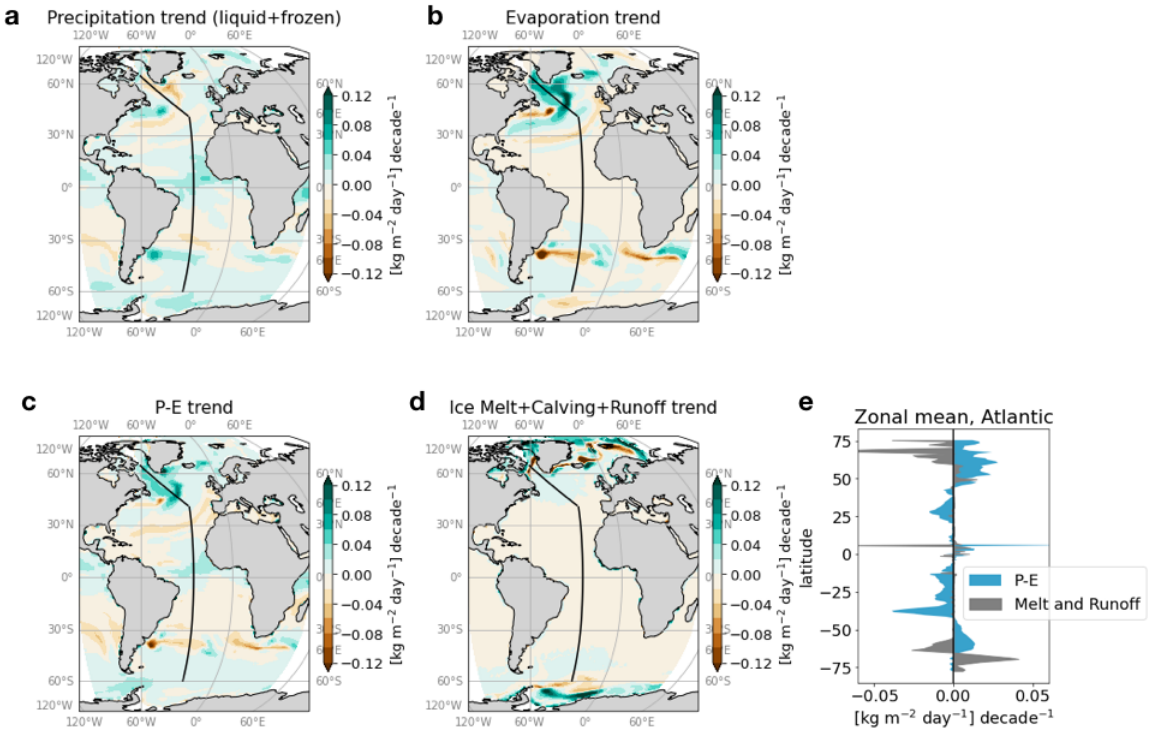


Figure 1.6: **Freshwater flux trends in response to CO_2 forcing.** 200-year freshwater flux trends in the Standard 1%-to-doubling experiment.

retreat leads to a strongly offsetting positive and negative freshwater flux trend, which we expect has a small effect on salinity trends in Intermediate Waters.

1.9.3 Ventilation changes in climate effect largely attributed to hydrological effect

Figure 3a in the main text compares the total oxygen changes due to the climate effect and hydrological effect while Figure 3b breaks down the oxygen change due to the hydrological effect in terms of contributions from ventilation, saturation, and biology ($\Delta O_{2Hydro,vent}$, $\Delta O_{2Hydro,sat}$, $\Delta O_{2Hydro,bio}$). Here, in Figure 1.7 we provide the contributions from ventilation, saturation, and biology to the climate effect. We note in particular that the increased ventilation due to the hydrological effect in Mode Waters appears to drive a similar ventilation increase in Mode Waters in the total climate effect. This hydrological cycle - driven ventilation increase is opposed by the decline in solubility of oxygen, so that there is no net change in oxygen in Mode Waters in the climate effect. Similarly, the decreased ventilation in Deep Waters due to the hydrological effect appears to explain much of the ventilation decrease in the total climate effect. In the total climate effect, the ventilation decline doubles the oxygen loss due to solubility alone. Illustrative visual sections through the mid-Atlantic Ocean showing the total response of oxygen to the climate effect and the hydrological effect, are provided in the main text (Figure 3). Here in Figure 1.8 we provide visuals along the same section of the contributions from $\Delta O_{2Clim,vent}$ and $\Delta O_{2Clim,sat}$, as well as $\Delta O_{2Hydro,vent}$ and $\Delta O_{2Hydro,sat}$.

1.9.4 Masks for SSS restoring setup and Atlantic Ocean analysis

In this study, we link the robust 'salty-get-saltier, fresh-get-fresher' SSS trend patterns to ocean ventilation and oxygen content by restoring SSS to its pre-industrial climatological values. The thermodynamic argument supporting the amplification of the hydrological cycle does not apply to changes in freshwater flux tied to seasonal sea ice formation and melt, and how they would evolve in response to warming. Consequently, the SSS restoring is only applied to regions that do not experience seasonal sea ice in our pre-industrial control

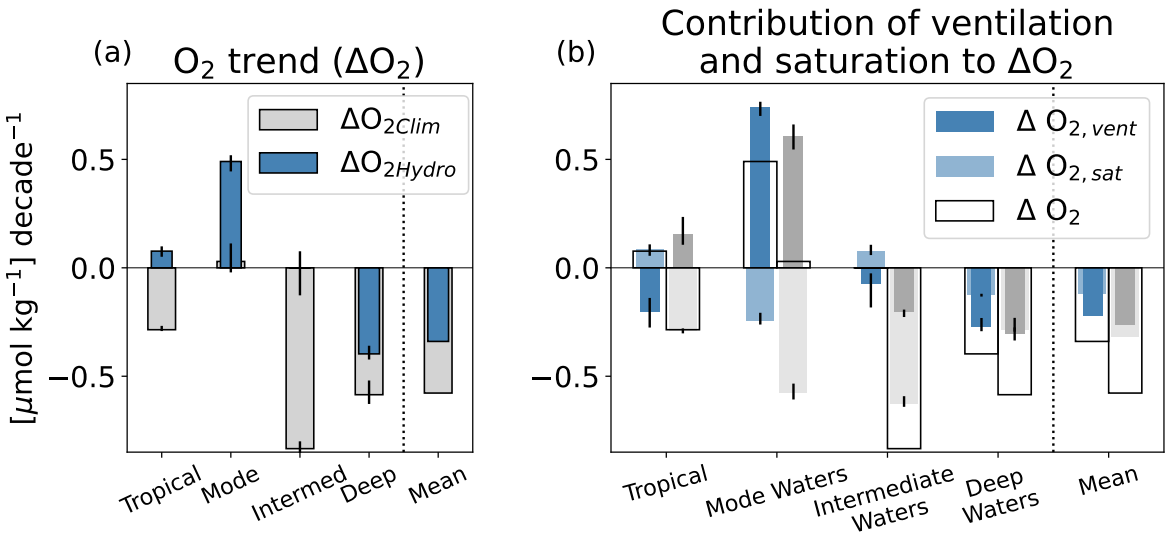


Figure 1.7: **Mean trends in (de)oxygenation and drivers.** (a) Ensemble mean change in oxygen in Atlantic Ocean water masses due to climate effect (grey) and hydrological effect (blue), as in Figure 4a. (b) Contribution of ventilation (bold) and saturation (faded) to climate effect (grey) and hydrological effect (blue). Contribution of biological activity to climate effect and hydrological effect is also shown in green. Black outlines indicate the total oxygen change in panel (a), which is the sum of the three components. Error bars represent the range across five ensemble members.

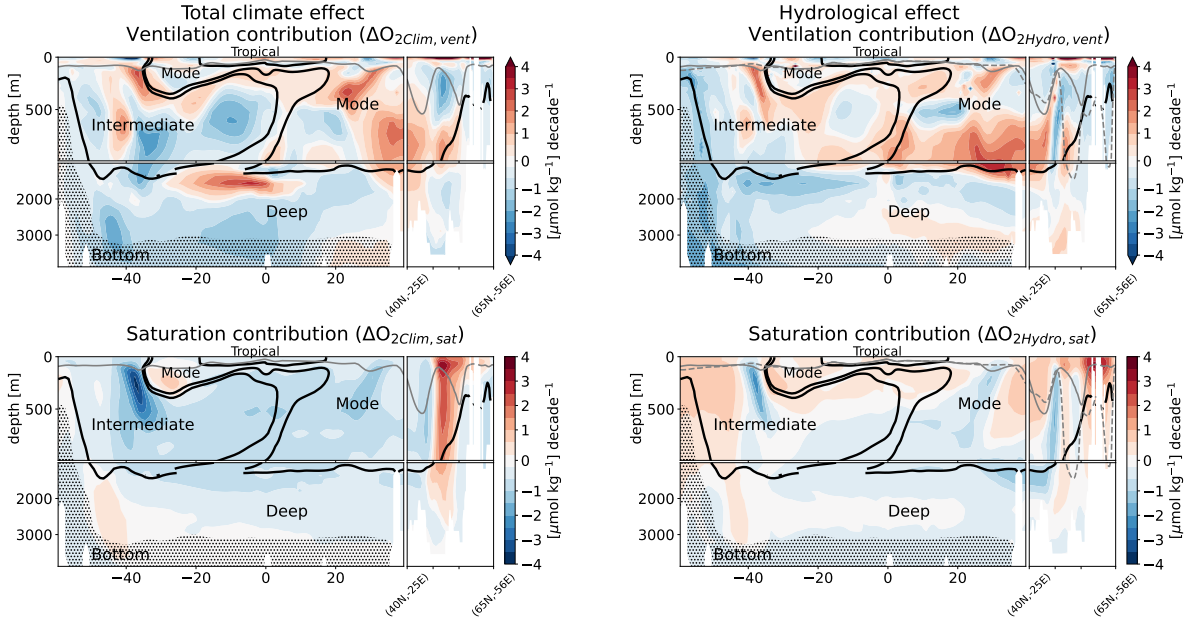


Figure 1.8: **(De)oxygenation due to ventilation change and saturation change along Atlantic Ocean section.** The contributions of ventilation and saturation to the oxygen changes in Figure 3 c, d.

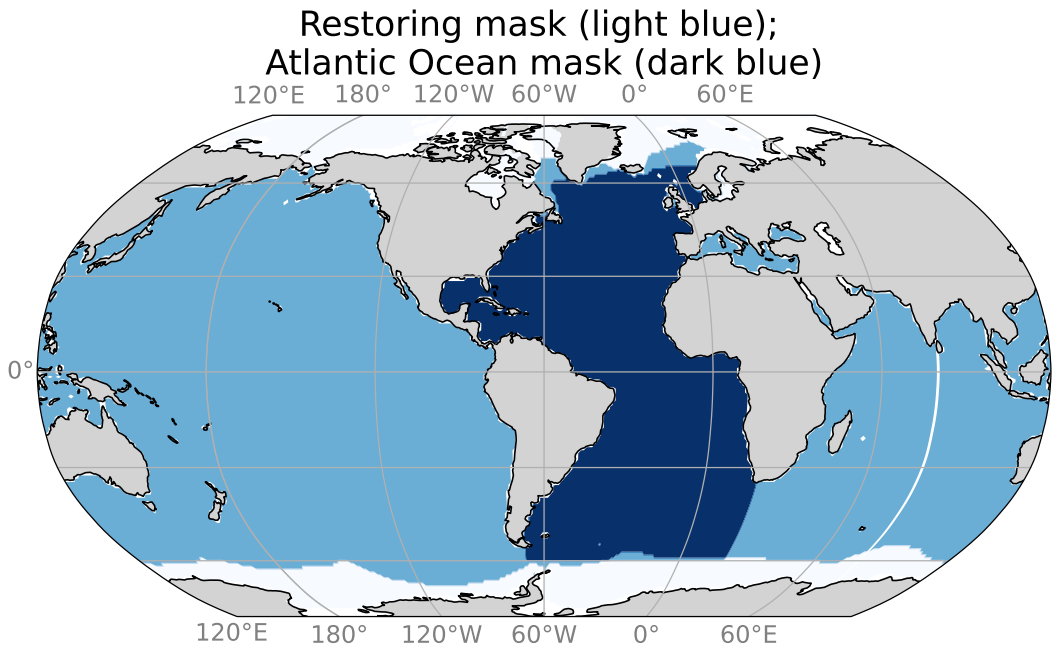


Figure 1.9: **Mask of SSS restoring location, and Atlantic Ocean.** Global restoring of sea surface salinity is only applied in the light and dark blue locations, but is not applied where there is seasonal sea ice in pre-industrial control run (white regions). Dark blue mask based on 'regionmask' Python package is used to isolate Atlantic Ocean water masses in Figures 2,4, and Supplemental Figure 3.

experiment (light blue color in Figure 1.9). The mask used to define the Atlantic Ocean in this study is based on the 'regionmask' Python package and shown by the darker blue area in Figure 1.9.

2

Carbon: Influence of hydrological cycle amplification on ocean pH and carbonate chemistry

2.1 Abstract

The invasion of anthropogenic carbon into the global ocean and the associated changes in pH and carbonate chemistry are largely controlled by the increase in atmospheric CO_2 concentration, but climate change further modulates the magnitude and regional patterns of acidification and chemical changes. Notably, global warming slightly weakens the air-sea CO_2 flux and weakens the large-scale circulation. However, warming alone does not fully account for the projected regional patterns in carbonate chemistry and pH in response to climate change. In addition to warming, climate models project an amplification of the

hydrological cycle (air-sea freshwater fluxes), which has the potential to introduce patterns in seawater chemistry. Here we use an Earth System Model to suggest that this hydrological cycle amplification can account for the bulk of the regional patterns in carbonate chemistry and pH which are not explained by the CO_2 increase and warming alone.

2.2 Introduction

The ocean has absorbed 25-30% of anthropogenic CO_2 emissions, slowing warming in the surface atmosphere but decreasing the pH ($-\log_{10}[H^+]$) of the ocean [75, 76]. This ocean acidification has especially adverse effects on marine organisms that secrete calcium carbonate shells, as calcium carbonate is less stable at lower pH, and can also have ripple effects throughout the ecosystem [77]. The rates of carbon uptake and ocean acidification in response to anthropogenic forcing are largely determined by the rate of CO_2 emissions, which directly increases the partial pressure gradient of CO_2 across the sea surface and leads to a flux of CO_2 into the ocean, which can be considered the direct 'CO_2 effect'. As the ocean warms, it absorbs CO_2 more slowly but acidifies more quickly. This modulation of the direct CO_2 effect by warming, as well as other physical and biological changes that accompany a CO_2 increase, can be considered the effects of climate change, a 'climate effect' [78, 79, 80] ('carbon-climate feedback' in these studies). Globally, the climate effect is relatively small in climate models (up to 10% of the direct CO_2 effect, depending on the variable of interest; [80]), but with strong regional variation in magnitude.

Prior work has attributed regional trends in DIC, Alkalinity (the charge balance of seawater which represents its capacity to buffer acids), and pH to shifts in surface winds, biological activity, and ocean circulation, both over the historical period and in future projections [81, 82, 83, 84]. However, models disagree on the changes in magnitude and spatial pattern of future changes in these processes, and the evolution of the spatially-resolved climate effect in carbonate chemistry remains uncertain as a result [82, 85].

A robust feature of climate change projections that has been shown to strongly modulate the climate effect (in temperature) is an amplification of the hydrological cycle [49, 70]. We explore its impacts on carbonate chemistry and pH, and show that the freshwater fluxes and temperature changes associated with hydrological cycle amplification may explain much of the regional pattern in the climate effect in carbonate chemistry and pH. This 'amplification of the hydrological cycle' refers to enhanced spatial patterns of net air-sea freshwater fluxes (precipitation-evaporation) [6, 7]. These freshwater fluxes amplify pre-existing mean spatial patterns of sea surface salinity (SSS) at low and mid latitudes where the hydrological cycle is strongest [8] (see also Figure 2.1a), leading to a 'salty-get-saltier, fresh-get-fresher' rule of thumb for SSS changes.

Hydrological cycle amplification could influence regional patterns in the climate effect in carbonate chemistry in two ways. First, freshwater fluxes can directly change the concentration of dissolved carbonate species, potentially increasing the concentration of DIC and Alkalinity in 'salty-get-saltier' regions and decreasing the concentration of DIC and Alkalinity in 'fresh-get-fresher' regions, with opposing effects on pH. Second, these changes in salinity modify the ocean circulation, enhancing ocean heat uptake in the subsurface subtropical Atlantic Ocean and weakening the surface atmospheric warming [49, 70] (see also Figure 2.1b). This relative cooling could drive increases in surface DIC and pH that oppose the decreases due to warming in the climate effect. Here, we use a global Earth System Model to quantify the contribution of freshwater fluxes and thermal effects to DIC, Alkalinity, and pH changes in the climate effect and the hydrological effect, to better understand the mechanisms that drive large-scale regional patterns. After demonstrating the surface DIC and Alkalinity responses to hydrological cycle amplification, we tie these changes to their impacts on surface pH and subsurface carbon storage. Our results suggest that hydrological cycle amplification tends to strengthen the net acidification due to the climate effect in regions that freshen, and weaken this acidification in regions that salinify. It also tends to enhance the efficiency of DIC storage in intermediate-depth water masses, regardless of salinity change, due to a

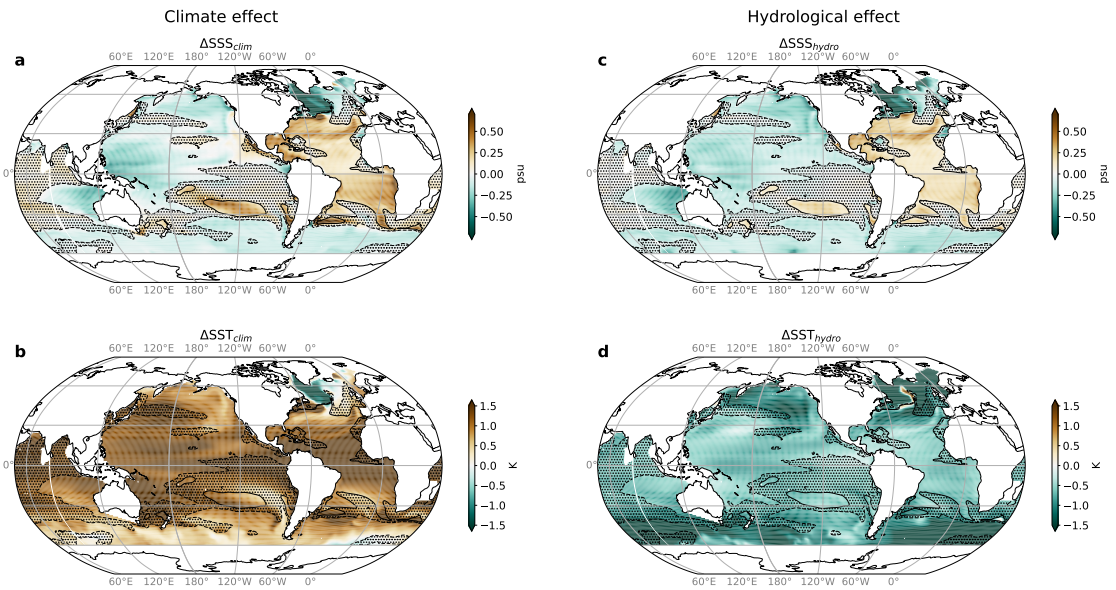


Figure 2.1: **Sea surface salinity (SSS) and temperature (SST) changes associated with climate and hydrological effects.** (a, b) SSS and SST change with climate effect (Standard minus Fix-Clim experiments) which includes hydrological effect and other changes, notably global warming; (c, d) SSS and SST change with hydrological effect (Standard minus Fix-SSS experiments), which weakens surface warming and reinforces SSS patterns. Black contours indicate $\Delta\text{SSS}_{hydro} = +0.1$ psu (solid) or -0.1 psu (dashed). Stippling indicates regions where ΔSSS_{hydro} is small ($|\Delta\text{SSS}_{hydro}| < 0.1$ psu); these regions are excluded from later analysis. Non-stippled areas (where $|\Delta\text{SSS}_{hydro}| > 0.1$ psu) are used to define 'saltier' and 'fresher' regions in later figures.

favorable offset between ocean heat uptake and dilution due to freshwater fluxes over the outcrop region.

2.3 Methods

2.3.1 Earth System Model and experiments to isolate hydrological and climate effects

We use the Geophysical Fluid Dynamics Laboratory Earth System Model 2M (ESM2M), which is fully described in [59, 60]. The version of ESM2M used here (public release 5.0.2) uses the atmosphere model AM2 with a horizontal resolution of approximately 50 km, and

ocean model MOM5 with a horizontal resolution of approximately 100km, as well as the land model LM3.0 and ocean biogeochemical model TOPAZ2. In order to isolate the signature of increasing atmospheric CO_2 and the associated amplification of the hydrological cycle, we force the model with a strong atmospheric CO_2 increase of 1% per year, beginning from the pre-industrial concentration of 286 ppm, until the CO_2 level doubles after 70 years. During years 71-100 the CO_2 level is held fixed at double the pre-industrial concentration (562 ppm), so that the entire experiment is 100 years long. We compare three different experiments with this 1%-to-doubling CO_2 forcing.

In the first experiment, the model freely responds to the prescribed atmospheric CO_2 ('Standard'), and the strength of the hydrological cycle intensifies with warming, amplifying patterns of freshwater fluxes and SSS. In the second experiment, SSS is nudged towards its pre-industrial monthly climatology with a restoring flux of freshwater ('Fix-SSS') as CO_2 increases along the same 1%-to-doubling trajectory. There is no restoring under seasonal sea ice. The freshwater restoring flux dilutes (or concentrates) all chemical species, although SSS is used to determine its strength. The difference between the Standard and Fix-SSS experiments provides an estimate of the impact of the hydrological cycle amplification on the ocean (including the direct freshwater flux and ocean circulation adjustment), and for a given variable X we define the change due to hydrological cycle amplification, the 'hydrological effect', in terms of the difference between these two simulations:

$$\Delta X_{hydro} = X_{Standard} - X_{Fix-SSS}$$

To contextualize the hydrological effect as a part of the total carbon-climate feedback, or 'climate effect', we also run a 'Fixed-Climate' experiment in which the same 1% to doubling atmospheric CO_2 increase interacts with ocean biogeochemistry but not with radiation so that there is no global warming (no change in climate). In this experiment, the ocean experiences carbon uptake due to atmospheric CO_2 increase, but no warming or hydrological

cycle amplification. The climate effect can therefore be defined [as in e.g. 70, 80, 82] by

$$\Delta X_{clim} = X_{Standard} - X_{Fix-Clim}$$

In this framework, we define $X_{Standard}$, $X_{Fix-Clim}$ and $X_{Fix-SSS}$ using the average over the last 30 years of each simulation (years 71-100) when atmospheric CO_2 is held steady at double the pre-industrial concentration and the system is beginning to equilibrate at this higher CO_2 level, to decrease the influence of internal variability or rapid adjustments to forcing. Results are presented between 55°S and approximately 60°N (following the contours of the North Atlantic basin) where the hydrological cycle is most active and the amplification of evaporation/precipitation patterns is most relevant, and remove high latitudes where the surface freshwater balance is instead dominated by ice-ocean interactions (see mask Figure 2.1).

ΔX_{clim} includes a contribution from ΔX_{hydro} as well as from other changes. For instance, the climate effect includes a significant surface warming, so that $\mathrm{SST}_{Standard}$ exceeds $\mathrm{SST}_{Fix-Clim}$ and $\Delta\mathrm{SST}_{clim}$ is positive (Figure 2.1c). However, hydrological cycle amplification moderates surface warming [70, 49], so that the global mean $\mathrm{SST}_{Standard}$ at the end of the Standard simulation is less than the mean $\mathrm{SST}_{Fix-SSS}$ simulated in response to CO_2 doubling but without hydrological amplifcation, and $\Delta\mathrm{SST}_{hydro}$ is negative (Figure 2.1d). Find further details on the Standard, Fix-SSS and Fix-Climate experiments in Chapter 1.

2.3.2 Freshwater and thermal contributions to DIC and Alkalinity changes

We quantify the influence of freshwater fluxes (dilution/concentration of DIC and Alkalinity) and temperature changes on DIC and Alkalinity in both the hydrological effect (whose influence is limited to these two changes) and the climate effect (whose influence is largely described by these two changes, but may also include other mechanisms e.g. CO_2 fluxes).

DIC is affected by both freshwater fluxes and temperature changes, so that we can decompose ΔDIC_{hydro} as follows:

$$\Delta DIC_{hydro} = \Delta DIC_{FW,hydro} + \Delta DIC_{thermal,hydro} + R_{DIC,hydro}$$

where $\Delta DIC_{FW,hydro}$ and $\Delta DIC_{thermal,hydro}$ correspond to contributions from dilution or concentration by freshwater fluxes (FW) and changes due to a temperature change (thermal). The residual R includes all other processes that affect DIC and Alkalinity (e.g., air-sea fluxes of CO_2, calcium carbonate dissolution, biological usage or re-mineralization of carbon, and salinity) as well as co-variations between the thermal and freshwater effects and errors in our method of estimating these effects.

In contrast, Alkalinity is not directly sensitive to temperature so that its hydrological effect can be approximated as:

$$\Delta Alk_{hydro} = \Delta Alk_{FW,hydro} + R_{Alk,hydro}$$

In analogy, we can attribute the total climate effect in DIC and Alkalinity to freshwater and thermal effects:

$$\Delta DIC_{clim} = \Delta DIC_{FW,clim} + \Delta DIC_{thermal,clim} + R_{DIC,clim}$$

$$\Delta Alk_{clim} = \Delta Alk_{FW,clim} + R_{Alk,clim}$$

The various residuals R are quantified in Figures S1 and S2. We are largely successful in reconstructing the hydrological effect, and R is generally small relative to ΔDIC_{hydro} and ΔAlk_{hydro} (error <5 μmol/kg at a point relative to total changes of 15-40 μmol/kg; Figures 2.2, 2.7). The error is somewhat more significant in reconstructing the climate effect (ΔDIC_{clim} and ΔAlk_{clim}) (Figure 2.8), especially for DIC (error <8 μmol/kg). This is most likely due to the fact that the climate effect leads to anomalous air-sea CO_2 fluxes which

change DIC and can indirectly lead to changes in Alkalinity.

We quantify the effect of freshwater fluxes on Alkalinity and DIC ($\Delta\text{Alk}_{FW,hydro}$, $\Delta\text{DIC}_{FW,hydro}$, $\Delta\text{Alk}_{FW,clim}$, $\Delta\text{DIC}_{FW,clim}$) with a simple conservation argument: if the quantity of DIC, Alkalinity, or salt in a model grid box remained constant, but a freshwater flux into or out of that grid box changed the concentration of each one, then they would all be diluted by the same fraction that can be evaluated from salinity (S) as

$$\begin{aligned} f_{FW,hydro} &= \Delta\text{S}_{hydro}/\text{S}_{Fix-SSS}, \\ f_{FW,clim} &= \Delta\text{S}_{clim}/\text{S}_{Fix-Clim} \end{aligned} \tag{2.1}$$

For example, if a freshwater flux into the surface in the Standard warming experiment diluted SSS by $f_{FW,hydro} = 5\%$ compared to the Fix-SSS experiment (i.e., $\text{SSS}_{Standard} = 0.95\ \text{SSS}_{Fix-SSS}$), then in the absence of other changes (e.g. biology, air-sea flux, temperature), the local surface DIC and Alkalinity would also be diluted by $f_{FW,hydro} = 5\%$ from the reference Fix-SSS concentrations ($\text{DIC}_{Standard} = 0.95\ \text{DIC}_{Fix-SSS}$; $\text{Alk}_{Standard} = 0.95\ \text{Alk}_{Fix-SSS}$). We can therefore approximate $\Delta\text{DIC}_{FW,hydro} = f_{FW,hydro}\text{DIC}_{Fix-SSS}$ and $\Delta\text{Alk}_{FW,hydro} = f_{FW,hydro}\text{Alk}_{Fix-SSS}$, and similarly for the climate effect. This approach is similar to the standard salinity normalization [86, 87], however we reference DIC and Alkalinity to the scenario with no hydrological cycle amplification (Fix-SSS experiment) whereas work using salinity normalization used a central salinity of 35 psu and DIC and Alkalinity values that tend to co-occur with this salinity of 35 psu. This approach includes the influences of mixing and transport (since they are included in the changes in salinity used to define f_{FW}) but assumes they affect salinity, Alkalinity, and DIC equally. Mixing and transport act on different spatial gradients for each variable (in the real ocean, and the ESM2M simulated ocean) and would therefore lead to different concentration changes, so we expect that this approach will work best in the mixed layer where all quantities are well mixed.

We estimate DIC changes due to thermal changes following [88], using a constant thermal

sensitivity $\frac{\partial DIC}{\partial T}$ of -7 $\frac{\mu mol/kg}{K}$:

$$\Delta \mathrm{DIC}_{thermal,hydro} = \frac{\partial DIC}{\partial T} \Delta \mathrm{T}_{hydro} = -7 \Delta \mathrm{T}_{hydro}$$

This approximation introduces some error since $\frac{\partial DIC}{\partial T}$ is not constant, but we find that our results do not change if we allow the sensitivity to vary at each model grid point and month. The estimated DIC change due to temperature changes is not sensitive to a different choice of constant within a range of 7±2 $\frac{\mu mol/kg}{K}$.

2.3.3 Attribution of surface pH changes to hydrological and climate effects

Equilibrium pH can be understood as a nonlinear function of DIC, Alkalinity, temperature (T), and salinity (S), so that a difference in pH between two model experiments or ocean chemical states can be interpreted in terms of the corresponding changes in DIC, Alkalinity, temperature, and salinity between these two states [as in e.g. 89]. An increase in DIC due to CO_2 dissolution produces H^+ ions and decreases pH, whereas an increase in Alkalinity represents a greater seawater buffering capacity and yields a higher pH. Temperature has a direct negative relationship with pH (warming ionizes water, thus decreasing pH), and an indirect positive relationship with pH (the solubility of DIC decreases with temperature and leads to an increase in pH). Salinity has a small effect on pH and will not be discussed in this study.

We define the 'hydrological effect' and 'climate effect' on pH as introduced above:

$$\Delta pH_{hydro} = pH(DIC_{Std}, Alk_{Std}, T_{Std}, S_{Std}) - pH(DIC_{Fix-SSS}, Alk_{Fix-SSS}, T_{Fix-SSS}, S_{Fix-SSS})$$

$$\Delta pH_{Clim} = pH(DIC_{Std}, Alk_{Std}, T_{Std}, S_{Std}) - pH(DIC_{Fix-Clim}, Alk_{Fix-Clim}, T_{Fix-Clim}, S_{Fix-Clim})$$

We next decompose pH changes into freshwater-driven and thermally-driven components

(and a residual due to errors in method and other drivers) using the marine carbonate chemistry solver PyCO2SYS [90].

$$\Delta pH_{hydro} = \Delta pH_{FW,hydro} + \Delta pH_{thermal,hydro} + R$$

Freshwater fluxes affect pH primarily through their effect on DIC and Alkalinity; we use the DIC and Alkalinity changes due to freshwater fluxes (as estimated in section 3) to evaluate the freshwater flux effect on pH. $\Delta\mathrm{pH}_{FW,hydro}$ is defined as the difference between the theoretical pH with the DIC and Alkalinity predicted from the effect of freshwater fluxes (in bold) and this theoretical pH and the reference $\mathrm{pH}_{Fix-SSS}$:

$$\Delta\mathrm{pH}_{FW,hydro} = \mathrm{pH}((f_{FW,hydro}+1)\mathbf{DIC_{Fix-SSS}}, (f_{FW,hydro}+1)\mathbf{Alk_{Fix-SSS}}, \mathrm{SST}_{Fix-SSS}, \mathrm{SSS}_{Fix-SSS}) - \mathrm{pH}_{Fix-SSS}$$

Similarly, the net change in pH due to direct and indirect (via DIC) thermal effects is estimated as:

$$\Delta\mathrm{pH}_{thermal,hydro} = \mathrm{pH}(\mathbf{DIC_{Fix-SSS}} + \mathbf{\Delta DIC_{T,hydro}}, \mathrm{Alk}_{Fix-SSS}, \mathbf{SST_{Std}}, \mathrm{SSS}_{Fix-SSS}) - \mathrm{pH}_{Fix-SSS}$$

In these estimates of $\Delta\mathrm{pH}_{FW,hydro}$, $\Delta\mathrm{pH}_{FW,clim}$, we estimate the reference $\Delta\mathrm{pH}_{Fix-SSS}$ and $\Delta\mathrm{pH}_{Fix-Clim}$ with PyCO2SYS.

2.3.4 Quantifying DIC changes in subsurface water masses

In Section 6 of this chapter, we quantify the influence of hydrological cycle amplification on interior DIC concentrations in subsurface Mode and Intermediate Waters (MIWs). We use the same decomposition ($\Delta\mathrm{DIC}_{hydro} \approx \Delta\mathrm{DIC}_{FW,hydro} + \Delta\mathrm{DIC}_{thermal,hydro}$) to understand the drivers of changes in DIC.

Mode and Intermediate Waters are defined with density and salinity thresholds, based on [61] and adjusted for global model biases (e.g. since ESM2M simulates lower than observed salinities throughout the ocean, these salinity thresholds are slightly lower than suggested by [61]). In the Atlantic Ocean, subtropical and subpolar Mode Waters are grouped into

one water mass, defined by mean density referenced to the surface (ρ_0) between 1025 and 1027.6 kg m^{-3}, and mean salinity greater than 35 psu. Antarctic Intermediate Waters exist in the same density range but with mean salinity below 34.8 psu. In the Indo-Pacific Ocean, Mode Waters (including central and eastern types) are defined between $1023.5 < \rho_0 < 1025.8$ kg m^{-3}. Intermediate Waters (including Antarctic and North Pacific Intermediate Waters) are defined by density $1025.8 < \rho_0 < 1027$ kg m^{-3}. In Figure 2.6, 'salty-get-saltier' MIWs (including only Atlantic Mode Waters), and 'fresh-get-fresher' type MIWs (including Atlantic Intermediate Waters, and all Indo-Pacific MIWs), categorized by the mean salinity change within each water mass, are grouped together in a mass-weighted average to visualize the mean effect of hydrological cycle amplification on MIWs.

2.4 DIC and Alkalinity increase in 'fresh-get-fresher' and decrease in 'salty-get-saltier' regions apparent in total climate effect

The total climate effect (ΔDIC_{clim} and ΔAlk_{clim}) leads to an increase in DIC and Alkalinity in the (sub)tropical Atlantic and southeast Pacific ocean (Figure 2.2a, b), where SSS increases (Figure 2.1a), but a decrease in both over the high latitude Atlantic Ocean and the remainder of the Indo-Pacific sea surface which all freshen. The hydrological effect appears to account for much of this pattern. The hydrological effect appears to account for the entire climate effect in surface Alkalinity (Figure 2.2 b, d). ΔDIC_{clim} is lower than ΔDIC_{hydro} everywhere (less positive or more negative) (Figure 2.2 a, c). This shift is very likely due to the effect of warming which leads to a decrease in DIC, and which we exclude when we isolate the hydrological effect from the total climate effect.

To understand the mechanisms and magnitude of change associated with this salinification and freshening, we compare the mean climate and hydrological effect averaged over

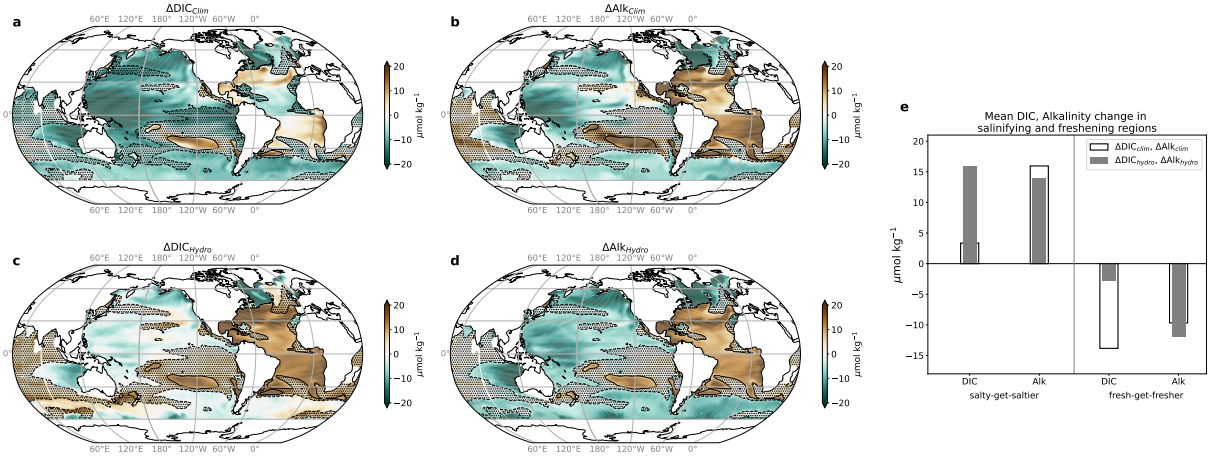


Figure 2.2: **DIC and Alkalinity response to climate and hydrological effects.** Change in surface (a) DIC and (b) Alkalinity due to the climate effect (Standard minus Fix-Clim experiments). (c) Mean change in DIC (black) and Alkalinity (grey) in salinifying ($\Delta SSS_{hydro} >$ 0.1 psu) and freshening ($\Delta SSS_{hydro} <$ -0.1 psu) regions shown in Figure 2.1. (d-f) are similar to (a-c) but for the hydrological effect (Standard minus Fix-SSS experiments). Stippled areas indicate regions that are neither salinifying nor freshening significantly ($|\Delta SSS_{hydro}| <$ 0.1 psu) and are not used in the analysis.

surface areas that experience salinification in excess 0.1 psu (the (sub)tropical Atlantic and southeast Pacific Oceans) and those that experience freshening stronger than -0.1 psu (the high-latitude Atlantic and remainder of the Indo-Pacific Oceans). By separating these regimes, we isolate the response of the ocean in regions of enhanced freshwater addition (freshening) or removal (salinification). In response to the total climate effect, DIC increases more weakly than Alkalinity over salinifying regions where SSS increases, ΔDIC_{clim} = +2 μmol/kg and ΔAlk_{clim} = +16 μmol/kg , and decreases more strongly over freshening regions where SSS decreases, ΔDIC_{clim} = -13 umol/kg while ΔAlk_{clim} = -10 umol/kg (black empty bars in Figures 2.2e and 2.3). In contrast, in response to the hydrological effect alone, DIC increases more strongly than Alkalinity in salinifying regions, ΔDIC_{hydro} = +16 umol/kg while ΔAlk_{hydro} = +14 umol/kg, and decreases more weakly in freshening regions, ΔDIC_{hydro} = -5 umol/kg and ΔAlk_{hydro} = -12 umol/kg (grey bars in Figures 2.2e and 2.3). We next demonstrate that the similar ΔAlk_{hydro} and ΔAlk_{clim} reflects the fact that Alkalinity does not respond to the other primary mechanisms driving the climate effect (CO_2

fluxes, temperature). Although the DIC change has a similar spatial pattern as Alkalinity, we show that its magnitude is modulated by a thermal component (warming in the climate effect and cooling in the hydrological effect).

The change in freshwater fluxes is very similar in both the total climate effect and in the hydrological effect, however Alkalinity is slightly more sensitive to freshwater fluxes than DIC (Figure 2.9, 2.3). Averaged over salinifying regions, DIC and Alkalinity increase 17 and 19 umol/kg in response to the climate effect; they increase slightly less in the hydrological effect, by 12 and 14 umol/kg. Over freshening regions, DIC and Alkalinity decrease -9 and -10 umol/kg in response to the climate effect. They decrease more in response to the hydrological effect alone, -13 and -14 umol/kg (Figure 2.3). This larger magnitude of $\Delta \mathrm{Alk}_{FW}$ relative to $\Delta \mathrm{DIC}_{FW}$, in each regime and experiment, is a consequence of the greater mean value of Alkalinity at the sea surface [61]. Indeed, when we evaluate $\Delta \mathrm{X}_{FW} = \mathrm{X}_{Fix-SSS}\ f_{FW}$, $\Delta \mathrm{Alk}_{FW}$ is slightly greater than $\Delta \mathrm{DIC}_{FW}$ due to the greater reference $\mathrm{Alk}_{Fix-SSS}$ (e.g. $\mathrm{X} \cdot 5\% < (\mathrm{X}+1) \cdot 5\%$).

In addition to dilution/concentration by freshwater fluxes, DIC is also strongly affected by temperature changes in both the climate effect (with an SST increase) and the hydrological effect (with an SST decrease). The SST and corresponding DIC changes are nearly spatially uniform (Figures 2.1c, d and S3b, e). Surface warming in the climate effect decreases DIC concentrations in both salinifying and freshening regions (by -9 and -7 umol/kg on average), while surface cooling in the hydrological effect increases DIC concentrations in both (by +5 and +7 umol/kg) (Figure 2.3). The weaker $\Delta \mathrm{DIC}_{thermal,clim}$ in freshening, relative to salinifying, regions is a consequence of the SST decrease (and positive $\Delta \mathrm{DIC}_{thermal,clim}$) in the Labrador Sea associated with a weakening of the overturning circulation, a common transient response of climate models to global warming and North Atlantic freshening [91, 69]. The greater $\Delta \mathrm{DIC}_{thermal,hydro}$ in freshening regions is a consequence of slightly stronger cooling at high latitudes where deep isopycnal mixing enhances the surface temperature response, while the cooling in the (sub)tropics is weaker. Despite these small differences, the

$\Delta DIC_{thermal,hydro}$ and $\Delta DIC_{thermal,clim}$ are uniform in sign and quite similar in magnitude in both regimes, leading to a contrast between the net climate and hydrological effects where $\Delta DIC_{clim} < \Delta Alk_{clim}$, while $\Delta DIC_{hydro} > \Delta Alk_{hydro}$ (black empty and filled bars in Figure 2.3). In summary, the spatial pattern of DIC and Alkalinity changes in both the climate effect and hydrological effect are determined in sign by freshwater fluxes associated with hydrological cycle amplification while the magnitude of DIC changes is modulated by SST.

Close agreement between the freshwater flux changes ($f_{FW,clim}$ and $f_{FW,hydro}$; see equation 2.1) is expected since freshwater flux patterns in the total climate effect are primarily related to the amplification of the hydrological cycle (Figure 2.1a, b). The fact that these values do not exactly agree (empty and filled blue bars in Figure 2.3) is most likely a consequence of differences in atmospheric and oceanic circulation between the two model experiments. These differences lead to a spatial re-distribution of freshwater fluxes, which results in slightly more intense salinification in the 'salty-get-saltier' regime and less intense freshening in the 'fresh-get-fresher' regime in the total climate effect in these simulations (boundaries of 'salty-get-saltier' and 'fresh-get-fresher' regimes are identical, defined in terms of ΔSSS_{hydro}).

The residuals in the decomposition of DIC and Alkalinity into freshwater and thermal components suggest that these effects account for most of the response of surface carbonate chemistry to the hydrological effect, and inform but less completely account for the response to the total climate effect (R_{hydro} <2 umol/kg; R_{clim} <6 umol/kg; yellow bars in Figure 2.3) (see also Figures 2.7, 2.8). Errors in ΔDIC_{clim} appear to be primarily related to CO_2 fluxes. For the climate effect, the estimate from this decomposition is biased high for DIC in 'salty-get-saltier' regions, likely due to weakened CO_2 uptake in these regions for which we do not account (Figure 2.10). In 'fresh-get-fresher' regions, the decomposition is biased low, consistent with enhanced CO_2 uptake. The decomposition is more successful at accounting for the hydrological effect. Agreement is within 2 umol/kg, when averaged over these regions, biased slightly high in 'salty-get-saltier' regions and low in 'fresh-get-fresher' regions. As in the climate effect, these changes are most likely related to anomalous CO_2 uptake: ESM2M

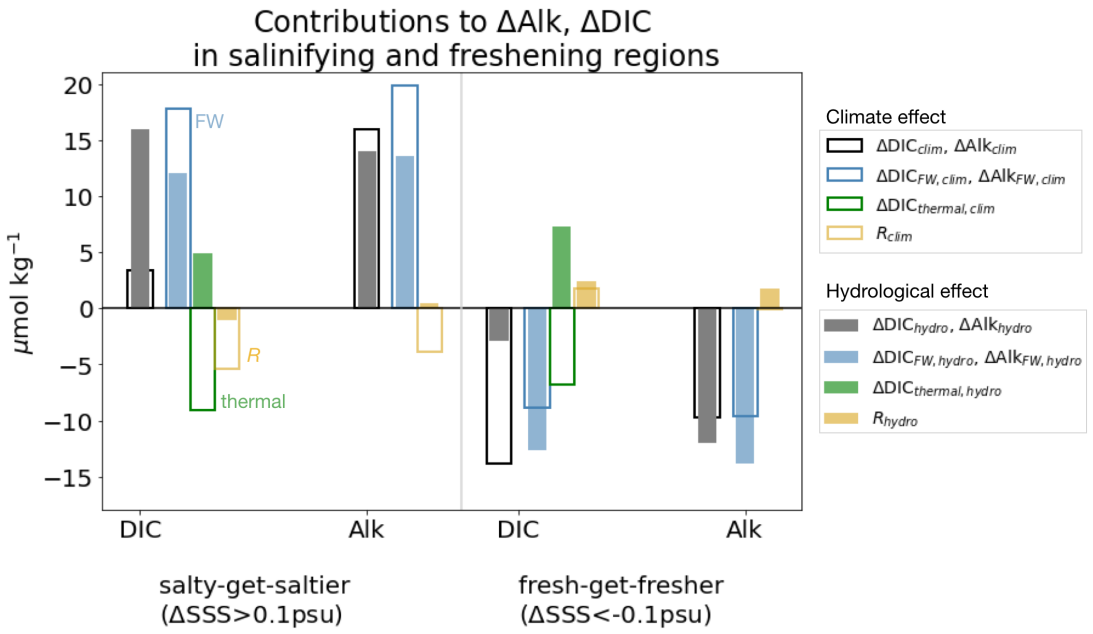


Figure 2.3: **Thermal and freshwater components of DIC and Alkalinity changes in 'fresh-get-fresher' and 'salty-get-saltier' regions.** Change in surface DIC and Alkalinity concentrations in response to the the climate effect (empty bars) and the hydrological effect (filled bars) in salinifying and freshening regions (as in Figures 2.4c and 2.2e). Black and grey bars represent total Δ_{clim} and Δ_{hydro}, and are identical to those in Figure 2.2e. Blue bars represent change in DIC or Alkalinity due to freshwater fluxes. Green bars represent change in DIC due to SST change.

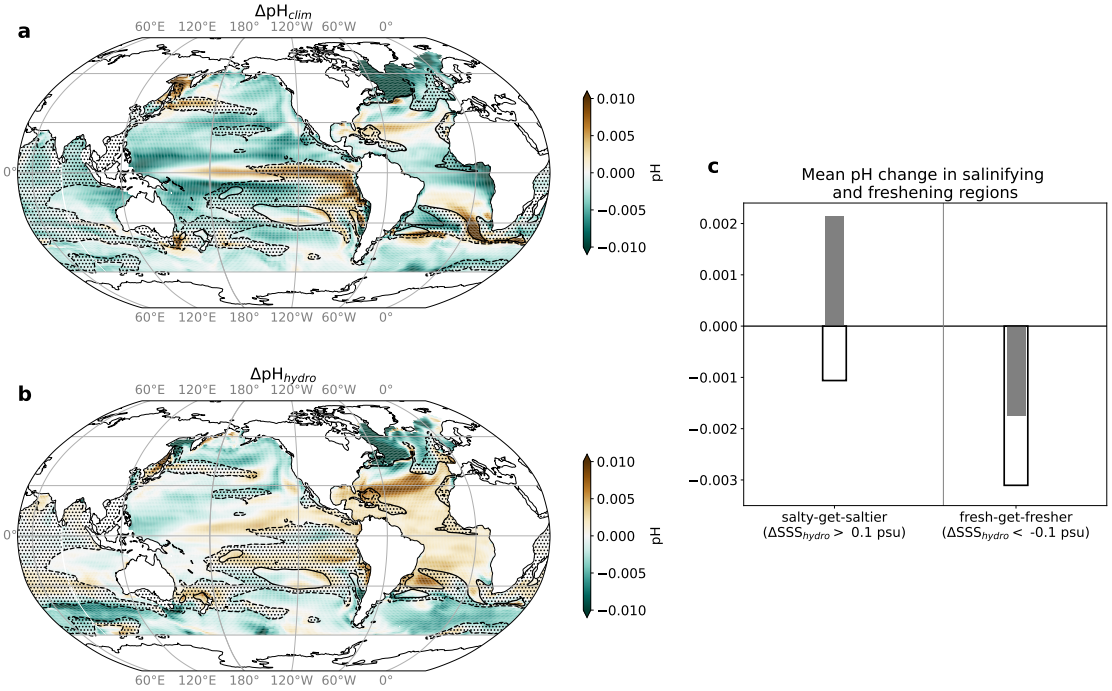


Figure 2.4: **pH response to climate and hydrological effects.** (a) Change in surface pH due to the climate effect (Standard minus Fix-Clim experiments). (b) Mean change in salinifying ($\Delta SSS_{hydro} > 0.1$ psu) and freshening ($\Delta SSS_{hydro} <$ -0.1 psu) regions outlined in Figure 2.1. Panels (c, d) are as in (a, b) but for the hydrological effect (Standard minus Fix-SSS experiments). Stippled areas indicate regions that are neither salinifying nor freshening significantly ($|\Delta SSS_{hydro}| < 0.1$ psu) and are not used in the analysis.

simulates a weakened uptake in salinifying regions and enhanced uptake in freshening regions on average, consistent with the expected increase in pCO_2 with DIC which leads to outgassing (in this case, weakened uptake). Errors in the reconstruction of Alkalinity do not have one obvious source, but represent the combined errors in our method and unaccounted-for biological changes.

2.5 Acidification weakened in 'salty-get-saltier' regions and exacerbated in 'fresh-get-fresher' regions

The climate effect tends to decrease pH (ΔpH_{clim}; Figure 2.4a), although an increase is found in the subtropical Atlantic Ocean, where salinity increases, as well as the equatorial Pacific Ocean. As a result of this pattern, the climate effect enhances acidification more weakly in 'salty-get-saltier' regions than 'fresh-get-fresher' regions (-0.001 and -0.005; black empty bars in Figures 2.4c, 2.5). When we isolate the hydrological effect from the climate effect (ΔpH_{hydro}; Figure 2.4b), we find it contributes to the pH increase in the subtropical Atlantic as the surface becomes saltier, and enhances the pH decrease in the subpolar oceans which become fresher. ΔpH_{clim} is generally lower than ΔpH_{hydro} (more negative or less positive), which is likely due to the influence of warming [14]. The hydrological effect opposes acidification in 'salty-get-saltier' regions but contributes to acidification over 'fresh-get-fresher' regions (+0.002 and -0.001; grey bars in Figures 2.4c, 2.5). Neither warming nor the hydrological effect fully account for the positive ΔpH_{Clim} in the upwelling region of the equatorial Pacific, where this model projects a weakened upwelling of cold and high-DIC waters, and accompanying flux of CO_2 into the surface (Figures 2.1b, 2.10a). This enhanced acidification is also not seen in the total projected pH change over the 21_{st} century, including the direct CO_2 effect and climate effect [37, 28].

We next interpret these pH changes due to the climate and hydrological effects in terms of a thermal effect (in which the changes in DIC and SST offset one another) and a freshwater flux effect (in which changes in DIC and Alkalinity offset one another), using the thermal and freshwater components of DIC and Alkalinity changes presented in Section 3 (Figure 2.5). The freshwater and thermal components of the climate effect ($\Delta pH_{FW,clim}$ and $\Delta pH_{thermal,clim}$) tend to oppose one another, except in the (sub)tropical Pacific Ocean where both act to decrease pH (Figure 2.11). As a result, we will attribute the acidification in 'fresh-get-fresher' and 'salty-get-saltier' regions to a different dominant driver in each region.

Due to the inverted SST change (decrease in the hydrological effect and increase in the climate effect), these freshwater and thermal components tend to add in the hydrological effect (Figure 2.11), and both components contribute to the pH increase in 'salty-get-saltier' regions and decrease in 'fresh-get-fresher' regions (Figure 2.5).

The freshwater effects ($\Delta\text{pH}_{FW,clim}$, $\Delta\text{pH}_{FW,hydro}$) are dominated by changes in Alkalinity ($\Delta\text{Alk}_{FW,clim}$, $\Delta\text{Alk}_{FW,hydro}$) and are positively related to ΔSSS for both the climate and freshwater effects (Figure 2.5). pH is almost equally sensitive to Alkalinity and DIC in the modern surface ocean, and ΔAlk_{FW} always exceeds ΔDIC_{FW} (due to the FW contribution scaling with the mean value, and the higher mean Alkalinity), so the sign of ΔAlk_{FW} drives the sign of the ΔpH_{FW} pattern. As a result, $\Delta\text{pH}_{FW,clim}$ and $\Delta\text{pH}_{FW,hydro}$ are positive in the salinifying (sub)tropical Atlantic and negative where the sea surface freshens in the high latitude Atlantic and much of the Indo-Pacific. The mean $\Delta\text{pH}_{FW,clim}$ is +/- 0.001 in salinifying and freshening regions, respectively (blue empty bars in Figure 2.5). $\Delta\text{pH}_{FW,hydro}$ is similar to $\Delta\text{pH}_{FW,clim}$ but slightly lower in each regime (less positive and more negative), consistent with the more intense Alkalinity increase in salinifying regions and weaker decrease in freshening regions (Figure 2.3).

The sign of the net thermal effect on pH is not uniform, despite ubiquitous warming in the climate effect and cooling in the hydrological effect, but varies with latitude. $\Delta\text{pH}_{thermal}$ is driven by the direct effect of warming in the (sub)tropical ocean, where it is negative in the climate effect and positive in the hydrological effect, but is driven by the indirect effect of warming in the higher latitude oceans, where it is positive in the climate effect due to DIC decrease and negative in the hydrological effect due to DIC increase (Figure 2.11). The indirect effect is greater at higher latitudes because the thermal sensitivity of DIC increases in colder temperatures, and the sensitivity of pH to DIC increases in waters with greater mean DIC concentrations, both conditions which occur at higher latitudes. The opposed SST changes in the climate and thermal effect lead to oppositely signed $\Delta\text{pH}_{thermal,clim}$ and $\Delta\text{pH}_{thermal,hydro}$ in each regime. The dominance of the direct effect in the (sub)tropics leads

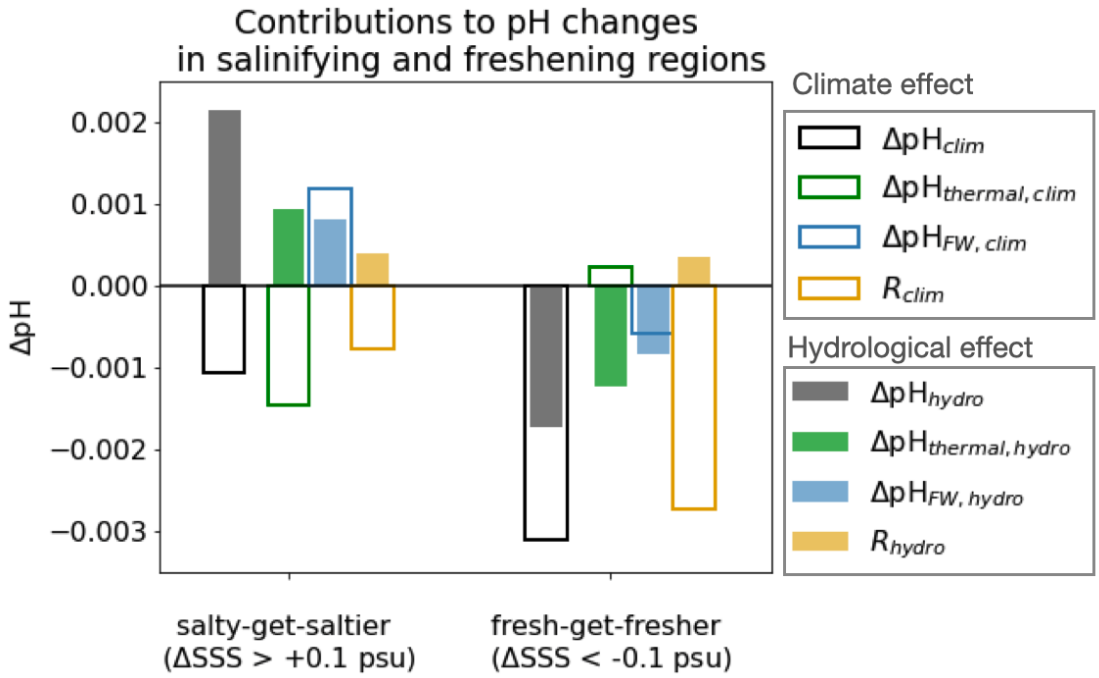


Figure 2.5: **Thermal and freshwater components of pH changes in 'fresh-get-fresher' and 'salty-get-saltier' regions.** Change in surface pH in the climate effect (empty bars) and the hydrological effect (filled bars), in 'salty-get-saltier' and 'fresh-get-fresher' regions (as shown in Figure 2.1). Black and grey bars represent total simulated pH change and are identical to those in Figure 2.4c. Blue bars represent contribution of freshwater effect (via dilution of DIC and Alkalinity). Green bars represent contribution of thermal effect (via SST change and DIC change due to SST).

to a negative $\Delta pH_{thermal,clim}$ of -0.001, and positive $\Delta pH_{thermal,hydro}$ of +0.001 in salinifying regions. The enhanced indirect effect at higher latitudes drives the mean effect in freshening regions where $\Delta pH_{thermal,clim}$ is weakly positive and $\Delta pH_{thermal,hydro} \approx$ -0.001 (green bars in Figure 2.5). In the climate effect, the direct effect of SST drives the mean pH decrease in 'salty-get-saltier' regions while the dilution of Alkalinity drives the pH decrease in 'fresh-get-fresher' regions. In the hydrological effect, both components contribute to the pH increase in 'salty-get-saltier' regions and decrease in 'fresh-get-fresher' regions.

The combined freshwater and thermal effects correctly predict the sign of pH changes, but better reconstruct the magnitude of the hydrological effect than of the climate effect (yellow residuals greater for climate effect in Figure 2.5). The sum of these two components

underestimates the magnitude of the total simulated pH decrease in the climate effect (predicting a weak decrease relative to the simulated ΔpH_{clim} -0.001 and -0.003 in salinifying and freshening regions). The weakened air-sea CO_2 flux cannot explain the enhanced acidification, suggesting that this inaccuracy is related to error in our reconstructions of $\Delta Alk_{FW,clim}$, $\Delta DIC_{FW,clim}$, and $\Delta DIC_{thermal,clim}$, as well as the covariation between drivers of pH changes.

2.6 Freshwater fluxes and ocean heat redistribution enhance subsurface carbon storage

Changes in surface freshwater fluxes with hydrological cycle amplification and the accompanying redistribution of heat between the ocean and atmosphere not only influence chemistry at the surface but also impact the ocean interior, in particular the storage of carbon in subsurface waters. Changes in surface freshwater fluxes are most intense at low and mid latitudes where Mode and Intermediate Waters (MIWs) are subducted [92]. These waters enter the ocean interior and ventilate the subsurface ocean (100-1000 m depth) on 20-100 year timescales, strongly contributing to the storage of carbon and heat in the ocean [93, 67, 94]. We group these MIW into two categories, the ones that subduct in 'salty-get-saltier' regions (Atlantic subtropical and subpolar Mode Waters; Figure 2.12) and the ones that subduct in 'fresh-get-fresher' regions (Antarctic Intermediate Waters, North Pacific Intermediate Waters, and Indo-Pacific Mode Waters; Figure 2.12). In both MIW categories, the climate effect slightly reduces DIC concentrations and hence carbon storage (ΔDIC_{clim} = -0.5 umol/kg in salinifying MIW and -3 umol/kg on average in freshening MIW, black empty bars in Figure 2.6), in line with the expectation that the solubility effect of warming on DIC dominates the total climate effect. We find, however, that the hydrological effect opposes the climate effect and surprisingly helps to sustain carbon storage in all MIWs, increasing DIC concentrations in both salinifying (ΔDIC_{hydro}= +11umol/kg) and freshening (ΔDIC_{hydro} = +0.7umol/kg) subsurface MIW (grey bars in Figure 2.6).

In response to hydrological cycle amplification, subduction of 'salty-get-saltier' MIWs is enhanced and they take up more heat from the atmosphere, while subduction of 'fresh-get-fresher' MIWs is weakened, and their heat uptake is diminished. This leads to opposing freshwater and thermal effects on DIC. In salinifying Atlantic Mode waters, freshwater fluxes lead to an overall increase in DIC (of +11 umol/kg; blue bars), but are opposed by a thermal effect which decreases DIC (-1.5 umol/kg). The predicted increase of 9.5 umol/kg slightly underestimates the real increase of 11 umol/kg (yellow bars represent this error in Figure 2.6). In 'fresh-get-fresher' MIWs, DIC is diluted with freshwater input by -2 umol/kg, but this decrease is overwhelmed by the thermal effect which increases DIC by +4 umol/kg. The predicted increase of +2 umol/kg overestimates the real increase of +0.7 umol/kg. Due to the strength of the freshwater effect in salinifying MIW and the thermal effect in freshening MIW, all MIWs experience an increase in DIC in response to the hydrological effect. This increase opposes the climate effect, which is dominated by the decrease in solubility of DIC as seawater temperature increases.

2.7 Summary

Our results suggest that the changes in Alkalinity and DIC linked to hydrological cycle amplification contribute as strongly as warming alone to the spatial pattern of the climate effect on Alkalinity and DIC. The hydrological effect explains the surface DIC increase in the low to mid latitude Atlantic Ocean in the total climate effect, and the increased strength of the DIC decrease at higher latitudes. Nearly the entire climate effect in surface Alkalinity is accounted for by this hydrological effect, via the direct dilution or concentration of Alkalinity by freshwater fluxes. The previously un-explained climate effect in surface pH in the subtropical Atlantic Ocean, which opposes acidification unlike much of the rest of the climate effect, can be accounted for by the increase in Alkalinity and decrease in surface warming due to hydrological cycle amplification, while amplified acidification at high lati-

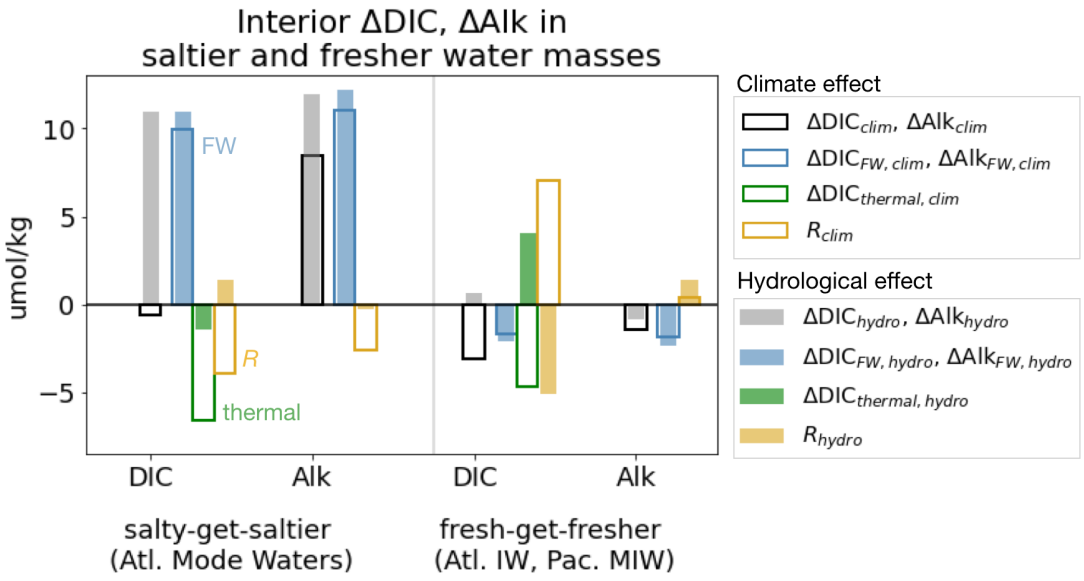


Figure 2.6: **Changes in DIC, Alkalinity due to freshwater fluxes and altered ocean heat uptake in 'fresh-get-fresher' and 'salty-get-saltier' water masses.** The change in DIC and Alkalinity concentrations in response to the climate effect (empty bars) and the hydrological effect (filled bars), in Mode and Intermediate water masses, grouped into those that get saltier (Atlantic Mode Waters) and those that get fresher (Atlantic Antarctic Intermediate Waters as well as Pacific Mode and Intermediate Waters, which respond similarly). Estimated change in DIC or Alkalinity concentration from freshwater fluxes (referenced to interior salinity changes) in blue, and change in DIC concentration from temperature changes in green.

tudes is partly attributed to the dilution of Alkalinity and the enhanced DIC concentration associated with weakened surface warming. We expect these results remain similar in other climate models because the amplification of the hydrological cycle itself, and its impact on ocean heat uptake and SST, have been shown to be consistent in different GCMs [70, 49, 6].

We note that the the role of freshwater fluxes on marine carbonate chemistry (our 'freshwater component') is traditionally removed by a salinity normalization [since 86]. The prevalence of this practice implies that there is a strong influence of freshwater fluxes on seawater chemistry, but this influence is rarely studied. We show that, although the traditional salinity normalization is largely successful at removing the direct effect of freshwater fluxes on DIC and Alkalinity individually, since Alkalinity has a greater mean value it will change more, leading to a non-zero net change in pH due to freshwater fluxes. As the future trend in freshwater fluxes is quite robust, this is an insightful entry point to better understanding the large scale spatial pattern of the climate effect.

Finally, we find that hydrological cycle amplification supports carbon storage in all Mode and Intermediate Waters, opposing the decrease due to ocean heat uptake - but that the reason for this enhanced carbon storage differs between salinifying and freshening water masses. In salinifying Atlantic Mode Waters, this increase is directly due to evaporation which enhances the DIC concentration in the outcrop region. In freshening Mode and Intermediate Waters across ocean basins, the weakened ocean heat uptake (associated with surface freshening, which weakens subduction) enhances the solubility of DIC. This solubility improvement barely wins out over the direct dilution to lead to a much smaller increase in DIC in the 'fresh-get-fresher' types whereas our results show a strong increase in DIC in 'salty-get-saltier' types. This positive ΔDIC_{hydro} in MIW may be the reason that the carbon-climate feedback acts to increase DIC in Atlantic Mode Waters in other Earth System Models [85, their Fig. 10d]. In the Atlantic Ocean, the small magnitude of the signal in freshening MIWs is due to an invasion of neighboring 'salty-get-saltier' water masses, and in the Pacific Ocean, this is due to the small amplitude of the hydrological effect, consistent

with a small total climate effect [as also shown in 82]. The resulting enhancement of carbon storage efficiency in Mode and Intermediate Waters likely contributes to the large quantities of anthropogenic carbon they currently hold [93]. This effect also suggests that, while global ocean carbon uptake can be expected to weaken with warming, this weakening could be milder in Mode and Intermediate Waters [85]. Deeper in the ocean, the evolution of the climate effect will depend strongly on ice-ocean interactions at high latitudes where these waters are formed [95]. Although these interactions are not constrained by the amplification of the hydrological cycle considered here, the dilution due to freshwater fluxes and temperature change associated with ocean heat uptake remain relevant mechanisms for determining the efficiency of carbon storage in the deep ocean.

2.8 Supplemental Figures

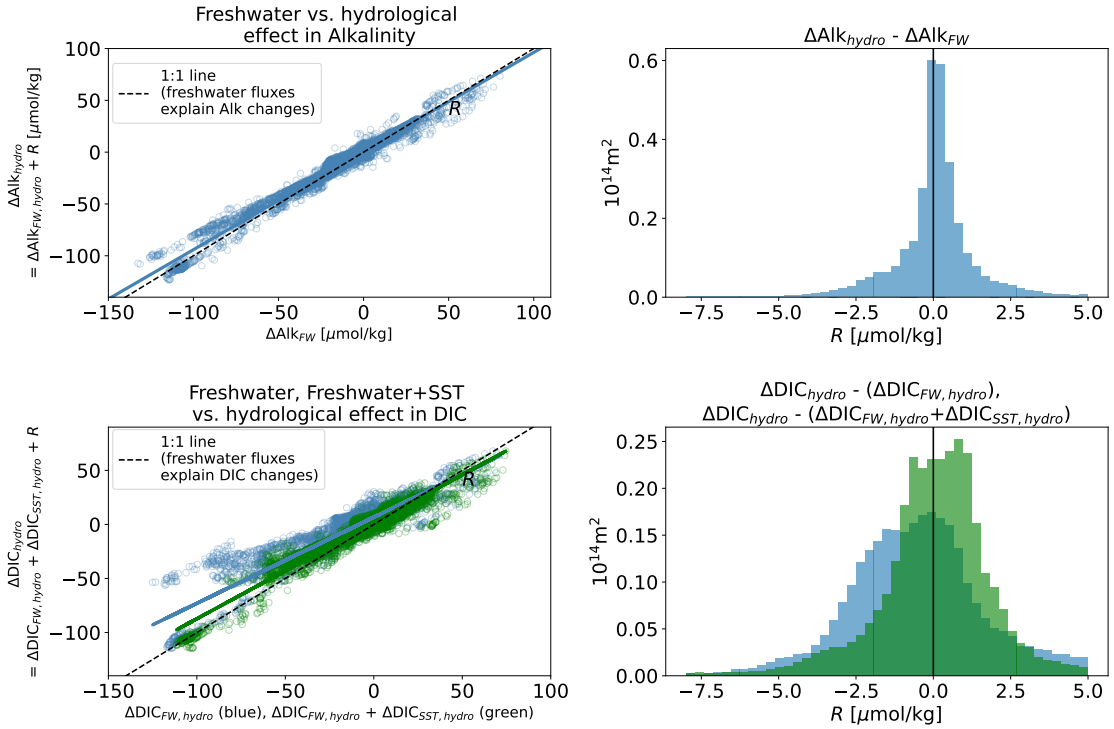


Figure 2.7: **Ability of freshwater, SST decomposition to reconstruct spatial pattern of changes in surface DIC and Alkalinity with hydrological effect.** Agreement of 'freshwater effect' ($\Delta\text{Alk}_{FW,hydro}$) with ΔAlk_{hydro} (top), and agreement of 'freshwater + SST effects' ($\Delta\text{DIC}_{FW,hydro}$+$\Delta\text{DIC}_{SST,hydro}$) with ΔDIC_{hydro} (bottom). Left hand side: scatter and unweighted regression of simulated surface ΔAlk_{hydro} or ΔDIC_{hydro} against the Δ_{hydro} predicted by our decomposition (for Alkalinity, $\Delta\text{Alk}_{FW,hydro}$; for DIC, $\Delta\text{DIC}_{FW,hydro}$ in blue and $\Delta\text{DIC}_{FW,hydro}$+$\Delta\text{DIC}_{SST,hydro}$ in green), at each surface location. Scatter around the fit is the error R. Right hand distributions represent area weighted values of R for Alkalinity (top) and DIC (bottom).

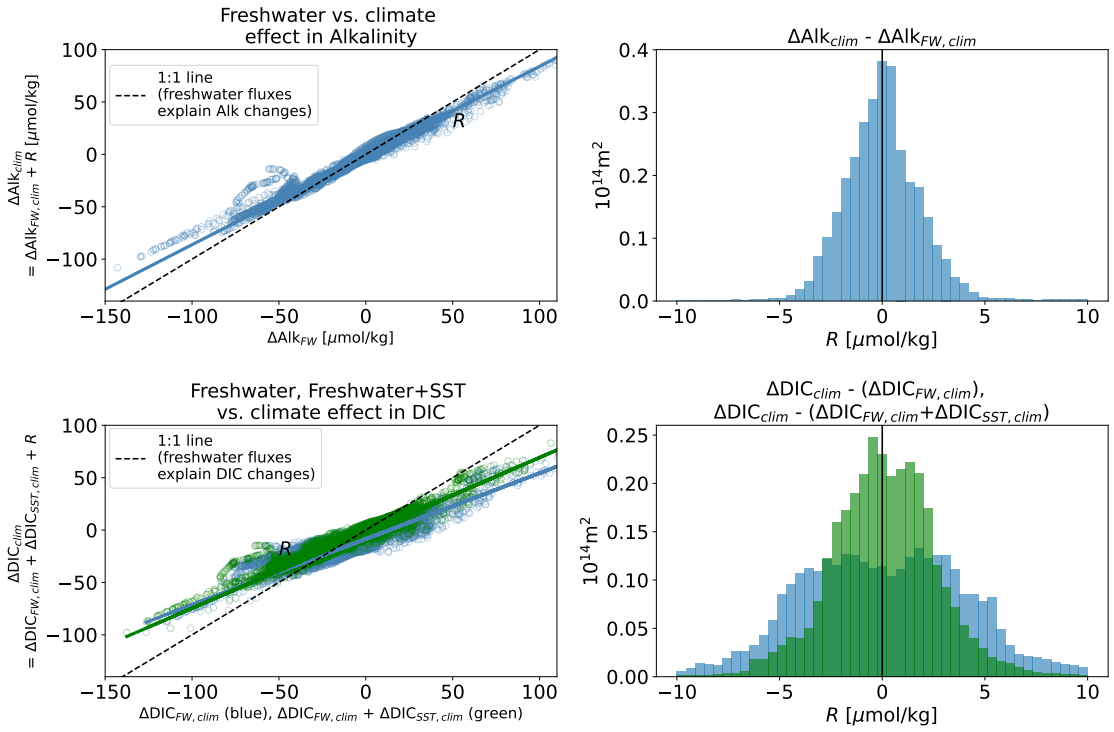


Figure 2.8: **Ability of freshwater, SST decomposition to reconstruct spatial pattern of changes in surface DIC and Alkalinity with climate effect.** As in Figure 2.7 but for the climate effect.

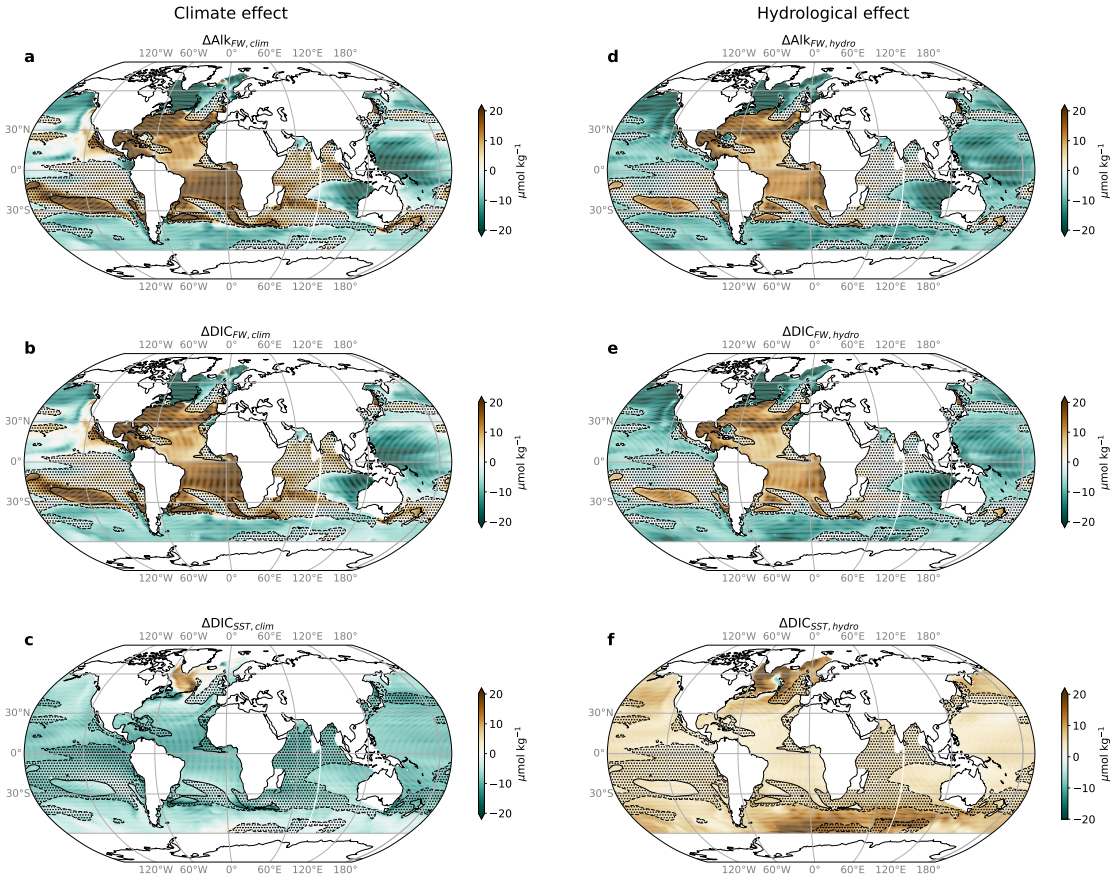


Figure 2.9: **Thermal and freshwater components of DIC and Alkalinity changes.** (a-c) change attributed to freshwater ($\Delta\text{Alk}_{FW,clim} = f_{FW,clim}\text{Alk}_{Fix-Clim}$, $\Delta\text{DIC}_{FW,clim} = f_{FW,clim}\text{DIC}_{Fix-Clim}$) and thermal ($\Delta\text{DIC}_{thermal,clim}$ = -7ΔSST_{clim}) components in climate effect; (d-f) change attributed to freshwater ($\Delta\text{Alk}_{FW,hydro} = f_{FW,hydro}\text{Alk}_{Fix-SSS}$, $\Delta\text{DIC}_{FW,hydro} = f_{FW,hydro}\text{DIC}_{Fix-SSS}$) and thermal ($\Delta\text{DIC}_{thermal,hydro}$ = -7ΔSST_{hydro}) components in hydrological effect.

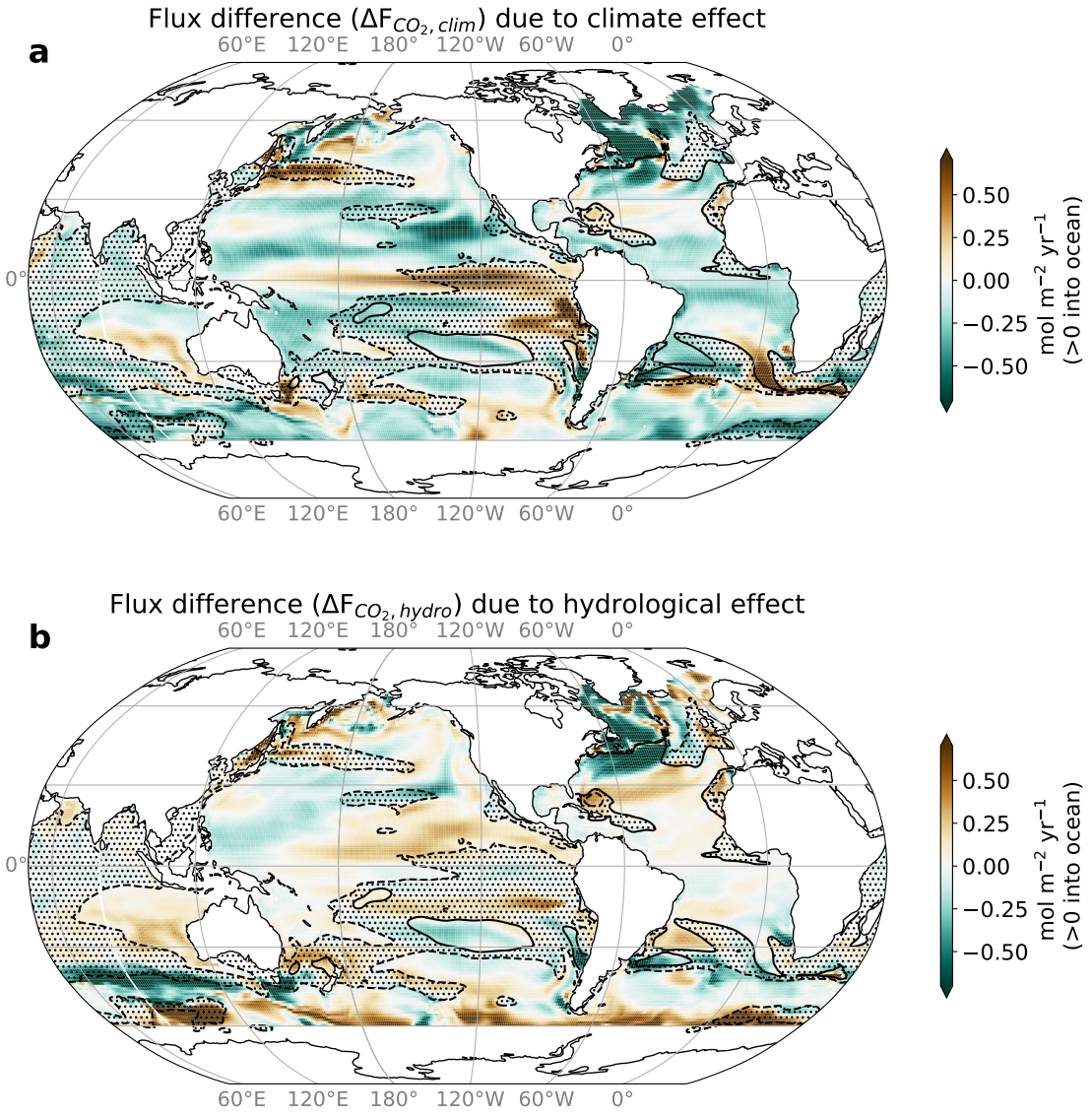


Figure 2.10: Air-sea flux of CO_2, difference due to (a) climate effect and (b) hydrological effect. Stippling where ΔSSS_{hydro} is small, as in Figures 1, 2, 4.

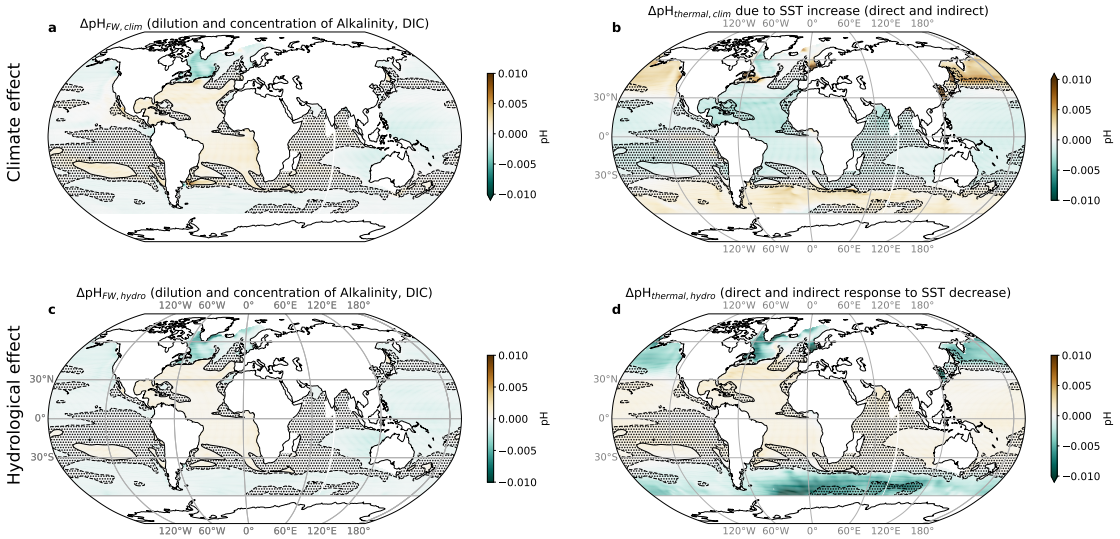


Figure 2.11: **Thermal and freshwater components of pH changes.** Change in surface pH due to (a, b) the climate effect and (c, d) due to the hydrological effect. Panels (a, c) isolate net freshwater effect due to dilution of Alkalinity and DIC; panels (b, d) isolate net thermal effect due to SST change and DIC change associated with SST.

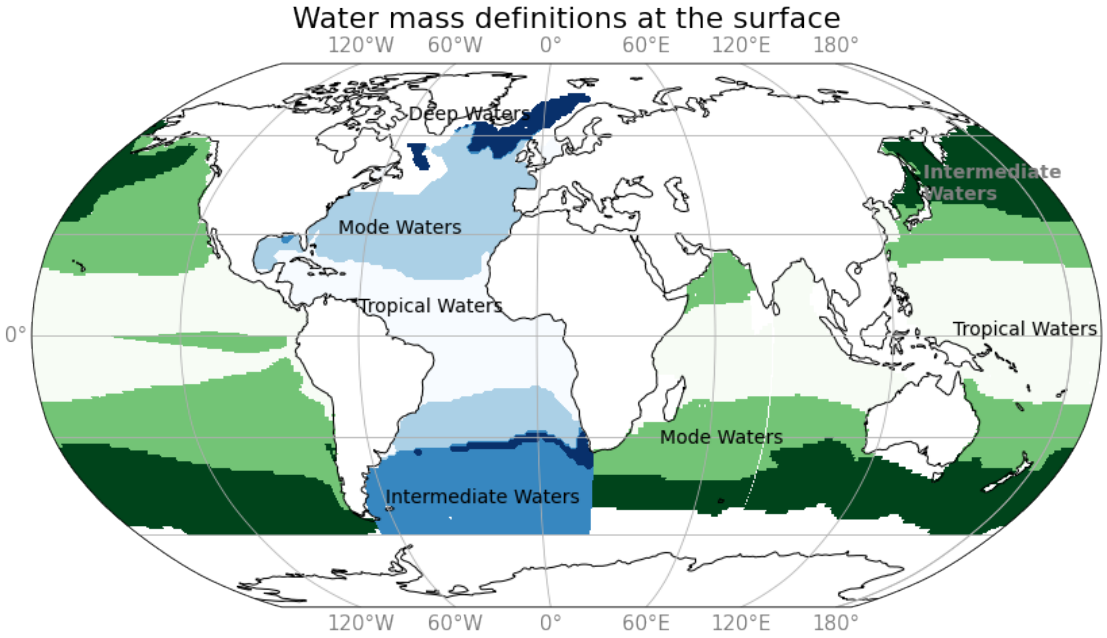


Figure 2.12: Water mass outcrop regions at the sea surface. Green follows density thresholds for Indo-Pacific; blue follows thresholds of density and salinity in Atlantic. Mode and Intermediate water masses are used in Figure 6.

3

Heat: Cause of the intense tropics-wide tropospheric warming in response to El Niño

Please find the published manuscript below.

Cause of the Intense Tropics-Wide Tropospheric Warming in Response to El Niño

A. HOGIKYAN,[a] L. RESPLANDY,[b,c] AND S. FUEGLISTALER[a,b]

[a] *Atmospheric and Oceanic Sciences Program, Princeton University, Princeton, New Jersey*
[b] *Geosciences Department, Princeton University, Princeton, New Jersey*
[c] *High Meadows Environmental Institute, Princeton University, Princeton, New Jersey*

(Manuscript received 17 September 2021, in final form 7 December 2021)

ABSTRACT: During El Niño events, a strong tropics-wide warming of the free troposphere is observed (of order 1 K at 300 hPa). This warming plays an important role for the teleconnection processes associated with El Niño but it remains unclear what initiates this warming. Since convective quasi-equilibrium only holds in regions of deep convection, the strong free-tropospheric warming implies that the warmest surface waters (where atmospheric deep convection occurs) must warm during El Niño. We analyze the evolution of the oceanic mixed layer heat budget over El Niño events as function of sea surface temperature (SST). Data from the ERA5 and an unforced simulation of a coupled climate model both confirm that SSTs during an El Niño event increase at the high end of the SST distribution. The data show that this is due to an anomalous heat flux from the atmosphere into the ocean caused by a decrease in evaporation due anomalously weak low-level winds (i.e., relative to the wind speed observed in the domain of deep convection in the climatological base state). It is hypothesized that the more zonally symmetric circulation during El Niño is responsible for the weakening of low-level winds. The result of a substantial heat flux into the ocean in the domain of atmospheric deep convection (the opposite of the canonical heat flux out of the ocean into the atmosphere observed in the cold eastern Pacific) caused by a decrease in low-level wind speed implies that the prominent tropospheric warming results from mechanical forcing.

KEYWORDS: ENSO; Energy budget/balance; Tropical variability

1. Introduction

El Niño–Southern Oscillation (ENSO) is the largest source of natural interannual variability in the climate system. During ENSO events, teleconnections propagate the perturbation originating in the tropical Pacific Ocean throughout the tropics and into the extratropics (Yulaeva and Wallace 1994; Deser and Wallace 1990; Rasmusson and Wallace 1983; Klein et al. 1999; Chiang and Sobel 2002; Lintner and Chiang 2007; Ciasto and England 2011; Hoerling et al. 1997; Alexander et al. 2002; Liu and Alexander 2007; Su et al. 2001; Cai et al. 2019; Bony et al. 1997; Wang 2000; Latif and Grötzner 2000; Soden 1997; Trenberth et al. 2002; Lau and Nath 1996). In addition to the geographic rearrangement of the atmospheric general circulation with a weakening of the Walker cell and a strengthening of the Hadley cell in the tropics, a strong warming during El Niño events is observed throughout the tropical troposphere (and the inverse effects, with a cooling, during La Niña) (Fig. 1) (Trenberth et al. 2002; Yulaeva and Wallace 1994; Sobel et al. 2002; Chiang and Sobel 2002; Alexander et al. 2002; Kumar and Hoerling 2003; Su et al. 2005; Lintner and Chiang 2005). The temperature increase in the tropical free troposphere initiates some teleconnection processes and has direct impacts on the surface energy budget in regions outside the equatorial Pacific over the tropical Indian and Atlantic Oceans (Chiang and Lintner 2005; Lintner and Chiang 2005, 2007), as well as the extratropics (e.g., Yulaeva and Wallace 1994; Rasmusson and Wallace 1983).

The atmospheric temperature perturbations due to ENSO are so large that they distort global-mean temperature trends even on multidecadal time scales and must be carefully removed for estimates of global warming (Hurrell and Trenberth 1998; Po-Chedley and Fu 2012; Santer et al. 2001; Dessler 2010, 2013; Trenberth et al. 2015; Po-Chedley et al. 2021).

Here, we focus on identifying the process that leads to the strong tropical and global tropospheric warming during El Niño (and cooling for La Niña). Specifically, we argue that the well-documented and well-understood warming of the sea surface in the eastern Pacific Ocean (Philander 1983; Battisti and Hirst 1989; Wang et al. 2017; Wang and McPhaden 2000; Vialard et al. 2001; Wang et al. 1999; Zebiak and Cane 1987; Neelin et al. 1998) is insufficient to explain the tropospheric warming because the sea surface temperature of the eastern Pacific is not strongly coupled to the temperature of the free troposphere. The coupling between sea surface temperature (SST) and the temperature of the free troposphere is highly nonlinear. To efficiently produce the observed warming in the tropical free troposphere, there must be an increase in subcloud moist static energy (MSE) in the domain experiencing deep atmospheric convection (Neelin and Held 1987; Graham and Barnett 1987; Raymond et al. 2009; Emanuel 1995; Randall and Emanuel 2000; Sobel and Bretherton 2000; Flannaghan et al. 2014; Fueglistaler et al. 2015; Tuel 2019). This domain with deep convection is characterized by high SSTs (i.e., over the ocean, subcloud MSE is highly correlated with SST as relative humidity variations are small; for simplicity we refer to SST rather than subcloud MSE). The warming of the cold eastern Pacific may be large (+1°–3°C with respect to the climatology), but as long as SSTs at the high end of the frequency distribution—where deep convection occurs—are not warming, the impact on free-tropospheric temperature is small. Instead, there must be a mechanism that allows the

Corresponding author: A. Hogikyan, hogikyan@princeton.edu

DOI: 10.1175/JCLI-D-21-0728.1

© 2022 American Meteorological Society. For information regarding reuse of this content and general copyright information, consult the AMS Copyright Policy (www.ametsoc.org/PUBSReuseLicenses).

Brought to you by PRINCETON UNIVERSITY LIBRARY | Unauthenticated | Downloaded 04/21/22 08:14 PM UTC

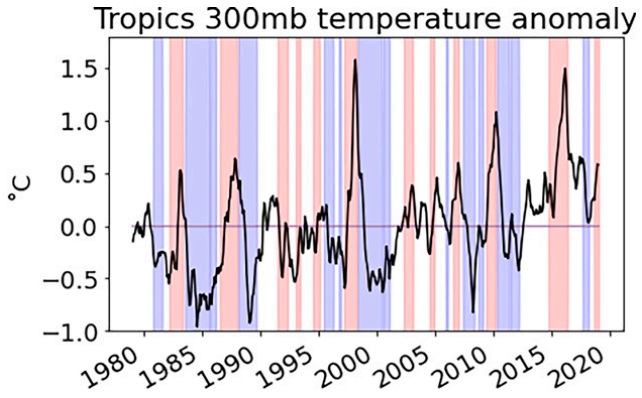


FIG. 1. The tropical-mean (30°S–30°N) atmospheric temperature at 300 mb from ERA5, with the climatological seasonal cycle removed and smoothed. Red (blue) shading indicates a Niño-3.4 index greater (less) than 0.6 (–0.6). El Niño events analyzed in Fig. 3 are 1982/83, 1986/87, 1991/92, 1997/98, 2002/03, 2009/10, and 2015/16 (NOAA/CPC).

high end of tropical SSTs to increase, and this increase in subcloud MSE leads to the strong warming of the free troposphere. The geographical rearrangement of SSTs and the locations of deep convection as observed during ENSO events (Zhang et al. 1995; Wang 1995) does not in itself explain a warming in the domain of atmospheric deep convection. An adiabatic redistribution of the volume of warm water and its exposure to the surface (Jin 1997, 1996; Meinen and McPhaden 2000; Ballester et al. 2015; Cheng et al. 2019; Picaut 1997) can lead to a warming at intermediate SSTs (i.e., a change in the shape of the distribution function, but not a change in the maximum). Since deep convection occurs over a range at the high end, but not exclusively at the maximum SSTs (Zhang 1993; Zhang and Fueglistaler 2020), this could impact the free-tropospheric temperature. However, SSTs are observed to warm remarkably uniformly [i.e., with small change of the shape of the probability distribution (Sobel et al. 2002; Fueglistaler 2019)] and the results presented below suggest the dominant process to be a heat flux into the ocean in the domain of atmospheric deep convection.

We find that the processes controlling the free-tropospheric warming and cooling are remarkably linear with respect to ENSO state and the results presented here apply for El Niño and La Niña (see the appendix). For simplicity, the following discussion therefore focuses on El Niño and results for La Niña are deferred to the appendix. We analyze data from both a reanalysis and a coupled atmosphere–ocean general circulation model (GCM) and show that indeed the domain with atmospheric deep convection is anomalously warm during El Niño—the high end of SSTs is higher than in the climatological mean state. Both the reanalysis data and the coupled GCM indicate that the SST increase in these regions is due to anomalously low surface winds. That is, the surface winds in the regions where deep convection is observed (which differs geographically during El Niño from the climatological base state) are lower during El Niño than in the climatological base state. This heat flux into the ocean in the warmest parts of the tropics partly opposes a large heat flux out of the ocean in colder regions, especially the eastern equatorial Pacific.

2. Methods

To understand why the tropical free-tropospheric temperature increases during El Niño, we must understand changes in conditions in the regions where atmospheric deep convection occurs, and the conventional geographical frame of reference (latitude and longitude) is not well suited to this task. Because of the geographical rearrangement of the general circulation during El Niño (Trenberth and Caron 2001; Trenberth and Smith 2009; Mayer et al. 2016, 2013; Trenberth et al. 2002; Trenberth and Stepaniak 2003; Trenberth et al. 2015), local changes are generally dominated by a shift in patterns. Broadly speaking, the warm waters where atmospheric deep convection is frequent expand eastward from their climatological location in the western tropical Pacific (e.g., Picaut 1997). Local changes in the western tropical Pacific are dominated by the fact that high SSTs and therefore convection vacate, while local changes in the central equatorial Pacific are dominated by the fact that high SSTs and convection enter this region. However, the conditions *within convective regions* are very similar *regardless* of whether they are in the west or central Pacific. Viewed on a map, this geographical shift in convective regions, which does not affect the tropospheric temperature, overwhelms the signal from the subtle change in conditions within the domain of deep convection, which is responsible for the tropospheric temperature change.

We solve this problem by analyzing the data as a function of SST, similarly to Fueglistaler (2019) and Sobel et al. (2002). As explained above, deep convection occurs at the high end of the SST distribution (Graham and Barnett 1987; Zhang 1993; Brown and Bretherton 1997; Sobel et al. 2002), irrespective of where (geographically) these regions are. Consequently, SSTs underlying deep convection most strongly influence the temperature of the free troposphere. As a result, high SSTs must increase during El Niño in order for the free troposphere to warm as observed. Both Fueglistaler (2019) and Sobel et al. (2002) noted that SSTs at the high end of the distribution indeed do increase during El Niño, but did not address the question of why they increase. By following convective regions as they move in geographical space, we are able to directly compare the conditions in regions of deep convection during El Niño (or La Niña) with those in the climatological base state.

a. Percentiles

For each month, we sort all data over the tropical ocean (30°S–30°N) according to that month's SST field. After sorting by SST rank, we average the data (monthly means of SST, radiative fluxes, sensible and latent heat fluxes, and winds) in 100 equal area bins (i.e., each bin corresponds to 1% of the tropical ocean area). The transformation from the more common frequency distribution (PDF) as function of intensity (as e.g., in Sobel et al. 2002) to "SST percentile space" (as e.g., in Fueglistaler 2019) is motivated by the fact that interpretation of results is more direct: each bin has equal weight (facilitating

Brought to you by PRINCETON UNIVERSITY LIBRARY | Unauthenticated | Downloaded 04/21/22 08:14 PM UTC

visual quantitative analysis) and departures from a uniform shift of the probability density distribution can be detected by eye. In the conventional PDF perspective, it is difficult to determine visually from the difference between two PDFs whether the difference is a uniform shift (e.g., homogeneous warming) or a significant change in the shape of the PDF (e.g., the warming of only the warmest waters)—as in both cases the difference between the PDFs is a seesaw. In the SST percentile space, however, a uniform shift translates into a constant anomaly whereas a change in the shape of the PDF yields a departure from this constant anomaly.

To provide some intuition for the "SST percentile"-space, we show in Fig. 2a the climatological mean SST from ERA5 as a function of SST percentile and averaged into equal-area bins. Figure 2b shows the corresponding rainfall (i.e., rainfall binned according to the underlying SST) in terms of fraction of total rainfall per bin. Results for the GFDL-FLOR simulation are very similar (see Fig. A1 in the appendix). The well-known nonlinear behavior of rainfall as a function of SSTs with a threshold for deep convection around 26°C (e.g., Zhang 1993) is reflected in the increase in rainfall fraction around the 50th percentile. In the following, all data are shown for the full range of percentiles, but for simplicity in the description of the results we refer to the top 30% (i.e., from the 70th percentile upward; gray shaded) as the "deep convective domain"; the results and conclusions do not depend on the exact value for the percentile.

Finally, we note that while the variance within each bin is small for SST by construction, this may not be the case for all other variables. In particular, in bins at intermediate SSTs one may average data from regions with frequent deep convection with data from regions with little deep convection. Also, variables need not have a monotonic relation with SSTs. For instance, the decline in mean rainfall in the highest SST percentiles is associated with the lack of convection over the Red Sea, South China Sea, and Arabian Sea despite their very high SSTs (Fig. 2a). These caveats notwithstanding, sorting by SST is a simple and efficient method to isolate the deep convective regime over tropical oceans.

b. Mixed layer budget

Changes in SST closely follow changes in the temperature of the oceanic surface mixed layer. Consequently, we use the energy budget for the mixed layer to determine the source of the SST increase during El Niño. Terms forcing the oceanic mixed layer temperature (T) can be grouped into two categories: subsurface dynamics including oceanic mixing and advection (subscript "subs"), and surface energy budget changes including turbulent and radiative fluxes (subscript "Qsfc"):

$$\frac{\partial T}{\partial t} = \left(\frac{\partial T}{\partial t}\right)_{\text{Qsfc}} + \left(\frac{\partial T}{\partial t}\right)_{\text{subs}}, \tag{1}$$

with

$$\left(\frac{\partial T}{\partial t}\right)_{\text{Qsfc}} = \frac{(R_{\text{dn}} - R_{\text{up}} - \mathcal{L} - \mathcal{S})}{\rho c_p H}, \tag{2}$$

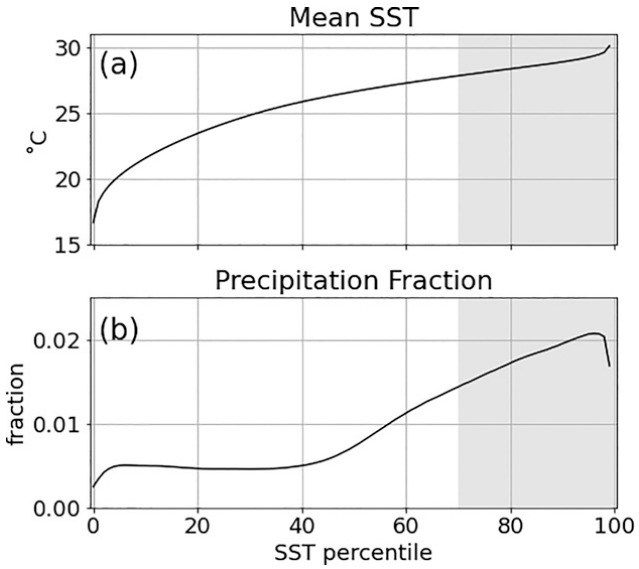


FIG. 2. (top) Mean distribution of SST and (bottom) normalized precipitation distribution in equal-area SST percentiles in ERA5. Shading highlights the top (i.e., warmest) 30 percentiles, where most rainfall occurs. The top 30 percentiles approximately represent the regions of deep atmospheric convection on which this study focuses.

where $R_{\text{dn}} - R_{\text{up}}$ is the net radiative (longwave and shortwave) flux into the ocean, $\mathcal{L}$ is the latent heat flux due to evaporation from the sea surface, and $\mathcal{S}$ is the sensible heat flux from the sea surface to the atmosphere. ρ is the density of seawater, c_p is the heat capacity of seawater, and H is the depth of the mixed layer, defined where ρ is 0.03 kg m^{-3} greater than at the surface.

On a monthly time scale, the change in SST is approximately equal to the change in the mixed layer temperature. Thus integration of Eq. (1) over several months gives a reliable estimate of the SST change over that period:

$$\Delta\text{SST} \approx \Delta T = \Delta T_{\text{Qsfc}} + \Delta T_{\text{subs}}. \tag{3}$$

We find that turbulent and radiative fluxes largely control the mixed layer temperature in warm tropical regions (~70%–100%), and we estimate ΔT_{subs} as a residual from $\Delta T - \Delta T_{\text{Qsfc}}$. We assume that 95% of incident shortwave radiation is absorbed within the mixed layer and 5% penetrates below, a conservative assumption for the 70–100-m-deep mixed layers in the warmer parts of the tropical ocean (Iudicone et al. 2008; Mobley and Mobley 1994). The energy budget is calculated entirely in Eulerian space and the resultant ΔT_{Qsfc} and ΔT_{subs} terms are subsequently averaged in their corresponding SST percentile bins.

c. ENSO index

We calculate a normalized Niño-3.4 index following Trenberth (1997) (see also Sullivan et al. 2016): 1) calculate the mean SST in the region 5°S–5°N, 170°–120°W, 2) smooth with a rectangular 5-month filter, and 3) divide by the temporal standard deviation of the smoothed time series. El Niño months are defined when

Brought to you by PRINCETON UNIVERSITY LIBRARY | Unauthenticated | Downloaded 04/21/22 08:14 PM UTC

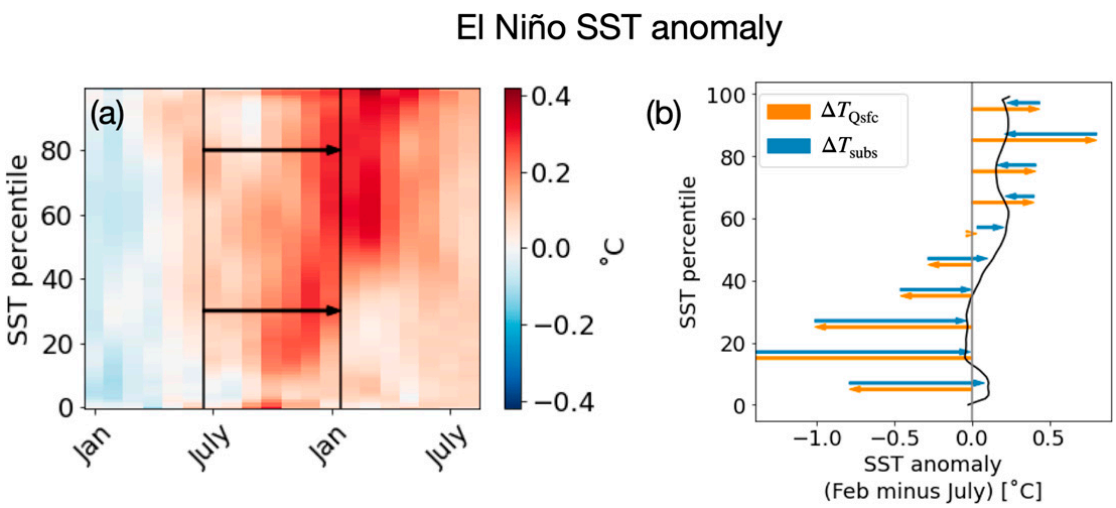


FIG. 3. (a) The ERA5 SST anomaly during a composite El Niño in SST percentiles and (b) the contribution to its growth from July to February from surface and subsurface heating. In (b), the subsurface (ΔT_{subs} includes ocean mixing and advection; blue arrows) and surface heat flux (ΔT_{Qsfc}; orange arrows) effects together account for the SST change (black line) [Eq. (3)]. (Result from GFDL-FLOR in Fig. A2.)

the normalized index exceeds 0.6. (This criterion is applied to calculate the composite result shown in Fig. 4.)

3. Data

We use data both from a free-running atmosphere–ocean coupled global climate model and from a reanalysis. The Forecast Oriented Low Ocean Resolution configuration of the Geophysical Fluid Dynamics Laboratory (GFDL) coupled climate model is referred to here as GFDL-FLOR (Vecchi et al. 2014). This model uses the nominal 1°-resolution ocean and sea ice model from GFDL-CM2.1 (Delworth et al. 2006) but a higher-resolution (0.5°) atmosphere from the GFDL-CM2.5 (Delworth et al. 2012) model and an improved land model (LM3; Milly et al. 2014). The ocean resolution telescopes to 0.333° meridional spacing near the equator. We use 100 years of FLOR results from a preindustrial control experiment, in which atmospheric CO_2 concentrations, aerosol and solar forcing are prescribed at 1860 levels (Yang et al. 2019). We also use data from the European Centre for Medium-Range Weather Forecasts (ECMWF) reanalysis version 5 (ERA5), a reconstruction of the climate state since 1979. ERA5 assimilates historical observations onto a global 30-km grid (Hersbach et al. 2019). For our analysis, all ERA5 data were linearly detrended at each location (except for the data shown in Fig. 1). We analyze the time period January 1979–February 2019, which includes seven El Niño events (1982/83, 1986/87, 1991/92, 1997/98, 2002/03, 2009/10, 2015/16) according to the criterion of the NOAA Climate Prediction Center.

The two data sources are complementary. The observationally constrained ERA5 more closely represents observed ENSO events, but only covers 40 years. The FLOR simulation, although an imperfect representation of ENSO conditions, is run for 100 years and results are highly statistically significant. The key results of interest here are very similar in ERA5 and FLOR. We therefore chose to show results in the following only for ERA5. The results based on the FLOR simulation are provided in the appendix.

4. Results

Figure 3 shows the evolution of El Niño SST anomalies in SST percentile space. ERA5 data shown in this figure uses the El Niño events listed above, with the data composited on the calendar year, beginning in the summer before an El Niño event begins, and ending with the summer after the El Niño event peaks (e.g., Philander 1983). Figure 3a shows that the colder percentiles (~20th–70th) warm over the period from July to January. These percentiles contain the eastern equatorial Pacific during El Niño events, and the warm signal in the east Pacific is responsible for the positive anomaly in these bins. The adiabatic redistribution of water from the "warm pool" in the western Pacific (Jin 1997, 1996; Meinen and McPhaden 2000) also contributes to the positive anomaly at intermediate SSTs (~40th–70th percentiles). That is, an adiabatic redistribution of the warmer water masses with a shoaling of the thermocline, and increase in areal extent at the surface, leads to a change in shape of the SST distribution but does not lead to a temperature increase at the high end of the SST distribution. Figure 3 shows that warming also occurs at the high end of the SST distribution where deep convection occurs (≳70th percentile, see also normalized rainfall distribution in Fig. 2b) over the period November–March, with a peak in February of approximately +0.4 K.

Figure 3b shows the surface layer heat budget. In the nonconvective domain (lower percentiles), the ocean loses heat to the atmosphere during El Niño (negative ΔT_{Qsfc}), which largely balances the subsurface convergence of heat from mixing and advection (positive ΔT_{subs}). Conversely, at the higher percentiles where deep convection occurs, the ocean gains heat from the atmosphere (positive ΔT_{Qsfc}) while the subsurface

Brought to you by PRINCETON UNIVERSITY LIBRARY | Unauthenticated | Downloaded 04/21/22 08:14 PM UTC

terms show a slight divergence of this energy input (negative ΔT_{subs}). Thus, the observed warming at the high end of the SST distribution is not due to oceanic processes (i.e., adiabatic redistribution of water masses and/or changes in subsurface mixing and advection) but due to an anomalous heat flux from the atmosphere to the ocean.

The results for the colder regions (e.g., eastern Pacific) as shown in Fig. 3 are consistent with prior knowledge of the surface energy budget in cold tropical regions during El Niño (e.g., Wang 2000; Lloyd et al. 2011), and we turn our attention to the anomalous heat flux from the atmosphere into the ocean at the high end of the SST distribution where deep convection occurs.

Analysis of the surface heat budget terms shows that the changes in solar radiation oppose the net anomalous heat flux into the ocean at high percentiles, while the increases in longwave radiation emitted from the ground and the increase in atmospheric back-radiation simply reflect the shift to a warmer state (Fig. A6). Changes in solar radiation act as a weak negative feedback on SST changes in the convective domain in ERA5 and a strong negative feedback in GFDL-FLOR (Fig. A6). Therefore, in neither dataset can the change in solar radiation explain the change in SST. Instead, we find that the forcing term is the latent heat flux due to evaporation. Both Figs. 4a and A6 show that evaporation decreases over the warm end of the SST distribution during El Niño. Note that this change should not be confused with the well-documented evaporation changes observed in a fixed geographic frame of reference. By virtue of sorting by SST, the changes seen here reflect a change in the conditions in the domain where deep convection occurs, and not a spatial redistribution of convective regions. But why does evaporation decrease in the convective domain during El Niño events?

The evaporation rate depends on the surface wind speed (U) and surface moisture deficit (Δq), as parameterized in the bulk formula for the latent heat flux $\mathcal{L}$ (Large and Yeager 2004, 2009): $\mathcal{L} \propto U\Delta q$. We find that the monthly mean anomalies in $\mathcal{L}$ can be attributed to the anomalies in monthly mean U and Δq to a good approximation:

$$\partial \ln(\mathcal{L}) = \partial \ln(U) + \partial \ln(\Delta q) + R, \tag{4}$$

where U represents the surface wind speed, including both horizontal components and the contribution from parameterized subgrid-scale gusts at the surface $\left(U = \sqrt{u^2 + v^2 + u_{\text{gusts}}{}^2}\right)$. The surface humidity deficit Δq is defined as the difference between the saturation specific humidity at SST and the specific humidity of near-surface air. We find we can neglect the contribution of the parameterized gusts (Fig. A3) and focus on the total U in Fig. 4. R is the contribution from 1) the correlated deviations of the monthly means of wind and moisture deficit, as well as 2) that from variations in other parameters in the bulk formula for $\mathcal{L}$, which are not constant in GFDL-FLOR but are approximated as constant here (air density ρ_a and the specific heat of vaporization L). We find that the contribution from R is small, and we do not discuss it further (see Fig. A3 for a quantification of R in GFDL-FLOR). In Fig. 4c, $\partial \ln(U) + R$ is calculated as a residual.

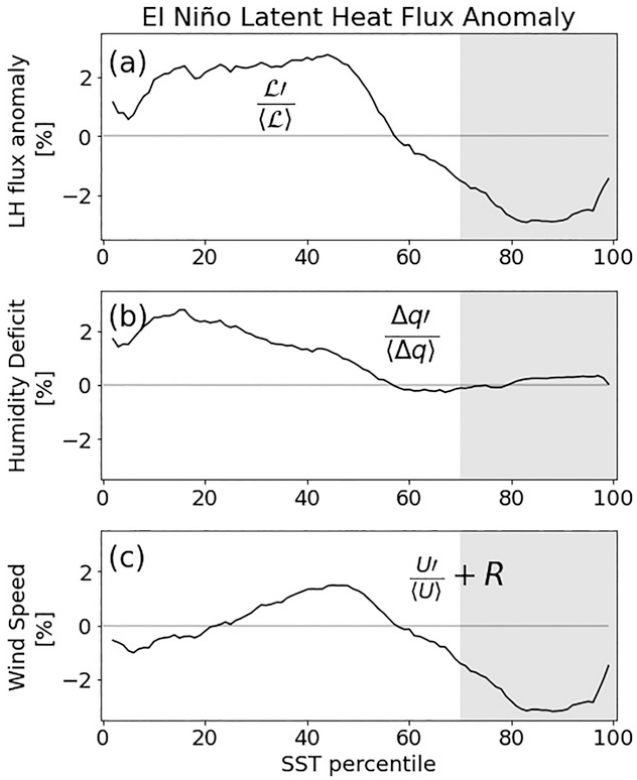


FIG. 4. (a) The anomalous latent heat flux in SST percentiles during El Niño months in the ERA5, as a fraction of the mean flux. This anomaly is approximately the sum of (b) the anomalous humidity deficit at the sea surface and (c) the anomalous surface wind speed [Eq. (4)], i.e., the black lines in (b) and (c) add to the black line in (a). The right y axis in (a), shows the normalized mean distribution of rainfall (blue). The shaded region above the 70th percentile approximates the deep convective domain and contains most of the rainfall. (Result from GFDL-FLOR in Fig. A3.)

Figure 4 shows that in the colder parts (unshaded), the increase in evaporation rate ($\mathcal{L}$) is controlled by an increase in moisture deficit (Δq; Fig. 4b). This is expected in regions where the SST increases due to a reduced supply of cold waters from the subsurface terms such as the upwelling region in the eastern Pacific [positive ΔT_{subs}; Eq. (1)], and is consistent with current understanding (e.g., Lloyd et al. 2011; Wang 2000; Zhang and McPhaden 2010). The counterintuitive heat flux *into* the ocean at the high end of the SST distribution (shaded), however, is controlled by the change in the wind term (U, Fig. 4c). This means that the SST increase in regions with atmospheric deep convection is mechanically forced by a decrease in surface winds.

The surface wind–evaporation feedback during El Niño is well documented and understood in geographical space: As the cold regions warm and the warm pool expands eastward, SSTs in the central Pacific reach the convective threshold, and deep convection sets in. Associated with this local change of regime is a decrease in wind speed (since the wind speed is in general lower in the convective than in the nonconvective domain), which contributes to the warming there (Zhang et al. 1995; Wang 1995; Zhang and McPhaden 1995). However, this

Brought to you by PRINCETON UNIVERSITY LIBRARY | Unauthenticated | Downloaded 04/21/22 08:14 PM UTC

recognized feedback does not make a prediction as to whether the wind speed in the domain of deep convection during El Niño is any different from the wind speed in the domain with deep convection in the climatological base state. By sorting the data by SST, we demonstrate that the wind speed, and consequently evaporation, is anomalously low in the domain with deep convection (Fig. 4), and this result is consistent between ERA5 (Fig. 4) and GFDL-FLOR (Fig. A3).

5. Conclusions

The more zonally symmetric atmospheric circulation (a weaker Walker cell) during El Niño events is associated with lower wind speeds in the domain where atmospheric deep convection occurs than in the base state. That is, surface winds are always weak in the convective domain, but they are even weaker during El Niño. The decrease in wind speed in this domain leads to an anomalous heat flux into the ocean, which leads to an increase in SSTs, and consequently to the prominent warming of the tropical (and eventually global) free troposphere due to convective quasi-equilibrium.

The result that a mechanical forcing (wind) leads to the prominent warming signal of ENSO has implications for our understanding of El Niño's effect on the global energy budget (Xie and Kosaka 2017; Po-Chedley et al. 2021). The release of energy from the ocean to the atmosphere in the colder tropical regions is partly opposed by this input of heat into the ocean at the high end of the SST distribution. In turn, the atmospheric warming (and associated surface warming) from the heat input into the ocean also affects outgoing longwave radiation (Radley et al. 2014; Ceppi and Fueglistaler 2021). Our result opens new perspectives on understanding the mechanisms linking oceanic heat content changes and surface temperature trends, and how they are affected by ENSO (Po-Chedley et al. 2021) and the interdecadal Pacific oscillation, which has a similar structure as ENSO (Meehl and Hu 2006; Meehl et al. 2011; Xie et al. 2016). While heat fluxes out of the ocean driven by natural variability are generally accompanied by a mean warming of the sea surface (as at cold percentiles here), our results show that at warm tropical SSTs, an increase in temperature during El Niño is instead driven by a heat flux into the ocean.

Acknowledgments. A.K.H. acknowledges support from the National Science Foundation Graduate Research Fellowship Program under Grant DGE-2039656. Any opinions, findings, and conclusions or recommendations expressed in this material are those of the author and do not necessarily reflect the views of the National Science Foundation. The authors thank Wenchang Yang for making available the FLOR pre-industrial control experiment (Yang et al. 2019). The authors declare no competing financial interests.

Data availability statement. ERA5 data were downloaded from the Copernicus Climate Data Store in January 2020 (Hersbach et al. 2019). The processed data from GFDL-FLOR used in this study are hosted by Dataspace (https://doi.org/10.34770/g7fe-hs07). The NOAA/CPC information identifying El Niño events is available online (https://origin.cpc.ncep.noaa.gov/products/analysis_monitoring/ensostuff/ONI_v5.php) on the page "Historical El Niño and La Niña episodes (1950-present): Cold and Warm Episodes by Season."

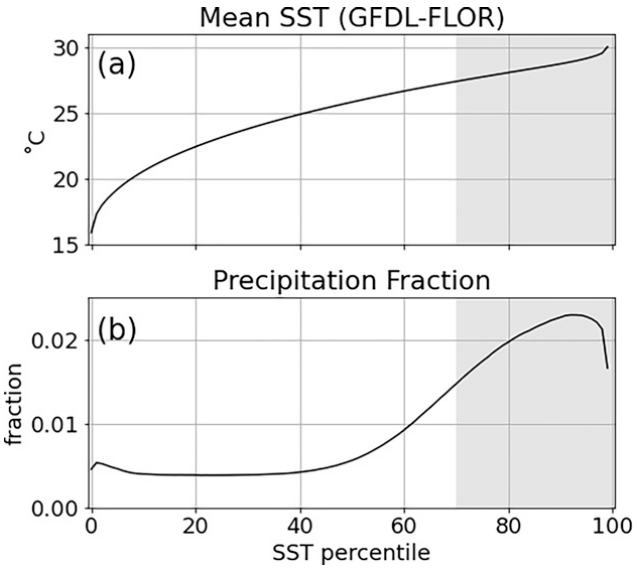


FIG. A1. As in Fig. 2, but for GFDL-FLOR.

APPENDIX

Results in GFDL-FLOR, and during La Niña

For clarity, we have presented our arguments based on the data for El Niño as represented in ERA5. Here, we show that one arrives at the same conclusion when analyzing a free-running coupled ocean–atmosphere model, and when analyzing La Niña instead of El Niño.

Figure A1 shows the mean distribution of SST (Fig. A1a) and precipitation (Fig. A1b) in SST percentiles in GFDL-FLOR. Just as in ERA5, SST increases monotonically, albeit with faster increases and decreases at very low and high percentiles. The small, much colder area at very low percentiles is made up of the subtropics and coastal upwelling regions. The small, much warmer area at very warm percentiles represents coastal seas that are heated by insolation (clouds do not form because offshore winds advect very dry air toward the ocean; cf. precipitation distribution in Fig. A1b) such as the Red Sea and China Sea. The precipitation distribution is known to have a strong nonlinear dependence on SST, and much of the total tropical rainfall falls in regions of deep convection. The 70th percentile approximates the convective threshold of 27°–28°C, as is shown in Fig. A1a.

Figure A2 is the same as Fig. 3, but with data from GFDL-FLOR. The main result is the warming in high SST percentiles associated with an anomalous heat flux from the atmosphere into the ocean, just as in ERA5.

Figure A3 is the same as Fig. 4, but with data from GFDL-FLOR. As in ERA5, the anomalous decrease in

Brought to you by PRINCETON UNIVERSITY LIBRARY | Unauthenticated | Downloaded 04/21/22 08:14 PM UTC

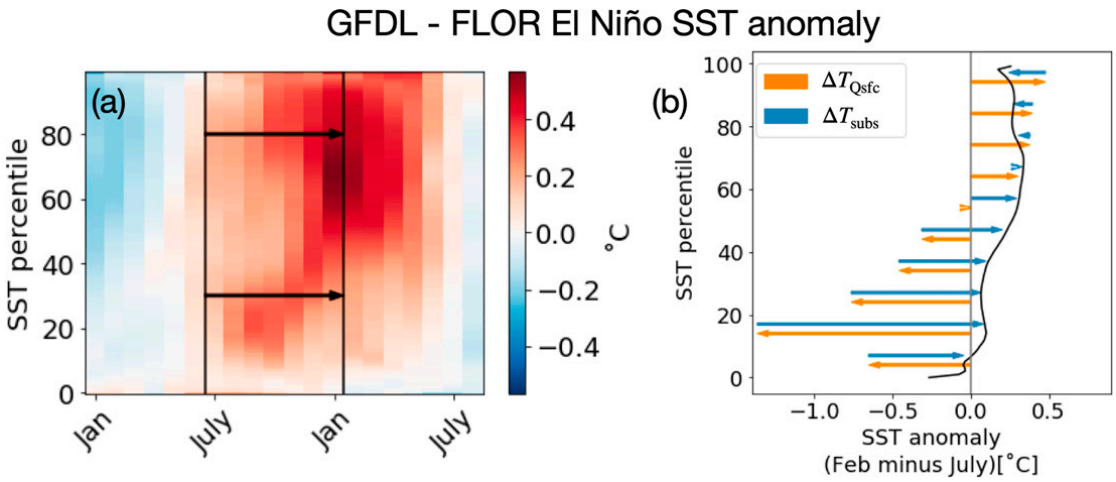


FIG. A2. As in Fig. 3, but for GFDL-FLOR.

latent heat flux at the warm end of the SST distribution is driven by a decrease in wind speed. The sign change in the latent heat flux anomaly (positive at low percentiles, then negative in high percentiles) occurs at a slightly higher percentile than in ERA5, but more importantly the decrease in $\mathcal{L}$ occurs over the convective regime (shaded region; see precipitation distribution in Fig. A3a). This decreased latent heat flux is clearly tied to a decrease in wind speed (Fig. A3c), as in ERA5. Furthermore, we are able to confirm that the decreased wind speed at high SSTs is not a product of the parameterization of convective gustiness (u_{gusts}) in this particular model. We test this by assigning u_{gusts} a constant value everywhere, and calculating the El Niño surface wind speed (U) anomaly with this constant u_{gusts}. The fact that the dashed (constant u_{gusts}) and solid (varying u_{gusts}) lines agree at warm SSTs suggests that the decreases wind speed in the domain of deep convection at high SSTs is driven by the resolved wind, and as such by the large-scale wind pattern.

Figure A4 shows the SST and heat flux anomalies as in Figs. 3 (ERA5) and A2 (GFDL-FLOR), but during a composite La Niña event and from both datasets, as labeled. The El Niño-La Niña succession in GFDL-FLOR is more regular, and somewhat faster, than in ERA5. As a result, in January–May (at the beginning of Figs. A4a and A4c), the SST anomalies in ERA5 and GFDL-FLOR differ because the anomaly fields in GFDL-FLOR are recovering from the prior El Niño. But during the La Niña event (from July to January, and the subsequent decay) the evolution is similar and both show a heat flux from the ocean to the atmosphere at the warm end of the SST distribution (i.e., the opposite of the signal during El Niño).

Figure A5 shows the cause of the latent heat flux anomalies during La Niña (i.e., the equivalent to Figs. 4 and A3, for La Niña). Both ERA5 and GFDL-FLOR show a decrease in wind speed at the high end of the SST distribution (again, opposing the signal observed during El Niño). And as during El Niño, the increase in wind speed in the convective domain is found even with a constant u_{gusts} (Fig. A5c).

Figure A6 shows the anomalous surface energy budget, with Q_{net} dominated by the anomalous latent heat flux, during El Niño (Figs. A6a,b) and La Niña (Figs. A6c,d). Note that surface heating by shortwave radiation (SW) is less than usual in warm, rainy regions during El Niño in both the reanalysis and GCM (and the inverse, during La Niña). The redistribution of clouds therefore opposes the SST increase in the convective domain during El Niño.

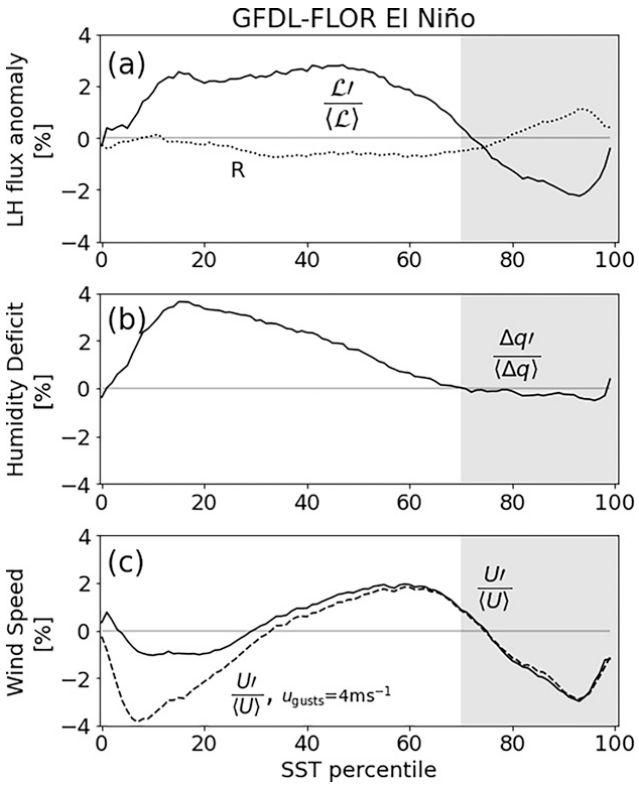


FIG. A3. As in Fig. 4, but for GFDL-FLOR. In (c), the dashed line represents the U anomaly that would be found if u_{gusts} maintained a constant value everywhere of 4 m s^{-1} (near its average value).

Brought to you by PRINCETON UNIVERSITY LIBRARY | Unauthenticated | Downloaded 04/21/22 08:14 PM UTC

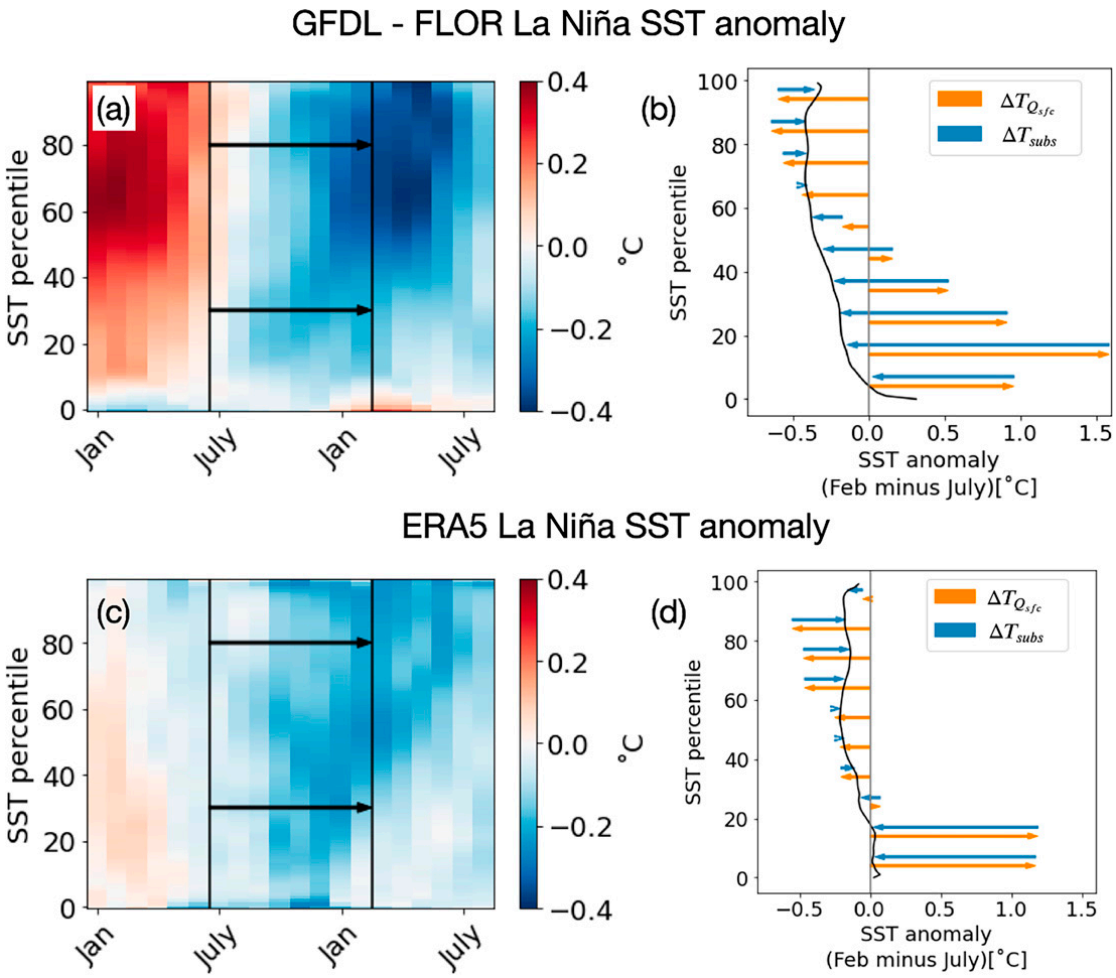


FIG. A4. As in Figs. 3 and A4, but for La Niña. Includes data from (bottom) ERA5 and (top) GFDL-FLOR.

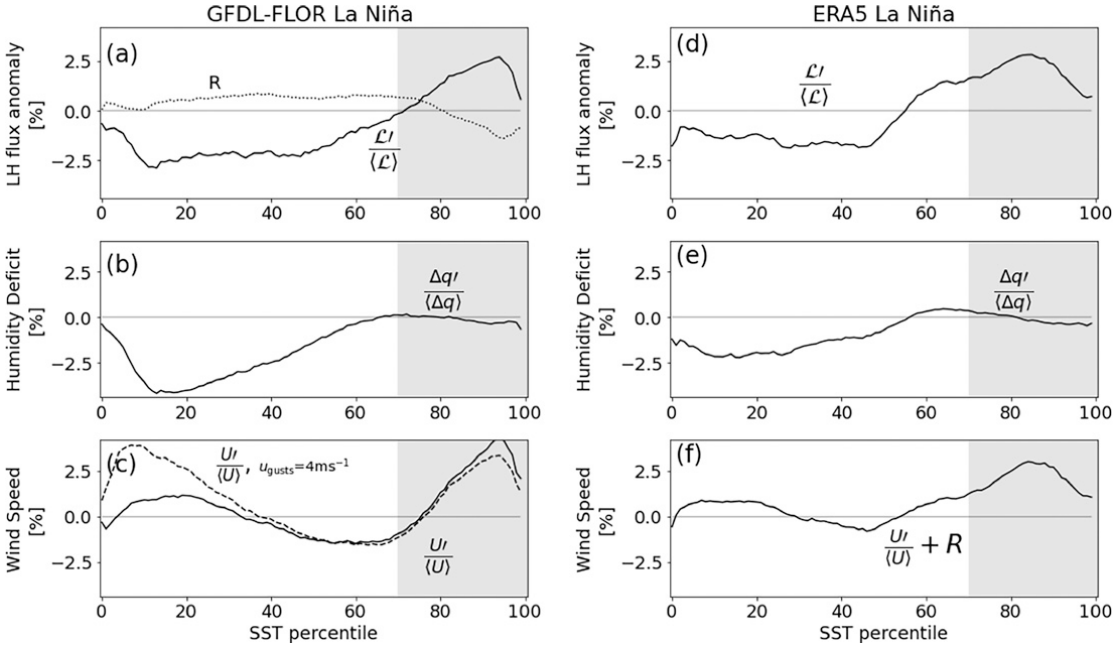


FIG. A5. As in Figs. 4 and A5, but for La Niña. Includes data from (right) ERA5 and (left) GFDL-FLOR.

Brought to you by PRINCETON UNIVERSITY LIBRARY | Unauthenticated | Downloaded 04/21/22 08:14 PM UTC

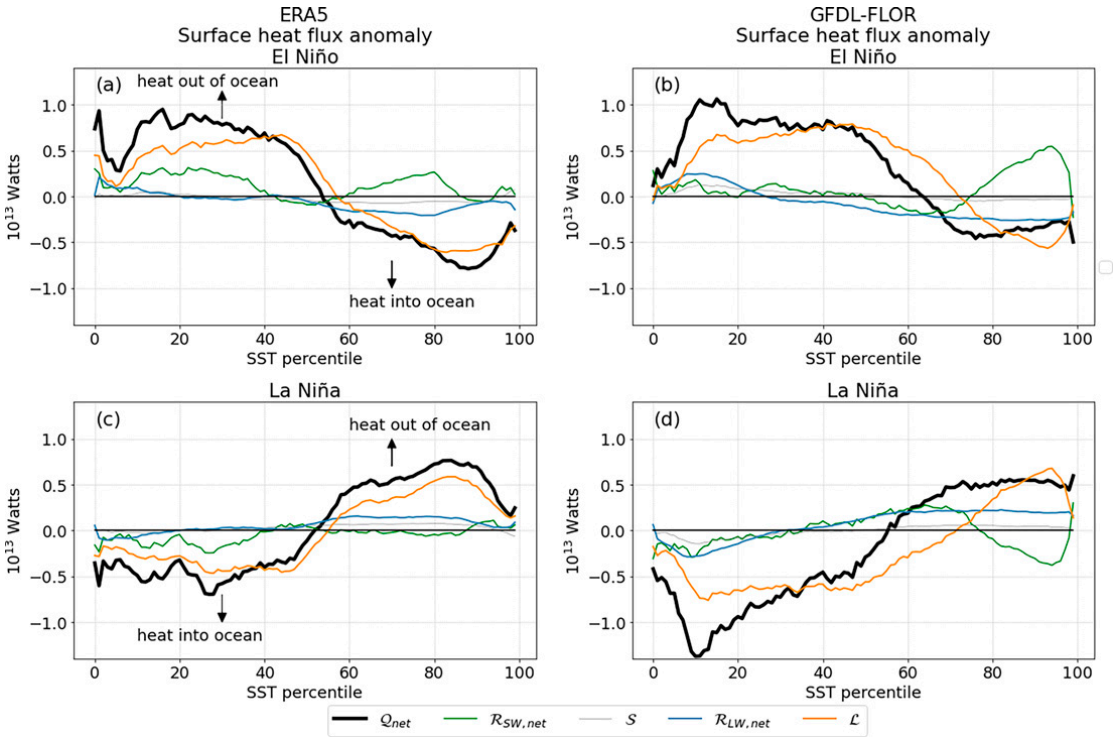


FIG. A6. Anomalous surface energy fluxes over tropical oceans (30°S–30°N) during (top) El Niño and (bottom) La Niña. El Niño months are defined to be months when the normalized Niño-3.4 index exceeds 0.6, while La Niña months are those when the index is less than −0.6. The net (down − up) longwave and shortwave components of $\mathcal{R}$ are shown separately as $\mathcal{R}_{\mathrm{LW,net}}$ and $\mathcal{R}_{\mathrm{SW,net}}$, respectively. Positive indicates a heat flux out of the ocean into the atmosphere. Results are from (left) ERA5 and (right) GFDL-FLOR.

REFERENCES

Alexander, M. A., I. Bladé, M. Newman, J. R. Lanzante, N.-C. Lau, and J. D. Scott, 2002: The atmospheric bridge: The influence of ENSO teleconnections on air–sea interaction over the global oceans. *J. Climate*, **15**, 2205–2231, https://doi.org/10.1175/1520-0442(2002)015<2205:TABTIO>2.0.CO;2.

Ballester, J., S. Bordoni, D. Petrova, and X. Rodó, 2015: On the dynamical mechanisms explaining the western Pacific subsurface temperature buildup leading to ENSO events. *Geophys. Res. Lett.*, **42**, 2961–2967, https://doi.org/10.1002/2015GL063701.

Battisti, D. S., and A. C. Hirst, 1989: Interannual variability in a tropical atmosphere–ocean model: Influence of the basic state, ocean geometry and nonlinearity. *J. Atmos. Sci.*, **46**, 1687–1712, https://doi.org/10.1175/1520-0469(1989)046<1687:IVIATA>2.0.CO;2.

Bony, S., K. Lau, and Y. Sud, 1997: Sea surface temperature and large-scale circulation influences on tropical greenhouse effect and cloud radiative forcing. *J. Climate*, **10**, 2055–2077, https://doi.org/10.1175/1520-0442(1997)010<2055:SSTALS>2.0.CO;2.

Brown, R. G., and C. S. Bretherton, 1997: A test of the strict quasi-equilibrium theory on long time and space scales. *J. Atmos. Sci.*, **54**, 624–638, https://doi.org/10.1175/1520-0469(1997)054<0624:ATOTSQ>2.0.CO;2.

Cai, W., and Coauthors, 2019: Pantropical climate interactions. *Science*, **363**, eaav4236, https://doi.org/10.1126/science.aav4236.

Ceppi, P., and S. Fueglistaler, 2021: The El Niño–Southern Oscillation pattern effect. *Geophys. Res. Lett.*, **48**, e2021GL095261, https://doi.org/10.1029/2021GL095261.

Cheng, L., K. E. Trenberth, J. T. Fasullo, M. Mayer, M. Balmaseda, and J. Zhu, 2019: Evolution of ocean heat content related to ENSO. *J. Climate*, **32**, 3529–3556, https://doi.org/10.1175/JCLI-D-18-0607.1.

Chiang, J. C., and A. H. Sobel, 2002: Tropical tropospheric temperature variations caused by ENSO and their influence on the remote tropical climate. *J. Climate*, **15**, 2616–2631, https://doi.org/10.1175/1520-0442(2002)015<2616:TTTVCB>2.0.CO;2.

——, and B. R. Lintner, 2005: Mechanisms of remote tropical surface warming during El Niño. *J. Climate*, **18**, 4130–4149, https://doi.org/10.1175/JCLI3529.1.

Ciasto, L. M., and M. H. England, 2011: Observed ENSO teleconnections to Southern Ocean SST anomalies diagnosed from a surface mixed layer heat budget. *Geophys. Res. Lett.*, **38**, L09701, https://doi.org/10.1029/2011GL046895.

Delworth, T. L., and Coauthors, 2006: GFDL's CM2 global coupled climate models. Part I: Formulation and simulation characteristics. *J. Climate*, **19**, 643–674, https://doi.org/10.1175/JCLI3629.1.

——, and Coauthors, 2012: Simulated climate and climate change in the GFDL CM2.5 high-resolution coupled climate model. *J. Climate*, **25**, 2755–2781, https://doi.org/10.1175/JCLI-D-11-00316.1.

Deser, C., and J. M. Wallace, 1990: Large-scale atmospheric circulation features of warm and cold episodes in the tropical Pacific. *J. Climate*, **3**, 1254–1281, https://doi.org/10.1175/1520-0442(1990)003<1254:LSACFO>2.0.CO;2.

Dessler, A. E., 2010: A determination of the cloud feedback from climate variations over the past decade. *Science*, **330**, 1523–1527, https://doi.org/10.1126/science.1192546.

Brought to you by PRINCETON UNIVERSITY LIBRARY | Unauthenticated | Downloaded 04/21/22 08:14 PM UTC

——, 2013: Observations of climate feedbacks over 2000–10 and comparisons to climate models. *J. Climate*, **26**, 333–342, https://doi.org/10.1175/JCLI-D-11-00640.1.

Emanuel, K. A., 1995: On thermally direct circulations in moist atmospheres. *J. Atmos. Sci.*, **52**, 1529–1534, https://doi.org/10.1175/1520-0469(1995)052<1529:OTDCIM>2.0.CO;2.

Flannaghan, T. J., S. Fueglistaler, I. M. Held, S. Po-Chedley, B. Wyman, and M. Zhao, 2014: Tropical temperature trends in atmospheric general circulation model simulations and the impact of uncertainties in observed SSTs. *J. Geophys. Res. Atmos.*, **119**, 13 327–13 337, https://doi.org/10.1002/2014JD022365.

Fueglistaler, S., 2019: Observational evidence for two modes of coupling between sea surface temperatures, tropospheric temperature profile, and shortwave cloud radiative effect in the tropics. *Geophys. Res. Lett.*, **46**, 9890–9898, https://doi.org/10.1029/2019GL083990.

——, C. Radley, and I. M. Held, 2015: The distribution of precipitation and the spread in tropical upper tropospheric temperature trends in CMIP5/AMIP simulations. *Geophys. Res. Lett.*, **42**, 6000–6007, https://doi.org/10.1002/2015GL064966.

Graham, N., and T. Barnett, 1987: Sea surface temperature, surface wind divergence, and convection over tropical oceans. *Science*, **238**, 657–659, https://doi.org/10.1126/science.238.4827.657.

Hersbach, H., and Coauthors, 2019: ERA5 monthly averaged data on single levels from 1979 to present. Copernicus Climate Change Service (C3S) Climate Data Store (CDS), accessed January 2019, https://doi.org/10.24381/cds.f17050d7.

Hoerling, M. P., A. Kumar, and M. Zhong, 1997: El Niño, La Niña, and the nonlinearity of their teleconnections. *J. Climate*, **10**, 1769–1786, https://doi.org/10.1175/1520-0442(1997)010<1769:ENOLNA>2.0.CO;2.

Hurrell, J. W., and K. E. Trenberth, 1998: Difficulties in obtaining reliable temperature trends: Reconciling the surface and satellite microwave sounding unit records. *J. Climate*, **11**, 945–967, https://doi.org/10.1175/1520-0442(1998)011<0945:DIORTT>2.0.CO;2.

Iudicone, D., G. Madec, and T. J. McDougall, 2008: Water-mass transformations in a neutral density framework and the key role of light penetration. *J. Phys. Oceanogr.*, **38**, 1357–1376, https://doi.org/10.1175/2007JPO3464.1.

Jin, F.-F., 1996: Tropical ocean-atmosphere interaction, the Pacific cold tongue, and the El Niño-Southern Oscillation. *Science*, **274**, 76–78, https://doi.org/10.1126/science.274.5284.76.

——, 1997: An equatorial ocean recharge paradigm for ENSO. Part I: Conceptual model. *J. Atmos. Sci.*, **54**, 811–829, https://doi.org/10.1175/1520-0469(1997)054<0811:AEORPF>2.0.CO;2.

Klein, S. A., B. J. Soden, and N.-C. Lau, 1999: Remote sea surface temperature variations during ENSO: Evidence for a tropical atmospheric bridge. *J. Climate*, **12**, 917–932, https://doi.org/10.1175/1520-0442(1999)012<0917:RSSTVD>2.0.CO;2.

Kumar, A., and M. P. Hoerling, 2003: The nature and causes for the delayed atmospheric response to El Niño. *J. Climate*, **16**, 1391–1403, https://doi.org/10.1175/1520-0442-16.9.1391.

Large, W. G., and S. G. Yeager, 2004: Diurnal to decadal global forcing for ocean and sea-ice models: The data sets and flux climatologies. NCAR Tech. Note NCAR/TN-460+STR, 105 pp., https://doi.org/10.5065/D6KK98Q6.

——, and ——, 2009: The global climatology of an interannually varying air–sea flux data set. *Climate Dyn.*, **33**, 341–364, https://doi.org/10.1007/s00382-008-0441-3.

Latif, M., and A. Grötzner, 2000: The equatorial Atlantic oscillation and its response to ENSO. *Climate Dyn.*, **16**, 213–218, https://doi.org/10.1007/s003820050014.

Lau, N.-C., and M. J. Nath, 1996: The role of the "atmospheric bridge" in linking tropical Pacific ENSO events to extratropical SST anomalies. *J. Climate*, **9**, 2036–2057, https://doi.org/10.1175/1520-0442(1996)009<2036:TROTBI>2.0.CO;2.

Lintner, B. R., and J. C. Chiang, 2005: Reorganization of tropical climate during El Niño: A weak temperature gradient approach. *J. Climate*, **18**, 5312–5329, https://doi.org/10.1175/JCLI3580.1.

——, and ——, 2007: Adjustment of the remote tropical climate to El Niño conditions. *J. Climate*, **20**, 2544–2557, https://doi.org/10.1175/JCLI4138.1.

Liu, Z., and M. Alexander, 2007: Atmospheric bridge, oceanic tunnel, and global climatic teleconnections. *Rev. Geophys.*, **45**, RG2005, https://doi.org/10.1029/2005RG000172.

Lloyd, J., E. Guilyardi, and H. Weller, 2011: The role of atmosphere feedbacks during ENSO in the CMIP3 models. Part II: Using AMIP runs to understand the heat flux feedback mechanisms. *Climate Dyn.*, **37**, 1271–1292, https://doi.org/10.1007/s00382-010-0895-y.

Mayer, M., K. E. Trenberth, L. Haimberger, and J. T. Fasullo, 2013: The response of tropical atmospheric energy budgets to ENSO. *J. Climate*, **26**, 4710–4724, https://doi.org/10.1175/JCLI-D-12-00681.1.

——, J. T. Fasullo, K. E. Trenberth, and L. Haimberger, 2016: ENSO-driven energy budget perturbations in observations and CMIP models. *Climate Dyn.*, **47**, 4009–4029, https://doi.org/10.1007/s00382-016-3057-z.

Meehl, G. A., and A. Hu, 2006: Megadroughts in the Indian monsoon region and southwest North America and a mechanism for associated multidecadal Pacific sea surface temperature anomalies. *J. Climate*, **19**, 1605–1623, https://doi.org/10.1175/JCLI3675.1.

——, J. M. Arblaster, J. T. Fasullo, A. Hu, and K. E. Trenberth, 2011: Model-based evidence of deep-ocean heat uptake during surface-temperature hiatus periods. *Nat. Climate Change*, **1**, 360–364, https://doi.org/10.1038/nclimate1229.

Meinen, C. S., and M. J. McPhaden, 2000: Observations of warm water volume changes in the equatorial Pacific and their relationship to El Niño and La Niña. *J. Climate*, **13**, 3551–3559, https://doi.org/10.1175/1520-0442(2000)013<3551:OOWWVC>2.0.CO;2.

Milly, P. C. D., and Coauthors, 2014: An enhanced model of land water and energy for global hydrologic and earth-system studies. *J. Hydrometeor.*, **15**, 1739–1761, https://doi.org/10.1175/JHM-D-13-0162.1.

Mobley, C. D., and C. D. Mobley, 1994: *Light and Water: Radiative Transfer in Natural Waters*. Academic Press, 592 pp.

Neelin, J. D., and I. M. Held, 1987: Modeling tropical convergence based on the moist static energy budget. *Mon. Wea. Rev.*, **115**, 3–12, https://doi.org/10.1175/1520-0493(1987)115<0003:MTCBOT>2.0.CO;2.

——, D. S. Battisti, A. C. Hirst, F.-F. Jin, Y. Wakata, T. Yamagata, and S. E. Zebiak, 1998: ENSO theory. *J. Geophys. Res.*, **103**, 14 261–14 290, https://doi.org/10.1029/97JC03424.

Philander, S. G. H., 1983: El Niño–Southern Oscillation phenomena. *Nature*, **302**, 295–301, https://doi.org/10.1038/302295a0.

Picaut, J., 1997: An advective-reflective conceptual model for the oscillatory nature of the ENSO. *Science*, **277**, 663–666, https://doi.org/10.1126/science.277.5326.663.

Po-Chedley, S., and Q. Fu, 2012: Discrepancies in tropical upper tropospheric warming between atmospheric circulation models and satellites. *Environ. Res. Lett.*, **7**, 044018, https://doi.org/10.1088/1748-9326/7/4/044018.

Brought to you by PRINCETON UNIVERSITY LIBRARY | Unauthenticated | Downloaded 04/21/22 08:14 PM UTC

——, B. D. Santer, S. Fueglistaler, M. D. Zelinka, P. J. Cameron-Smith, J. F. Painter, and Q. Fu, 2021: Natural variability contributes to model–satellite differences in tropical tropospheric warming. *Proc. Natl. Acad. Sci. USA*, **118**, e2020962118, https://doi.org/10.1073/pnas.2020962118.

Radley, C., S. Fueglistaler, and L. Donner, 2014: Cloud and radiative balance changes in response to ENSO in observations and models. *J. Climate*, **27**, 3100–3113, https://doi.org/10.1175/JCLI-D-13-00338.1.

Randall, D. A., and K. Emanuel, 2000: Quasi-equilibrium thinking. *General Circulation Model Development: Past, Present, and Future*, D. A. Randall, Ed., Elsevier Academic Press, 225–256.

Rasmusson, E. M., and J. M. Wallace, 1983: Meteorological aspects of the El Niño/Southern Oscillation. *Science*, **222**, 1195–1202, https://doi.org/10.1126/science.222.4629.1195.

Raymond, D. J., S. L. Sessions, A. H. Sobel, and Z. Fuchs, 2009: The mechanics of gross moist stability. *J. Adv. Model. Earth Syst.*, **1**, 9, https://doi.org/10.3894/JAMES.2009.1.9.

Santer, B. D., and Coauthors, 2001: Accounting for the effects of volcanoes and ENSO in comparisons of modeled and observed temperature trends. *J. Geophys. Res.*, **106**, 28 033–28 059, https://doi.org/10.1029/2000JD000189.

Sobel, A. H., and C. S. Bretherton, 2000: Modeling tropical precipitation in a single column. *J. Climate*, **13**, 4378–4392, https://doi.org/10.1175/1520-0442(2000)013<4378:MTPIAS>2.0.CO;2.

——, I. M. Held, and C. S. Bretherton, 2002: The ENSO signal in tropical tropospheric temperature. *J. Climate*, **15**, 2702–2706, https://doi.org/10.1175/1520-0442(2002)015<2702:TESITT>2.0.CO;2.

Soden, B. J., 1997: Variations in the tropical greenhouse effect during El Niño. *J. Climate*, **10**, 1050–1055, https://doi.org/10.1175/1520-0442(1997)010<1050:VITTGE>2.0.CO;2.

Su, H., J. D. Neelin, and C. Chou, 2001: Tropical teleconnection and local response to SST anomalies during the 1997–1998 El Niño. *J. Geophys. Res.*, **106**, 20 025–20 043, https://doi.org/10.1029/2000JD000124.

——, ——, and J. E. Meyerson, 2005: Mechanisms for lagged atmospheric response to ENSO SST forcing. *J. Climate*, **18**, 4195–4215, https://doi.org/10.1175/JCLI3514.1.

Sullivan, A., J.-J. Luo, A. C. Hirst, D. Bi, W. Cai, and J. He, 2016: Robust contribution of decadal anomalies to the frequency of Central-Pacific El Niño. *Sci. Rep.*, **6**, 38540, https://doi.org/10.1038/srep38540.

Trenberth, K. E., 1997: The definition of El Niño. *Bull. Amer. Meteor. Soc.*, **78**, 2771–2777, https://doi.org/10.1175/1520-0477(1997)078<2771:TDOENO>2.0.CO;2.

——, and J. M. Caron, 2001: Estimates of meridional atmosphere and ocean heat transports. *J. Climate*, **14**, 3433–3443, https://doi.org/10.1175/1520-0442(2001)014<3433:EOMAAO>2.0.CO;2.

——, and D. P. Stepaniak, 2003: Covariability of components of poleward atmospheric energy transports on seasonal and interannual timescales. *J. Climate*, **16**, 3691–3705, https://doi.org/10.1175/1520-0442(2003)016<3691:COCOPA>2.0.CO;2.

——, and L. Smith, 2009: The three dimensional structure of the atmospheric energy budget: Methodology and evaluation. *Climate Dyn.*, **32**, 1065–1079, https://doi.org/10.1007/s00382-008-0389-3.

——, J. M. Caron, D. P. Stepaniak, and S. Worley, 2002: Evolution of El Niño–Southern Oscillation and global atmospheric surface temperatures. *J. Geophys. Res.*, **107**, 4065, https://doi.org/10.1029/2000JD000298.

——, Y. Zhang, J. T. Fasullo, and S. Taguchi, 2015: Climate variability and relationships between top-of-atmosphere radiation and temperatures on earth. *J. Geophys. Res. Atmos.*, **120**, 3642–3659, https://doi.org/10.1002/2014JD022887.

Tuel, A., 2019: Explaining differences between recent model and satellite tropospheric warming rates with tropical SSTs. *Geophys. Res. Lett.*, **46**, 9023–9030, https://doi.org/10.1029/2019GL083994.

Vecchi, G. A., and Coauthors, 2014: On the seasonal forecasting of regional tropical cyclone activity. *J. Climate*, **27**, 7994–8016, https://doi.org/10.1175/JCLI-D-14-00158.1.

Vialard, J., C. Menkes, J.-P. Boulanger, P. Delecluse, E. Guilyardi, M. J. McPhaden, and G. Madec, 2001: A model study of oceanic mechanisms affecting equatorial Pacific sea surface temperature during the 1997–98 El Niño. *J. Phys. Oceanogr.*, **31**, 1649–1675, https://doi.org/10.1175/1520-0485(2001)031<1649:AMSOOM>2.0.CO;2.

Wang, B., 1995: Transition from a cold to a warm state of the El Niño–Southern Oscillation cycle. *Meteor. Atmos. Phys.*, **56**, 17–32, https://doi.org/10.1007/BF01022519.

Wang, C., 2000: On the atmospheric responses to tropical Pacific heating during the mature phase of El Niño. *J. Atmos. Sci.*, **57**, 3767–3781, https://doi.org/10.1175/1520-0469(2000)057<3767:OTARTT>2.0.CO;2.

——, R. H. Weisberg, and J. I. Virmani, 1999: Western Pacific interannual variability associated with the El Niño–Southern Oscillation. *J. Geophys. Res.*, **104**, 5131–5149, https://doi.org/10.1029/1998JC900090.

——, C. Deser, J.-Y. Yu, P. DiNezio, and A. Clement, 2017: El Niño and Southern Oscillation (ENSO): A review. *Coral Reefs of the Eastern Tropical Pacific: Persistence and Loss in a Dynamic Environment*, P. W. Glynn, D. P. Manzello, and I. C. Enochs, Eds., Springer, 85–106.

Wang, W., and M. J. McPhaden, 2000: The surface-layer heat balance in the equatorial Pacific Ocean. Part II: Interannual variability. *J. Phys. Oceanogr.*, **30**, 2989–3008, https://doi.org/10.1175/1520-0485(2001)031<2989:TSLHBI>2.0.CO;2.

Xie, S.-P., and Y. Kosaka, 2017: What caused the global surface warming hiatus of 1998–2013? *Curr. Climate Change Rep.*, **3**, 128–140, https://doi.org/10.1007/s40641-017-0063-0.

——, ——, and Y. M. Okumura, 2016: Distinct energy budgets for anthropogenic and natural changes during global warming hiatus. *Nat. Geosci.*, **9**, 29–33, https://doi.org/10.1038/ngeo2581.

Yang, W., G. A. Vecchi, S. Fueglistaler, L. W. Horowitz, D. J. Luet, Á. G. Muñoz, D. Paynter, and S. Underwood, 2019: Climate impacts from large volcanic eruptions in a high-resolution climate model: The importance of forcing structure. *Geophys. Res. Lett.*, **46**, 7690–7699, https://doi.org/10.1029/2019GL082367.

Yulaeva, E., and J. M. Wallace, 1994: The signature of ENSO in global temperature and precipitation fields derived from the microwave sounding unit. *J. Climate*, **7**, 1719–1736, https://doi.org/10.1175/1520-0442(1994)007<1719:TSOEIG>2.0.CO;2.

Zebiak, S. E., and M. A. Cane, 1987: A model El Niño–Southern Oscillation. *Mon. Wea. Rev.*, **115**, 2262–2278, https://doi.org/10.1175/1520-0493(1987)115<2262:AMENO>2.0.CO;2.

Zhang, C., 1993: Large-scale variability of atmospheric deep convection in relation to sea surface temperature in the tropics. *J. Climate*, **6**, 1898–1913, https://doi.org/10.1175/1520-0442(1993)006<1898:LSVOAD>2.0.CO;2.

Brought to you by PRINCETON UNIVERSITY LIBRARY | Unauthenticated | Downloaded 04/21/22 08:14 PM UTC

Zhang, G. J., and M. J. McPhaden, 1995: The relationship between sea surface temperature and latent heat flux in the equatorial Pacific. *J. Climate*, **8**, 589–605, https://doi.org/10.1175/1520-0442(1995)008<0589:TRBSST>2.0.CO;2.

——, V. Ramanathan, and M. J. McPhaden, 1995: Convection-evaporation feedback in the equatorial Pacific. *J. Climate*, **8**, 3040–3051, https://doi.org/10.1175/1520-0442(1995)008<3040:CEFITE>2.0.CO;2.

Zhang, X., and M. J. McPhaden, 2010: Surface layer heat balance in the eastern equatorial Pacific Ocean on interannual time scales: Influence of local versus remote wind forcing. *J. Climate*, **23**, 4375–4394, https://doi.org/10.1175/2010JCLI3469.1.

Zhang, Y., and S. Fueglistaler, 2020: How tropical convection couples high moist static energy over land and ocean. *Geophys. Res. Lett.*, **47**, e2019GL086387, https://doi.org/10.1029/2019GL086387.

Brought to you by PRINCETON UNIVERSITY LIBRARY | Unauthenticated | Downloaded 04/21/22 08:14 PM UTC

4

Conclusions

This thesis demonstrates for the first time the spatial modulation of ocean de-oxygenation and the carbon-climate feedback by the amplification of the hydrological cycle, as well as the mechanisms linking surface and free-tropospheric warming during El Niño events. We build understanding by quantifying the role of each active mechanism (circulation, temperature, air-sea heat flux) in changing oxygen, carbon, and SST. We also demonstrate two complementary applications of climate models: (1) a perturbation experiment which isolates the role of freshwater fluxes in changing oceanic oxygen and carbon concentrations and (2) a surface energy budget in a fully coupled experiment which quantifies the contribution of air-sea and subsurface heat fluxes to a change in SST. The fully-coupled and experimental perturbation approaches are complementary: the fully-coupled approach better represents the quantitative contribution of each driver but requires prior intuition (e.g. about the independence of wind speed vs. longwave heat flux from the local monthly-mean SST anomaly), while the perturbation approach is useful for building intuition but provides less precise

quantitative estimates of the contributions from each mechanism due to non-linearities in the climate system (for example, due to non-linearity of equation of state of the ocean to salinity and temperature changes, and non-linearity of the carbonate system).

Chapters 1 and 2 add spatial structure to our mental model of how oxygen and carbon in the ocean are projected to respond to climate change in the coming decades. Not only does warming lead to oxygen loss and slow the overturning circulation, but hydrological cycle amplification leads to circulation changes that help maintain oxygen levels in Atlantic Mode Waters and hurry the loss along in Intermediate and Deep Waters. Not only does warming weaken carbon uptake, but the amplification of the hydrological cycle enhances the efficiency of carbon storage in Mode and Intermediate Waters directly in 'salty-get-saltier' regions, by increasing the concentration of DIC and Alkalinity in the outcrop region, and indirectly in 'fresh-get-fresher' regions, by decreasing ocean heat uptake which enhances the solubility of carbon. Freshwater fluxes (and salinity-driven circulation changes more broadly) could be expected to influence ocean biogeochemistry on shorter or longer timescales as well. For example, decadal variability in the Atlantic Meridional Overturning Circulation (AMOC) has been linked to a feedback between advection of mean salinity patterns and the associated buoyancy anomalies [96, 97]. These circulation changes could be expected to induce variability in the oxygen and carbon distributions both directly through advection and mixing, as well as indirectly through ocean heat uptake (temperature anomalies) which would modulate the solubility of oxygen and carbon. On longer millennial timescales, hydrological cycle amplification has been shown to strengthen the AMOC, in contrast to the weakening induced over the first several decades which we have considered here [98]. This strengthened AMOC could enhance the supply of oxygen and anthropogenic heat and carbon to the deep ocean [99] and may be an interesting case study for understanding the links between salinity, circulation, and biogeochemistry, especially if it modulates the partitioning of oxygen and carbon between the ocean and atmosphere and volume of oxygen minimum zones (where biogeochemical cycling is altered due to the very low concentration of oxygen). The inverse case

study under global cooling, where the hydrological cycle would slow and could be expected to weaken AMOC on millennial timescales (after the initial strengthening), might also be insightful for understanding reversibility in the climate system. However, in equilibrium, this salinity effect is likely to be dwarfed by that of warming or cooling (and, for future carbon uptake, the atmospheric CO_2 increase).

Chapter 3 demonstrates that SSTs in the tropical convective regime, which strongly affect the temperature of the tropical free troposphere, are modulated by the strength of surface winds and the corresponding perturbation latent heat flux. The results suggest that these surface wind anomalies are related to the rearrangement of the large-scale circulation, but future work could test this connection. As mentioned in the Introduction, the large-scale circulation and local temperature gradients, which collectively determine surface winds, are coupled on short timescales, making it challenging to disentangle the source of a surface wind anomaly [100, 101, 102]. Nevertheless, this result may suggest that there is a predictable relationship between the tropical atmospheric circulation and free-tropospheric temperature, and future work should aim to investigate whether a similar relationship holds on longer timescales. For example, does the CO_2-forced circulation weakening [103] lead to a particular increase in free-tropospheric temperature, by warming the surface in the convective regime? Such a change would be amplified rapidly by the surface atmosphere-ocean Bjerknes feedback [104]. What would the associated surface temperature pattern look like, and does that inform our expectation for the forced SST response, which is a major open research question at the moment? I look forward to seeing and contributing to future research on these open questions.

A

Appendix: A Synthesis of Global Coastal Ocean Greenhouse Gas Air-sea Fluxes

Please find the manuscript below.

A Synthesis of Global Coastal Ocean Greenhouse Gas Fluxes

L. Resplandy[1], A. Hogikyan[2], H. W. Bange[3], D. Bianchi[4], T. Weber[5], Wei-Jun Cai[6], S.C. Doney[7], K. Fennel[8], M. Gehlen[9], J. Hauck[10], F. Lacroix[11], P. Landschützer[12,13], C. Le Quéré[14], J. D. Müller[15], R. G.Najjar[16], A. Roobaert[17], J. Schwinger[18], S. Berthet[19], L. Bopp[20], T.T.T. Chau[9], M. Dai[21], N. Gruber[15], T. Ilyina[13], A. Kock[3*], M. Manizza[22], Z. Lachkar[23], G. G. Laruelle[17], E. Liao[1†], I.D. Lima[24], C. Nissen[10,25], C. Rödenbeck[26], R. Séférian[19], K. Toyama[27], H. Tsujino[27], P. Regnier[17]

[1]Department of Geosciences and High Meadows Environmental Institute, Princeton University, Princeton, NJ, USA
[2]Atmospheric and Oceanic Sciences Program, Princeton University, Princeton, NJ, USA
[3]GEOMAR Helmholtz Centre for Ocean Research Kiel, Kiel, Germany
[4]Department of Atmospheric and Oceanic Sciences, University of California Los Angeles, Los Angeles, CA, USA
[5]Department of Earth and Environmental Science, University of Rochester, NY, USA
[6]School of Marine Science and Policy, University of Delaware, Newark, Delaware, 19716, USA
[7]Department of Environmental Sciences, University of Virginia, Charlottesville, VA, USA
[8]Department of Oceanography, Dalhousie University, Halifax, Canada
[9]Laboratoire des Sciences du Climat et de l'Environnement, LSCE/IPSL, CEA-CNRS-UVSQ, Université Paris-Saclay, F-91191 Gif-sur-Yvette, France
[10]Alfred-Wegener-Institut, Helmholtz-Zentrum für Polar- und Meeresforschung, Germany
[11]Climate and Environmental Physics / Oeschger Centre for Climate Change Research (OCCR), University of Bern, Switzerland
[12]Flanders Marine Institute (VLIZ), Ostend Belgium
[13]Max Planck Institute for Meteorology, Hamburg, Germany
[14]School of Environmental Sciences, University of East Anglia, Norwich Research Park, NR4 7TJ, Norwich, UK
[15]Environmental Physics, Institute of Biogeochemistry and Pollutant Dynamics, ETH Zurich, Zürich, Switzerland
[16]Department of Meteorology and Atmospheric Science, The Pennsylvania State University, University Park, Pennsylvania, USA
[17]Dept. Geoscience, Environment and Society - BGEOSYS, Université Libre de Bruxelles, Brussels, Belgium
[18]NORCE Climate & Environment, Bjerknes Centre for Climate Research, Bergen, Norway
[19]CNRM, Université de Toulouse, Météo France, CNRS, Toulouse, France
[20]LMD/IPSL, ENS, Université PSL, École Polytechnique, Institut Polytechnique de Paris, Sorbonne Université, CNRS, Paris, France
[21]State Key Lab of Marine Environmental Science and College of Ocean and Earth Sciences, Xiamen University, Xiamen 361102, China
[22]Geosciences Research Division, Scripps Institution of Oceanography, University of California - San Diego, La Jolla, USA
[23]Arabian Center for Climate and Environmental Sciences, New York University Abu Dhabi, Abu Dhabi, United Arab Emirates
[24]Department of Marine Chemistry and Geochemistry, Woods Hole Oceanographic Institution, Woods Hole, MA, USA
[25]Department of Atmospheric and Oceanic Sciences and Institute of Arctic and Alpine Research, University of Colorado, Boulder, Colorado, USA
[26]MPI Biogeochemistry, Jena, Germany
[27]JMA Meteorological Research Institute, Tsukuba, Ibaraki, Japan

*now at State Office for the Environment of the State of Schleswig-Holstein, Flintbek, Germany
†now at School of Oceanography, Shang Jiao Tong University, Shanghai, 200030, China

Corresponding author: Laure Resplandy, laurer@princeton.edu

Key Points:

- We synthesize air-sea fluxes of CO_2, nitrous oxide and methane in the global coastal ocean using observation-based products and ocean models
- The coastal ocean CO_2 sink is 60% larger in ocean models than in observation-based products due to systematic differences in seasonality
- Coastal nitrous oxide and methane emissions offset 30-58% of net CO_2 coastal uptake radiative effect

Abstract

The coastal ocean contributes to regulating atmospheric greenhouse gas concentrations by taking up carbon dioxide (CO_2) and releasing nitrous oxide (N_2O) and methane (CH_4). Major advances have improved our understanding of the coastal air-sea exchanges of these three gasses since the first phase of the Regional Carbon Cycle Assessment and Processes (RECCAP in 2013), but a comprehensive view that integrates the three gasses at the global scale is still lacking. In this second phase (RECCAP2), we quantify global coastal ocean fluxes of CO_2, N_2O and CH_4 using an ensemble of global gap-filled observation-based products and ocean biogeochemical models. The global coastal ocean is a net sink of CO_2 in both observational products and models, but the magnitude of the median net global coastal uptake is ∼60% larger in models (-0.72 vs. -0.44 PgC yr^{-1}, 1998-2018, coastal ocean area of 77 million km^2). We attribute most of this model-product difference to the seasonality in sea surface CO_2 partial pressure at mid- and high-latitudes, where models simulate stronger winter CO_2 uptake. The global coastal ocean is a major source of N_2O (+0.70 $PgCO_2$-e yr^{-1} in observational product and +0.54 $PgCO_2$-e yr^{-1} in model median) and of CH_4 (+0.21 $PgCO_2$-e yr^{-1} in observational product), which offsets a substantial proportion of the net radiative effect of coastal CO_2 uptake (35-58% in CO_2 -equivalents). Data products and models need improvement to better resolve the spatio-temporal variability and long term trends in CO_2, N_2O and CH_4 in the global coastal ocean.

Plain Language Summary

The coastal ocean regulates greenhouse gases. It acts as a sink of carbon dioxide (CO_2) but also releases nitrous oxide (N_2O) and methane (CH_4) to the atmosphere. This synthesis contributes to the second phase of the Regional Carbon Cycle Assessment and Processes (RECCAP2) and provides a comprehensive view of the coastal air-sea fluxes of these three greenhouse gases at the global scale. We use a multi-faceted approach combining gap-filled observation-based products and ocean biogeochemical models. We show that the global coastal ocean is a net sink of CO_2 in both observational products and models, but the coastal uptake of CO_2 is ∼60% larger in models than in observation-based products due to model-product differences in seasonality. We also find that the coastal emissions of N_2O and CH_4 counteract a substantial part of the climate buffering effect of coastal CO_2 uptake (by 35-58% in CO_2 -equivalents). Improvements to resolve long term trends in CO_2, N_2O and CH_4 in the global coastal ocean are crucially needed.

1 Introduction

Coastal oceans play an important role in the global carbon cycle by serving as a hub of exchange between the land-aquatic continuum, sediments, the atmosphere, and the open ocean (Bauer et al., 2013; Chen & Borges, 2009; F. Mackenzie et al., 1998; Ward et al., 2020). They are often defined as ocean waters over continental shelves shallower than ∼200-m water depth, albeit sometimes extending further offshore (typically to 300 km from the coastline and 1000 m isobath, Laruelle et al., 2018). Coastal waters contribute to the global oceanic uptake of anthropogenic carbon by absorbing carbon dioxide (CO_2) directly from the atmosphere and by burying, transforming, or outgassing the carbon delivered by terrestrial ecosystems to the coastal ocean (e.g., Regnier et al., 2022).

A notable milestone in the efforts to quantify the CO_2 exchange between the atmosphere and coastal oceans was reached by Chen et al. (2013) during the first phase of the Regional Carbon Cycle Assessment and Processes (RECCAP), an international effort to establish the mean carbon balance and change over the period 1990–2009 for all subcontinents and ocean basins. These authors expanded on prior work at the scale of continental shelves (W.-J. Cai et al., 2006; Laruelle et al., 2010) and examined the global

atmospheric CO_2 uptake by coastal waters using a compilation of surface ocean partial pressure of CO_2 (pCO_2) data available for 87 shelves. They concluded that most coastal waters act as a sink for atmospheric CO_2, except for tropical coastal systems that were identified as weak CO_2 sources, and found the global coastal CO_2 uptake to be 0.4 PgC yr^{-1} (for a surface area of coastal waters of 30.3 million km^2).

Since the completion of RECCAP, the amount of available pCO_2 measurements in the coastal ocean has increased tremendously, reaching millions shortly after the RECCAP assessment was released (e.g., Surface Ocean CO_2 Atlas database SOCAT Bakker et al., 2014) and ∼19 million in the most recent publication (Bakker et al., 2022). In parallel, statistical gap-filling methods, initially developed for the open ocean, have been applied to these fast expanding datasets to resolve the spatio-temporal variability of the air-sea CO_2 flux in the coastal ocean (Laruelle et al., 2014; Roobaert et al., 2019; Landschützer et al., 2020; Chau et al., 2022). These global gap-filled observation-based coastal products led to a downward revision of the global coastal ocean CO_2 uptake to about half of the RECCAP value (0.15-0.20 PgC yr^{-1}, Roobaert et al., 2019; Chau et al., 2022). This downward revision was corroborated by a recent synthesis of 214 regionally aggregated CO_2 flux estimates, leading to a net uptake of 0.25 PgC yr^{-1} (Dai et al., 2022), although these assessments covered slightly different periods and coastal areas (1985-2019 and ∼22 million km^2 in Chau et al, 2022; 1998-2015 and 28 million km^2 in Roobaert et al., 2019; 1998-present and ∼30 million km^2 in Dai et al., 2022).

While coastal waters are a sink of CO_2, they are also the main oceanic source of two other important greenhouse gasses: nitrous oxide (N_2O) and methane (CH_4) (e.g., Weber et al., 2019; Yang et al., 2020; Saunois et al., 2020; Wan et al., 2022). RECCAP did not consider N_2O and CH_4, but recent studies have compiled oceanic N_2O and CH_4 measurements (Kock & Bange, 2015) and applied statistical gap-filling techniques similar to those employed for CO_2 to assess the global ocean air-sea N_2O and CH_4 fluxes (Weber et al., 2019; Yang et al., 2020). These studies have greatly improved the quantification of N_2O and CH_4 air-sea fluxes at the global scale, but coastal ocean N_2O and CH_4 emissions remain highly uncertain and the extent to which these emissions offset the present-day coastal CO_2 uptake is unknown.

Coastal air-sea fluxes of CO_2, N_2O and CH_4 have strong spatial and seasonal variability. Regional-scale observational and modeling studies have greatly improved the quantification of the mean and temporal variability of air-sea fluxes of greenhouse gasses in individual regions across the globe (e.g., Anderson et al., 2009; Gülzow et al., 2013; Turi et al., 2014; Arévalo-Martínez et al., 2015; Pipko et al., 2017; Mayer et al., 2018; Fennel et al., 2019; Gomez et al., 2020; Hauri et al., 2021; Louchard et al., 2021). However, the limited spatial coverage of these studies largely inhibits a global-scale perspective. Global gap-filled observational products and global ocean biogeochemical models now run at a reasonably high horizontal resolution (0.5° or higher) to simulate coastal CO_2 (Bourgeois et al., 2016; Lacroix et al., 2020, 2021; Roobaert et al., 2022) and N_2O (Ganesan et al., 2020; Stell et al., 2022; Berthet et al., 2022) fluxes, recently complemented these regional-scale studies.

As a result of observational and modeling advances since RECCAP, a global view of the coastal ocean's spatial and seasonal patterns in air-sea greenhouse gas fluxes has started to emerge, at least for CO_2 fluxes. Polar and subpolar coastal oceans, such as the northwest North Atlantic along the Canadian and US coast (Thomas et al., 2004; Fennel & Wilkin, 2009; Previdi et al., 2009; Signorini et al., 2013; Lachkar & Gruber, 2013; Laruelle et al., 2015; Cahill et al., 2016; Gustafsson et al., 2019), the European shelves (Thomas et al., 2004; Cossarini et al., 2015; Neumann et al., 2022; Gustafsson et al., 2019) and Arctic and Antarctic shelf (Arrigo et al., 2008; Pipko et al., 2017, 2021; Ouyang, Sciusco, et al., 2022) generally are strong sinks of CO_2 characterized by large seasonal variations, and likely account for about 90% of the annual global coastal CO_2 uptake (while representing ∼45% of the global coastal surface area, see Laruelle et al., 2014; Roobaert et

al., 2019; Dai et al., 2022). There are exceptions with subpolar and polar shelves where outgassing has been identified, such as the Scotian Shelf (Rutherford et al., 2021; Rutherford & Fennel, 2022) or the Laptev Sea in the Arctic (Anderson et al., 2009). Coastal upwelling regions, such as the nearshore California Current, are sources of CO_2 to the atmosphere with a marked seasonality that follows the upwelling dynamics (Lachkar & Gruber, 2013; Dai et al., 2013; Turi et al., 2014; Fiechter et al., 2014; Damien et al., 2023). Tropical systems, such as the Gulf of Mexico (Xue et al., 2016; Laurent et al., 2017) and the South China Sea (Wan et al., 2022), are mostly identified as weak CO_2 sources with weak seasonal variability (Laruelle et al., 2014, 2015; Roobaert et al., 2019; Dai et al., 2022). Our knowledge of N_2O and CH_4 variability in the global coastal ocean is more limited, but gap-filled products and global models suggest that N_2O and CH_4 annual emissions strongly vary between coastal regions (e.g., Weber et al., 2019; Yang et al., 2020; Ganesan et al., 2020; Stell et al., 2022). These products and models offer a remarkable opportunity to establish a greenhouse gas budget for the global coastal ocean, and improve our understanding of its spatial and seasonal variability.

Rising atmospheric CO_2 levels influence coastal CO_2 uptake on multi-decadal timescales. Prior syntheses at the global scale including RECCAP (W.-J. Cai et al., 2006; Laruelle et al., 2010; Chen et al., 2013; Bauer et al., 2013; Regnier et al., 2013) and at the regional scale (Liu et al., 2018; Fennel & Testa, 2019; Legge et al., 2020) clearly support the view that the coastal ocean is currently a sink of atmospheric CO_2, but the extent to which it has changed on longer time-scales remains controversial (see Dai et al., 2022, for a review). F. T. Mackenzie et al. (2005) from a modeling perspective and later W. Cai et al. (2021) from observations first hypothesized that the potential of the coastal ocean to act as a sink for CO_2 might be increasing with time. This view is increasingly supported by time series analyses that suggest that trends in sea surface pCO_2 are overall weaker than the atmospheric pCO_2 trend in most coastal regions. This finding further implies an intensified CO_2 uptake or decreased outgassing, although potential trends in winds and sea ice may also play a role (Bauer et al., 2013; Wang et al., 2017; Laruelle et al., 2018; Dai et al., 2022). However, exceptions have been identified in regions where coastal ocean pCO_2 increases at a similar rate (i.e., near-zero changes in the flux) or even at higher rates (i.e., reduced CO_2 uptake or intensified outgassing) than atmospheric pCO_2 (e.g., California Current, South and Mid Atlantic Bight, Baltic Sea Reimer et al., 2017; Laruelle et al., 2018; Schneider & Müller, 2018; Dai et al., 2022). The quantification of coastal CO_2 flux trends from observations is, however, still strongly restricted by the limited spatial coverage and/or the relatively short duration of time series.

Global ocean biogeochemical models offer an attractive means of assessing long term trends in air-sea CO_2 flux densities in the coastal ocean and how they differ from those of the open ocean (Regnier et al., 2022). Two such models, with reasonable agreement in regions where time series are available (0.2-0.5° resolution in Bourgeois et al., 2016; 0.4° resolution in Lacroix et al., 2021), suggest that the global coastal CO_2 sink density has increased at a slightly slower rate than the open ocean CO_2 sink since the preindustrial era, even when accounting for increasing global nutrient sources via river and atmospheric transports (Lacroix et al., 2020). Both models, however, have important limitations and potential biases related to their representation of fine-scale hydrodynamics of shelf circulation and biophysical processes that impact biogeochemical cycling in the shallow ocean (Mathis et al., 2022; Rutherford & Fennel, 2018).

In this second phase of the Regional Carbon Cycle Assessment and Processes (RECCAP2), we aim to address gaps in our understanding of air-sea greenhouse gas fluxes for the global coastal ocean using a multi-methodological approach that relies on an ensemble of global gap-filled observation-based products and ocean biogeochemical models. Our objectives are threefold. First, we revisit the estimate of the net coastal ocean CO_2 flux, and combine it with CH_4 and N_2O emissions to derive a global climatological coastal ocean budget of greenhouse gas fluxes (section 3.1). Second, we analyze the spatial and sea-

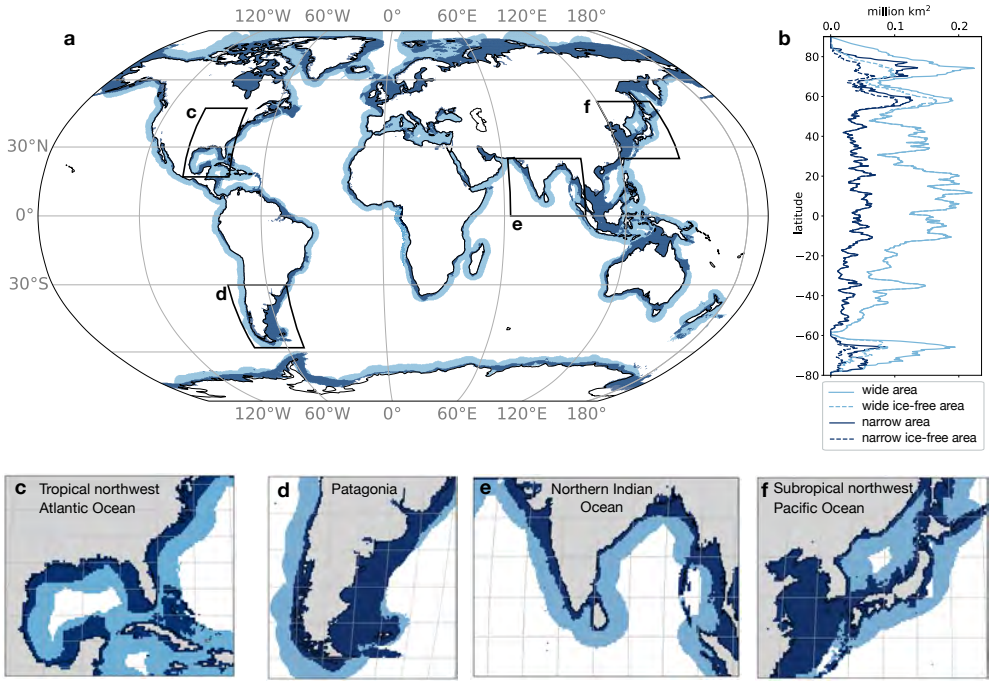


Figure 1. a) Coastal masks used in this study for the wide (dark + light blue) and narrow (dark blue) coastal oceans, b) Surface area (in km^2) at each latitude in the wide (light blue) and narrow (dark blue) coastal ocean masks (solid lines) and the 1998-2018 averaged sea-ice free surface area (dashed lines). c-f) Insets showing the extent of the narrow and wide coastal oceans in four coastal regions. Sea ice coverage used in b is from NOAA OISST. See Methods for details.

sonal variability in the CO_2 flux density and how it might differ from that of the open ocean, and examine spatial patterns in coastal CH_4 and N_2O fluxes (sections 3.2 and 3.3). Third, we investigate trends in the coastal CO_2 flux over the last four decades (section 3.3). This synthesis does not cover the seasonal and interannual variability in N_2O and CH_4 fluxes, as these temporal scales are either unresolved (CH_4) or have not yet been analyzed (N_2O) in the coastal ocean. We consider the net contemporary air-sea fluxes (natural + anthropogenic) of CO_2, N_2O and CH_4 using the 1998-2018 period (except if specified otherwise). Our approach combines observation-based and model-based estimates with different strengths and limitations discussed in Section 4.

2 Methods

2.1 Coastal ocean definition and analysis period

Different definitions of coastal oceans are used in the literature (Chen et al., 2013; Laruelle et al., 2017). We primarily use a "wide" coastal ocean definition following Laruelle et al. (2017), where the seaward boundary is 300 km from shore or the 1000-m isobath, whichever is further from shore, amounting to a total coastal ocean area of 77.2 million km^2 (Fig 1). This wide coastal ocean definition allows us to examine coastally influenced regions of the ocean, i.e., that part of the ocean that is impacted by the presence of the coastal boundary, while also maximizing the number of observation-based and model-based estimates we can use in this study (i.e., a narrower definition would exclude prod-

ucts of lower horizontal resolution). This wide coastal ocean area is, however, more than twice the surface area commonly used to examine coastal ocean biogeochemical dynamics (e.g. Chen et al., 2013). We therefore further use a "narrow" coastal ocean definition, which is delimited by the shelf break (defined as the isobath with maximum slope increase in the 0-1000 m interval) and amounting to a total area of 28 million km^2 (see details in Laruelle et al., 2013, 2014). See Figure 1 for maps and area latitudinal distribution of the narrow and wide coastal waters. The landward boundary in the masks used to define the narrow and wide coastal oceans excludes estuaries and coastal vegetation, which are described in (Rosentreter et al., 2023).

The analysis is done over the 1998-2018 period to maximize the number of models and observation-based products available (see Tables 1-3 for periods covered by models and observation-based products). Note that this period differs from the one used in the open-ocean RECCAP2 studies that analyze oceanic CO_2 fluxes since 1985. All trends are calculated as linear trends over the 1998-2018 period.

2.2 Datasets

We use observation-based and model-based estimates with different strengths and limitations. Notably, gap-filled global observational-based products rely on observations that are often too sparse to capture the full range of spatio-temporal variability in coastal regions (except in densely sampled regions such as major parts of the North American and European ocean margins) and are highly sensitive to the wind product and the choice of the gas exchange coefficient formulation (e.g., Roobaert et al., 2018). In contrast, ocean biogeochemical models can be associated with systematic biases. For instance, only some of the models used here include land-sea riverine carbon inputs which sustain an oceanic CO_2 outgassing flux, and land-sea nutrient inputs which would yield an opposing biologically-driven oceanic CO_2 uptake in coastal waters (Resplandy et al., 2018; Hauck et al., 2020; Regnier et al., 2022; Gao et al., 2023, see Tables 1-3).

2.2.1 Observation-based pCO_2-products

We use 4 global pCO_2-products that provide global monthly gridded surface ocean pCO_2 (noted pCO_2 here) and air-sea CO_2 flux fields based on observations from the SOCAT database which compiles surface ocean pCO_2 observations and provides a subset after quality control (Bakker et al., 2016, 2022). Three of them use neural network-based interpolation methods: Coastal-SOM-FFN (Laruelle et al., 2017; Roobaert et al., 2019, 2022), merged-SOM-FFN (Landschützer et al., 2020) and CMEMS-LSCE-FFNN (which we refer as CMEMS, Chau et al., 2022), while the fourth product, Carboscope-1, uses a simple statistical representation of mixed-layer biogeochemistry fitted to the pCO_2 data (Rödenbeck et al., 2022). All these products are using SOCAT pCO_2 observations and are therefore not independent (see SI for details on SOCAT versions and Fig. S1 for SOCAT data coverage). In particular, the Merged-SOM-FFN product merged the Coastal-SOM-FFN (Laruelle et al., 2017) with an open ocean SOM-FFN product (Landschützer et al., 2014) to produce a global ocean product; the Coastal-SOM-FFN and Merged-SOM-FFN are therefore identical in the nearshore coastal region and only differ in the more offshore band of the wide coastal domain (see details in Landschützer et al., 2020). Coastal-SOM-FFN (and therefore also the near-shore product in Merged-SOM-FFN) was designed for the coastal ocean and uses coastal SOCAT data for their neural network training. In the three other products that use both open ocean and coastal ocean data (i.e. CMEMS, Carboscope-1 and offshore portion of Merged-SOM-FFN), the coastal estimate may be strongly influenced by open-ocean information extrapolated towards the coast. See Tables 1-3 and Supplementary Information S1 for details on pCO_2-products (e.g., period, wind speed product, gas exchange formulation).

Carboscope-1 and CMEMS products resolve interannual variability over the whole 1998-2018 period and may be used to estimate decadal trends, while Coastal-SOM-FFN and Merged-SOM-FFN provide a 1998-2015 monthly climatology and do not resolve interannual variability. pCO_2-products often have unrealistic pCO_2 values under sea-ice (Laruelle et al., 2017). We therefore used the sea-ice fraction from the NOAA-OISST product (Reynolds et al., 2007) to mask pCO_2 and CO_2 flux values under sea-ice in the four products. We mask both to keep consistency but this method should not impact the flux dramatically since it is often inhibited by sea-ice in flux formulations. In this study, we also filled the missing values north of 75N in CMEMS using the Coastal-SOM-FFN climatology. This approach only marginally impacts the results (adds -0.03 PgC yr^{-1} to the wide coastal ocean net CO_2 flux) because the surface area north of 75N contributes 5 million km^2 to the wide coastal ocean (6% of the total wide area) but only 1.4 million km^2 is ice-free on average for the entire study period. This filled-in version of CMEMS is referred to as CMEMS* and we report no long-term trend in the Arctic for this product.

We also illustrate the sensitivity of the flux in pCO_2-products to the choice of the wind speed product and gas transfer coefficient (k_w) formulation (e.g., Roobaert et al., 2018) by presenting a second version of the Coastal-SOM-FFN flux product but with a different wind product and k_w (labeled Coastal-SOM-FFN-k_w) in which the CO_2 flux is calculated as $F = k_w\ Ko\ (pCO_{2a} - pCO_2)$ where Ko is the gas solubility and pCO_{2a} the atmospheric pCO_2. The default version of Coastal-SOM-FFN uses the ERA5 wind speeds and the k_w formulation from (Ho et al., 2011), whereas Coastal-SOM-FFN-k_w uses JRA55v1.3 winds and the Wanninkhof (1992) k_w formulation (i.e., wind and formulation used in some ocean biogeochemical models, see Tables 1-3 for details on k_w parametrization and wind products used in models and products). The four pCO_2-products are used for the analysis of the wide and narrow coastal oceans, and the three pCO_2-products that extend outside of the coastal domain are used for the open ocean (CMEMS*, Merged-SOM-FFN, and Carboscope-1). Coastal-SOM-FFN-k_w is only shown in the wide coastal ocean for discussion and is not used to compute the pCO_2-product median.

2.2.2 Observation-based N_2O and CH_4 flux products

We used two observation-based estimates of the N_2O and CH_4 fluxes. In each case, we use an estimate based on a simple extrapolation of the MEMENTO (MarinE MethanE and NiTrous Oxide) database to the 45 MARgins and CATchments Segmentation (MARCATS, Figure S2) coastal regions (referred to as MARCATS-N2O and MARCATS-CH4 Kock & Bange, 2015), and an estimate that extrapolates MEMENTO and supplementary observations to a global 0.25-degree climatology using supervised machine learning models (Weber et al., 2019; Yang et al., 2020, referred to as Weber-CH4 and Yang-N2O). The MARCATS-N2O and MARCATS-CH4 products provide an annual mean value based on data from 1980 to 2016, Yang-N2O provides a monthly climatology for 1988-2017 and Weber-CH4 an annual mean value for 1999-2016 (Table 1). In Yang-N2O surface N_2O disequilibrium was extrapolated globally using an ensemble of 100 Random Regression Forest (RRF) models, and in Weber-CH4 surface CH_4 disequilibrium was extrapolated using 1000 RRF models and 1000 Artificial Neural Network (ANN) models. In both cases, diffusive fluxes were calculated and uncertainty propagated by coupling the mapped disequilibrium to multiple high-resolution wind reanalysis products (two in Yang-N2O, four in Weber-CH4), and multiple piston velocity parameterizations (two in Yang-N2O and four in Weber-CH4). These estimates for each gas are not independent as they use the same MEMENTO database. The Yang-N2O and Weber-CH4 products use interpolation techniques to fill observational gaps, but the lack of observations likely leads to large uncertainties in coastal regions.

For CH_4 emissions, the contribution from gas bubble plumes must be taken into account in addition to the diffusive flux (arising from the air-sea difference in partial pres-

sure and a gas exchange coefficient). The MEMENTO database allows the calculation of the diffusive CH_4 flux only, because CH_4 from bubble plumes are usually not captured by the conventional CH_4 measurements based on discrete samples or continuous underway measurement systems. An estimate of the ebullitive (i.e. bubbling) CH_4 fluxes is, however, included in Weber-CH4 (but not in MARCATS-CH4), by combining previous seafloor emissions estimates with models of bubble transfer to the surface (Weber et al., 2019). We evaluated the uncertainty on the net Weber-CH4 flux in the narrow and wide coastal oceans from the quadrature of uncertainties on diffusive and ebullitive fluxes, using a 50% uncertainty on diffusive flux and a 60% uncertainty on ebullitive flux (Weber et al., 2019). More details on these products can be found in Supplementary Information S1.

2.2.3 Ocean models for CO_2 and N_2O fluxes

For CO_2, we used 15 ocean general circulation models coupled with biogeochemical modules: 11 are global and 4 are regional models, all covering the study period of 1998-2018 except CCSM-WHOI which ends in 2017 (see details in Tables 2-3). Most global models have native horizontal grid resolutions varying between 0.25° and 1° in the coastal domain, except FESOM-HR which has an unstructured mesh that reaches higher resolution (see Fig S3) and MPIOM-HAMMOC, NEMO-PlankTOM12 and CCSM-WHOI which have a coarser resolution of ∼1.5°, ∼2° and ∼3° respectively (Table 2). The regional models covering the Indian Ocean (NYUAD-ROMS-Indian) and Northwest Atlantic Ocean (NW-Atl) have horizontal resolutions of approximately 10 km. The regional models covering the Atlantic (ETHZ-ROMS-Atl) and Pacific Ocean (ETHZ-ROMS-Pac) have resolution varying in space between 4 km and 120 km: the ETHZ-ROMS-Atl telescopes to focus on the Amazon outflow region where the resolution is higher and the ROMS-ETHZ-Pac grid focuses on the California Current region (Table 3). We note that some of these models include land-sea nutrient and carbon inputs by rivers, while others do not. Details on these models can be found in Tables 2-3 and Supplementary information S1.

For N_2O, we use 5 models: three of them are also used for CO_2 (CNRM-HR, CNRM-LR, and NEMO-PlankTOM5) and cover the full study period (1998-2018), while the two other models are from the ECCO family (ECCO-Darwin and ECCO2-Darwin) in which the circulation is optimized to capture the distribution of tracers such as temperature and salinity in the ocean but cover shorter periods (ECCO-Darwin for 1997-2013 and ECCO2-Darwin for 2006-2013). See Table 2 and Supplementary Information S1 for further details and references on each model.

Model-based analyses in this study use all global models available for the wide coastal ocean (i.e. 11 models for CO_2 and 5 for N_2O), but subsets of models with higher native horizontal resolution are used for the narrow coastal ocean (4 models for CO_2: CNRM-HR, FESOM-HR, MOM6, MRI-ESM2.1, and 3 models for N_2O: CNRM-HR, ECCO-Darwin and ECCO2-Darwin, see Table 2). Global averages and integrated fluxes are based on the global models, while regional models were used in addition to the global models for the analysis at the grid-point scale (e.g. maps).

2.3 Grid harmonization and coastal waters area rescaling

All models and data products were re-gridded from their native grid onto the same 1/4° grid for analysis. Yet, due to differences in horizontal resolution and ocean-land mask definition, observational products and ocean biogeochemical models can have different coastal ocean areas, even after they have been re-gridded to the same 1/4° grid (for example, wide coastal ocean areas resolved by the models range from 34 to 76 million km^2 vs. 77.2 million km^2 in the mask of Laruelle et al. (2017), see Tables 1-3 and Fig 1). To minimize the effect of this common issue, most results are presented as area-weighted

averages of CO_2, N_2O and CH_4 flux densities (per m^2) and surface ocean pCO_2 masked using time varying ice-free surface to account for fractional sea ice coverage (in μatm). We used the ice fraction from the NOAA-OISST product for pCO_2-products and the ice fraction of each individual model for models. For the globally integrated CO_2 flux (in PgC yr^{-1}), we used the globally averaged CO_2 flux densities found in each pCO_2-product and model for the narrow and wide coastal oceans and multiplied them by the corresponding coastal area of Laruelle et al. (2017, narrow area = 28 million km^2; wide area = 77 million km^2). We did not apply this area rescaling to the globally integrated fluxes of N_2O and CH_4 given the smaller number of products/models available.

2.4 Calculation of CO_2 equivalents global coastal fluxes and uncertainties

We computed CO_2 equivalent fluxes of N_2O and CH_4 to provide a global greenhouse gas flux integral (i.e., spatially integrated annual net air-sea flux of greenhouse gasses) in gigatonnes of CO_2 equivalent ($PgCO_2$-e) for the wide coastal ocean. We used the Intergovernmental Panel on Climate Change (IPCC) Assessment Report 6 (Arias et al., 2021) updated 100-year global warming potential for N_2O ($GWP_{N2O} = 273$, i.e. the 100-year time integrated radiative forcing from the instantaneous release of 1 kg of N_2O is 273 times larger than the forcing of 1 kg of CO_2) and for CH_4 of non-fossil fuel origin ($GWP_{CH4} = 27.2$). We calculated two budgets for the wide coastal ocean: one using observation-based flux products only and one using mostly models. The observation-based budget uses the global gap-filled observational products, i.e. the 4 pCO_2-product median flux for CO_2 (CMEMS*, Carboscope-1, Coastal-SOM-FFN and Merged-SOM-FFN), the Yang-N2O flux for N_2O and the Weber-CH4 flux for CH_4. Uncertainty bars presented for this observation-based budget give the ranges of all products presented in this study, i.e. the 4 pCO_2-product range for CO_2, the 2 observational-product range for N_2O (Yang-N2O and MARCATS-N2O) and the 2 observational-product range for CH_4 (i.e. the low bound corresponds to the low uncertainty bound of Weber-CH4 and the high bound to the value of MARCATS-CH4). The model-based budget uses the 11 global model median flux for CO_2, the 4 global model median flux for N_2O, and the product-based Weber-CH4 flux for CH_4 as no model is available. Uncertainty bars presented for this model-based budget are the 11-model range for CO_2, the 4-model range for N_2O, and the 2 observational product range for CH_4 (same as the product-based budget described above).

3 Results

3.1 Global coastal ocean greenhouse gas fluxes

In this section, we present a compilation of observation-based and modeled net air-sea fluxes of CO_2 (4 pCO_2-products and 11 global ocean models), N_2O (2 observation-based products and 4 global ocean models) and CH_4 (2 observation-based products) in the global coastal ocean (Figure 2), and assess the contribution of the coastal ocean to the atmospheric greenhouse gas budget by combining the three gasses using a single CO_2-equivalent flux (Figure 3).

3.1.1 Net coastal CO_2 uptake

The pCO_2-products yield a weaker net CO_2 uptake than the global ocean biogeochemical models in the wide coastal ocean during the 1998-2018 period (Figure 2a). The pCO_2-product estimates (-0.59 to -0.37 PgC yr^{-1}) fall at the upper (less negative) end of the model range (-0.92 to -0.38 PgC yr^{-1}), and in the pCO_2-product flux median (-0.44 PgC yr^{-1}) is about two thirds of the model median (-0.72 PgC yr^{-1}). Most of this model-product mismatch can be attributed to differences in ocean pCO_2 seasonality at mid- and high-latitudes (poleward of 25N and 25S), which tend to reinforce the north-

ern hemisphere winter uptake in models compared to pCO_2-products (see details in section 3.2.2). These differences in pCO_2 seasonality are likely to be further amplified by differences in wind speed and gas exchange coefficient formulation (see Methods and Table 1-3). For instance, the net CO_2 uptake in the Coastal-SOM-FFN product increases by about 50% and falls closer to the model median when changing the wind speed product (from ERA5 to JRA55) and gas exchange coefficient formulation (from Ho et al., 2011 to Wanninkhof 1992) used to compute the flux (from -0.44 PgC yr^{-1} in Coastal-SOM-FFN to -0.65 PgC yr^{-1} in Coastal-SOM-FFN-k_w, blue dot vs. blue circle in Figure 2a, see further details in section 3.2.2).

Another factor that can explain part of the model-product discrepancy is the absence of land-sea carbon and nutrient inputs in many of the global ocean biogeochemical models (see Table 2). The missing land-sea carbon inputs and associated CO_2 outgassing would result in a stronger CO_2 uptake at the scale of the global ocean but the proportion of this land-driven CO_2 outgassing occurring in the coastal ocean, and therefore the bias introduced here in our model-based estimates, is very poorly constrained. Open-ocean RECCAP2 chapters used a model-based estimate of the spatial distribution of this land-driven CO_2 outgassing (Lacroix et al., 2020) scaled up to match an independent bottom up constraint on its global magnitude (0.65±0.3 PgC/yr Regnier et al., 2022). This combined estimate suggests that the missing land-driven outgassing could amount to 0.12 PgC yr^{-1} in the wide coastal ocean, potentially explaining part of the gap between pCO_2-products and model median, despite the large unconstrained uncertainty of this estimate. In contrast, the missing land-sea nutrient inputs could reduce the biologically-driven uptake of CO_2 in coastal waters and potentially offset the bias tied to the lack of land-sea carbon inputs (Gao et al., 2023). However, we find no clear relationship between the strength of the simulated net coastal CO_2 uptake and the presence or absence or land-sea inputs in the global ocean biogeochemical models used here (i.e., models with weaker coastal CO_2 uptake more in line with pCO_2-products are not systematically the ones with land-sea inputs), suggesting that land-driven inputs are likely not the main factor in this discrepancy. In addition, we note that using the subset of four global models with higher horizontal resolution (CNRM-HR, FESOM-HR, MOM6, MRI-ESM2.1 with nominal resolution of 0.5 degree or higher), which are likely to better capture coastal dynamics, yields a slightly weaker net CO_2 uptake (median of -0.65 PgC yr^{-1} for only four models vs. -0.72 PgC yr^{-1} for all global models), slightly closer to the pCO_2-products median (-0.44 PgC yr^{-1}) and in relatively good agreement with one of the pCO_2-products (-0.59 PgC yr^{-1} in CMEMS*, Figure 2a).

We can compare the net CO_2 flux estimates presented here to prior work using the narrower definition of the coastal ocean ending at the shelf break (28 million km^2), a domain more aligned with the definition used in past studies (Supplementary Table S2). For this comparison we include all pCO_2-products, but use only the subset of four global models with higher horizontal resolution. We find that the narrow coastal ocean accounts for about half of the wide coastal ocean CO_2 uptake (-0.22 out of -0.44 PgC yr^{-1} for the 4-pCO_2-product median and -0.34 PgC yr^{-1} out of the -0.65 PgC yr^{-1} for the 4-model median), while only accounting for about a third of the surface area. The pCO_2-product median in the narrow coastal ocean (-0.22 PgC yr^{-1}) is consistent with the most recent observation-based estimates (Roobaert et al., 2019; Dai et al., 2022; Regnier et al., 2022), but the four pCO_2-products span a relatively large range with differences of the order of a factor 2 (-0.12 PgC yr^{-1} in Carboscope-1 and -0.31 PgC yr^{-1} in CMEMS*, see Table S2 for estimates). The 4-model median simulates a slightly stronger sink (-0.34 PgC yr^{-1}) than these most recent estimates (although it is similar to the estimate of Regnier et al., 2022) but again differences in pCO_2 seasonality, and potentially in wind speed and gas exchange formulation could explain part of this discrepancy. Similarly to the wide coastal ocean, the net CO_2 sink increases by nearly 50% in the narrow coastal ocean from Coastal-SOM-FFN to Coastal-SOM-FFN-k_w (from -0.21 to -0.31 PgC yr^{-1}, blue dot vs. circle, Figure 2a).

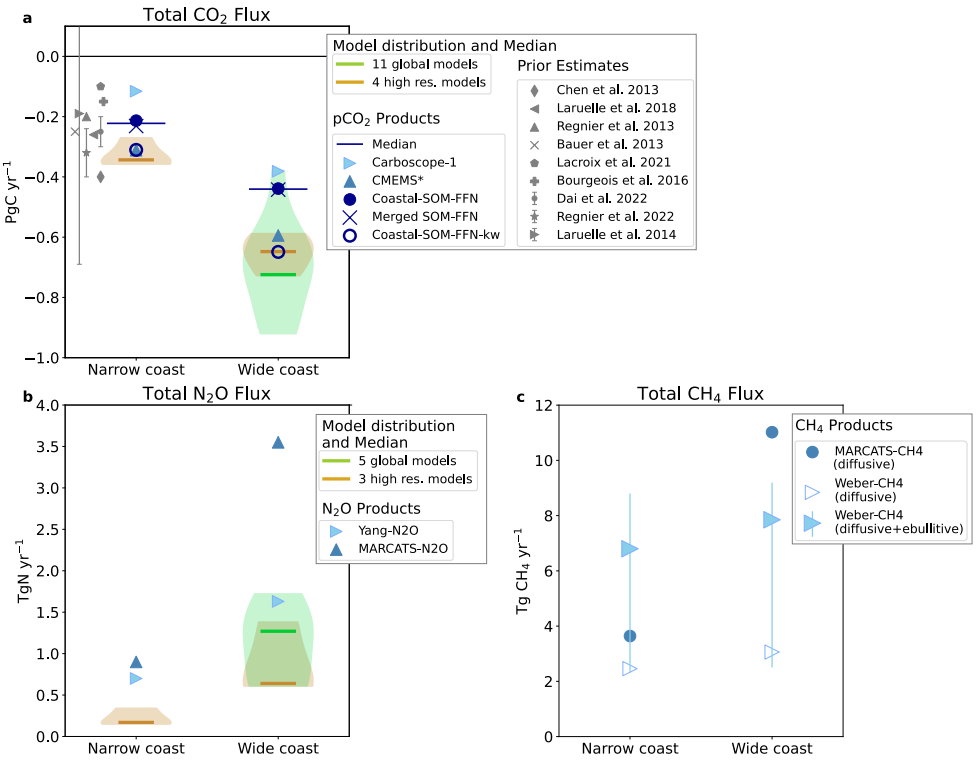


Figure 2. Net globally-integrated coastal fluxes of a) CO_2 [PgC yr^{-1}], b) N_2O [Tg N yr^{-1}] and c) CH_4 [Tg CH_4 yr^{-1}] over the narrow and wide coastal oceans. The model distribution (violin) and median (thick lines) are shown for the full ensemble available in the wide coastal ocean (11 models for CO_2 and 4 for N_2O) and a subset of higher resolution models for the narrow coastal ocean (4 models for CO_2 and 2 for N_2O, see Methods and Table 2 for details). Symbols indicate observation-based products (blue) and previous estimates available for the narrow coastal ocean (grey in panel a, listed in Supplementary Table S2). Coastal-SOM-FFN-k_w, which is a second version of Coastal-SOM-FFN computed using different wind speed and k_w formulation (empty circle, see Methods) is not used in the calculation of the pCO_2-product median. Weber-CH4 total flux (diffusive+ebbullitive) and diffusive contribution (comparable to MARCATS-CH4 flux) are shown in panel c.

3.1.2 Net N_2O and CH_4 coastal emissions

Estimates of the global coastal emissions of N_2O range from 0.14 to 0.90 Tg N yr^{-1} in the narrow coastal ocean and from 0.60 to 3.56 Tg N yr^{-1} in the wide coastal ocean (Figure 2 b). Part of this considerable variability comes from differences between model-based and observation-based estimates, but also from systematic differences between the two observation-based products (MARCATS-N2O and Yang-N2O). In the wide coastal ocean, the Yang-N2O estimate (1.63 Tg N yr^{-1}) falls at the high end of the model estimates (0.60 to 1.73 Tg N yr^{-1}), while MARCATS-N2O yields N_2O emissions that are more than twice the emissions of Yang-N2O (3.56 Tg N yr^{-1}, Figure 2 b). This finding implies that global ocean biogeochemical models emission estimates are overall lower than those of the observation-based products. Furthermore, the subset of 3 high-resolution models generally simulate N_2O emissions that are lower than the full set of 5 models and therefore lower than both observation-based estimates (3-model median of 0.64 Tg N yr^{-1} vs. 5-model median of 1.27 Tg N yr^{-1} for the wide coastal ocean, Figure 2 b).

In the narrow coastal ocean, the two observation-based estimates are in relatively good agreement (0.90 Tg N yr^{-1} in MARCATS-N2O and 0.70 Tg N yr^{-1} in Yang-N2O), while the subset of 3 high resolution global ocean models simulate emissions that are again about 2-4 times lower (0.14 to 0.35 Tg N yr^{-1}). The Yang-N2O product suggests that the narrow coastal ocean accounts for about 50% of the emissions of the wide coastal ocean, while in the subset of 3 global ocean models and MARCATS-N2O it only accounts for about 25% (Figure 2b). We note, however, that the particularly low model values in both the 5-model ensemble and the 3-model high resolution subset are from ECCO-Darwin and ECCO2-Darwin (0.60-0.64 Tg N yr^{-1} in the wide and 0.14-0.17 Tg N yr^{-1} in the narrow coastal ocean) which are based on the same model and are therefore not independent. The fact that global ocean biogeochemical models underestimate coastal N_2O fluxes, in particular nearshore, is likely due to unresolved (e.g. complex microbial production/consumption, sedimentary processes, production in estuarine and coastal vegetation systems transported to the coastal ocean) or spatially under-resolved processes (e.g. high production and remineralization in shallow shelves, and shallow coastal oxygen minimum zones where N_2O emissions take place). Another potential source of bias might be the undersampling of coastal waters in the observations (see Table S1). In particular, observations might be biased high because they are often performed in hotspots of emissions rather than in regions that reflect the mean conditions.

Global CH_4 emissions in Weber-CH4 include both the diffusive and ebullitive (bubbling) components, and are estimated to be 6.80 [2.30-8.8] Tg CH_4 yr^{-1} for the narrow coastal ocean and 7.85 [2.50-9.20] Tg CH_4 yr^{-1} for the wide coastal ocean (Figure 2c). Note that the flux estimates presented here are observation-based only because no model-based estimates are available. The CH_4 flux from Weber-CH4 is dominated by the ebullitive flux which occurs mostly in shallow waters of the narrow coastal ocean (accounting for 4.33 Tg CH_4 yr^{-1} in the narrow and 4.79 Tg CH_4 yr^{-1} in the wide coastal ocean). Subtracting the ebullitive flux from the total Weber-CH4 fluxes results in a CH_4 diffusive flux of 2.46 [1.23-3.69] Tg CH_4 yr^{-1} in the narrow coastal ocean, which is in relatively good agreement with the diffusive flux estimated from MARCATS-CH4 (3.64 Tg CH_4 yr^{-1}). In contrast, the diffusive flux of 3.06 [1.53, 4.59] Tg CH_4 yr^{-1} obtained in the wide coastal ocean in Weber-CH4 has a central value $\sim$3.5 times smaller than the diffusive flux of MARCATS-CH4 (11.02 Tg CH_4 yr^{-1}).

The observation-based estimates of the N_2O emissions and the diffusive flux of CH_4 vary by about 20-30% in the narrow coastal ocean and by about a factor 2 to 3.5 in the wide coastal ocean. The increase in the spread amongst these observational products (which use the same datasets and are therefore not independent) reflects the low number of oceanic N_2O and CH_4 measurements to date, in particular in many coastal regions, as compared to CO_2. Specifically, the observation density decreases by about a factor 3 from narrow to wide (number of observations per million km^2 three times lower in the wide coastal

ocean in more than 30 of the 45 regions used for the interpolation, see Table S1). Significant differences between the observation-based estimates (MARCATS-N2O, MARCATS-CH4 on the one hand, and Yang-N2O and Weber-CH4 on the other hand) can result from (i) applying different approaches for estimating the air-sea gas exchange in combination with using different wind speed products (e.g., Garbe et al., 2014) and (ii) applying different inter- and extrapolation techniques which can introduce significant uncertainties when applied to sparse data. The increase in discrepancy from narrow to wide coastal waters suggests that MARCATS-N2O and MARCATS-CH4 may extrapolate local observations over spatial domains where they are not representative anymore. In contrast, the neural networks of Yang-N2O and Weber-CH4, albeit also relying on the same MEMENTO dataset, may better capture spatial patterns, such as the overall decrease in CH_4 emissions as the shelf water depth increases.

3.1.3 Combined coastal greenhouse gas emissions

We combined CO_2, N_2O and CH_4 fluxes from observation-based and model-based estimates for the wide coastal ocean using CO_2-equivalent (Figure 3). We find that from a net radiative perspective, N_2O and CH_4 coastal emissions offset much of the coastal CO_2 sink, by ∼58% in the product-based budget and ∼30% in the model-based budget. As a result, the net greenhouse gas flux into the coastal ocean is -0.66 $PgCO_2$-e yr^{-1} in the product-based budget (-1.58 $PgCO_2$-e yr^{-1} CO_2 flux offset by +0.70 and +0.21 $PgCO_2$-e yr^{-1} of N_2O and CH_4) and -1.81 $PgCO_2$-e yr^{-1} in the model-based budget (-2.57 $PgCO_2$-e yr^{-1} CO_2 flux offset by +0.54 and +0.21 $PgCO_2$-e yr^{-1} of N_2O and CH_4, Figure 3). Most of the difference between the product- and model-based budgets presented here come from the stronger CO_2 uptake in the models mentioned above. There are, however, very few global coastal N_2O and CH_4 estimates and the spread amongst the products and models is large (1 to 2 $PgCO_2$-e yr^{-1}), indicating that the compensation of the coastal carbon sink could be substantially different from the 30-58% found here.

3.2 Coastal CO_2 dynamics

3.2.1 Contrast between coastal ocean and open ocean

When averaged globally, models and pCO_2-products show lower mean surface ocean pCO_2 and lower CO_2 flux densities (i.e. more uptake) in narrow and wide coastal oceans than in the open ocean (Figure 4). As shown previously for the coastal-SOM-FFN product (Roobaert et al., 2019), this coastal to open ocean difference is however attributable to the increasing contribution of polar waters, characterized by lower flux densities and stronger sinks, to the total surface area from open ocean to narrow coastal domains (polar coastal waters account for 29% of the narrow coastal ocean, 17% of the wide coastal ocean and 2% of open ocean waters, contributions calculated as the percentage of ice-free surface area located poleward of 50 degrees based on NOAA's OISST ice product, Figure 1). This apparent gradient is found in the median of the four pCO_2 products, which shows an increase in global mean sea surface pCO_2 from the narrow coastal ocean to the wide coastal ocean (+ 15 µatm from 350 to 365 µatm) and from wide coastal ocean to the open ocean (+7 µatm from 365 to 372 µatm for the 1998-2018 period, Figure 4a). The only pCO_2-product among the four that does not capture this coastal to open-ocean difference is Carboscope-1, likely because of potential biases in the Arctic Ocean (pCO_2 values generally higher in Carboscope-1 than in other pCO_2-products and models). The 11-model median simulates slightly higher ocean pCO_2 than the product median but also captures an increase in global mean pCO_2 from wide coastal ocean to open ocean (+6 µatm from 369 to 375 µatm) similar to the pCO_2-products. Using the subset of four higher resolution models in the narrow coastal ocean corroborates the presence of this difference in simulated ocean pCO_2. The 4-model median shows a consistently lower mean pCO_2 in the narrow coastal ocean (363 µatm), compared to the wide coastal ocean (370 µatm) and to the open ocean (373 µatm). Thus, although observation-based and mod-

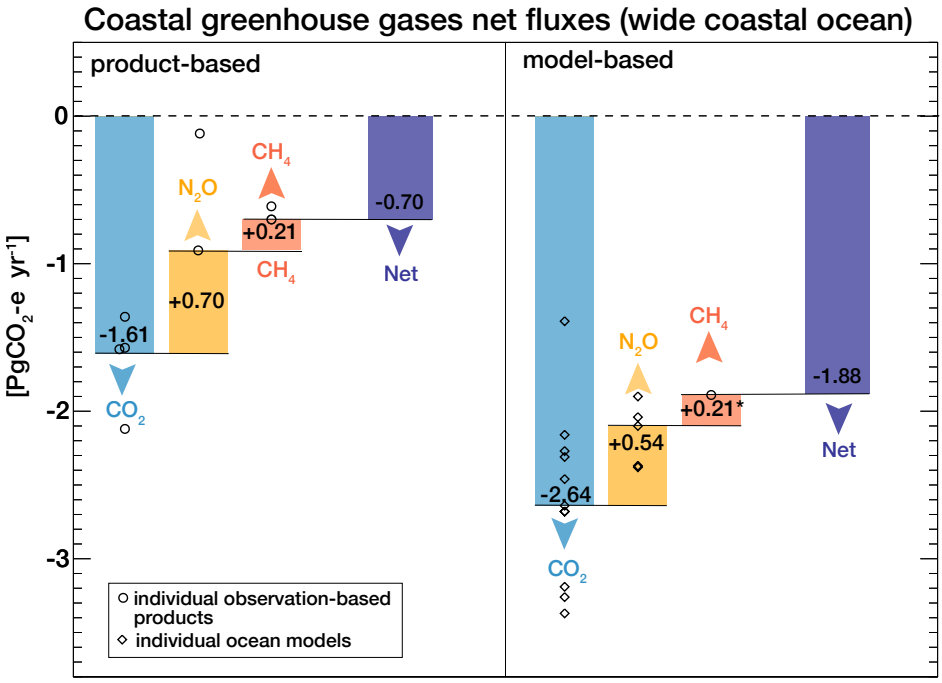


Figure 3. Greenhouse gas air-sea flux in the wide coastal ocean and influence on net atmospheric radiative balance (using $PgCO_2$-e yr^{-1}) based on observational products and models of CO_2, N_2O and CH_4 fluxes. Observations-based central values are from 4 pCO_2-products, Yang-N2O and Weber-CH4. Model-based central values are from the 11 global models for CO_2, 4 global models for N_2O, but the Weber-CH4 product is used for CH_4 as indicated by the asterisk (no model available for CH_4, hence minimizing the difference between the two assessments). Individual models and observation-based product estimates are shown by symbols. The net GHG flux in $PgCO_2$-e yr^{-1} corresponds to the sum of the three gasses' contributions.

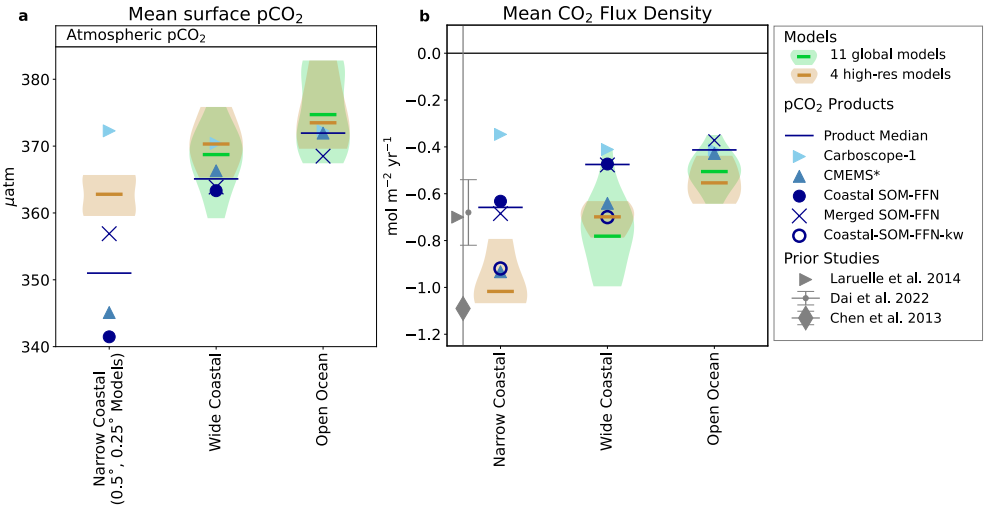


Figure 4. Comparison of globally-averaged coastal ocean and open ocean: a) sea surface pCO_2 [µatm] and b) flux density [mol C m^2 yr^{-1}] averaged over narrow coastal ocean, wide coastal ocean and open ocean waters in pCO_2-products and ocean models. The model distribution (violin) and median (thick lines) are shown for the full ensemble available in the wide coastal ocean (11 global models in green) and a subset of higher resolution models for the narrow coastal ocean (4 global models in tan, see Methods and Table 2 for details). Symbols indicate global pCO_2-based products (blue), previous estimates (in grey, see Supplementary Table S2 for details). Coastal-SOM-FFN-k_w, which is a second version of Coastal-SOM-FFN computed using different wind speed and k_w formulation (empty circle, see Methods) is not used in the pCO_2-product median.

eled pCO_2 values show discrepancies in the mean within each domain, the narrow coastal to open ocean differences derived from observations and models are in remarkable agreement, and amount to about 10-15 µatm. A consequence of these differences in sea surface pCO_2 is that the mean partial pressure difference with the atmosphere (mean pCO_{2a} of 385 µatm for 1998-2018) is higher in the coastal ocean than in the open ocean. As a result, air-sea CO_2 flux densities are lower (stronger uptake) in the narrow coastal ocean (-1.02 and -0.66 mol m^2 yr^{-1} for 4-model and 4-product medians) than in open ocean waters (-0.55 and -0.41 mol m^2 yr^{-1} for 4-model and 4-product medians, Figure 4b). In between, the wide coastal ocean shares characteristics of narrow coastal ocean and open ocean waters and is characterized by intermediate CO_2 flux densities (-0.70 and -0.48 mol m^2 yr^{-1} for 4-model and 4-product medians, Figure 4b).

3.2.2 Spatial and seasonal variability in coastal CO_2 sources and sinks

Coastal air-sea CO_2 flux densities are characterized by latitudinal gradients captured by both pCO_2-products and models (Figure 5). Mid- and high-latitude regions (poleward of 25° of latitude) are characterized by annual mean surface ocean pCO_2 lower than the atmosphere (pCO_{2a}=385 ppm for 1998-2018) and thus by oceanic CO_2 uptake, whereas tropical coastal oceans (equatorward of 25° of latitude) are generally associated with pCO_2 similar or slightly higher than the atmospheric level and weak or near-zero CO_2 outgassing (Figure 5 and S4). When averaged latitudinally over the wide coastal ocean, models and products follow a similar pattern, with most negative flux densities (<-1 mol m^2 yr^{-1},

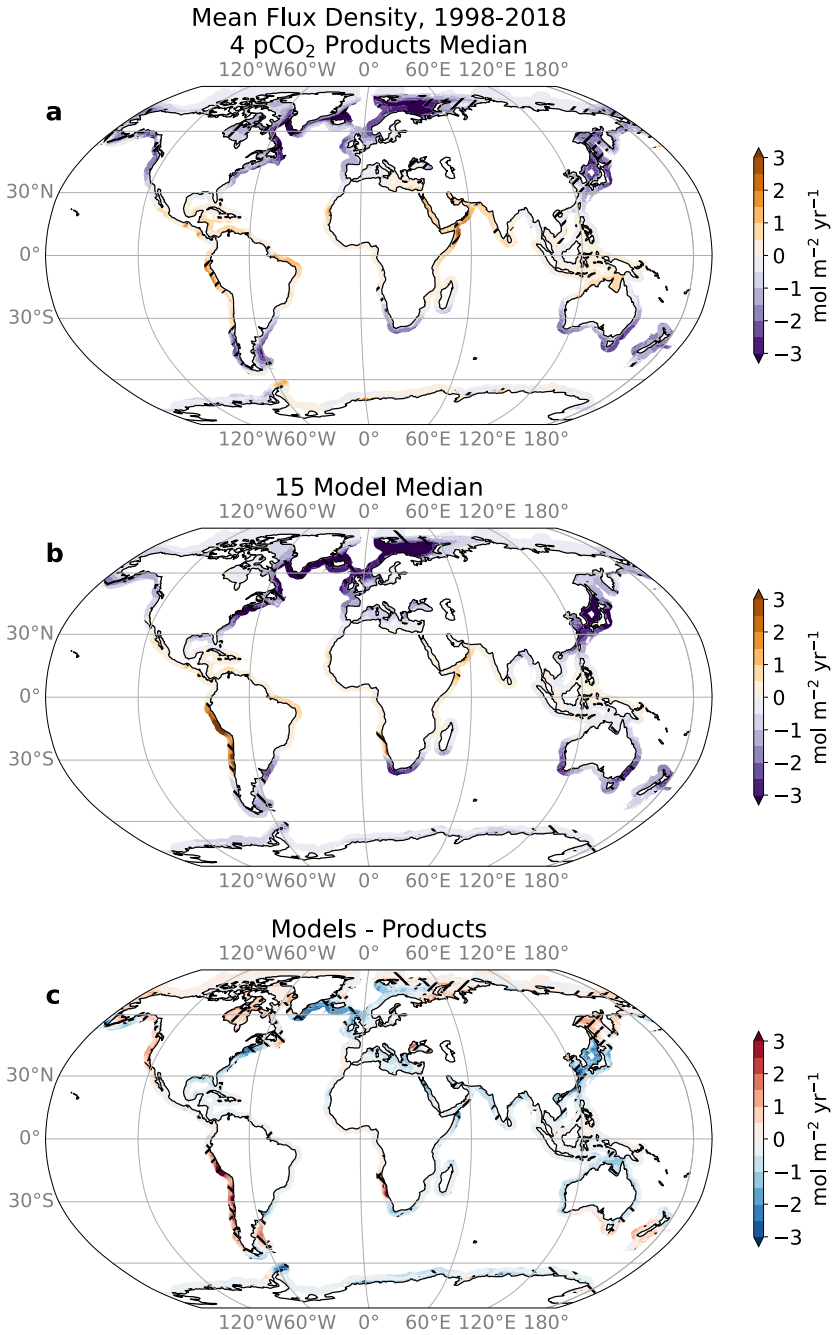


Figure 5. Annual-mean CO_2 flux density [mol C m^2 yr^{-1}] in the wide coastal ocean for a) the median across the 4 pCO_2-products, b) the median across the 15 models, and c) the difference between model and pCO_2-product medians. The model-median is calculated using the 11 global models and the 4 regional models where available. Hatching indicates the coastal area with root mean square difference (RMSD) greater than 0.60 mol C m^2 yr^{-1} across pCO_2 products (panels a and c) or 0.95 mol C m^2 yr^{-1} across models (panels b and c) (in both cases the RMSD values correspond to the 20% of coastal area with highest RMSD).

i.e. strongest sinks) at mid-latitudes in both hemispheres (50°S-25°S and 25°N-50°N) and high latitudes in the northern hemisphere (50°N-80°N), and weak sources in the tropical band (typically between 0 and 0.5 mol m^2 yr^{-1} in 25°S-25°N, Figure 6a). Largest departures between pCO_2-products and models are found in the northern mid- and high latitudes, where the model median flux densities are often more negative (stronger sink) than the pCO_2-product median (down to -4 mol m^2 yr^{-1} in models vs. -2 mol m^2 yr^{-1} in pCO_2-products, Figure 6a). These systematically more negative flux densities in the models extend over large coastal areas of the northern hemisphere, including the shelves of western boundary currents (Gulf Stream and Kuroshio), the Norwegian Sea and the southern Greenland basin (blue colors in Figure 5 c), and therefore largely explain the stronger globally integrated coastal sink found in the model median (Fig 2 a). These northern hemisphere regions are relatively well sampled by the SOCAT pCO_2 database (Fig S1), suggesting that the model-product difference might be largely attributable to model biases. Models and pCO_2-products also differ on Antarctic shelves, in particular around the Antarctic Peninsula (around 60°S which is also relatively well sampled compared to the rest of the coastal ocean) where models simulate a weak sink (about -1 mol m^2 yr^{-1}) but pCO_2-products show a weak source (about +1 mol m^2 yr^{-1}, Figure 5 and Figure 6a). On the Antarctic shelves, however, the model-product mismatch in CO_2 flux density is confined to a relatively small surface area and the impact on the net global flux is smaller compared to the mismatch found in the northern extratropics. We note that the model median yields less negative or more positive flux densities (i.e. weaker sinks or stronger sources) in some coastal regions, such as the California Current, Peruvian margin, Sea of Okhotsk or Hudson Bay (red colors in Figure 5 c), which offsets part of the stronger sinks simulated in northern and southern extratropical latitudes in the latitudinal mean and global integral.

The global coastal ocean is a sink of CO_2 in all seasons, and pCO_2-products and global ocean biogeochemical models largely agree on the latitudinal patterns in seasonality (Figure 6c-f). Yet, model-product differences emerge in the phasing and amplitude of the seasonality, in particular north of 25°N (Figure 6c-f). In the pCO_2-products, the seasonal amplitude of the air-sea CO_2 flux is similar in both hemispheres and shows a strong latitudinal contrast between: i) the tropics (25°S-25°N), where the seasonal amplitude is small (absolute values <1 mol m^2 yr^{-1}) and the weak CO_2 source becomes even smaller in winter; ii) the mid-latitudes (50°S-25°S and 25°N-50°N), where the seasonal amplitude is relatively large (absolute values of 1-2.5 mol m^2 yr^{-1}) and the sink is stronger in winter and spring; and iii) high-latitudes (poleward of 50°N and 50°S), where the seasonal amplitude is also large (similar to mid-latitudes) but the CO_2 sink is stronger in summer (except in the Arctic, north of 80 degree N, where the seasonal amplitude is small, Figure 6b-f). In contrast, the CO_2 sink in the model median is systematically stronger in winter than in summer at all latitudes (except around Antarctica) and does not reproduce the latitudinal change in seasonal phasing obtained in the pCO_2-products (from stronger winter uptake in the tropics to stronger summer uptake at high-latitudes, Figure 6b). In addition, the seasonal amplitude of the CO_2 flux is 50-100% larger in the models at mid-latitudes (despite having a similar phasing, i.e. stronger sink in winter and spring, Figure 6b). As a result of these latitudinal differences in phasing, the products show little seasonality when averaged globally across coastal waters (net median flux of -0.35 PgC yr^{-1} for DJF vs. -0.32 PgC yr^{-1} for JJA, Figure 7a). This is largely explained by compensations between mid-latitudes (stronger uptake in winter) and high-latitudes (strong uptake in summer) within each hemisphere (Fig 6), which results in a relatively weak seasonality in both the northern (-0.24 in DJF and -0.22 in JJA) and southern (-0.11 PgC yr^{-1} in DJF and -0.10 PgC yr^{-1} in JJA) hemispheres (Figure 7b-c). In the case of the 11-model median, however, this compensation is much weaker and the seasonal cycle is stronger, especially in the northern hemisphere (-0.73 in DJF and 0.00 PgC yr^{-1} in JJA, Figure 7b-c). As a result, the global coastal ocean in the model median displays a marked seasonality controlled by the seasonality of the northern hemisphere, resulting in a net global coastal sink for DJF (-1.15 PgC yr^{-1}) that is about four times

the sink for JJA (-0.29 PgC yr^{-1}, Figure 7). This model-product difference in CO_2 flux seasonality and specifically the extremely large boreal winter uptake explains the stronger annual mean global CO_2 sink found in the model median compared to the pCO_2-products (Figures 2 a, 6 a and 7b).

Model-product differences in CO_2 flux seasonality are largely tied to differences in the surface ocean pCO_2. The stronger flux seasonality at mid-latitudes in models and the opposed flux seasonality at high latitudes (i.e., stronger uptake in winter in models vs. stronger uptake in summer in products) are both explained by the higher summer ocean pCO_2 (leading to weaker summer uptake) and the lower winter ocean pCO_2 (leading to stronger winter uptake) found in the model median compared to the pCO_2-product median (Supplementary Figure S5). Differences in ocean pCO_2 can be amplified by the choice of wind speed and gas exchange coefficient formulation. The comparison of the two Coastal-SOM-FFN versions reveals that both the high-latitude summer uptake and the mid-latitude winter uptake are enhanced in Coastal-SOM-FFN-k_w compared to Coastal-SOM-FFN (Figure 7 and S6). This enhancement occurs in both hemispheres but the impact of the northern hemisphere on the global coastal annual mean uptake is larger due to the larger coastal surface area. Despite these systematic differences found between the model median and pCO_2-product median in the annual mean and seasonal flux, some models reproduce better the latitudinal pattern expected from the pCO_2-products, in particular the stronger summer uptake at high-latitude in the northern hemisphere (e.g., MOM6-Princeton and MPIOM-HAMOCC, see individual models in Figure S7 and thin green lines overlapping with thin blue lines in Figure 6). We note that this systematic model/product difference in seasonality is also found in the open ocean but that the amplitude of this mismatch is amplified in the coastal ocean (see Figures S7 and S8).

3.2.3 Trends in coastal ocean pCO_2 and air-sea CO_2 flux

For the 1998–2018 period, global coastal pCO_2 trends are slightly weaker than the atmospheric pCO_2 trend (+20.7 μatm/decade) in the two time-varying pCO_2-products (about +17-18 μatm/decade in the wide coastal ocean) and models (+17-20 μatm/decade in the wide coastal ocean; see Figure 8a,c). In the narrow coastal ocean, the pCO_2 trends from the pCO_2-products are lower than in the wide coastal ocean, and fall halfway between the two central values published in previous observation-based estimates (+16-17 μatm/decade vs. +19.3 μatm/decade in Wang et al., 2017 and +13 μatm/decade in Laruelle et al., 2018). In contrast, the pCO_2 trends found in the subset of four high resolution ocean biogeochemical models are higher in the narrow coastal ocean (+19.8 μatm/decade) than in the wide coastal ocean, and in good agreement with the highest of the previous observation-based estimate (Wang et al., 2017).

The trend difference between atmospheric and oceanic pCO_2 leads to an increase in the coastal carbon sink from 1998 to 2018 in pCO_2-products and models (flux density trends between -0.15 and -0.04 mol m^2 yr^{-1} per decade in the wide coastal ocean, Figure 8b,d). Yet, because the rate of increase in coastal pCO_2 is lower in the pCO_2-products than in the models, their respective CO_2 uptake trend is larger (Figure 8c). This is consistent with the expectation that a slower increase in sea surface pCO_2, which does not closely follow the atmospheric pCO_2 trend, should result in a stronger increase of the flux density (e.g., Laruelle et al., 2018). Our results show, however, that pCO_2 trends and flux trends are not directly proportional, suggesting that factors other than pCO_2 variability are at play. These include trends in sea-ice cover (e.g., sea-ice retreat influence on flux trends in the Arctic Ocean) and/or in surface winds (via their effect on the gas exchange transfer velocity). For instance, the Carboscope-1 pCO_2 trends are slightly weaker than the CMEMS* pCO_2 trends in the narrow and wide coastal oceans, and yet the increase in the coastal sink is lower in Carboscope-1 than in CMEMS* (Figure 8c,d). In addition, observation-based CO_2 flux estimation shows that the largest coastal CO_2 sink region in the Arctic Ocean, the Chukchi Sea, is increasing due to increased ice-free

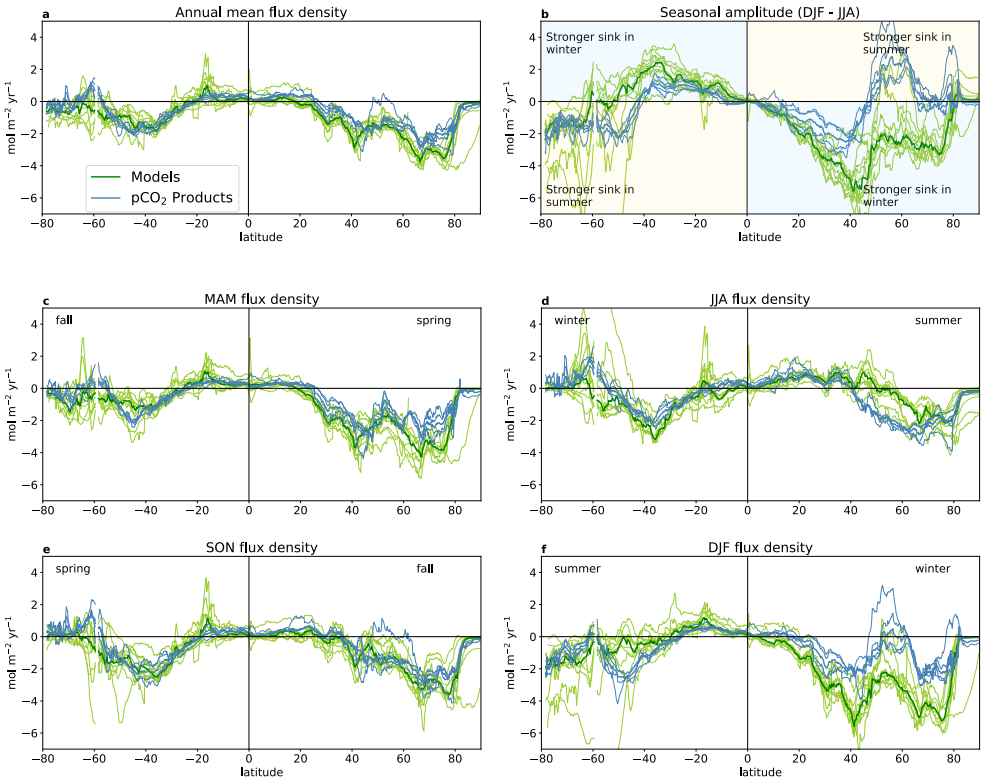


Figure 6. Latitudinal distribution of coastal ocean CO_2 flux and seasonal amplitude (using the wide coastal ocean). Latitudinal distribution of a) annual mean flux density, b) seasonal flux density amplitude, calculated as December-February (DJF) minus June-August (JJA), the blue (orange) quadrants indicate when the ocean uptake is stronger in winter (summer). c-f) seasonal mean flux density for March-May (MAM), JJA, September-November (SON) and DJF. Product and model medians are shown with thick lines and the individual 11 global models and 4 products with thin lines. Units are in mol C m^{-2} yr^{-1} in all panels for consistency, converting from per month to per year also for the 3-month periods.

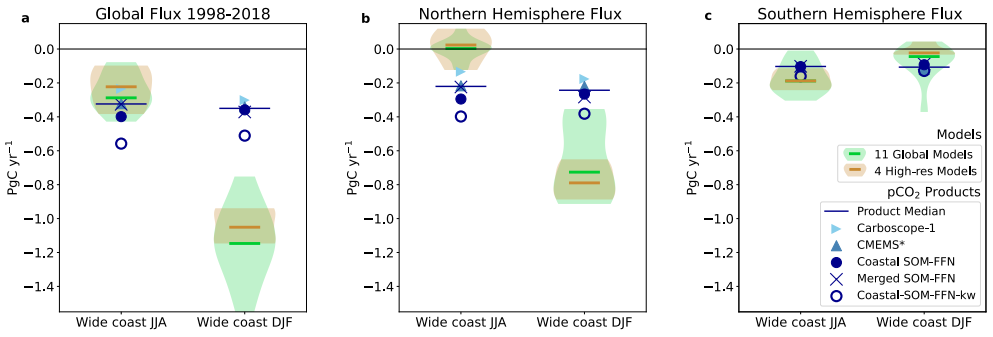


Figure 7. Net air-sea CO_2 flux in June-August (JJA) and December-February (DJF) for a) the global coastal ocean, b-c) the northern and southern hemispheres. The model distribution (violin) and median (thick lines) are shown for the full ensemble available (11 global models in green) and a subset of higher resolution models (4 global models in tan, see Methods and Table 2 for details). Symbols indicate global pCO_2-based products (blue), prior estimates (grey, see Supplementary Table S2 for details). Coastal-SOM-FFN-k_w, which is a second version of Coastal-SOM-FFN computed using different wind speed and k_w formulation (empty circle, see Methods) is not used in the pCO_2-product median. Units are in PgC yr^{-1} in all panels for consistency, using a 12-month scale up value for the 3-month periods.

area, longer sea-ice free period, and increased biological production rate (which keeps sea surface pCO_2 increase rate nearly zero) (Ouyang, Collins, et al., 2022). Another example of the decoupling between pCO_2 trends and flux trends is found in the coastal to open ocean difference. The global ocean biogeochemical model ensemble simulates smaller differences between atmospheric and oceanic pCO_2 trends in the coastal ocean than in the open ocean, resulting in a weaker increase in the carbon sink in the coastal ocean (following here the expected link between pCO_2 and flux trends, Figure 8c-d). In contrast to the models, both time-resolving pCO_2-products reveal higher differences between atmospheric and oceanic pCO_2 trends in the coastal ocean than in the open ocean (Figure 8c), which would suggest a stronger trend in the flux density in the coastal ocean (i.e. a stronger increase in the uptake). However, this expected increase in the uptake is only found in CMEMS* but not in Carboscope-1 (Figure 8d). A precise understanding of the trends in all parameters that control the air-sea fluxes of CO_2 and of the methodological differences in the pCO_2 mapping and flux calculation is crucial to understanding the evolving coastal ocean carbon sink.

Inconsistencies between pCO_2 trends and flux trends arise from the complex and uncertain interplay between the spatio-temporal changes in ocean pCO_2, wind speed and sea-ice coverage. In particular, trends in ocean pCO_2 and therefore in ΔpCO_2 (difference between coastal ocean surface ocean pCO_2 and atmospheric pCO_2) strongly differ between coastal regions, as well as between the two time-varying pCO_2-products (Figure S9). CMEMS*, as well as the multi-model median, show more negative ΔpCO_2 trends (potentially stronger uptake or weaker sources with time) in mid-to-high latitudes, but less negative or even positive ΔpCO_2 trends in the tropics and in the Arctic (Figure S10). In contrast, the Carbscope-1 product shows strongly negative ΔpCO_2 trends in the Arctic, and much larger variability in trends at other latitudes. These differences in ΔpCO_2 trends largely translate into consistent flux density trends (negative ΔpCO_2 trends generally yield negative flux trends, i.e., stronger uptake or weaker sources with time, Figures 9 and S10). However we note that in many regions, the ΔpCO_2 trends are amplified or dampened by trends in wind speed and sea-ice coverage, which are also strongly

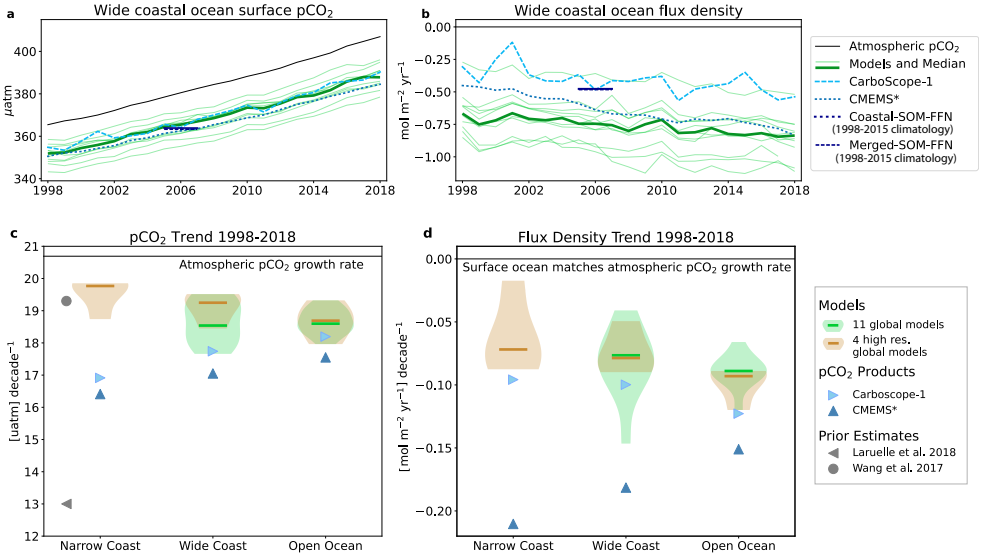


Figure 8. Temporal evolution of the global annual mean a) surface ocean pCO_2 [µatm] and b) net air-sea CO_2 flux density [mol C m^{-2} yr^{-1}] in the four pCO_2-products (blue lines) and the 11 global ocean models (thin green lines) and model median (thick green lines) in the wide coastal ocean. Trends in c) ocean surface pCO_2 [µatm $decade^{-1}$] and d) flux density [mol C m^{-2} yr^{-1}] for narrow coastal ocean, wide coastal ocean and open ocean waters. The model distribution (violin) and median (thick lines) are shown for the full model ensemble (11 global models in green) and a subset of higher resolution models (4 global models in tan, see Methods and Table 2 for details). Symbols show the trends for the two time-varying pCO_2-based products (Carboscope-1 and CMEMS* in blue) and prior estimates (in grey, see Table S1 for details).

spatially heterogeneous (see sea-ice trends in Figure S11). This effect is highlighted by the spatial differences and sometimes even a switch in sign between ΔpCO_2 trends and air-sea CO_2 flux trends in the model median in sea-ice regions (hatching in Figure 9). This is true, for instance, in the Arctic where the ocean models tend to simulate an increase in ocean CO_2 uptake despite a positive trend in ΔpCO_2 (i.e., ocean pCO_2 increases at a high rate than atmospheric pCO_2 which would reduce ocean uptake with constant sea-ice coverage and winds, Figures 9 and S10). This decoupling between CO_2 flux and ΔpCO_2 in the Arctic is indeed associated with a decrease in sea ice coverage in most models (Figure S11) and an increase in wind speed in two of the wind products that are widely used in these models (JRA-55 and ERA-5, Figure S12 and Tables 2-3), both effects inducing an increase in the flux with time despite the reduction in ΔpCO_2. These results clearly indicate that the global coastal sink is increasing. Yet, the magnitude of this increase, its spatial patterns and how it compares to the open ocean are still uncertain.

3.3 Coastal nitrous oxide and methane spatial variability

The spatial distribution of the coastal N_2O fluxes computed with the observation-based (i.e., Yang-N2O) and a mean of the model-based approaches are shown in Figure 10. Coastal N_2O fluxes are generally positive, indicating that coastal areas are a source of atmospheric N_2O. Flux densities vary considerably, from 0 (= equilibrium with the atmosphere) to about 10 g N m^{-2} yr^{-1}. The results from Yang-N2O reveal hotspots of N_2O emissions in eastern boundary upwelling systems, the upwelling areas of the north-

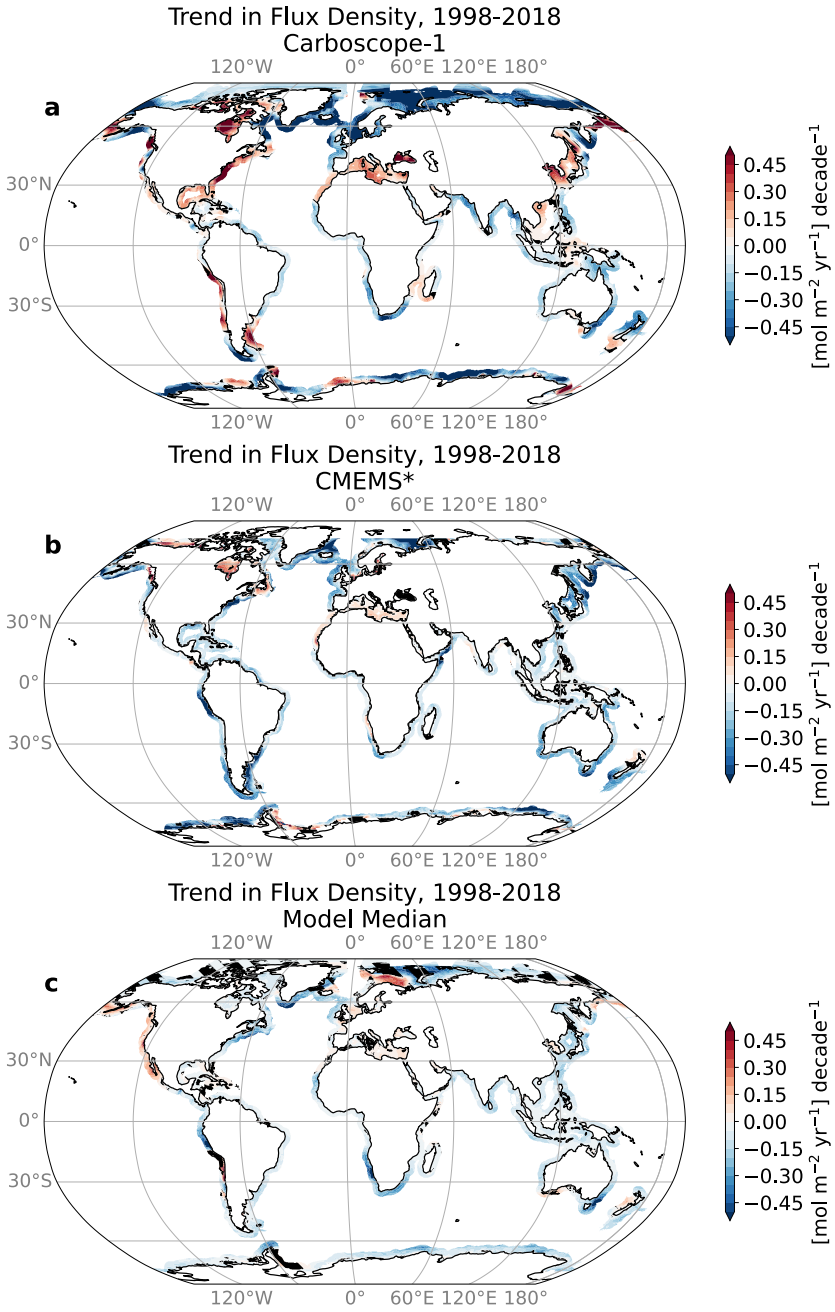


Figure 9. 1998-2018 trend in CO_2 flux [mol C m^{-2} yr^{-1}] for a) Carboscope-1; b) CMEMS* (area north of 75° N removed) c) multi-model median (global and regional models). Hatching indicates regions where the flux trend has a different sign than the ΔpCO_2 trend (shown in Figure S10), highlighting the influence of wind and/or sea-ice trends. Negative values indicate that the ocean uptake increases or the ocean outgassing decreases with time (both leading to more carbon accumulation in the ocean).

western Indian Ocean, the subpolar North Pacific, the Baltic Sea, the Black Sea and the shallow marginal seas of Southeast and East Asia. These are generally characterized by high surface productivity, low subsurface oxygen, and shallow oxyclines. High N_2O emissions from these regions thus likely reflects subsurface water-column production by a combination of nitrification and denitrification pathways, both of which are enhanced in the presence of low O_2 and high remineralization rates, and subsequent transport to the surface by upwelling and mixing processes. Similar hotspot regions are detected in the model-ensemble median, although with somewhat reduced magnitude relative to the observational products, and with the notable exception of marginal seas in Asia and Europe, suggesting that global models might not fully capture the nitrogen cycle in these regions, or the mechanisms transporting N_2O-laden waters to the surface. In addition, the model-ensemble also identifies mid-latitude western boundary systems, including the US East Coast, the North Pacific east of Japan, the southeast coast of Australia, and the southeastern tip of Africa, as additional areas of intense N_2O emissions that are not captured by the Yang-N2O product. Notably, these regions are not generally characterized by high surface productivity and low subsurface O_2 as coastal upwelling systems, although vigorous mixing along western boundary currents may favor local N_2O outgassing in the models. Most of these regions are also not densely sampled by observations in the MEMENTO database, in particular along the US, South Africa, and Japan eastern coasts, and thus the Yang-N2O observational extrapolation may be poorly constrained there. The magnitude of the flux in these hotspots often differs among the data products and model-ensemble (Figure 10c). The N_2O flux distributions shown in Figure 10 likely reflect the fact that enhanced coastal N_2O concentrations – and thus enhanced N_2O emissions fluxes – are associated with enhanced land-sea inputs of nitrogen (as nitrate or ammonium) or with upwelling of N_2O-enriched subsurface water masses in upwelling systems.

The spatial distribution of the coastal CH_4 fluxes computed with the observation-based Weber-CH4 product are shown in Figure 11. Coastal CH_4 fluxes are generally positive and range from 0 to 0.4 g CH_4 m^{-2} yr^{-1} indicating that coastal areas are a source of atmospheric CH_4. Patterns in CH_4 emissions in Weber-CH4 are largely correlated to water depth with most intense emissions coccuring at depth shallower than 50 m (Figure 11). Indeed, coastal emissions of CH_4 are largely fueled by benthic-sourced biogenic methane, which is produced via methanogenesis in anoxic sediments and released diffusively into the overlying water column (Reeburgh, 2007; Arndt et al., 2013; Bourgeois et al., 2016). The benthic CH_4 source is enhanced in coastal waters where the rapid organic matter flux to the seafloor drives sediment anoxia and rapid sediment accumulation inhibits the growth of methane oxidizing microbes (e.g., Egger et al., 2016). Furthermore, aerobic respiration acts as an efficient sink of CH_4 in the water column (Mao et al., 2022), meaning that transfer from the seafloor to the surface must be extremely rapid if CH_4 is to be emitted to the atmosphere. Ebullition (bubbling) from CH_4-enriched sediments can provide an important alternative pathway for CH_4 to surface (Rehder et al., 1998), but CH_4 is rapidly stripped from rising bubbles (McGinnis et al., 2006) and a small fraction reaches the surface only in shallow water depths. This further strengthens the coastal-offshore gradient in CH_4 emissions, and explains why total emissions differ very little between the narrow and wide coast regions in Weber-CH4 (Figure 2c). Coastal CH_4 emissions are further enhanced in hotspots under significant influence of freshwater discharge (Rosentreter et al., 2021), which due to their low sulfate concentration, promote the degradation of organic matter through the methanogenesis pathway. In addition to the biogenic CH_4 production pathway, CH_4 emissions can also be driven by geologically sourced methane, originating from shallow seafloor seeps fed by hydrocarbon reservoirs or high-latitude hydrates (Ruppel & Kessler, 2017; Puglini et al., 2020). Overall, the distribution of coastal CH_4 emissions (Figure 11) can largely be understood in terms of water depth, organic matter production and delivery to sediments, and freshwater inputs.

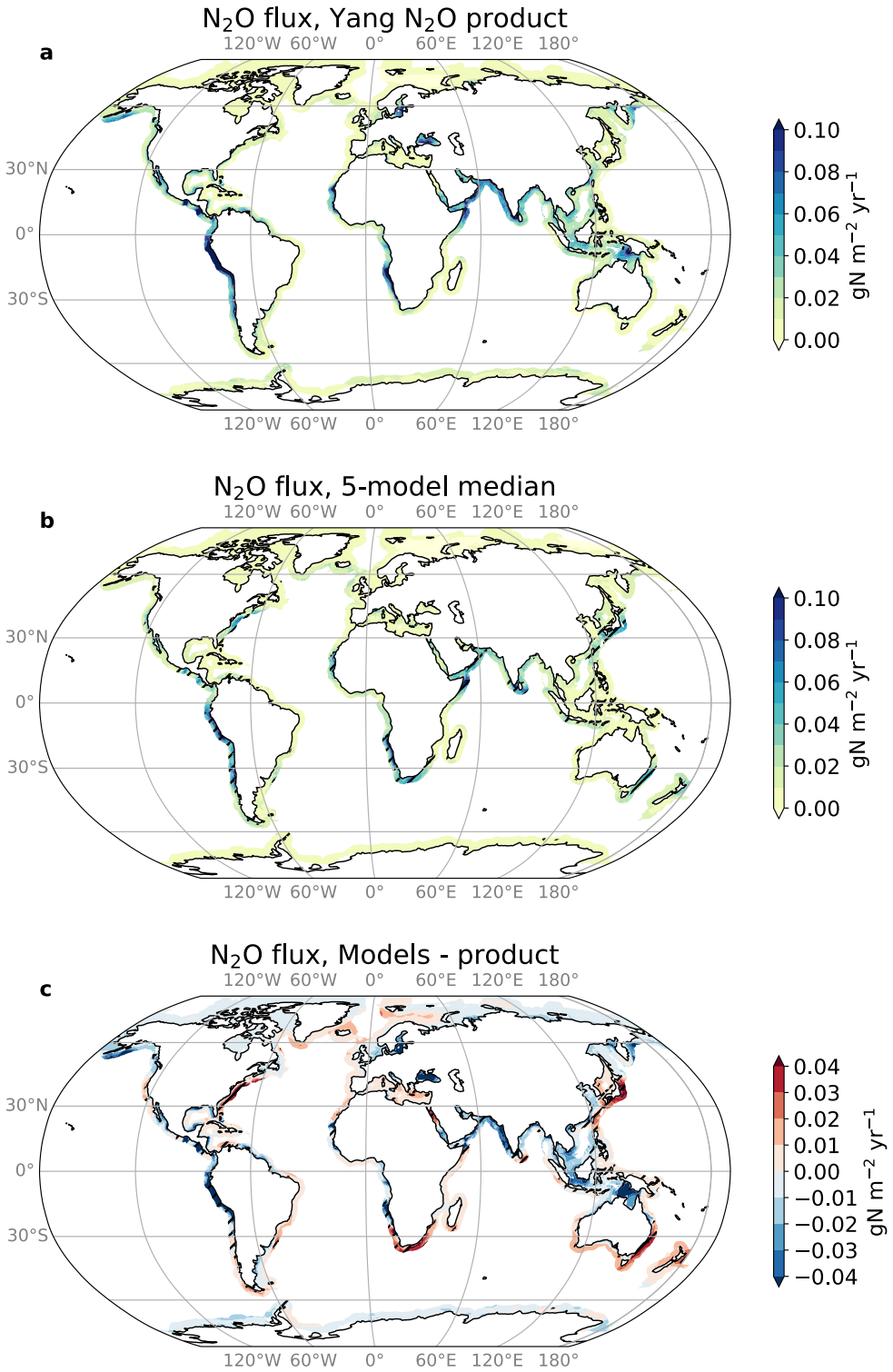


Figure 10. Maps of coastal N_2O flux (in g N m^{-2} yr^{-1}) from a) Yang-N2O product and b) the mean of the 5 global ocean models that simulate N_2O (CNRM-LR, CNRM-HR, ECCO-Darwin, ECCO2-Darwin, and NEMO-PlankTOM5). Hatching in panels b-c shows where RMSD among models exceeds 0.016 g N m^{-2} yr^{-1} (RMSD threshold corresponds to the 20% of coastal area with highest RMSD).

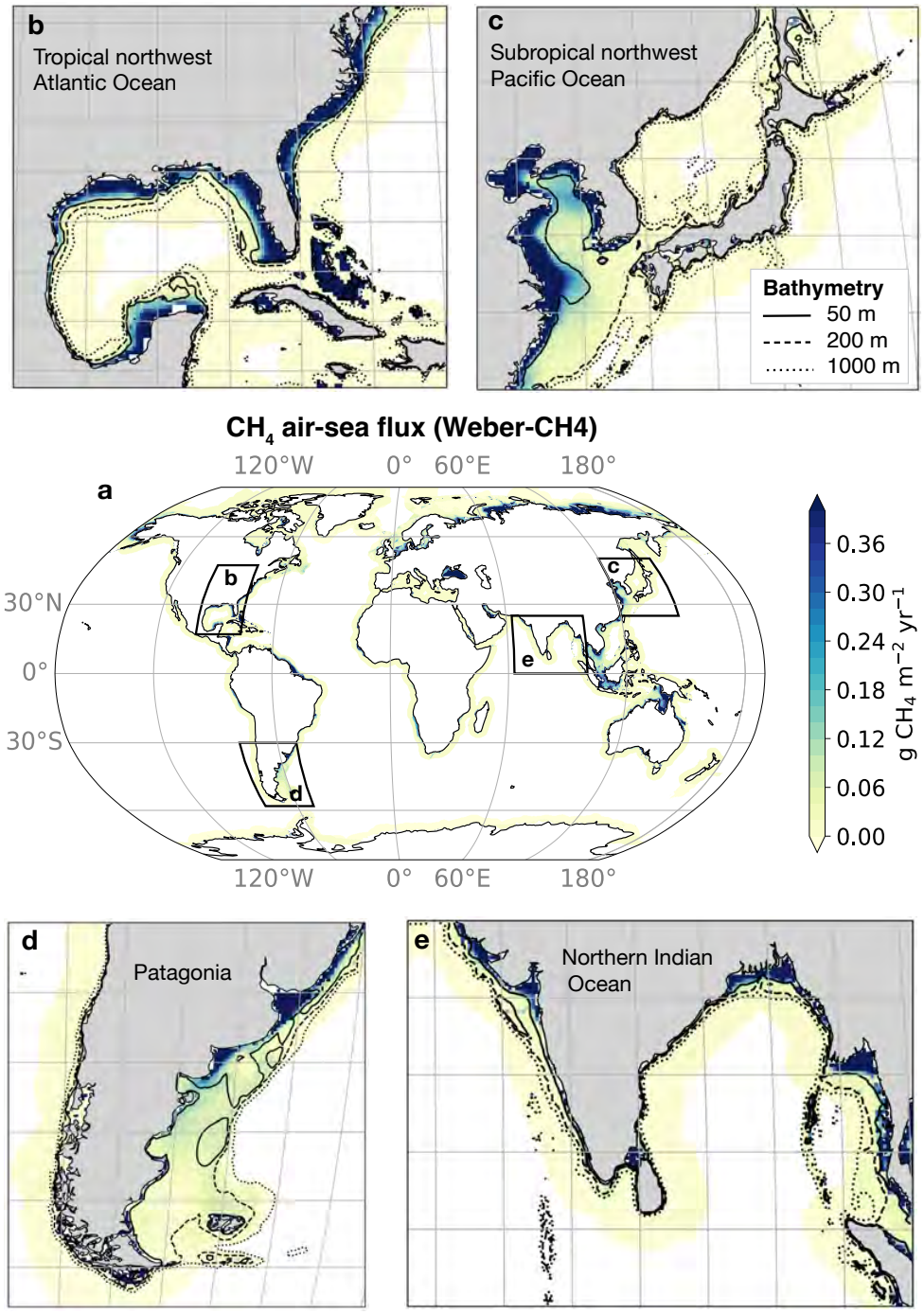


Figure 11. a) Global maps of coastal CH_4 flux from the Weber-CH4 product (includes diffusive and ebullitive flux, in g CH_4 m^{-2} yr^{-1}); b-e) insets show the CH_4 flux in four coastal regions along with 50, 200 and 1000 m bathymetry contours. CH_4 emissions are most intense in shallow coastal environments.

4 Discussion

4.1 Coastal CO_2 fluxes

This study presents a synthesis of the global coastal ocean air-sea CO_2 fluxes combining observational pCO_2-based products and an ensemble of ocean biogeochemical models. We confirm the hypothesis put forward in prior work (Laruelle et al., 2010, 2014; Roobaert et al., 2019; Dai et al., 2022) that when averaged globally, CO_2 flux densities are more negative (stronger sinks) in the coastal ocean than in the open ocean waters. As put forward by Roobaert et al. (2019), we find that the differences between coastal and open ocean flux densities are largely explained by the disproportionate contribution of high latitude systems (generally strong sinks) to the coastal ocean surface area. Global ocean biogeochemical models and pCO_2-products agree relatively well on the coast-to-open ocean contrast in CO_2 flux densities, but recent syntheses of discrete observations (Cao et al., 2020; Dai et al., 2022) find stronger heterogeneity than the global pCO_2-products and global ocean models presented here, suggesting that gap-filling approaches and global ocean models might smooth some of the coastal ocean spatial variability. Despite the good agreement on the coast-to-open ocean differences, the global ocean biogeochemical models yield a net median CO_2 uptake in the wide coastal ocean that is about 0.28 PgC stronger than the one inferred from pCO_2-products for the 1998-2018 period, equivalent to a ∼60% stronger sink (-0.44 PgC yr^{-1} for products vs. -0.72 PgC yr^{-1} for models in the wide coastal ocean). This mismatch of model- and product-based work in the net coastal CO_2 sink arises from a combination of factors, including strong differences in the coastal CO_2 flux seasonality (themselves attributed to differences in ocean pCO_2 seasonality and potentially wind speed and gas exchange transfer coefficient formulation) resulting in a stronger wintertime CO_2 uptake in northern subpolar and polar coastal systems in models.

4.1.1 Seasonality

The seasonality in the four pCO_2-products used here falls into three latitudinal regimes. Tropical coastal waters (25°S-25°N) are characterized by small seasonal amplitudes and a stronger sink or weaker source in winter, both attributed to the weak seasonal thermal changes that slightly reduce surface ocean pCO_2 in winter (Laruelle et al., 2014; Roobaert et al., 2019). Mid-latitude coastal waters (50°S-25°S and 25°N-50°N) are characterized by larger seasonal amplitudes and a stronger CO_2 sink in winter and spring, likely due to the combined effect of thermal changes which lowers ocean pCO_2 in winter, biological drawdown of dissolved inorganic carbon (DIC) which further lowers pCO_2 during the spring bloom, and the influence of stronger winds in winter (Laruelle et al., 2014; Roobaert et al., 2022). High latitude coastal waters (poleward of 50°N and 50°S) are characterized by seasonal variations similar in magnitude to mid-latitudes, but where the maximum CO_2 uptake occurs in summer in response to intense biological drawdown. The biologically-driven uptake in high-latitude systems peaks a few months later than in mid-latitude systems because of the poleward propagation of the bloom (Siegel et al., 2002; Roobaert et al., 2019, 2022; Ouyang, Collins, et al., 2022). This marked seasonality in CO_2 fluxes contrasts with the RECCAP synthesis which found very little seasonality in global coastal CO_2 flux densities, although the results were deemed inconclusive because of the sparse data and averaging process required to analyze the data available at the time (Chen et al., 2013). The results found here are, however, consistent with more recent work. In particular, the transition from thermally driven systems in the tropics (stronger winter sinks) to biologically driven systems at high latitudes (stronger summer sinks), and the increase in seasonal amplitude from tropical to high-latitude systems found in the pCO_2-products, are consistent with the global seasonal patterns in the coastal ocean described by (Roobaert et al., 2019), the global open ocean seasonality patterns assessed in the framework of RECCAP2 (Rodgers et al., submitted to the RECCAP2 special is-

sue), and supported by field and remote sensing studies at regional scale (Signorini et al., 2013; Ouyang, Collins, et al., 2022; Tu et al., 2021).

Our synthesis reveals, however, strong differences in seasonality between pCO_2-products and global ocean biogeochemical models. The model median simulates a weak CO_2 flux seasonality in tropical coastal oceans similarly to the pCO_2-products, but yields a CO_2 uptake that is stronger in winter at mid- and high-latitudes. This is likely due to a weaker contribution of biologically induced seasonality compared to thermal changes in the models, which would explain the lower surface ocean pCO_2 simulated in winter (due to an underestimated upward transport of remineralized DIC) and the higher pCO_2 simulated in spring/summer (due to a weaker biological drawdown). Part of these systematic differences compensate in the global mean coastal flux (winter vs. summer, northern vs. southern hemisphere), but because the model-product difference is larger in winter in the northern hemisphere, the net CO_2 uptake in the wide coastal ocean is about 60% larger in the model median. The RECCAP2 chapter on open ocean seasonality (Rodgers et al., submitted to the RECCAP2 special issue), finds a similar systematic bias in model winter-to-summer pCO_2, which they attribute to a generally too small surface DIC seasonal cycle in models compared to observation-based reconstructions. This bias is particularly evident in the subpolar North Atlantic and North Pacific Oceans, where it manifests itself not only as a difference in amplitude but also in phasing. In these regions, the simulated too low DIC seasonality results in a thermal control of the pCO_2 seasonality in the global ocean biogeochemical models and thus in a phase shift of the seasonal pCO_2 cycle compared to the observation-based estimate dominated by non-thermal forcing. This suggests that the systematically stronger winter sink and weaker summer sink found in northern coastal waters in the models are at least partly attributable to general biases in the biogeochemical (e.g., bloom dynamics) or physical (e.g., vertical mixing) components of the ocean models, rather than a characteristic of the models that is specific to the coastal ocean. See details in the RECCAP2 studies of (Rodgers et al., submitted to the RECCAP2 special issue). Nevertheless, we find that the amplitude of this systematic model/product difference in seasonality is amplified in the coastal ocean (see Figures S7-S8).

Differences in ocean pCO_2 seasonality between models and pCO_2 products can be amplified by differences in gas exchange coefficient k_w, either through the influence of winds or the gas exchange coefficient formulation (which are different across the different ocean biogeochemical models and pCO_2-products, Tables 1-3), and maybe to a lesser extent spatio-temporal differences in sea-ice cover (e.g., lower ice cover in some products/models could yield stronger fluxes). In models, the surface pCO_2 and k_w are tightly coupled in the sense that a larger k_w drives down the air-sea pCO_2 disequilibrium and therefore the air-sea CO_2 flux. In contrast, the calculation of the flux in pCO_2 products (except for Carboscope-1 which links fluxes and pCO_2 changes in a mixed-layer carbon budget equation) is done offline without any compensatory effect between k_w and air-sea pCO_2 disequilibrium. Therefore, the observation-based flux assessments are even more sensitive to the choice of the wind and k_w parameterization. For instance, we find that the net global coastal CO_2 uptake in the Coastal-SOM-FFN product is increased by nearly 50% in the wide and the narrow coastal ocean when changing the wind product (from ERA-interim to JRAv1.3) and gas exchange parametrization (from Ho et al., 2011 to Wanninkhof 1992, see Table 1). These results are in line with published literature that assessed the impact of k_w parametrizations on global air-sea CO_2 fluxes (Boutin et al., 2009; Roobaert et al., 2018; Reichl & Deike, 2020), but highlights that its influence is also crucial in the coastal ocean, because of the disproportionate contribution of mid- to high-latitude/high-wind systems in the total coastal area. Furthermore, global wind-based gas exchange parameterization might not capture the complexity of the coastal ocean processes, such as the influence of bubbles entrained by wave breaking (Deike & Melville, 2018; Woolf et al., 2019), the presence of high surfactant concentrations (Pereira et al., 2018), or fine scale water-side convection (Gutiérrez-Loza et al., 2022).

4.1.2 Land-sea fluxes

An additional factor that can explain part of the difference in the net CO_2 uptake between pCO_2-products and models is the presence of systematic bias in global ocean biogeochemical models, in particular the contribution of carbon and nutrient land-sea riverine inputs or the models' horizontal resolution and ability to resolve coastal dynamics. At pre-industrial times (and assuming steady-state consistent with stable ice-core atmosphere CO_2 values; Elsig et al., 2009), the supply of carbon from land must have been balanced by burial in sediments and an outgassing of CO_2 from the ocean to the atmosphere. This land-driven outgassing flux, recently estimated to be 0.65±0.3 PgC yr^{-1} (mean±2-sigma) for the global open ocean (Regnier et al., 2022, note that this outgassing of 0.65 PgC yr^{-1} is quantified for the open ocean outside of the narrow coastal ocean and thus include part of the wide coastal ocean), is still active today and therefore partially offsets the ingassing CO_2 flux that is directly driven by anthropogenic CO_2 emissions to the atmosphere (e.g., Resplandy et al., 2018; Friedlingstein et al., 2022; Regnier et al., 2022). Observation-based pCO_2-products estimate the net contemporary flux of CO_2, and therefore implicitly include the fluxes of natural and anthropogenic carbon, as well as the outgassing fluxes of carbon from land origin (e.g., Hauck et al., 2020). Most models, however, do not, or only partially include this land-sea carbon inputs (see Tables 2-3) and are therefore likely to overestimate the net CO_2 ocean uptake, in particular in coastal waters adjacent to the land (Lacroix et al., 2020).

In globally integrated estimates, such as analyzed in the Global Carbon Budget (e.g., Friedlingstein et al., 2022) or the IPCC (Arias et al., 2021), the net air-sea CO_2 flux can in principle be adjusted for the outgassing of carbon from land to isolate the oceanic net sink, or it can be used to shed light on differences between modeled and observation-based flux estimates (e.g., Hauck et al., 2020; Friedlingstein et al., 2022). The RECCAP2 open ocean chapters estimated the spatial distribution of this land-driven CO_2 outgassing by upscaling the spatial distribution from Lacroix et al. (2020) using the global outgassing number of Regnier et al. (2022). This estimate suggests that 0.12 PgC yr^{-1} out of the 0.65 PgC yr^{-1} of land-driven CO_2 outgassing occurs in the wide coastal ocean, which could explain part of the model-product discrepancy. It is important to recognize, however, that the spatial distribution of this land-driven outgassing and contribution to the coastal ocean air-sea flux are very poorly constrained. In particular, we note that the model used to estimate the land-driven outgassing pattern (Lacroix et al., 2020) is lacking some of the processes that control the magnitude (hence the upscaling to match the global number of 0.65 PgC yr^{-1} from Regnier et al. (2022) but also the spatial distribution of this outgassing (e.g., CO_2 uptake by coastal vegetation). Another factor to consider is the land-sea input of nutrients which promotes biological CO_2 uptake in coastal waters downstream of the river mouth (e.g., Louchard et al., 2021; Terhaar et al., 2021; Gao et al., 2023), potentially offsetting the land-driven CO_2 outgassing associated with carbon runoffs, although we do not expect the patterns of the CO_2 outgassing and biological CO_2 uptake to match. In the model ensemble considered here models either include both carbon and nutrient land-sea inputs or neither (Tables 2 and 3). This might explain why models with land-sea carbon inputs did not systematically yield weaker CO_2 uptake in the coastal ocean compared to the one without land-sea inputs. Finally, we find that the subset of global ocean biogeochemical models with highest spatial resolution yields a slightly weaker net CO_2 uptake (-0.65 PgC yr^{-1}) in better agreement with the pCO_2-products than the full model ensemble. The small number of models in that subset (4) makes any statistical argument about resolution difficult. Yet, this result suggests that a better representation of fine scale coastal dynamics could improve the representation of the CO_2 flux, likely by improving the representation of the physical and biogeochemical processes controlling CO_2 seasonality in the northern hemisphere (Laurent et al., 2021; Rutherford et al., 2021; Rutherford & Fennel, 2022).

4.1.3 Trends

This synthesis indicates that the coastal ocean CO_2 sink has increased between 1998 and 2018, in line with the expectation from previous work that showed surface pCO_2 in the narrow coastal ocean increasing at a smaller rate than in the atmosphere (Wang et al., 2017; Laruelle et al., 2018). The rate at which the coastal sink has increased is, however, poorly constrained by the models and products presented here (flux density trend varies by a factor 2 between the two time-varying pCO_2-products and by a factor 3 between the 11 models). In addition, it is still unclear if this increase in the global coastal CO_2 sink is comparable, slower or faster than in the open ocean due to the inconsistent responses found in models and the two time-varying pCO_2-products but also in prior modeling and observation-based work (Bourgeois et al., 2016; Wang et al., 2017; Laruelle et al., 2018; Lacroix et al., 2021). The CMEMS* pCO_2-product suggests that the CO_2 uptake increases faster in the coastal ocean than in the open ocean, which is in line with the prior observation-based results of Laruelle et al. (2018). In contrast,the ensemble of 11 global ocean models and the Carboscope-1 pCO_2-product suggest that the coastal ocean sink is increasing at a slightly smaller rate than the open ocean, a result in line with another other prior work based on pCO_2 observations (Wang et al., 2017) and global ocean biogeochemical models (Bourgeois et al., 2016; Lacroix et al., 2021). Bourgeois et al. (2016) explains this weaker increase in the coastal carbon sink by a bottleneck in offshore transport which leads to anthropogenic carbon accumulation and limits the ability of coastal waters to take up anthropogenic carbon. Although we do not quantify surface residence time or off-shelf transport in this study, our finding that the modeled CO_2 sink increases at a lower rate in the coastal region than in the open ocean lends support for this interpretation. Other processes at play could explain this behavior. For instance, relatively shallow waters in coastal oceans might limit the exchanges with deep (free of anthropogenic CO_2) waters, such that the coastal ocean surface layer saturates more quickly with additional CO_2 added to the atmosphere. In models, this slower rate is associated with regions of increased outgassing or reduced uptake, although mid-to-high latitudes can be strongly increasing CO_2 sinks as suggested by observations (Laruelle et al., 2018). However, the regions controlling this slower rate of increase vary across models (e.g., North Pacific, Mediterranean Sea and Parts of the Arctic in the model median in this study vs. tropical ocean and parts of the Arctic in Lacroix et al., 2021), highlighting further the uncertainties that remain in constraining coastal trends.

The slower increasing pCO_2 trend in the coastal ocean was attributed in these model-based studies to an increased outgassing or reduced uptake in tropical and river-dominated Arctic shelves, while mid-to-high latitudes were found to be strongly increasing CO_2 sinks as suggested by observations. Part of the discrepancies between the estimates of the CO_2 flux trends are likely to arise from the sparse temporal pCO_2 observational coverage. For instance the prior studies of Wang et al. (2017) and Laruelle et al. (2018) only covered a small portion of the coastal surface area and might not be representative of the global ocean. This is supported by regional studies that identified coastal ocean pCO_2 trend weaker than the atmospheric pCO_2 trend (i.e. potentially yielding intensified CO_2 uptake or decreased outgassing) such as the northern Gulf Stream margin, the South China Sea, the Sea of Japan, the North Sea and the Antarctic Peninsula (Bauer et al., 2013; Wang et al., 2017; Laruelle et al., 2018; Dai et al., 2022), but also regions where coastal ocean pCO_2 increases at a similar rate (i.e. near-zero changes in the flux) or even higher rates (i.e. reduced CO_2 uptake or intensified outgassing) than atmospheric pCO_2, such as in the Baltic Sea (Schneider & Müller, 2018), the California Current or along the eastern US coast (Reimer et al., 2017; Laruelle et al., 2018; Salisbury & Jönsson, 2018; Xu et al., 2020; Dai et al., 2022). Another source of discrepancy is the decoupling found between global coastal pCO_2 trends and flux trends, suggesting that the CO_2 flux trends are sensitive to trends in winds and sea-ice (via the gas exchange coefficient), and how they combine with the pCO_2 trends. This sensitivity to sea-ice and winds is likely more pronounced in the observation-based estimates, which rely on an "offline" calculation of

the flux (no mechanistic link between pCO_2 disequilibrium, wind and sea-ice, except for CarboScope-1), or even more simply assume that slower trends in coastal ocean pCO_2 translate into faster growing coastal CO_2 flux (e.g., Laruelle et al., 2018), an assumption that is not fulfilled in the 2 pCO_2-products used in this study (although it does work in the multi-model median).

4.1.4 Conclusions

The systematic differences found between the ensemble median of global ocean models and pCO_2-products (including the larger net annual mean CO_2 uptake found in global ocean models, the different timing of mid- and high-latitude seasonality and the large range found in flux density trends) should be interpreted with caution. First, some models are capturing better than others the patterns reconstructed by the pCO_2-products. In particular, some models are able to reproduce the stronger summer sink found at high-latitudes, or simulate a net annual mean CO_2 flux that better matches the product-based estimates. In addition, differences between products and models do not necessarily equate to model bias, as regions of largest product-model mismatch also often correspond to regions where the observational sampling is sparse (68% of the wide coastal ocean surface area was never sampled, and of the sampled area, 33% has data for only one month in a single year, Figure S1) and where the spread across the observation-based products and across the global models is the highest (hatching on Figure 5a,b). In contrast, coastal regions that are relatively well sampled by observations and well constrained by the products generally correspond to regions of agreement between the observation-based and model-based estimates (Roobaert et al., 2022). Thus, while we have overall more confidence in the observation-based estimates of the ocean carbon sink, the uncertainties associated with these reconstructed estimates remain high. This precludes a clear conclusion about whether the observation or model-based estimates are closer to the truth.

4.2 Coastal N_2O and CH4

The coastal ocean is a substantial source of atmospheric N_2O (Yang et al., 2020) and a minor source of atmospheric CH_4 (Weber et al., 2019; Saunois et al., 2020). The N_2O flux estimates presented here for the narrow coastal ocean (0.14 to 0.75 Tg N yr^{-1}) are at the lower end of previous estimates of the mean global N_2O fluxes from nearshore coastal systems (including shelves, estuaries and upwelling regions) which range from 0.7 to 6.7 Tg N yr^{-1} (Bange et al., 1996; Seitzinger & Kroeze, 1998). The mean CH_4 flux estimates for the narrow coastal ocean (2.46-3.19 Tg CH_4 yr^{-1} for the diffusive flux and up to 6.79 Tg CH_4 yr^{-1} when accounting for the ebullitive flux in the narrow coastal ocean) are in good agreement with a recently published mean CH_4 flux from shelves (0 - 200 m water depth) of 5.7 Tg CH_4 yr^{-1} (Rosentreter et al., 2021). Nevertheless, quantitative estimates of N_2O and CH_4 emissions remain highly uncertain. Estimates of N_2O emissions in this study vary by a factor of 5-6 in both the narrow and wide coastal ocean, and central values of CH_4 emissions by a factor up to 3.5. The smaller range found here for CH_4 likely reflects the fewer number of estimates available (2 observation-based products only vs. 5 global ocean models and 2 observation-based products for N_2O) rather than stronger constraints on the emissions.

Current observational products only provide a climatological view of N_2O and annual mean view of CH_4 emissions, with limited or missing information on (i) seasonal and inter-annual variability, (ii) fine-scale (i.e., few 10s of km or less) land-ocean gradients, (iii) the effects of mesoscale and submesoscale features such as eddies (Grundle et al., 2017), and (iv) extreme events such as storms and marine heat waves (Borges et al., 2019; Gindorf et al., 2022). Aspects of air-sea gas exchange, such as the effects of surface micro-layers on these gasses (Kock et al., 2012) remain also poorly understood. In parallel, commonly adopted model parameterizations greatly simplify complex source and sink processes that are the focus of ongoing research. For example, there remains

significant uncertainty in the relative importance of the various (micro)biological and photochemical processes driving the production and consumption of N_2O and CH_4 in coastal waters and sediments, and their potential responses to changing oceanic conditions (Bange, 2022). Methane can be produced aerobically in-situ in surface waters, providing the most direct route to the atmosphere. This process has mostly been studied in the open ocean where decomposition of methylphosphonate (MPn, a component of semi-labile dissolved organic matter) appears to be the dominant methanogenesis pathway (Karl et al., 2008; Repeta et al., 2016). Recent evidence suggests the MPn pathway is also active in some coastal waters (Mao et al., 2022), but its importance relative to benthic-sourced CH_4 in coastal waters remains unclear. Additional sources of N_2O and CH_4 remain poorly characterized and are not represented by models, including submarine groundwater discharge (Arévalo-Martínez et al., 2023) and production associated with marine microplastic (Royer et al., 2018; Su et al., 2022), submerged aquatic vegetation (Rosentreter et al., 2021; Hilt et al., 2022; Roth et al., 2023; Rosentreter et al., 2023), and zooplankton (Schmale et al., 2018).

Our study reveals that while coastal N_2O flux emissions from observational products and models generally agree in terms of main patterns and magnitude, emission hotspots in productive, low-O_2 upwelling systems appear to be underestimated by models, suggesting deficiencies in model circulation and parameterization of low-O_2 sources. In contrast, models point to coastal N_2O flux hotspots along mid-latitude western boundaries that are not evident in observational reconstructions. The reason for this mismatch remains unclear, but likely reflects lack of observations from these regions, which could limit the ability of reconstructions to capture coastal hotspots, and potential model biases. The recently proposed Global N_2O Ocean Observation Network (N_2O-ON) (Bange et al., 2019; Bange, 2022) might help to better constrain and understand temporal and spatial variability as well as reduce uncertainties in current global N_2O oceanic emission estimates.

Ongoing environmental changes such as ocean warming, decreasing pH, loss of dissolved oxygen, and eutrophication might significantly alter the production and consumption of both N_2O and CH_4 as well as their distribution patterns in coastal waters and, consequently, their release to the atmosphere (e.g., Rees et al., 2022; Zhou et al., 2023). However, our knowledge of recent trends on which future emissions scenarios of N_2O and CH_4 from the coastal ocean rely upon are still far from complete. In particular, hydrate dissolution due to ocean warming may enhance this flux at the seafloor, but only at the feather-edge of the hydrate stability zone, which occurs in ∼400 m deep water in mid-latitudes – which could be too deep for the methane to make it to the surface and escape to the atmosphere (Joung et al., 2022). Shallow hydrocarbon-fed seep fields allow for more efficient methane release to atmosphere (Hovland et al., 1993), but their impact appears to be highly localized (Joung et al., 2020), and the global-scale contribution of geological CH_4 to marine emissions remains highly uncertain (Etiope et al., 2019). Understanding CH_4 oxidation dynamics in coastal environments is therefore an important focus area for future research. Although N_2O-ON was originally designed for N_2O only, adding measurements of CH_4 will be facilitated by deploying instruments on the basis of the same technique used for N_2O measurements (i.e. cavity-enhanced absorption spectroscopy), providing new opportunities to establish long-term time-series for these two greenhouse gasses.

4.3 Coastal greenhouse gas atmospheric influence

This synthesis provides an estimate of the coastal contribution to the atmospheric greenhouse gas budget using an ensemble of observation-based products and global ocean biogeochemical models (in CO_2-equivalent). In both products and models, we find that a significant proportion of the coastal CO_2 uptake (∼35-55%) is offset by N_2O and CH_4 emissions, despite large uncertainties in the magnitude of the mean CO_2 uptake (large

uptake in models) and relatively limited numbers of observation-based products and models available for N_2O and CH_4 fluxes. This offset is significantly larger than in the global ocean, for which a value of about 10% can be calculated based on the CO_2 (Le Quéré et al., 2018), N_2O (Tian et al., 2020), and CH_4 (Saunois et al., 2020) global budgets by the GCP. A smaller offset value on the order of 10-20% has also been reported for estuaries and coastal vegetated ecosystems (Rosentreter et al., 2023), highlighting that the radiative balance on the shelves results from a significant contribution of the 3 greenhouse gasses. Such an offset does not occur in inland waters either (rivers, lakes and reservoirs), as freshwater aquatic systems are a net source of CO_2, CH_4 and N_2O (Battin et al., 2023)(also Lauerwald et al., in revision for the RECCAP2 special issue), with CO_2 and CH_4 contributing roughly 75% and 25% to the 100-year time-scale global wearing potential, respectively, while N_2O is only a marginal contributor. Integrating the three compartments of the land-to-ocean aquatic continuum (LOAC) from streams to the coastal oceans (i.e., inland waters, estuaries and coastal vegetation, and coastal ocean waters (Regnier et al., 2013, 2022), we find that the LOAC is a net source of greenhouse gasses. Indeed, the 8.3 (range of 5.8-12.7) $PgCO_2$-e yr^{-1} emitted by inland waters are only partly compensated by the net uptakes of 0.4 (range 0.2-0.7) $PgCO_2$-e yr^{-1} from estuaries and coastal vegetation and 1.3 (range 0.7-1.8) $PgCO_2$-e yr^{-1} from wide coastal waters. For the 100 year time horizon, the LOAC as a whole thus emits about 6.6 $PgCO_2$-e yr^{-1} globally.

Acknowledgments

The authors have no conflicts of interest. A.K.H. acknowledges support from the National Science Foundation (NSF) Graduate Research Fellowship Program under Grant DGE-2039656. Any opinions, findings, and conclusions or recommendations expressed in this material are those of the author and do not necessarily reflect the views of the NSF. L.R. and E.L. were partly funded by National Oceanic and Atmospheric Administration award NA21OAR4310119. L.R. and M.M. thank NASA for financial support via the grant NASA OCO-2 Science Team Grant 80NSSC18K0893. L.R. additionally thank the Princeton Institute for Computational Science and Engineering (PICSciE) for High Performance Computing (HPC) provision, storage and support. D.B. acknowledges support from NSF grant OCE-1847687, and computational resources from the Expanse system at the San Diego Supercomputer Center through allocation TG-OCE170017 from the Advanced Cyber infrastructure Coordination Ecosystem: Services and Support (ACCESS) program, which is supported by NSF grants 2138259, 2138286, 2138307, 2137603, and 2138296. J.D.M. and N.G. acknowledge support from the European Union's Horizon 2020 research and innovation programme under grant agreement no. 821003 (project 4C) and no. 820989 (project COMFORT). N.G. additionally thanks for the support of the Swiss National Science Foundation through grant agreement no 175787 (Project X-EBUS). J.S. was supported by the Research Council of Norway (grant no 270061) and acknowledges provision of HPC and storage resources by UNINET/sigma2 (nn/ns9560k). C.L.Q. was funded by the UK Royal Society (grant no. RP\R1\191063). Simulations of the NEMO-PlankTOM model were carried out by D. Willis on the HPC Cluster supported by the Research and Specialist Computing Support service at the University of East Anglia. G.G.L. is a research associate of the FRS-FNRS at the Université Libre de Bruxelles. Finally, we thank the RECCAP2 organisers and scientific steering committee for coordinating and supporting this effort.

Table 1. Description of observation-based products used in this study, including the wind speed product and gas exchange coefficient (k_w) formulation used to compute the fluxes. W92, H11, W14, L13, N00 stands for k_w-formulations from Wanninkhof (1992); Ho et al. (2011); Wanninkhof (2014); Liang et al. (2013); Nightingale et al. (2000) respectively. Mon and Ann stands for monthly and annual mean frequencies. Wide coastal areas are calculated after the products and models have been regridded on the 0.25°x 0.25° grid. Further details and references on observation-based products and models are provided in Supplementary Material.

Product	Gasses	land-sea inputs	Domain	Frequency/period in this study	Horizontal resolution	wide area (million km^2)	wind speed and k_w	Reference
Carboscope-1	CO_2	N/A	Global	Mon[a] 1998-2018	1°	73.9	JRA55-do v1.5.0 W92[b]	(Rödenbeck et al., 2022)
CMEMS*	CO_2	N/A	Global[c]	Mon 1998-2018	1°	55.8	ERA5 W14[b]	(Chau et al., 2022)
Coastal-SOM-FFN	CO_2	N/A	Global	Mon 1998-2015	0.25°	77.2	ERA-interim H11	(Roobaert et al., 2019)
Coastal-SOM-FFN-k_w	CO_2	N/A	Global	Mon 1998-2015	0.25°	77.2	JRAv1.3 W92	
Merged-SOM-FFN	CO_2	N/A	Global	Mon 1998-2015	0.25°	77.2	ERA-interim H11	(Landschützer et al., 2020)
Yang-N2O	N_2O	N/A	Global	Mon 1998-2015	0.25°	73.4	ERA-5 W14[b], L13[b]	(Yang et al., 2020)
Weber-CH4	CH_4	N/A	Global	Ann 1999-2016	0.25°	73.7	ERA-5 W14[b], L13[b]	(Weber et al., 2019)
MARCATS-N2O & MARCATS-CH4	N_2O, CH_4	N/A	Global	Ann 1980-2016	regional[d]	77.2	NCEP II N00	(Kock & Bange, 2015)

[a]From originally daily.
[b]Scaled to global ocean mean value of 16.5 cm/h.
[c]Missing Arctic filled with Coastal-SOM-FFN climatology north of 75°N.
[d]No gap filling, one value per MARgins and CATchments Segmentation (MARCATS).

Table 2. Description of global ocean biogeochemical models used in this study, including the wind speed product and gas exchange coefficient (k_w) formulation used to compute the fluxes. W92 and W14 stand for k_w-formulations from Wanninkhof (1992, 2014) respectively. Mon stands for monthly frequency. Wide coastal areas are calculated after the products and models have been regridded on the 0.25°x 0.25° grid. Further details and references on observation-based products and models are provided in Supplementary Material.

Model	Gasses	land-sea inputs	Domain	Frequency/period in this study	Horizontal resolution	wide area (million km^2)	wind speed and k_w	Reference
CCSM-WHOI	CO_2	No	Global	Mon 1998-2017	3.6°lon 0.8-1.8°lat	34.5	NCEP W92	Doney et al. (2009)
CNRM-LR	CO_2,N_2O	Yes	Global	Mon 1998-2018	1°lon 0.3-1°lat	64.8	JRA55-do W14	Séférian et al. (2019)
CNRM-HR	CO_2,N_2O	Yes	Global	Mon 1998-2018	0.25°	71.3	JRA55-do W14	Berthet et al. (2019)
FESOM-LR	CO_2	No	Global	Mon 1998-2018	unstructured ∼1°	75.5	JRA55-do W14	Hauck et al. (2020)
FESOM-HR	CO_2	No	Global	Mon 1998-2018	unstructured ∼0.25°	76.4	JRA55-do W14	Hauck et al. (2020)
IPSL	CO_2	Yes	Global	Mon 1998-2018	1°lon 0.3-1°lat	65	JRA55-do W14	Bopp et al. (2015)
MOM6-Princeton	CO_2	Yes[a]	Global	Mon 1998-2018	0.5°lon 0.25-0.5°lat	63.8	JRA55-do v1.3 W92	Liao et al. (2020)
MPIOM-HAMMOC	CO_2	Yes	Global	Mon 1998-2018	1.5°	44.5	NCEP W14	Ilyina et al. (2013)
MRI-ESM2.1	CO_2	No	Global	Mon 1998-2018	1°lon 0.3-0.5°lat	66.3	JRA55-do W14	Yukimoto et al. (2019)
NEMO-PlankTOM12	CO_2	Yes	Global	Mon 1998-2018	2°lon 0.3-1.5°lat	62.8	NCEP W92	Wright et al. (2021)
NEMO-PlankTOM5	N_2O	Yes	Global	Mon 1998-2018	2°lon 0.3-1.5°lat	62.8	NCEP W92	Buitenhuis et al. (2018)
NorESM-OC2.0	CO_2,N_2O	Yes	Global	Mon 1998-2018	nominal 1°	63.9	JRAv1.3 W14	Tjiputra et al. (2020)
ECCO-Darwin	N_2O	No	Global	Mon 1997-2014	1/3°lon	66.5	ERA-Interim W92	Carroll et al. (2020)
ECCO2-Darwin	N_2O	No	Global	Mon 2006-2013	1/6°lon	90.5	ECMWF & JRA-55 W92	Manizza et al. (2019)

[a]Carbon inputs are only partial and calculated to roughly balance burial.

Table 3. Description of regional ocean biogeochemical models used in this study, including the wind speed product and gas exchange coefficient (k_w) formulation used to compute the fluxes. W92, H06 and W14 stand for k_w-formulations from Wanninkhof (1992); Ho et al. (2006); Wanninkhof (2014) respectively. Mon stands for monthly frequency. Further details and references on observation-based products and models are provided in Supplementary Material.

Model	Gasses	land-sea inputs	Domain	Frequency/period in this study	Horizontal resolution	wind speed and k_w	Reference
ETHZ-ROMS-Atl	CO_2	Yes	regional Atlantic Ocean	Mon 1998-2018	∼4-120 km[a]	ERA5 W14	Louchard et al. (2021)
ETHZ-ROMS-Pac	CO_2	Yes	regional Pacific Ocean	Mon 1998-2018	∼4-60 km[b]	ERA5 W14	Desmet et al. (2022)
ACM-NWAtl	CO_2	Yes	Regional Northwest Atlantic (36.3 to 53.8N; -74.6 to -45.2 E)	Mon 1998-2018	∼9.5 km	ERA-interim H06, W14	Rutherford et al. (2021)
NYUAD-ROMS-Indian	CO_2	nutrients no carbon	regional Indian Ocean (31.5°S to 31°N; 30°E to 120°E)	Mon 1998-2018	1/10°	ERA-interim W14	Lachkar et al. (2021)

[a]highest resolution in Amazon plume and western Africa (2 poles).
[b]highest resolution in California Current (1 pole).

manuscript submitted to *Global Biogeochemical Cycles*

Open Research

All of the RECCAP2 data will be made available in a public repository before publication.

Author contributions

- Conceptualization (Ideas; formulation or evolution of overarching research goals and aims): L.R., P.R.
- Data curation (Management activities to annotate (produce metadata), scrub data and maintain research data (including software code, where it is necessary for interpreting the data itself) for initial use and later re-use): A.K.H.,L.B., S.B., S.C.D., K.F., J.H., N.G., C.L.Q., E.L., I.D.L, J.D.M, C.N., L.R., J.S., R.S., K.T., H.T., D.B., T.T.T.C., M.G., A.K, P.L., G.G.L, A.R., C.R., T.W.
- Formal analysis (Application of statistical, mathematical, computational, or other formal techniques to analyse or synthesize study data): A.K.H., L.R.
- Funding acquisition (Acquisition of the financial support for the project leading to this publication): L.R.
- Investigation (Conducting a research and investigation process, specifically performing the experiments, or data/evidence collection): L.B., S.B., S.C.D., K.F., J.H., N.G., C.L.Q., E.L., I.D.L, J.D.M, C.N., L.R., J.S., R.S., K.T., H.T., D.W., D.B., T.T.T.C., M.G., A.K, P.L., G.G.L, A.R., C.R., T.W.
- Methodology (Development or design of methodology; creation of models): A.K.H., L.R., P.R.
- Project administration (Management and coordination responsibility for the research activity planning and execution): N.G., J.H., J.D.M., L.R., P.R.
- Software (Programming, software development; designing computer programs; implementation of the computer code and supporting algorithms; testing of existing code components): A.K.H., L.R.
- Supervision (Oversight and leadership responsibility for the research activity planning and execution, including mentorship external to the core team): L.R., P.R., N.G., J.H., J.D.M.
- Visualization (Preparation, creation and/or presentation of the published work, specifically visualization/data presentation): A.K.H., L.R.
- Writing – original draft (Preparation, creation and/or presentation of the published work, specifically writing the initial draft (including substantive translation)): L.R., P.R., H.W.B, D.B., T.W.
- Writing – review and editing (Preparation, creation and/or presentation of the published work by those from the original research group, specifically critical review, commentary or revision – including pre- or post-publication stages): All co-authors.

References

Anderson, L. G., Jutterström, S., Hjalmarsson, S., Wåhlström, I., & Semiletov, I. P. (2009, October). Out-gassing of CO $_2$ from Siberian Shelf seas by terrestrial organic matter decomposition. *Geophysical Research Letters*, *36*(20), L20601. Retrieved 2023-02-14, from `http://doi.wiley.com/10.1029/2009GL040046` doi: 10.1029/2009GL040046

Arias, P. A., Bellouin, N., Coppola, E., Jones, R. G., Krinner, G., Marotzke, J., ... Zickfeld, K. (2021). Technical Summary. In V. Masson-Delmotte et al. (Eds.), *Climate Change 2021: The Physical Science Basis. Contribution of Working Group I to the Sixth Assessment Report of the Intergovernmental Panel on Climate Change.* Cambridge, UK and New York, NY, USA: Cambridge University Press. Retrieved from `https://www.ipcc.ch/report/ar6/`

wg1/downloads/report/IPCC_AR6_WGI_TS.pdf (Type: Book Section) doi: 10.1017/9781009157896.002

Arndt, S., Jørgensen, B., LaRowe, D., Middelburg, J., Pancost, R., & Regnier, P. (2013, August). Quantifying the degradation of organic matter in marine sediments: A review and synthesis. *Earth-Science Reviews*, *123*, 53–86. Retrieved 2023-02-27, from https://linkinghub.elsevier.com/retrieve/pii/S0012825213000512 doi: 10.1016/j.earscirev.2013.02.008

Arrigo, K. R., van Dijken, G., & Long, M. (2008, November). Coastal Southern Ocean: A strong anthropogenic CO $_2$ sink. *Geophysical Research Letters*, *35*(21), L21602. Retrieved 2023-02-14, from http://doi.wiley.com/10.1029/2008GL035624 doi: 10.1029/2008GL035624

Arévalo-Martínez, D. L., Haroon, A., Bange, H. W., Erkul, E., Jegen, M., Moosdorf, N., ... Weymer, B. A. (2023, February). Ideas and perspectives: Land–ocean connectivity through groundwater. *Biogeosciences*, *20*(3), 647–662. Retrieved 2023-03-27, from https://bg.copernicus.org/articles/20/647/2023/ doi: 10.5194/bg-20-647-2023

Arévalo-Martínez, D. L., Kock, A., Löscher, C. R., Schmitz, R. A., & Bange, H. W. (2015, July). Massive nitrous oxide emissions from the tropical South Pacific Ocean. *Nature Geoscience*, *8*(7), 530–533. Retrieved 2023-02-14, from http://www.nature.com/articles/ngeo2469 doi: 10.1038/ngeo2469

Bakker, D. C. E., Alin, S. R., Becker, M., Bittig, H. C., Castaño-Primo, R., Feely, R. A., ... Wilson, D. (2022). *Surface Ocean CO2 Atlas Database Version 2022 (SOCATv2022) (NCEI Accession 0253659).* NOAA National Centers for Environmental Information. Retrieved 2023-02-14, from https://www.ncei.noaa.gov/archive/accession/0253659 (Type: dataset) doi: 10.25921/1H9F-NB73

Bakker, D. C. E., Pfeil, B., Landa, C. S., Metzl, N., O'Brien, K. M., Olsen, A., ... Xu, S. (2016, September). A multi-decade record of high-quality fCO_2 data in version 3 of the Surface Ocean CO_2 Atlas (SOCAT). *Earth System Science Data*, *8*(2), 383–413. Retrieved from https://www.earth-syst-sci-data.net/8/383/2016/ doi: https://doi.org/10.5194/essd-8-383-2016

Bakker, D. C. E., Pfeil, B., Smith, K., Hankin, S., Olsen, A., Alin, S. R., ... Watson, A. J. (2014, March). An update to the Surface Ocean CO₂ Atlas (SOCAT version 2). *Earth System Science Data*, *6*(1), 69–90. Retrieved 2023-03-23, from https://essd.copernicus.org/articles/6/69/2014/ doi: 10.5194/essd-6-69-2014

Bange, H. W. (2022, December). Non-CO2 greenhouse gases (N2O, CH4, CO) and the ocean. *One Earth*, *5*(12), 1316–1318. Retrieved 2023-02-14, from https://linkinghub.elsevier.com/retrieve/pii/S2590332222005875 doi: 10.1016/j.oneear.2022.11.011

Bange, H. W., Arévalo-Martínez, D. L., de la Paz, M., Farías, L., Kaiser, J., Kock, A., ... Wilson, S. T. (2019, April). A Harmonized Nitrous Oxide (N2O) Ocean Observation Network for the 21st Century. *Frontiers in Marine Science*, *6*, 157. Retrieved 2023-02-14, from https://www.frontiersin.org/article/10.3389/fmars.2019.00157/full doi: 10.3389/fmars.2019.00157

Bange, H. W., Rapsomanikis, S., & Andreae, M. O. (1996). Nitrous oxide in coastal waters. *Global Biogeochemical Cycles*, *10*(1), 197–207. Retrieved 2023-02-14, from https://onlinelibrary.wiley.com/doi/abs/10.1029/95GB03834 (_eprint: https://onlinelibrary.wiley.com/doi/pdf/10.1029/95GB03834) doi: 10.1029/95GB03834

Battin, T. J., Lauerwald, R., Bernhardt, E. S., Bertuzzo, E., Gener, L. G., Hall, R. O., ... Regnier, P. (2023, January). River ecosystem metabolism and carbon biogeochemistry in a changing world. *Nature*, *613*(7944), 449–459. Retrieved 2023-03-27, from https://www.nature.com/articles/s41586-022-05500-8 (Number: 7944 Publisher: Nature Publishing Group)

doi: 10.1038/s41586-022-05500-8

Bauer, J. E., Cai, W.-J., Raymond, P. A., Bianchi, T. S., Hopkinson, C. S., & Regnier, P. A. G. (2013, December). The changing carbon cycle of the coastal ocean. *Nature*, *504*(7478), 61–70. Retrieved 2016-01-12, from http://www.nature.com/nature/journal/v504/n7478/abs/nature12857.html doi: 10.1038/nature12857

Berthet, S., Jouanno, J., Séférian, R., Gehlen, M., & Llovel, W. (2022, August). How does the phytoplankton-light feedback affect marine N_2O inventory? *Earth Syst. Dynam. Discuss.*. Retrieved 2023-03-01, from https://esd.copernicus.org/preprints/esd-2022-28/ doi: 10.5194/esd-2022-28

Berthet, S., Séférian, R., Bricaud, C., Chevallier, M., Voldoire, A., & Ethé, C. (2019, June). Evaluation of an Online Grid-Coarsening Algorithm in a Global Eddy-Admitting Ocean Biogeochemical Model. *Journal of Advances in Modeling Earth Systems*, *11*(6), 1759–1783. Retrieved 2023-03-01, from https://onlinelibrary.wiley.com/doi/abs/10.1029/2019MS001644 doi: 10.1029/2019MS001644

Bopp, L., Lévy, M., Resplandy, L., & Sallée, J. B. (2015, August). Pathways of anthropogenic carbon subduction in the global ocean. *Geophysical Research Letters*, *42*(15), 2015GL065073. Retrieved 2015-09-14, from http://onlinelibrary.wiley.com/doi/10.1002/2015GL065073/abstract doi: 10.1002/2015GL065073

Bourgeois, T., Orr, J. C., Resplandy, L., Terhaar, J., Ethé, C., Gehlen, M., & Bopp, L. (2016, July). Coastal-ocean uptake of anthropogenic carbon. *Biogeosciences*, *13*(14), 4167–4185. Retrieved 2016-09-23, from http://www.biogeosciences.net/13/4167/2016/ doi: 10.5194/bg-13-4167-2016

Boutin, J., Quilfen, Y., Merlivat, L., & Piolle, J. F. (2009, April). Global average of air-sea CO_2 transfer velocity from QuikSCAT scatterometer wind speeds. *Journal of Geophysical Research*, *114*(C4), C04007. Retrieved 2023-03-22, from http://doi.wiley.com/10.1029/2007JC004168 doi: 10.1029/2007JC004168

Buitenhuis, E. T., Suntharalingam, P., & Le Quéré, C. (2018, April). Constraints on global oceanic emissions of N2O from observations and models. *Biogeosciences*, *15*(7), 2161–2175. Retrieved 2023-02-07, from https://bg.copernicus.org/articles/15/2161/2018/ (Publisher: Copernicus GmbH) doi: 10.5194/bg-15-2161-2018

Cahill, B., Wilkin, J., Fennel, K., Vandemark, D., & Friedrichs, M. A. M. (2016, February). Interannual and seasonal variabilities in air-sea CO_2 fluxes along the U.S. eastern continental shelf and their sensitivity to increasing air temperatures and variable winds: U.S. East Coast Shelf Air-Sea CO_2 Fluxes. *Journal of Geophysical Research: Biogeosciences*, *121*(2), 295–311. Retrieved 2023-03-23, from http://doi.wiley.com/10.1002/2015JG002939 doi: 10.1002/2015JG002939

Cai, W., Yang, K., Wu, L., Huang, G., Santoso, A., Ng, B., ... Yamagata, T. (2021, January). Opposite response of strong and moderate positive Indian Ocean Dipole to global warming. *Nature Climate Change*, *11*(1), 27–32. Retrieved 2022-01-28, from http://www.nature.com/articles/s41558-020-00943-1 doi: 10.1038/s41558-020-00943-1

Cai, W.-J., Dai, M., & Wang, Y. (2006). Air-sea exchange of carbon dioxide in ocean margins: A province-based synthesis. *Geophysical Research Letters*, *33*(12), L12603. Retrieved 2021-09-03, from http://doi.wiley.com/10.1029/2006GL026219 doi: 10.1029/2006GL026219

Cao, Z., Yang, W., Zhao, Y., Guo, X., Yin, Z., Du, C., ... Dai, M. (2020, April). Diagnosis of CO2 dynamics and fluxes in global coastal oceans. *National Science Review*, *7*(4), 786–797. Retrieved 2021-09-03, from https://academic.oup.com/nsr/article/7/4/786/5542784 doi:

10.1093/nsr/nwz105

Carroll, D., Menemenlis, D., Adkins, J. F., Bowman, K. W., Brix, H., Dutkiewicz, S., ... Zhang, H. (2020, October). The ECCO-Darwin Data-Assimilative Global Ocean Biogeochemistry Model: Estimates of Seasonal to Multidecadal Surface Ocean p CO $_2$ and Air-Sea CO $_2$ Flux. *Journal of Advances in Modeling Earth Systems*, *12*(10). Retrieved 2023-02-15, from https://onlinelibrary.wiley.com/doi/10.1029/2019MS001888 doi: 10.1029/2019MS001888

Chau, T. T. T., Gehlen, M., & Chevallier, F. (2022, February). A seamless ensemble-based reconstruction of surface ocean pCO2and air–sea CO2 fluxes over the global coastal and open oceans. *Biogeosciences*, *19*(4), 1087–1109. Retrieved 2023-02-15, from https://bg.copernicus.org/articles/19/1087/2022/ doi: 10.5194/bg-19-1087-2022

Chen, C.-T. A., & Borges, A. V. (2009, April). Reconciling opposing views on carbon cycling in the coastal ocean: Continental shelves as sinks and near-shore ecosystems as sources of atmospheric CO2. *Deep Sea Research Part II: Topical Studies in Oceanography*, *56*(8-10), 578–590. Retrieved 2021-09-03, from https://linkinghub.elsevier.com/retrieve/pii/S0967064509000162 doi: 10.1016/j.dsr2.2009.01.001

Chen, C.-T. A., Huang, T.-H., Chen, Y.-C., Bai, Y., He, X., & Kang, Y. (2013, October). Air–sea exchanges of CO2 in the world's coastal seas. *Biogeosciences*, *10*(10), 6509–6544. Retrieved 2021-09-03, from https://bg.copernicus.org/articles/10/6509/2013/ doi: 10.5194/bg-10-6509-2013

Cossarini, G., Querin, S., & Solidoro, C. (2015, October). The continental shelf carbon pump in the northern Adriatic Sea (Mediterranean Sea): Influence of wintertime variability. *Ecological Modelling*, *314*, 118–134. Retrieved 2023-03-23, from https://linkinghub.elsevier.com/retrieve/pii/S0304380015003300 doi: 10.1016/j.ecolmodel.2015.07.024

Dai, M., Cao, Z., Guo, X., Zhai, W., Liu, Z., Yin, Z., ... Du, C. (2013). Why are some marginal seas sources of atmospheric CO2? *Geophysical Research Letters*, *40*(10), 2154–2158. Retrieved 2022-04-26, from https://onlinelibrary.wiley.com/doi/abs/10.1002/grl.50390 (_eprint: https://onlinelibrary.wiley.com/doi/pdf/10.1002/grl.50390) doi: 10.1002/grl.50390

Dai, M., Su, J., Zhao, Y., Hofmann, E. E., Cao, Z., Cai, W.-J., ... Wang, Z. (2022). Carbon Fluxes in the Coastal Ocean: Synthesis, Boundary Processes, and Future Trends. *Annual Review of Earth and Planetary Sciences*, *50*(1), 593–626. Retrieved 2022-09-26, from https://doi.org/10.1146/annurev-earth-032320-090746 (_eprint: https://doi.org/10.1146/annurev-earth-032320-090746) doi: 10.1146/annurev-earth-032320-090746

Damien, P., Bianchi, D., McWilliams, J. C., Kessouri, F., Deutsch, C., Chen, R., & Renault, L. (2023). Enhanced Biogeochemical Cycling Along the U.S. West Coast Shelf. *Global Biogeochemical Cycles*, *37*(1), e2022GB007572. Retrieved 2023-02-14, from https://onlinelibrary.wiley.com/doi/abs/10.1029/2022GB007572 (_eprint: https://onlinelibrary.wiley.com/doi/pdf/10.1029/2022GB007572) doi: 10.1029/2022GB007572

Deike, L., & Melville, W. K. (2018). Gas Transfer by Breaking Waves. *Geophysical Research Letters*, *45*(19), 10,482–10,492. Retrieved 2021-11-15, from https://onlinelibrary.wiley.com/doi/abs/10.1029/2018GL078758 (_eprint: https://onlinelibrary.wiley.com/doi/pdf/10.1029/2018GL078758) doi: 10.1029/2018GL078758

Desmet, F., Gruber, N., Köhn, E. E., Münnich, M., & Vogt, M. (2022, May). Tracking the Space-Time Evolution of Ocean Acidification Extremes in the California Current System and Northeast Pacific. *Journal of Geophysical Research:*

Oceans, *127*(5). Retrieved 2023-03-27, from https://onlinelibrary.wiley.com/doi/10.1029/2021JC018159 doi: 10.1029/2021JC018159

Doney, S. C., Lima, I., Feely, R. A., Glover, D. M., Lindsay, K., Mahowald, N., ... Wanninkhof, R. (2009, April). Mechanisms governing interannual variability in upper-ocean inorganic carbon system and air–sea CO2 fluxes: Physical climate and atmospheric dust. *Deep Sea Research Part II: Topical Studies in Oceanography*, *56*(8-10), 640–655. Retrieved 2018-09-13, from http://linkinghub.elsevier.com/retrieve/pii/S096706450800427X doi: 10.1016/j.dsr2.2008.12.006

Egger, M., Lenstra, W., Jong, D., Meysman, F. J. R., Sapart, C. J., van der Veen, C., ... Slomp, C. P. (2016, August). Rapid Sediment Accumulation Results in High Methane Effluxes from Coastal Sediments. *PLoS ONE*, *11*(8), e0161609. Retrieved 2023-03-22, from https://www.ncbi.nlm.nih.gov/pmc/articles/PMC4999275/ doi: 10.1371/journal.pone.0161609

Elsig, J., Schmitt, J., Leuenberger, D., Schneider, R., Eyer, M., Leuenberger, M., ... Stocker, T. F. (2009, September). Stable isotope constraints on Holocene carbon cycle changes from an Antarctic ice core. *Nature*, *461*(7263), 507–510. Retrieved 2023-03-27, from https://www.nature.com/articles/nature08393 (Number: 7263 Publisher: Nature Publishing Group) doi: 10.1038/nature08393

Etiope, G., Ciotoli, G., Schwietzke, S., & Schoell, M. (2019, January). Gridded maps of geological methane emissions and their isotopic signature. *Earth System Science Data*, *11*(1), 1–22. Retrieved 2023-03-27, from https://essd.copernicus.org/articles/11/1/2019/ (Publisher: Copernicus GmbH) doi: 10.5194/essd-11-1-2019

Fennel, K., Alin, S., Barbero, L., Evans, W., Bourgeois, T., Cooley, S., ... Wang, Z. A. (2019, March). Carbon cycling in the North American coastal ocean: a synthesis. *Biogeosciences*, *16*(6), 1281–1304. Retrieved 2023-02-14, from https://bg.copernicus.org/articles/16/1281/2019/ doi: 10.5194/bg-16-1281-2019

Fennel, K., & Testa, J. M. (2019, January). Biogeochemical Controls on Coastal Hypoxia. *Annual Review of Marine Science*, *11*(1), 105–130. Retrieved 2020-09-08, from http://www.annualreviews.org/doi/10.1146/annurev-marine-010318-095138 (Publisher: Annual Reviews) doi: 10.1146/annurev-marine-010318-095138

Fennel, K., & Wilkin, J. (2009, September). Quantifying biological carbon export for the northwest North Atlantic continental shelves. *Geophysical Research Letters*, *36*(18), L18605. Retrieved 2023-02-15, from http://doi.wiley.com/10.1029/2009GL039818 doi: 10.1029/2009GL039818

Fiechter, J., Curchitser, E. N., Edwards, C. A., Chai, F., Goebel, N. L., & Chavez, F. P. (2014). Air-sea CO2 fluxes in the California Current: Impacts of model resolution and coastal topography. *Global Biogeochemical Cycles*, *28*(4), 371–385. Retrieved 2023-02-28, from https://onlinelibrary.wiley.com/doi/abs/10.1002/2013GB004683 (_eprint: https://onlinelibrary.wiley.com/doi/pdf/10.1002/2013GB004683) doi: 10.1002/2013GB004683

Friedlingstein, P., O'Sullivan, M., Jones, M. W., Andrew, R. M., Gregor, L., Hauck, J., ... Zheng, B. (2022). Global Carbon Budget 2022. *Earth System Science Data*, *14*(11), 4811–4900. Retrieved from https://essd.copernicus.org/articles/14/4811/2022/ doi: 10.5194/essd-14-4811-2022

Ganesan, A. L., Manizza, M., Morgan, E. J., Harth, C. M., Kozlova, E., Lueker, T., ... Rigby, M. (2020, July). Marine Nitrous Oxide Emissions From Three Eastern Boundary Upwelling Systems Inferred From Atmospheric Observations. *Geophysical Research Letters*, *47*(14). Retrieved 2023-02-15, from https://onlinelibrary.wiley.com/doi/10.1029/2020GL087822 doi:

10.1029/2020GL087822

Gao, S., Schwinger, J., Tjiputra, J., Bethke, I., Hartmann, J., Mayorga, E., & Heinze, C. (2023, January). Riverine impact on future projections of marine primary production and carbon uptake. *Biogeosciences*, *20*(1), 93–119. Retrieved 2023-02-23, from https://bg.copernicus.org/articles/20/93/2023/ (Publisher: Copernicus GmbH) doi: 10.5194/bg-20-93-2023

Garbe, C. S., Rutgersson, A., Boutin, J., de Leeuw, G., Delille, B., Fairall, C. W., ... Zappa, C. J. (2014). Transfer Across the Air-Sea Interface. In P. S. Liss & M. T. Johnson (Eds.), *Ocean-Atmosphere Interactions of Gases and Particles* (pp. 55–112). Berlin, Heidelberg: Springer. Retrieved 2023-02-14, from https://doi.org/10.1007/978-3-642-25643-1_2 doi: 10.1007/978-3-642-25643-1_2

Gomez, F. A., Wanninkhof, R., Barbero, L., Lee, S.-K., & Hernandez Jr., F. J. (2020, March). Seasonal patterns of surface inorganic carbon system variables in the Gulf of Mexico inferred from a regional high-resolution ocean biogeochemical model. *Biogeosciences*, *17*(6), 1685–1700. Retrieved 2023-02-14, from https://bg.copernicus.org/articles/17/1685/2020/ doi: 10.5194/bg-17-1685-2020

Grundle, D. S., Löscher, C. R., Krahmann, G., Altabet, M. A., Bange, H. W., Karstensen, J., ... Fiedler, B. (2017, July). Low oxygen eddies in the eastern tropical North Atlantic: Implications for N2O cycling. *Scientific Reports*, *7*(1), 4806. Retrieved 2023-02-14, from https://www.nature.com/articles/s41598-017-04745-y doi: 10.1038/s41598-017-04745-y

Gustafsson, E., Hagens, M., Sun, X., Reed, D. C., Humborg, C., Slomp, C. P., & Gustafsson, B. G. (2019, January). Sedimentary alkalinity generation and long-term alkalinity development in the Baltic Sea. *Biogeosciences*, *16*(2), 437–456. Retrieved 2023-02-14, from https://bg.copernicus.org/articles/16/437/2019/ doi: 10.5194/bg-16-437-2019

Gutiérrez-Loza, L., Nilsson, E., Wallin, M. B., Sahlée, E., & Rutgersson, A. (2022, December). On physical mechanisms enhancing air–sea CO_2 exchange. *Biogeosciences*, *19*(24), 5645–5665. Retrieved 2023-03-22, from https://bg.copernicus.org/articles/19/5645/2022/ doi: 10.5194/bg-19-5645-2022

Gülzow, W., Rehder, G., Schneider v. Deimling, J., Seifert, T., & Tóth, Z. (2013, January). One year of continuous measurements constraining methane emissions from the Baltic Sea to the atmosphere using a ship of opportunity. *Biogeosciences*, *10*(1), 81–99. Retrieved 2023-02-14, from https://bg.copernicus.org/articles/10/81/2013/ doi: 10.5194/bg-10-81-2013

Hauck, J., Zeising, M., Le Quéré, C., Gruber, N., Bakker, D. C. E., Bopp, L., ... Séférian, R. (2020). Consistency and Challenges in the Ocean Carbon Sink Estimate for the Global Carbon Budget. *Frontiers in Marine Science*, *7*. Retrieved 2020-12-18, from https://www.frontiersin.org/articles/10.3389/fmars.2020.571720/full (Publisher: Frontiers) doi: 10.3389/fmars.2020.571720

Hauri, C., Pagès, R., McDonnell, A. M. P., Stuecker, M. F., Danielson, S. L., Hedstrom, K., ... Doney, S. C. (2021, September). Modulation of ocean acidification by decadal climate variability in the Gulf of Alaska. *Communications Earth & Environment*, *2*(1), 191. Retrieved 2023-02-14, from https://www.nature.com/articles/s43247-021-00254-z doi: 10.1038/s43247-021-00254-z

Hilt, S., Grossart, H., McGinnis, D. F., & Keppler, F. (2022, November). Potential role of submerged macrophytes for oxic methane production in aquatic ecosystems. *Limnology and Oceanography*, *67*(S2). Retrieved 2023-02-20, from https://onlinelibrary.wiley.com/doi/10.1002/lno.12095 doi: 10.1002/lno.12095

Ho, D. T., Law, C. S., Smith, M. J., Schlosser, P., Harvey, M., & Hill, P. (2006). Measurements of air-sea gas exchange at high wind speeds in the Southern Ocean: Implications for global parameterizations. *Geophysical Research Letters*, *33*(16). Retrieved 2019-06-25, from https://agupubs.onlinelibrary.wiley.com/doi/abs/10.1029/2006GL026817 doi: 10.1029/2006GL026817

Ho, D. T., Wanninkhof, R., Schlosser, P., Ullman, D. S., Hebert, D., & Sullivan, K. F. (2011, July). Toward a universal relationship between wind speed and gas exchange: Gas transfer velocities measured with ^{3}He/SF$_6$ during the Southern Ocean Gas Exchange Experiment. *Journal of Geophysical Research*, *116*, C00F04. Retrieved 2023-02-15, from http://doi.wiley.com/10.1029/2010JC006854 doi: 10.1029/2010JC006854

Hovland, M., Judd, A., & Burke, R. (1993, January). The global flux of methane from shallow submarine sediments. *Chemosphere*, *26*(1-4), 559–578. Retrieved 2023-02-23, from https://linkinghub.elsevier.com/retrieve/pii/0045653593904428 doi: 10.1016/0045-6535(93)90442-8

Ilyina, T., Six, K. D., Segschneider, J., Maier-Reimer, E., Li, H., & Núñez-Riboni, I. (2013, June). Global ocean biogeochemistry model HAMOCC: Model architecture and performance as component of the MPI-Earth system model in different CMIP5 experimental realizations. *Journal of Advances in Modeling Earth Systems*, *5*(2), 287–315. Retrieved 2023-02-15, from https://onlinelibrary.wiley.com/doi/10.1029/2012MS000178 doi: 10.1029/2012MS000178

Joung, D., Leonte, M., Valentine, D. L., Sparrow, K. J., Weber, T., & Kessler, J. D. (2020, October). Radiocarbon in Marine Methane Reveals Patchy Impact of Seeps on Surface Waters. *Geophysical Research Letters*, *47*(20). Retrieved 2023-03-27, from https://onlinelibrary.wiley.com/doi/10.1029/2020GL089516 doi: 10.1029/2020GL089516

Joung, D., Ruppel, C., Southon, J., Weber, T. S., & Kessler, J. D. (2022, November). Negligible atmospheric release of methane from decomposing hydrates in mid-latitude oceans. *Nature Geoscience*, *15*(11), 885–891. Retrieved 2023-03-27, from https://www.nature.com/articles/s41561-022-01044-8 doi: 10.1038/s41561-022-01044-8

Karl, D. M., Beversdorf, L., Björkman, K. M., Church, M. J., Martinez, A., & Delong, E. F. (2008, July). Aerobic production of methane in the sea. *Nature Geoscience*, *1*(7), 473–478. Retrieved 2023-03-27, from https://www.nature.com/articles/ngeo234 (Number: 7 Publisher: Nature Publishing Group) doi: 10.1038/ngeo234

Kock, A., & Bange, H. (2015, February). Counting the Ocean's Greenhouse Gas Emissions. *Eos*, *96*. Retrieved 2023-02-14, from https://eos.org/project-updates/counting-oceans-greenhouse-gas-emissions doi: 10.1029/2015EO023665

Kock, A., Schafstall, J., Dengler, M., Brandt, P., & Bange, H. W. (2012, March). Sea-to-air and diapycnal nitrous oxide fluxes in the eastern tropical North Atlantic Ocean. *Biogeosciences*, *9*(3), 957–964. Retrieved 2023-02-14, from https://bg.copernicus.org/articles/9/957/2012/ (Publisher: Copernicus GmbH) doi: 10.5194/bg-9-957-2012

Lachkar, Z., & Gruber, N. (2013, January). Response of biological production and air–sea CO2 fluxes to upwelling intensification in the California and Canary Current Systems. *Journal of Marine Systems*, *109-110*, 149–160. Retrieved 2023-02-15, from https://www.sciencedirect.com/science/article/pii/S092479631200108X doi: 10.1016/j.jmarsys.2012.04.003

Lachkar, Z., Mehari, M., Al Azhar, M., Lévy, M., & Smith, S. (2021, October). Fast local warming is the main driver of recent deoxygenation in the northern Arabian Sea. *Biogeosciences*, *18*(20), 5831–5849. Retrieved 2023-02-15, from https://bg.copernicus.org/articles/18/5831/2021/ doi:

10.5194/bg-18-5831-2021

Lacroix, F., Ilyina, T., & Hartmann, J. (2020, January). Oceanic CO_2 outgassing and biological production hotspots induced by pre-industrial river loads of nutrients and carbon in a global modeling approach. *Biogeosciences*, *17*(1), 55–88. Retrieved 2020-05-05, from https://www.biogeosciences.net/17/55/2020/ doi: https://doi.org/10.5194/bg-17-55-2020

Lacroix, F., Ilyina, T., Laruelle, G. G., & Regnier, P. (2021). Reconstructing the Preindustrial Coastal Carbon Cycle Through a Global Ocean Circulation Model: Was the Global Continental Shelf Already Both Autotrophic and a CO2 Sink? *Global Biogeochemical Cycles*, *35*(2), e2020GB006603. Retrieved 2021-09-03, from https://agupubs.onlinelibrary.wiley.com/doi/abs/10.1029/2020GB006603 doi: 10.1029/2020GB006603

Landschützer, P., Gruber, N., Bakker, D. C. E., & Schuster, U. (2014, September). Recent variability of the global ocean carbon sink. *Global Biogeochemical Cycles*, *28*(9), 927–949. Retrieved 2015-08-11, from http://onlinelibrary.wiley.com/doi/10.1002/2014GB004853/abstract doi: 10.1002/2014GB004853

Landschützer, P., Laruelle, G. G., Roobaert, A., & Regnier, P. (2020, October). A uniform pCO2 climatology combining open and coastal oceans. *Earth System Science Data*, *12*(4), 2537–2553. Retrieved 2023-02-14, from https://essd.copernicus.org/articles/12/2537/2020/ doi: 10.5194/essd-12-2537-2020

Laruelle, G. G., Cai, W.-J., Hu, X., Gruber, N., Mackenzie, F. T., & Regnier, P. (2018, January). Continental shelves as a variable but increasing global sink for atmospheric carbon dioxide. *Nature Communications*, *9*, 454. Retrieved 2021-09-03, from https://www.ncbi.nlm.nih.gov/pmc/articles/PMC5792465/ doi: 10.1038/s41467-017-02738-z

Laruelle, G. G., Dürr, H. H., Lauerwald, R., Hartmann, J., Slomp, C. P., Goossens, N., & Regnier, P. A. G. (2013, May). Global multi-scale segmentation of continental and coastal waters from the watersheds to the continental margins. *Hydrology and Earth System Sciences*, *17*(5), 2029–2051. Retrieved 2020-03-27, from https://www.hydrol-earth-syst-sci.net/17/2029/2013/ doi: 10.5194/hess-17-2029-2013

Laruelle, G. G., Dürr, H. H., Slomp, C. P., & Borges, A. V. (2010). Evaluation of sinks and sources of CO2 in the global coastal ocean using a spatially-explicit typology of estuaries and continental shelves. *Geophysical Research Letters*, *37*(15). Retrieved 2021-09-03, from https://agupubs.onlinelibrary.wiley.com/doi/abs/10.1029/2010GL043691 (_eprint: https://agupubs.onlinelibrary.wiley.com/doi/pdf/10.1029/2010GL043691) doi: 10.1029/2010GL043691

Laruelle, G. G., Landschützer, P., Gruber, N., Tison, J.-L., Delille, B., & Regnier, P. (2017, October). Global high-resolution monthly pCO2 climatology for the coastal ocean derived from neural network interpolation. *Biogeosciences*, *14*(19), 4545–4561. Retrieved 2019-08-29, from https://www.biogeosciences.net/14/4545/2017/ doi: 10.5194/bg-14-4545-2017

Laruelle, G. G., Lauerwald, R., Pfeil, B., & Regnier, P. (2014). Regionalized global budget of the CO2 exchange at the air-water interface in continental shelf seas. *Global Biogeochemical Cycles*, *28*(11), 1199–1214. Retrieved 2021-09-03, from https://agupubs.onlinelibrary.wiley.com/doi/abs/10.1002/2014GB004832 doi: 10.1002/2014GB004832

Laruelle, G. G., Lauerwald, R., Rotschi, J., Raymond, P. A., Hartmann, J., & Regnier, P. (2015, March). Seasonal response of air–water CO₂ exchange along the land–ocean aquatic continuum of the northeast North American coast. *Biogeosciences*, *12*(5), 1447–1458. Retrieved 2023-02-14, from https://bg.copernicus.org/articles/12/1447/

2015/ doi: 10.5194/bg-12-1447-2015

Laurent, A., Fennel, K., Cai, W., Huang, W., Barbero, L., & Wanninkhof, R. (2017, January). Eutrophication-induced acidification of coastal waters in the northern Gulf of Mexico: Insights into origin and processes from a coupled physical-biogeochemical model. *Geophysical Research Letters*, *44*(2), 946–956. Retrieved 2023-02-15, from https://onlinelibrary.wiley.com/doi/abs/10.1002/2016GL071881 doi: 10.1002/2016GL071881

Laurent, A., Fennel, K., & Kuhn, A. (2021, March). An observation-based evaluation and ranking of historical Earth system model simulations in the northwest North Atlantic Ocean. *Biogeosciences*, *18*(5), 1803–1822. Retrieved 2023-02-15, from https://bg.copernicus.org/articles/18/1803/2021/ doi: 10.5194/bg-18-1803-2021

Legge, O., Johnson, M., Hicks, N., Jickells, T., Diesing, M., Aldridge, J., ... Williamson, P. (2020, March). Carbon on the Northwest European Shelf: Contemporary Budget and Future Influences. *Frontiers in Marine Science*, *7*, 143. Retrieved 2023-02-14, from https://www.frontiersin.org/article/10.3389/fmars.2020.00143 doi: 10.3389/fmars.2020.00143

Le Quéré, C. L., Andrew, R. M., Friedlingstein, P., Sitch, S., Pongratz, J., Manning, A. C., ... Zhu, D. (2018, March). Global Carbon Budget 2017. *Earth System Science Data*, *10*(1), 405–448. Retrieved 2018-03-21, from https://www.earth-syst-sci-data.net/10/405/2018/ doi: https://doi.org/10.5194/essd-10-405-2018

Liang, J.-H., Deutsch, C., McWilliams, J. C., Baschek, B., Sullivan, P. P., & Chiba, D. (2013). Parameterizing bubble-mediated air-sea gas exchange and its effect on ocean ventilation. *Global Biogeochemical Cycles*, *27*(3), 894–905. Retrieved 2023-02-14, from https://onlinelibrary.wiley.com/doi/abs/10.1002/gbc.20080 doi: 10.1002/gbc.20080

Liao, E., Resplandy, L., Liu, J., & Bowman, K. W. (2020). Amplification of the Ocean Carbon Sink During El Niños: Role of Poleward Ekman Transport and Influence on Atmospheric CO2. *Global Biogeochemical Cycles*, *34*(9), e2020GB006574. Retrieved 2020-10-15, from http://agupubs.onlinelibrary.wiley.com/doi/abs/10.1029/2020GB006574 doi: 10.1029/2020GB006574

Liu, Q., Guo, X., Yin, Z., Zhou, K., Roberts, E. G., & Dai, M. (2018, November). Carbon fluxes in the China Seas: An overview and perspective. *Science China Earth Sciences*, *61*(11), 1564–1582. Retrieved 2023-02-14, from http://link.springer.com/10.1007/s11430-017-9267-4 doi: 10.1007/s11430-017-9267-4

Louchard, D., Gruber, N., & Münnich, M. (2021). The Impact of the Amazon on the Biological Pump and the Air-Sea CO2 Balance of the Western Tropical Atlantic. *Global Biogeochemical Cycles*, *35*(6), e2020GB006818. Retrieved 2021-09-22, from https://onlinelibrary.wiley.com/doi/abs/10.1029/2020GB006818 doi: 10.1029/2020GB006818

Mackenzie, F., Lerman, A., & Ver, L. (1998, May). Role of the continental margin in the global carbon balance during the past three centuries. *Geology*, *26*. doi: 10.1130/0091-7613(1998)026⟨0423:ROTCMI⟩2.3.CO;2

Mackenzie, F. T., Andersson, A. J., Lerman, A., & Ver, L. M. (2005). Boundary Exchanges in the Global Coastal Margin: Implications for the Organic and Inorganic Carbon Cycles. In *The Sea vol. 13* (pp. 193–225). (Eds Robinson, A. R. & Brink, K. H.) Harvard Univ. Press.

Manizza, M., Menemenlis, D., Zhang, H., & Miller, C. E. (2019). Modeling the Recent Changes in the Arctic Ocean CO $_2$ Sink (2006–2013). *Global Biogeochemical Cycles*, *33*(3), 420–438. Retrieved 2023-02-15, from https://onlinelibrary.wiley.com/doi/abs/10.1029/2018GB006070 doi: 10.1029/2018GB006070

Mao, S.-H., Zhang, H.-H., Zhuang, G.-C., Li, X.-J., Liu, Q., Zhou, Z., ... Yang, G.-

P. (2022, November). Aerobic oxidation of methane significantly reduces global diffusive methane emissions from shallow marine waters. *Nature Communications*, *13*(1), 7309. doi: 10.1038/s41467-022-35082-y

Mathis, M., Logemann, K., Maerz, J., Lacroix, F., Hagemann, S., Chegini, F., ... Schrum, C. (2022). Seamless integration of the coastal ocean in global marine carbon cycle modeling. *Journal of Advances in Modeling Earth Systems*, *n/a*(n/a), e2021MS002789. Retrieved 2022-08-22, from https://onlinelibrary.wiley.com/doi/abs/10.1029/2021MS002789 doi: 10.1029/2021MS002789

Mayer, B., Rixen, T., & Pohlmann, T. (2018). The Spatial and Temporal Variability of Air-Sea CO2 Fluxes and the Effect of Net Coral Reef Calcification in the Indonesian Seas: A Numerical Sensitivity Study. *Frontiers in Marine Science*, *5*. Retrieved 2023-02-14, from https://www.frontiersin.org/articles/10.3389/fmars.2018.00116

McGinnis, D. F., Greinert, J., Artemov, Y., Beaubien, S. E., & Wüest, A. (2006). Fate of rising methane bubbles in stratified waters: How much methane reaches the atmosphere? *Journal of Geophysical Research*, *111*(C9), C09007. Retrieved 2023-02-23, from http://doi.wiley.com/10.1029/2005JC003183 doi: 10.1029/2005JC003183

Neumann, T., Radtke, H., Cahill, B., Schmidt, M., & Rehder, G. (2022, November). Non-Redfieldian carbon model for the Baltic Sea (ERGOM version 1.2) – implementation and budget estimates. *Geoscientific Model Development*, *15*(22), 8473–8540. Retrieved 2023-02-14, from https://gmd.copernicus.org/articles/15/8473/2022/ doi: 10.5194/gmd-15-8473-2022

Nightingale, P. D., Malin, G., Law, C. S., Watson, A. J., Liss, P. S., Liddicoat, M. I., ... Upstill-Goddard, R. C. (2000, March). In situ evaluation of air-sea gas exchange parameterizations using novel conservative and volatile tracers. *Global Biogeochemical Cycles*, *14*(1), 373–387. Retrieved 2023-02-15, from http://doi.wiley.com/10.1029/1999GB900091 doi: 10.1029/1999GB900091

Ouyang, Z., Collins, A., Li, Y., Qi, D., Arrigo, K. R., Zhuang, Y., ... Cai, W. (2022, August). Seasonal Water Mass Evolution and Non-Redfield Dynamics Enhance CO $_2$ Uptake in the Chukchi Sea. *Journal of Geophysical Research: Oceans*, *127*(8). Retrieved 2023-02-14, from https://onlinelibrary.wiley.com/doi/10.1029/2021JC018326 doi: 10.1029/2021JC018326

Ouyang, Z., Sciusco, P., Jiao, T., Feron, S., Lei, C., Li, F., ... Chen, J. (2022, July). Albedo changes caused by future urbanization contribute to global warming. *Nature Communications*, *13*(1), 3800. Retrieved 2022-10-27, from https://www.nature.com/articles/s41467-022-31558-z (Number: 1 Publisher: Nature Publishing Group) doi: 10.1038/s41467-022-31558-z

Pereira, R., Ashton, I., Sabbaghzadeh, B., Shutler, J. D., & Upstill-Goddard, R. C. (2018, July). Reduced air–sea CO2 exchange in the Atlantic Ocean due to biological surfactants. *Nature Geoscience*, *11*(7), 492–496. Retrieved 2023-03-22, from http://www.nature.com/articles/s41561-018-0136-2 doi: 10.1038/s41561-018-0136-2

Pipko, I. I., Pugach, S. P., Luchin, V. A., Francis, O. P., Savelieva, N. I., Charkin, A. N., ... Semiletov, I. P. (2021, March). Surface CO2 system dynamics in the Gulf of Anadyr during the open water season. *Continental Shelf Research*, *217*, 104371. Retrieved 2023-02-14, from https://www.sciencedirect.com/science/article/pii/S0278434321000285 doi: 10.1016/j.csr.2021.104371

Pipko, I. I., Pugach, S. P., Semiletov, I. P., Anderson, L. G., Shakhova, N. E., Gustafsson, , ... Dudarev, O. V. (2017, November). The spatial and interannual dynamics of the surface water carbonate system and air–sea CO₂ fluxes in the outer shelf and slope of the Eurasian Arctic Ocean. *Ocean Science*, *13*(6), 997–1016. Retrieved 2023-

02-14, from https://os.copernicus.org/articles/13/997/2017/ doi: 10.5194/os-13-997-2017

Previdi, M., Fennel, K., Wilkin, J., & Haidvogel, D. (2009, October). Interannual variability in atmospheric CO 2 uptake on the northeast U.S. continental shelf. *Journal of Geophysical Research*, *114*(G4), G04003. Retrieved 2023-03-23, from http://doi.wiley.com/10.1029/2008JG000881 doi: 10.1029/2008JG000881

Puglini, M., Brovkin, V., Regnier, P., & Arndt, S. (2020, June). Assessing the potential for non-turbulent methane escape from the East Siberian Arctic Shelf. *Biogeosciences*, *17*(12), 3247–3275. Retrieved 2023-02-27, from https://bg.copernicus.org/articles/17/3247/2020/ doi: 10.5194/bg-17-3247-2020

Reeburgh, W. S. (2007, February). Oceanic Methane Biogeochemistry. *Chemical Reviews*, *107*(2), 486–513. Retrieved 2023-03-27, from https://pubs.acs.org/doi/10.1021/cr050362v doi: 10.1021/cr050362v

Rees, A. P., Bange, H. W., Arévalo-Martínez, D. L., Artioli, Y., Ashby, D. M., Brown, I., ... Turley, C. (2022, February). Nitrous oxide and methane in a changing Arctic Ocean. *Ambio*, *51*(2), 398–410. Retrieved 2023-03-22, from https://www.ncbi.nlm.nih.gov/pmc/articles/PMC8692636/ doi: 10.1007/s13280-021-01633-8

Regnier, P., Friedlingstein, P., Ciais, P., Mackenzie, F. T., Gruber, N., Janssens, I. A., ... Thullner, M. (2013, June). Anthropogenic perturbation of the carbon fluxes from land to ocean. *Nature Geoscience*, *6*(8), 597–607. Retrieved 2015-06-25, from http://www.nature.com/doifinder/10.1038/ngeo1830 doi: 10.1038/ngeo1830

Regnier, P., Resplandy, L., Najjar, R. G., & Ciais, P. (2022, March). The land-to-ocean loops of the global carbon cycle. *Nature*, *603*(7901), 401–410. Retrieved 2022-04-18, from https://www.nature.com/articles/s41586-021-04339-9 doi: 10.1038/s41586-021-04339-9

Rehder, G., Keir, R. S., Suess, E., & Pohlmann, T. (1998, September). The Multiple Sources and Patterns of Methane in North Sea Waters. *Aquatic Geochemistry*, *4*(3), 403–427. Retrieved 2023-02-14, from https://doi.org/10.1023/A:1009644600833 doi: 10.1023/A:1009644600833

Reichl, B. G., & Deike, L. (2020). Contribution of Sea-State Dependent Bubbles to Air-Sea Carbon Dioxide Fluxes. *Geophysical Research Letters*, *47*(9), e2020GL087267. Retrieved 2021-10-08, from https://onlinelibrary.wiley.com/doi/abs/10.1029/2020GL087267 (_eprint: https://onlinelibrary.wiley.com/doi/pdf/10.1029/2020GL087267) doi: 10.1029/2020GL087267

Reimer, J. J., Wang, H., Vargas, R., & Cai, W. (2017, December). Multidecadal *f* CO 2 Increase Along the United States Southeast Coastal Margin. *Journal of Geophysical Research: Oceans*, *122*(12), 10061–10072. Retrieved 2023-03-23, from https://onlinelibrary.wiley.com/doi/10.1002/2017JC013170 doi: 10.1002/2017JC013170

Repeta, D. J., Ferrón, S., Sosa, O. A., Johnson, C. G., Repeta, L. D., Acker, M., ... Karl, D. M. (2016, December). Marine methane paradox explained by bacterial degradation of dissolved organic matter. *Nature Geoscience*, *9*(12), 884–887. Retrieved 2023-03-27, from http://www.nature.com/articles/ngeo2837 doi: 10.1038/ngeo2837

Resplandy, L., Keeling, R. F., Rödenbeck, C., Stephens, B. B., Khatiwala, S., Rodgers, K. B., ... Tans, P. P. (2018). Revision of global carbon fluxes based on a reassessment of oceanic and riverine carbon transport. *Nature Geoscience*, *11*, 504–509. Retrieved 2018-06-11, from https://www.nature.com/articles/s41561-018-0151-3 doi: 10.1038/s41561-018-0151-3

Reynolds, R. W., Smith, T. M., Liu, C., Chelton, D. B., Casey, K. S., & Schlax,

M. G. (2007, November). Daily High-Resolution-Blended Analyses for Sea Surface Temperature. *Journal of Climate*, *20*(22), 5473–5496. Retrieved 2023-02-15, from http://journals.ametsoc.org/doi/10.1175/2007JCLI1824.1 doi: 10.1175/2007JCLI1824.1

Roobaert, A., Laruelle, G. G., Landschützer, P., Gruber, N., Chou, L., & Regnier, P. (2019). The Spatiotemporal Dynamics of the Sources and Sinks of CO2 in the Global Coastal Ocean. *Global Biogeochemical Cycles*, *33*(12), 1693–1714. Retrieved 2020-05-11, from http://agupubs.onlinelibrary.wiley.com/doi/abs/10.1029/2019GB006239 (_eprint: https://onlinelibrary.wiley.com/doi/pdf/10.1029/2019GB006239) doi: 10.1029/2019GB006239

Roobaert, A., Laruelle, G. G., Landschützer, P., & Regnier, P. (2018, March). Uncertainty in the global oceanic CO_2 uptake induced by wind forcing: quantification and spatial analysis. *Biogeosciences*, *15*(6), 1701–1720. Retrieved 2023-03-24, from https://bg.copernicus.org/articles/15/1701/2018/ doi: 10.5194/bg-15-1701-2018

Roobaert, A., Resplandy, L., Laruelle, G. G., Liao, E., & Regnier, P. (2022, January). A framework to evaluate and elucidate the driving mechanisms of coastal sea surface pCO2 seasonality using an ocean general circulation model (MOM6-COBALT). *Ocean Science*, *18*(1), 67–88. Retrieved 2022-03-17, from https://os.copernicus.org/articles/18/67/2022/ doi: 10.5194/os-18-67-2022

Rosentreter, J. A., Borges, A. V., Deemer, B. R., Holgerson, M. A., Liu, S., Song, C., ... Eyre, B. D. (2021, April). Half of global methane emissions come from highly variable aquatic ecosystem sources. *Nature Geoscience*, *14*(4), 225–230. Retrieved 2023-02-14, from http://www.nature.com/articles/s41561-021-00715-2 doi: 10.1038/s41561-021-00715-2

Rosentreter, J. A., Laruelle, G. G., & et al. (2023). Coastal vegetation and estuaries are collectively a greenhouse gas sink Nature Climate Change, Accepted, 2023. *Accepted in Nature Climate Change*.

Roth, F., Broman, E., Sun, X., Bonaglia, S., Nascimento, F., Prytherch, J., ... Norkko, A. (2023, January). Methane emissions offset atmospheric carbon dioxide uptake in coastal macroalgae, mixed vegetation and sediment ecosystems. *Nature Communications*, *14*(1), 42. Retrieved 2023-02-20, from https://www.nature.com/articles/s41467-022-35673-9 (Number: 1 Publisher: Nature Publishing Group) doi: 10.1038/s41467-022-35673-9

Royer, S.-J., Ferrón, S., Wilson, S. T., & Karl, D. M. (2018, August). Production of methane and ethylene from plastic in the environment. *PLOS ONE*, *13*(8), e0200574. Retrieved 2023-02-14, from https://dx.plos.org/10.1371/journal.pone.0200574 doi: 10.1371/journal.pone.0200574

Ruppel, C. D., & Kessler, J. D. (2017, March). The interaction of climate change and methane hydrates. *Reviews of Geophysics*, *55*(1), 126–168. Retrieved 2023-03-27, from https://onlinelibrary.wiley.com/doi/10.1002/2016RG000534 doi: 10.1002/2016RG000534

Rutherford, K., & Fennel, K. (2018, October). Diagnosing transit times on the northwestern North Atlantic continental shelf. *Ocean Science*, *14*(5), 1207–1221. Retrieved 2023-02-15, from https://os.copernicus.org/articles/14/1207/2018/ doi: 10.5194/os-14-1207-2018

Rutherford, K., & Fennel, K. (2022, March). Elucidating Coastal Ocean Carbon Transport Processes: A Novel Approach Applied to the Northwest North Atlantic Shelf. *Geophysical Research Letters*, *49*(6). Retrieved 2022-09-13, from https://onlinelibrary.wiley.com/doi/10.1029/2021GL097614 doi: 10.1029/2021GL097614

Rutherford, K., Fennel, K., Atamanchuk, D., Wallace, D., & Thomas, H. (2021, December). A modelling study of temporal and spatial pCO_2 variability on the

biologically active and temperature-dominated Scotian Shelf. *Biogeosciences*, *18*(23), 6271–6286. Retrieved 2023-02-15, from https://bg.copernicus.org/articles/18/6271/2021/ (Publisher: Copernicus GmbH) doi: 10.5194/bg-18-6271-2021

Rödenbeck, C., DeVries, T., Hauck, J., Le Quéré, C., & Keeling, R. F. (2022, May). Data-based estimates of interannual sea–air CO_2 flux variations 1957–2020 and their relation to environmental drivers. *Biogeosciences*, *19*(10), 2627–2652. Retrieved 2023-03-24, from https://bg.copernicus.org/articles/19/2627/2022/ (Publisher: Copernicus GmbH) doi: 10.5194/bg-19-2627-2022

Salisbury, J. E., & Jönsson, B. F. (2018, December). Rapid warming and salinity changes in the Gulf of Maine alter surface ocean carbonate parameters and hide ocean acidification. *Biogeochemistry*, *141*(3), 401–418. Retrieved 2023-03-27, from http://link.springer.com/10.1007/s10533-018-0505-3 doi: 10.1007/s10533-018-0505-3

Saunois, M., Stavert, A. R., Poulter, B., Bousquet, P., Canadell, J. G., Jackson, R. B., ... Zhuang, Q. (2020, July). The Global Methane Budget 2000–2017. *Earth System Science Data*, *12*(3), 1561–1623. Retrieved 2023-02-14, from https://essd.copernicus.org/articles/12/1561/2020/ doi: 10.5194/essd-12-1561-2020

Schmale, O., Wäge, J., Mohrholz, V., Wasmund, N., Gräwe, U., Rehder, G., ... Loick-Wilde, N. (2018, January). The contribution of zooplankton to methane supersaturation in the oxygenated upper waters of the central Baltic Sea: Methane supersaturation in the Baltic Sea. *Limnology and Oceanography*, *63*(1), 412–430. Retrieved 2023-02-20, from https://onlinelibrary.wiley.com/doi/10.1002/lno.10640 doi: 10.1002/lno.10640

Schneider, B., & Müller, J. D. (2018). *Biogeochemical Transformations in the Baltic Sea*. Cham: Springer International Publishing. Retrieved 2023-02-14, from http://link.springer.com/10.1007/978-3-319-61699-5 doi: 10.1007/978-3-319-61699-5

Seitzinger, S. P., & Kroeze, C. (1998). Global distribution of nitrous oxide production and N inputs in freshwater and coastal marine ecosystems. *Global Biogeochemical Cycles*, *12*(1), 93–113. Retrieved 2023-02-14, from https://onlinelibrary.wiley.com/doi/abs/10.1029/97GB03657 (_eprint: https://onlinelibrary.wiley.com/doi/pdf/10.1029/97GB03657) doi: 10.1029/97GB03657

Siegel, D. A., Doney, S. C., & Yoder, J. A. (2002, April). The North Atlantic Spring Phytoplankton Bloom and Sverdrup's Critical Depth Hypothesis. *Science*, *296*(5568), 730–733. Retrieved 2023-02-14, from https://www.science.org/doi/10.1126/science.1069174 doi: 10.1126/science.1069174

Signorini, S. R., Mannino, A., Najjar, R. G., Friedrichs, M. A. M., Cai, W.-J., Salisbury, J., ... Shadwick, E. (2013, October). Surface ocean p CO $_2$ seasonality and sea-air CO $_2$ flux estimates for the North American east coast: NORTH AMERICAN EAST COAST SEA-AIR CO $_2$ FLUXES. *Journal of Geophysical Research: Oceans*, *118*(10), 5439–5460. Retrieved 2023-02-14, from http://doi.wiley.com/10.1002/jgrc.20369 doi: 10.1002/jgrc.20369

Stell, A. C., Bertolacci, M., Zammit-Mangion, A., Rigby, M., Fraser, P. J., Harth, C. M., ... Ganesan, A. L. (2022, October). Modelling the growth of atmospheric nitrous oxide using a global hierarchical inversion. *Atmospheric Chemistry and Physics*, *22*(19), 12945–12960. Retrieved 2022-12-02, from https://acp.copernicus.org/articles/22/12945/2022/ doi: 10.5194/acp-22-12945-2022

Su, X., Yang, L., Yang, K., Tang, Y., Wen, T., Wang, Y., ... Zhu, Y.-g. (2022, July). Estuarine plastisphere as an overlooked source of N2O production. *Nature Communications*, *13*(1), 3884. Retrieved 2023-02-14, from

https://www.nature.com/articles/s41467-022-31584-x (Number: 1 Publisher: Nature Publishing Group) doi: 10.1038/s41467-022-31584-x

Séférian, R., Nabat, P., Michou, M., Saint-Martin, D., Voldoire, A., Colin, J., ... Madec, G. (2019). Evaluation of CNRM Earth System Model, CNRM-ESM2-1: Role of Earth System Processes in Present-Day and Future Climate. *Journal of Advances in Modeling Earth Systems*, *11*(12), 4182–4227. Retrieved 2023-03-01, from https://onlinelibrary.wiley.com/doi/abs/10.1029/2019MS001791 (_eprint: https://onlinelibrary.wiley.com/doi/pdf/10.1029/2019MS001791) doi: 10.1029/2019MS001791

Terhaar, J., Lauerwald, R., Regnier, P., Gruber, N., & Bopp, L. (2021, January). Around one third of current Arctic Ocean primary production sustained by rivers and coastal erosion. *Nature Communications*, *12*(1), 169. doi: 10.1038/s41467-020-20470-z

Thomas, H., Bozec, Y., Elkalay, K., & de Baar, H. J. W. (2004, May). Enhanced open ocean storage of CO2 from shelf sea pumping. *Science (New York, N.Y.)*, *304*(5673), 1005–1008. doi: 10.1126/science.1095491

Tian, H., Xu, R., Canadell, J. G., Thompson, R. L., Winiwarter, W., Suntharalingam, P., ... Yao, Y. (2020, October). A comprehensive quantification of global nitrous oxide sources and sinks. *Nature*, *586*(7828), 248–256. Retrieved 2023-02-14, from https://www.nature.com/articles/s41586-020-2780-0 doi: 10.1038/s41586-020-2780-0

Tjiputra, J. F., Schwinger, J., Bentsen, M., Morée, A. L., Gao, S., Bethke, I., ... Schulz, M. (2020, May). Ocean biogeochemistry in the Norwegian Earth System Model version 2 (NorESM2). *Geoscientific Model Development*, *13*(5), 2393–2431. Retrieved 2023-02-15, from https://gmd.copernicus.org/articles/13/2393/2020/ (Publisher: Copernicus GmbH) doi: 10.5194/gmd-13-2393-2020

Tu, Z., Le, C., Bai, Y., Jiang, Z., Wu, Y., Ouyang, Z., ... Qi, D. (2021, August). Increase in CO $_2$ Uptake Capacity in the Arctic Chukchi Sea During Summer Revealed by Satellite-Based Estimation. *Geophysical Research Letters*, *48*(15). Retrieved 2023-03-27, from https://onlinelibrary.wiley.com/doi/10.1029/2021GL093844 doi: 10.1029/2021GL093844

Turi, G., Lachkar, Z., & Gruber, N. (2014, February). Spatiotemporal variability and drivers of pCO2 and air–sea CO2 fluxes in the California Current System: an eddy-resolving modeling study. *Biogeosciences*, *11*(3), 671–690. Retrieved 2019-04-02, from https://www.biogeosciences.net/11/671/2014/ doi: 10.5194/bg-11-671-2014

Wan, X. S., Lin, H., Ward, B. B., Kao, S.-J., & Dai, M. (2022). Significant Seasonal N2O Dynamics Revealed by Multi-Year Observations in the Northern South China Sea. *Global Biogeochemical Cycles*, *36*(10), e2022GB007333. Retrieved 2023-02-14, from https://onlinelibrary.wiley.com/doi/abs/10.1029/2022GB007333 (_eprint: https://onlinelibrary.wiley.com/doi/pdf/10.1029/2022GB007333) doi: 10.1029/2022GB007333

Wang, H., Hu, X., Cai, W.-J., & Sterba-Boatwright, B. (2017). Decadal fCO2 trends in global ocean margins and adjacent boundary current-influenced areas. *Geophysical Research Letters*, *44*(17), 8962–8970. Retrieved 2022-04-15, from https://onlinelibrary.wiley.com/doi/abs/10.1002/2017GL074724 doi: 10.1002/2017GL074724

Wanninkhof, R. (1992, May). Relationship between wind speed and gas exchange over the ocean. *Journal of Geophysical Research: Oceans*, *97*(C5), 7373–7382. Retrieved 2015-06-22, from http://onlinelibrary.wiley.com/doi/10.1029/92JC00188/abstract doi: 10.1029/92JC00188

Wanninkhof, R. (2014, June). Relationship between wind speed and gas exchange

over the ocean revisited. *Limnology and Oceanography: Methods*, *12*(6), 351–362. Retrieved 2015-06-22, from http://onlinelibrary.wiley.com/doi/10.4319/lom.2014.12.351/abstract doi: 10.4319/lom.2014.12.351

Ward, N. D., Megonigal, J. P., Bond-Lamberty, B., Bailey, V. L., Butman, D., Canuel, E. A., ... Windham-Myers, L. (2020, May). Representing the function and sensitivity of coastal interfaces in Earth system models. *Nature Communications*, *11*(1), 2458. Retrieved 2023-02-14, from https://www.nature.com/articles/s41467-020-16236-2 (Number: 1 Publisher: Nature Publishing Group) doi: 10.1038/s41467-020-16236-2

Weber, T., Wiseman, N. A., & Kock, A. (2019, October). Global ocean methane emissions dominated by shallow coastal waters. *Nature Communications*, *10*(1), 4584. Retrieved 2020-10-21, from https://www.nature.com/articles/s41467-019-12541-7 (Number: 1 Publisher: Nature Publishing Group) doi: 10.1038/s41467-019-12541-7

Woolf, D., Shutler, J., Goddijn-Murphy, L., Watson, A., Chapron, B., Nightingale, P., ... Paul, F. (2019, December). Key Uncertainties in the Recent Air-Sea Flux of CO_2. *Global Biogeochemical Cycles*, *33*(12), 1548–1563. Retrieved 2023-04-03, from https://onlinelibrary.wiley.com/doi/abs/10.1029/2018GB006041 doi: 10.1029/2018GB006041

Wright, R. M., Le Quéré, C., Buitenhuis, E., Pitois, S., & Gibbons, M. J. (2021, February). Role of jellyfish in the plankton ecosystem revealed using a global ocean biogeochemical model. *Biogeosciences*, *18*(4), 1291–1320. Retrieved 2023-03-27, from https://bg.copernicus.org/articles/18/1291/2021/ (Publisher: Copernicus GmbH) doi: 10.5194/bg-18-1291-2021

Xu, Y., Cai, W., Wanninkhof, R., Salisbury, J., Reimer, J., & Chen, B. (2020, July). Long-Term Changes of Carbonate Chemistry Variables Along the North American East Coast. *Journal of Geophysical Research: Oceans*, *125*(7). Retrieved 2023-02-14, from https://onlinelibrary.wiley.com/doi/abs/10.1029/2019JC015982 doi: 10.1029/2019JC015982

Xue, Z., He, R., Fennel, K., Cai, W.-J., Lohrenz, S., Huang, W.-J., ... Zang, Z. (2016, August). Modeling <i>p</i>CO₂ variability in the Gulf of Mexico. *Biogeosciences*, *13*(15), 4359–4377. Retrieved 2023-02-14, from https://bg.copernicus.org/articles/13/4359/2016/ doi: 10.5194/bg-13-4359-2016

Yang, S., Chang, B. X., Warner, M. J., Weber, T. S., Bourbonnais, A. M., Santoro, A. E., ... Bianchi, D. (2020, June). Global reconstruction reduces the uncertainty of oceanic nitrous oxide emissions and reveals a vigorous seasonal cycle. *Proceedings of the National Academy of Sciences*, *117*(22), 11954–11960. Retrieved 2022-05-12, from https://www.pnas.org/doi/10.1073/pnas.1921914117 (Publisher: Proceedings of the National Academy of Sciences) doi: 10.1073/pnas.1921914117

Yukimoto, S., Kawai, H., Koshiro, T., Oshima, N., Yoshida, K., Urakawa, S., ... Ishii, M. (2019). The Meteorological Research Institute Earth System Model Version 2.0, MRI-ESM2.0: Description and Basic Evaluation of the Physical Component. *Journal of the Meteorological Society of Japan. Ser. II*, *97*(5), 931–965. Retrieved 2023-02-15, from https://www.jstage.jst.go.jp/article/jmsj/97/5/97_2019-051/_article doi: 10.2151/jmsj.2019-051

Zhou, J., Zheng, Y., Hou, L., An, Z., Chen, F., Liu, B., ... Liu, M. (2023, March). Effects of acidification on nitrification and associated nitrous oxide emission in estuarine and coastal waters. *Nature Communications*, *14*(1), 1380. Retrieved 2023-03-22, from https://www.nature.com/articles/s41467-023-37104-9 doi: 10.1038/s41467-023-37104-9

Supporting Information for 'A Synthesis of Global Coastal Ocean Greenhouse Gas Air-sea Fluxes'

L. Resplandy[1], A. Hogikyan[2], H. W. Bange[3], D. Bianchi[4], T. Weber[5], Wei-Jun Cai[6], S.C. Doney[7], K. Fennel[8], M. Gehlen[9], J. Hauck[10], F. Lacroix[11], P. Landschützer[12,13], C. Le Quéré[14], J. D. Müller[15], R. G.Najjar[16], A. Roobaert[17], J. Schwinger[18], S. Berthet[19], L. Bopp[20], T.T.T. Chau[9], M. Dai[21], N. Gruber[15], T. Ilyina[13], A. Kock[3*], M. Manizza[22], Z. Lachkar[23], G. G. Laruelle[17], E. Liao[1†], I.D. Lima[24], C. Nissen[10,25], C. Rödenbeck[26], R. Séférian[19], K. Toyama[27], H. Tsujino[27], P. Regnier[17]

[1]Department of Geosciences and High Meadows Environmental Institute, Princeton University, Princeton, NJ, USA
[2]Atmospheric and Oceanic Sciences Program, Princeton University, Princeton, NJ, USA
[3]GEOMAR Helmholtz Centre for Ocean Research Kiel, Kiel, Germany
[4]Department of Atmospheric and Oceanic Sciences, University of California Los Angeles, Los Angeles, CA, USA
[5]Department of Earth and Environmental Science, University of Rochester, NY, USA
[6]School of Marine Science and Policy, University of Delaware, Newark, Delaware, 19716, USA
[7]Department of Environmental Sciences, University of Virginia, Charlottesville, VA, USA
[8]Department of Oceanography, Dalhousie University, Halifax, Canada
[9]Laboratoire des Sciences du Climat et de l'Environnement, LSCE/IPSL, CEA-CNRS-UVSQ, Université Paris-Saclay, F-91191 Gif-sur-Yvette, France
[10]Alfred-Wegener-Institut, Helmholtz-Zentrum für Polar und Meeresforschung, Germany
[11]Climate and Environmental Physics / Oeschger Centre for Climate Change Research (OCCR), University of Bern, Switzerland
[12]Flanders Marine Institute (VLIZ), Ostend Belgium
[13]Max Planck Institute for Meteorology, Hamburg, Germany
[14]School of Environmental Sciences, University of East Anglia, Norwich Research Park, NR4 7TJ, Norwich, UK
[15]Environmental Physics, Institute of Biogeochemistry and Pollutant Dynamics, ETH Zurich, Zürich, Switzerland
[16]Department of Meteorology and Atmospheric Science, The Pennsylvania State University, University Park, Pennsylvania, USA
[17]Dept. Geoscience, Environment and Society - BGEOSYS, Université Libre de Bruxelles, Brussels, Belgium
[18]NORCE Climate & Environment, Bjerknes Centre for Climate Research, Bergen, Norway
[19]CNRM, Université de Toulouse, Météo France, CNRS, Toulouse, France
[20]LMD/IPSL, ENS, Université PSL, École Polytechnique, Institut Polytechnique de Paris, Sorbonne Université, CNRS, Paris, France
[21]State Key Lab of Marine Environmental Science and College of Ocean and Earth Sciences, Xiamen University, Xiamen 361102, China
[22]Geosciences Research Division, Scripps Institution of Oceanography, University of California - San Diego, La Jolla, USA
[23]Arabian Center for Climate and Environmental Sciences, New York University Abu Dhabi, Abu Dhabi, United Arab Emirates
[24]Department of Marine Chemistry and Geochemistry, Woods Hole Oceanographic Institution, Woods Hole, MA, USA
[25]Department of Atmospheric and Oceanic Sciences and Institute of Arctic and Alpine Research, University of Colorado, Boulder, Colorado, USA
[26]MPI Biogeochemistry, Jena, Germany
[27]JMA Meteorological Research Institute, Tsukuba, Ibaraki, Japan

Contents of this file

1. Text S1
2. Figures S1 to S12
3. Tables S1 to S3 (Table S3 provided as separate excel file per AGU requirements)

*now at State Office for the Environment of the State of Schleswig-Holstein, Flintbek, Germany
†now at School of Oceanography, Shang Jiao Tong University, Shanghai, 200030, China

Copyright 2023 by the American Geophysical Union.
0886-6236/23/$12.00

Text S1. Observation-based products and models description

S1.a pCO_2-products

CMEMS-LSCE-FFNN (CMEMS)

The CMEMS-LSCE-FFNN product (Chau et al., 2022) referred to here as CMEMS provides estimates of monthly pCO_2 and air-sea CO_2 fluxes over the global coastal ocean at a spatial resolution of 1×1 degree from 1985 to 2018. Main characteristics setting CMEMS-LSCE-FFNN apart from similar approaches are (1) model design, (2) ensemble-based estimates of pCO_2 and air-sea CO_2 fluxes and uncertainty, and (3) consistency of the coastal-ocean reconstruction and the open-ocean reconstruction (Chau et al., 2022). Coastal estimates were evaluated thoroughly from a global scale to ocean basins and at time-series stations. The coastal estimates are part of a global reconstruction of pCO_2 fields based on monthly gridded SOCATv2020 data of CO_2 fugacity covering both the open ocean and the coastal zone (Bakker et al., 2016) (see Figure S1). The reconstruction is based on an ensemble of 100 feed-forward neural networks (FFNN), with two-thirds of SOCAT data used for model training and one third kept for validation of reconstructed pCO_2 . The ensemble approach provides space-time varying uncertainty field (ensemble spread) associated with the best pCO_2 and air-sea fluxes' estimates (ensemble mean). These ensemble statistics permit the evaluation of reconstruction uncertainty over coastal regions with sparse data coverage. The seamless reconstruction of pCO_2 and air-sea fluxes over the global coastal and open ocean allows the assessment of gradients and horizontal variability of pCO_2 and air-sea CO_2 fluxes over the continental shelf and to the open ocean. The gas transfer velocity was calculated with 10-m ERA5 wind speed data (Hersbach et al., 2020) following the parameterization by Wanninkhof (2014). A scaling factor is applied such that the global average of kw equals to 16.5 cm h^{-1} (Naegler, 2009). Air-sea CO_2 fluxes are also scaled proportional to CMEMS-OSTIA sea ice fraction over polar and subpolar regions (S. Good et al., 2020).

Coastal-SOM-FFN

The coastal air-sea CO_2 product (referred here as coastal-SOM-FFN) is based on the continuous coastal pCO_2 product of Laruelle et al. (2017) that used the Self-Organizing Map Feed Forward method developed by Landschützer et al. (2013) but adapted for the coastal ocean to fill region without data. The method in a first step clusters coastal ocean regions into dynamic biogeochemical provinces. In a second step, a non-linear regression step links physical, biological and chemical proxy data with existing CO_2 measurements. The coastal ocean is thereby explicitly reconstructed with coastal-only observations from the SOCATv4 database. The established regression relationship is then used to fill areas where no observations exist (a more detailed description can be found in Landschützer et al. (2013) and Laruelle et al. (2017). The coastal domain defined by Laruelle et al. (2017) excludes estuaries and inland water bodies with an outer limit defined as 300 km away from the shoreline (total surface area of 77 million km^2). This pCO_2-product is available as monthly 0.25-degree maps for the 1998-2015 period. The SST, SSS, wind product and sea-ice used to calculate the air-sea CO_2 exchange derived from the daily NOAA OI SST V2 (Reynolds et al., 2007), the daily Hadley center EN4 SSS (S. A. Good et al., 2013), the monthly second moment of the 6-hour 0.25° global atmospheric reanalysis ERA-interim wind product (Dee et al., 2011) and the monthly mean of the daily 0.25° sea-ice dataset of Reynolds et al. (2007), respectively. We use the equation developed by (Ho et al., 2011) to calculate the gas exchange transfer velocity.

Merged-SOM-FFN

The air-sea CO_2 flux product based on Landschützer et al. (2020) (referred here as Merged-SOM-FFN) is built on the combination of the open ocean CO_2 product by Landschützer et al. (2014) using SOCATv5 and the coastal ocean product by Laruelle et al. (2017) using SOCATv4 (referred here as Coastal-SOM-FFN), both created using the Self-Organizing Map Feed Forward Network (SOM-FFN) method developed by Landschützer et al. (2013). Open ocean regions in the original product are broadly defined as all waters 1 degree off shore, whereas the coastal ocean in Laruelle et al. (2017) includes all ocean areas within 300 km offshore following the SOCAT definition (Bakker et al., 2016), whereas the overlap area is merged by simple error statistics (Landschützer et al., 2020). The merged climatology, presented in Landschützer et al. (2020), is available globally on a 0.25x0.25 degree grid to better resolve fine coastal characteristics and covers coastal ocean regions, shelf seas, as well as marginal seas. The dataset used to calculate the air-sea CO_2 flux (i.e., SST, SSS, wind) is the same as described for the coastal-SOM-FFN product.

Carboscope-1

The Carboscope pCO_2 interpolation is normally run at a resolution of 2 x 2.5 degree (version oc_v2021, update of Rödenbeck et al. (2013)) but we use here a higher-resolution version of 1 x 1 degree (CarboScope RunID oc_1x1_v2021) to better resolve spatial details. As a secondary change for computational feasibility, the calculation period has been shortened, now starting in 1988, with the valid period starting in 1992. We note that the Bayesian a-priori uncertainty is set according to a global normalization condition, even though the pCO_2 constraint is a local one; thus the effective local regularization strength in the 1 x 1 version might be somewhat different compared to that in the regular 2.5 x 2 version. This version uses SOCAT version 2021, sea ice coverage is based on HadISST 2.2.0.0 (Titchner & Rayner, 2014). Wind speed are from JRA55-do v1.5.0 (Tsujino et al., 2018) used quadratically as in (Wanninkhof, 1992), and global mean piston velocity are scaled to 16.5 cm h^{-1} but the normalization of the gas transfer velocity to a global long-term average of 16.5 cm h^{-1} might lead to slight differences in the local transfer velocities.

S1.b N_2O and CH_4 observation-based products

MARCATS-N2O and MARCATS-CH4

MARCATS-N2O and MARCATS-CH4 are based on the collection of in-situ concentration data of N_2O and CH_4 from the MEMENTO (MarinE MethanE and NiTrous Oxide) data base (Kock & Bange, 2015) and were computed at the scale of the 45 MARgins and CATchments Segmentation (MARCATS) regions (Laruelle et al., 2013) (Figure S2). For each MARCATS region, N_2O and CH_4 surface (1 - 10 m) concentration data were extracted from MEMENTO. Individual DN2O and DCH4 values (D = measured in-situ concentration – equilibrium concentration at the time of sampling) were calculated in two ways (i) using in-situ measurements of atmospheric N_2O or CH_4 mole fractions when archived together with the dissolved concentration data in MEMENTO or (ii) using zonally averaged atmospheric N_2O and CH_4 mole fractions computed with the data from the World Data Centre for Greenhouse Gases (WDCGG, https://gaw.kishou.go.jp/) for the respective sampling month. N_2O and CH_4 flux densities were calculated by multiplying DN2O and DCH4 with the air-sea transfer coefficient (kw) which was estimated with the wind speed parameterization for kw from (Nightingale et al., 2000). Wind speeds for the respective sampling

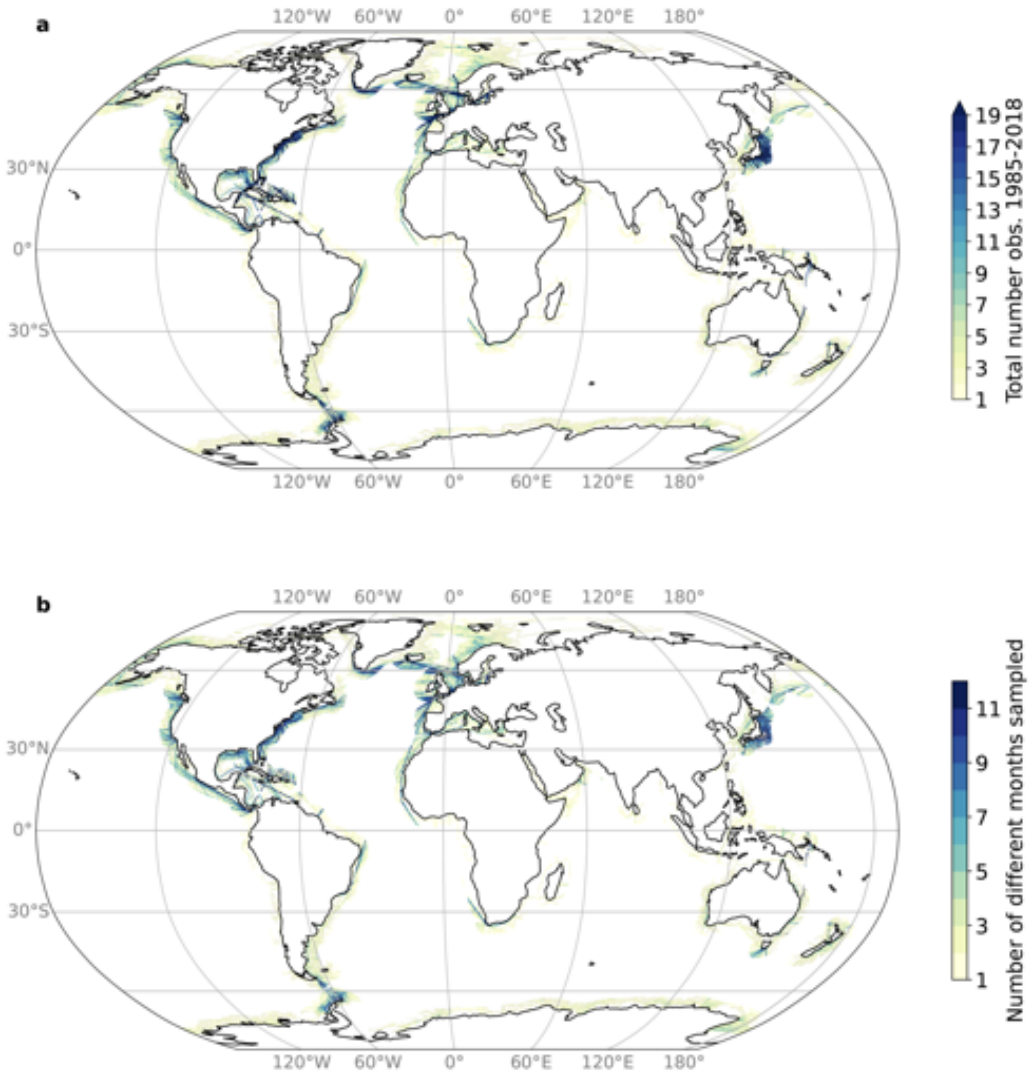


Figure S1. (a) areal coverage in 0.25 x 0.25 degree grid cells of SOCATv2.0 database calculated as the spatial density of the total number of observations 1985-2018 and (b) the number of distinct months sampled by SOCATv2.0 during this period. White areas represent where there are no observations (0 observations). See Methods and Laruelle et al. (2017) for definition of wide coastal ocean.

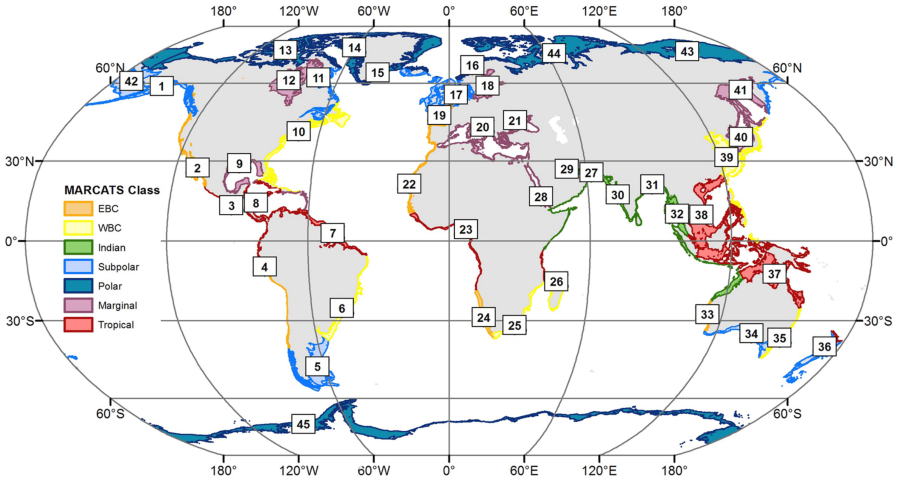


Figure S2. Locations of the 45 MARgins and CATchments Segmentation (MARCATS) regions (Laruelle et al., 2013) used to calculated the N_2O and CH_4 fluxes in MARCATS-N2O and MARCATS-CH4.

https://psl.noaa.gov) (Kanamitsu et al., 2002). Finally, the individual N_2O and CH_4 flux densities were averaged and extrapolated to the area of each MARCATS region to obtain an emission estimate for the individual MARCATS regions. The number of observatinos used in each MARCATS to derive the CH_4 and N_2O fluxes is listedin Table S2. MARCATS-N2O product has no observations in 6 MARCATS for the wide and 10 MARCATS for the narrow coastal oceans. Similarly, the MARCATS-CH4 has no observations in 8 MARCATS for the wide and 14 MARCATS for the narrow coastal oceans.

Yang-N2O

The N_2O air-sea flux reconstruction by Yang et al. (2020) is based on a synthesis of over 158,000 observations of N_2O mixing ratio, partial pressure, and concentration in the surface ocean from the MEMENTO database (Kock & Bange, 2015) and additional cruises (Yang et al., 2020). N_2O measurements are converted to surface N_2O mixing ratio anomalies using observations from the NOAA atmospheric flask dataset and extrapolated to a 0.25-degree resolution global monthly climatology using an ensemble of 100 random forest realizations. The random forest algorithm predicts N_2O mixing ratio anomalies based on their relationship to oceanographic predictors that include hydrographic variables, nutrients, oxygen, chlorophyll, net primary production, and seafloor depth. Reconstructed mixing ratio climatologies are used to estimate air-sea fluxes by applying a commonly used gas exchange parameterization (Wanninkhof, 2014). Two formulations of piston velocity are adopted: one based on a quadratic dependence on wind speed (Wanninkhof, 2014), and one that explicitly accounts for bubble-mediated fluxes (Liang et al., 2013). Sea ice cover, surface temperature, salinity and atmospheric pressure are taken from ERA5 reanalysis (Hersbach et al., 2020). Calculations are performed with two high-resolution wind products (ERA5 and Remote sensing Cross-Calibrated Multi-Platform version 2.0) that are available at 0.25, 6-hourly resolution for the period from 1988 to 2017, yielding four permutations of the piston velocity. The resulting ensemble of 400 global N_2O air–sea flux estimates is averaged in time to obtain monthly mean climatologies. A description of the dataset and methods is presented in (Yang et al., 2020). The compilation of N_2O measurements, the reconstructed global N_2O climatology and air-sea flux are available on the Biological and Chemical Oceanography Data Management Office (BCO-DMO) portal (DOI: 10.26008/1912/bco-dmo.810032.1). The code used to produce these datasets is archived on a public GitHub repository at https://github.com/yangsi7/mapping-ocean-n2o (DOI: 10.5281/zenodo.3757194).

Weber-CH4

The diffusive sea-air CH4 flux reconstruction by (Weber et al., 2019) is based on a compilation of 120,000 individual concentration and partial pressure measurements from the MEMENTO database (Kock & Bange, 2015) and additional cruise datasets (Weber et al., 2019). These measurements were converted to CH_4 disequilibrium using atmospheric partial pressure from the NOAA Global Monitoring Division archive, which has collected flask samples from a global network of monitoring stations since 1980 (www.esrl.noaa.gov/gmd/ccgg/) and extrapolated to a 0.25-degree monthly climatology using 10,000 artificial neural network and random regression forest models, each trained with 70% of the data. Air-sea fluxes were computed by combining each climatology with one of four piston velocity relationships (Wanninkhof, 1992, 2014; Nightingale et al., 2000; Liss & Merlivat, 1986), and one of four global wind products (ERA5, CCMP, NCEP, reanalysis products, and a blended WindSat/QuickSCAT satellite product). Flux calculations were conducted at daily resolution then integrated into an annual climatology representing the mean 1999-2016 flux. Ebullitive CH4 emissions to the atmosphere were estimated using literature ranges for the global ebullition rate from continental shelf sediments (Hornafius et al., 1999; Hovland et al., 1993) and a bubble transfer model to estimate the fraction of CH4 reaching the surface (McGinnis et al., 2006). Full methodology is described in Weber et al., 2019 and the product is available at https://figshare.com/articles/dataset/ocean_ch4_nc/9034451.

S1.c Global ocean biogeochemical models

CCSM-WHOI

The Community Earth System Model (CESM) is the global ocean component of a coupled climate/earth system model. The ocean component, the Biogeochemical Elemental Cycle (BEC) model, consists of an upper-ocean ecological module and a full-depth ocean biogeochemistry module both embedded in a three-dimensional (3-D) global physical ocean general circulation model. The physical model is the Parallel Ocean Program (POP) z-level, hydrostatic, primitive equation model. The specific CESM-LR version used here has coarse, non-eddy resolution and is described in detail in Doney et al. (2009). The ocean model is integrated in an uncoupled model forced with physical climate forcing from NCEP atmospheric reanalysis and satellite data products. The ecosystem module builds on traditional phytoplankton–zooplankton–detritus–nutrient food-web models and incorporates multi-nutrient limitation (N, P, Si, Fe) on phytoplankton growth and specific phytoplankton functional groups. The biogeochemical module includes full carbonate system thermodynamics and air–sea CO_2 and O2 fluxes, nitrogen fixation, denitrification and a dynamic iron cycle with atmospheric dust deposition, water-column scavenging and a continental sediment source. There are 14 main compartments: pico/nano-plankton, diatoms, and diazotrophs; zooplankton; suspended and sinking particulate detritus; and dissolved nitrate, ammonia, phosphorus, iron, silicate, oxygen, dissolved inorganic carbon, and alkalinity. The model was forced with the NCEP reanalysis and did not include nutrients or carbon inputs by rivers.

CNRM-LR and CNRM-HR

CNRM-LR and CNRM-HR are the Earth System Models of second generation developed by CNRM-CERFACS for the sixth phase of the Coupled Model Intercomparison Project (CMIP6). Their ocean component uses the Nucleus for European Models of the Ocean (NEMO) Version 3.6 (Madec et al., 2017) coupled to both the Global Experimental Leads and ice for ATmosphere and Ocean (GELATO) sea ice model (Salas Mélia, 2002) Version 6 and the marine biogeochemical model Pelagic Interaction Scheme for Carbon and Ecosystem Studies version 2-gas (PISCESv2-gas) (Aumont et al., 2015). In CNRM-LR, NEMOv3.6 operates on the eORCA1L75 grid, which offers a nominal resolution of 1 degree to which a latitudinal grid refinement of 1/3 degree is added in the tropics, while in CNRM-HR, NEMO is run on the eORCA025 grid having a 0.25 degree of horizontal resolution. Whatever the horizontal resolution, the ocean is described with 75 vertical layers using a vertical $z^\star$ coordinate with partial step bathymetry formulation (Bernard et al., 2006). The ocean layers are distributed unevenly as a function of depth with a resolution of 1 m at ocean surface to 200 m below 4000 m. Key differences between both configurations are detailed in Berthet et al. (2019). The simulations were forced at the surface by the atmospheric state of JRA55-do v1.5.0 (Tsujino et al., 2018). Atmospheric CO_2 concentration is given as annual means as specified by CMIP6 protocols and is linearly interpolated in time. Riverine inputs of dissolved inorganic carbon and alkalinity (Ludwig et al., 1996) as well as nutrients (Mayorga

Table S1. Number of observations and density [in observations per 10^6 km^2] from MEMENTO database used in each MARCATS to calculate the MARCATS-N2O and MARCATS-CH4 observational products in the wide and narrow coastals. See map in Figure S2 for MARCATS locations.

MARCATS	N_2O wide		N_2O narrow		CH_4 wide		CH_4 narrow	
	observations	density	observations	density	observations	density	observations	density
1	71	9	20	7	38	5	9	3
2	159	21	28	10	124	17	5	1
3	229	31	8	2	12	1	0	0
4	1301	179	551	204	20	2	13	4
5	248	34	129	47	26	3	15	5
6	539	74	148	54	4	0	1	0
7	375	51	250	92	4	0	0	0
8	136	18	0	0	0	0	0	0
9	0	0	0	0	1	0	0	0
10	575	79	411	152	0	0	0	0
11	259	35	0	0	2	0	0	0
12	0	0	0	0	0	0	0	0
13	130	17	130	48	117	16	102	37
14	28	3	7	2	13	1	7	2
15	472	65	70	25	28	3	0	0
16	519	71	330	122	28	3	3827	1420
17	1294	178	917	340	1013	139	1014	376
18	250	34	91	33	3312	457	15	5
19	457	63	481	178	629	86	648	240
20	102	14	39	14	111	15	52	19
21	3	0	4	1	32	4	24	8
22	1286	177	430	159	474	65	148	54
23	396	54	17	6	5	0	1	0
24	185	25	69	25	5	0	5	1
25	514	70	54	20	0	0	0	0
26	173	23	0	0	0	0	0	0
27	1306	180	6	2	557	76	1	0
28	0	0	0	0	0	0	0	0
29	0	0	0	0	0	0	0	0
30	243	33	47	17	16	2	1	0
31	289	39	22	8	55	7	62	23
32	321	44	21	7	20	2	24	8
33	476	65	76	28	7	0	0	0
34	88	12	20	7	53	7	12	4
35	276	38	206	76	113	15	144	53
36	144	19	16	5	43	5	10	3
37	37	5	37	13	7	0	3	1
38	182	25	129	47	89	12	46	17
39	253	34	111	41	72	9	48	17
40	0	0	0	0	0	0	0	0
41	0	0	0	0	22	3	3	1
42	62	8	48	17	17	2	13	4
43	33	4	17	6	659	90	655	243
44	48	6	0	0	85	11	36	13
45	1703	235	959	356	85	11	47	17

et al., 2010) are prescribed with a repeated seasonal cycle scaled on freshwater riverine inputs. Burial of carbon at the bottom of the ocean is emulated with a meta-model based on POC export (Aumont et al., 2015). Originally implemented by Martinez-Rey et al. (2015), the marine N_2O parameterization has benefited from a recoding and an improved calibration presented in Berthet et al. (2022). A comprehensive description of the configuration of the marine biogeochemical component is presented in Séférian et al. (2019).

FESOM-LR and FESOM-HR

We use the ocean circulation model FESOM1.4 (C. Wang et al., 2014) coupled to the ocean biogeochemical model REcoM2 (Hauck et al., 2020, 2013; Schourup-Kristensen et al., 2014). FESOM is an unstructured mesh model used in a low-resolution configuration (FESOM-LR) and a high-resolution configuration (FESOM-HR, see resolution meshes in Figure S3). The Regulated Ecosystem Model (REcoM) simulates the coupled cycles of carbon, nitrogen, silicic acid, iron and oxygen. In this version, it simulates two phytoplankton groups (small phytoplankton and diatoms) and one zooplankton group. It allows for variable stoichiometry in phytoplankton (C:N:Chl:CaCO3 for small phytoplankton and C:N:Chl:SI for diatoms), zooplankton (C:N) and detritus (C:N:Si). There are no inputs of carbon or nutrients by rivers and runoff. The FESOM-LR configuration is based on a coarse mesh with a global nominal resolution of 1 degree, which is increased to about 25 km north of 50°N and to about 1/3° in the equatorial belt, and is also moderately refined along the coasts (Sein et al., 2018). The model is started from initial conditions (World Ocean Atlas for nutrient fields (Garcia et al., 2014), Glodap for alkalinity and preindustrial dissolved inorganic carbon (Lauvset et al., 2016)). It is spun up from 1850-1957 years using repeated year atmospheric forcing from the year 1961. The atmospheric forcing fields for the spin-up and for the simulation period 1958 to 2018 are taken from the Japanese 55-year Reanalysis Version 1.4.0 (Tsujino et al., 2018). Further, spin-up and simulation period are forced with observed atmospheric CO_2 as provided by the Global Carbon Budget (Friedlingstein et al., 2020). Carbonate chemistry and air-sea CO_2 exchange are calculated with the mocsy routines (Orr et al., 2015) that apply a quadratic gas-exchange parameterization (Wanninkhof, 2014). This is the same model version as used in the Global Carbon Budget 2020

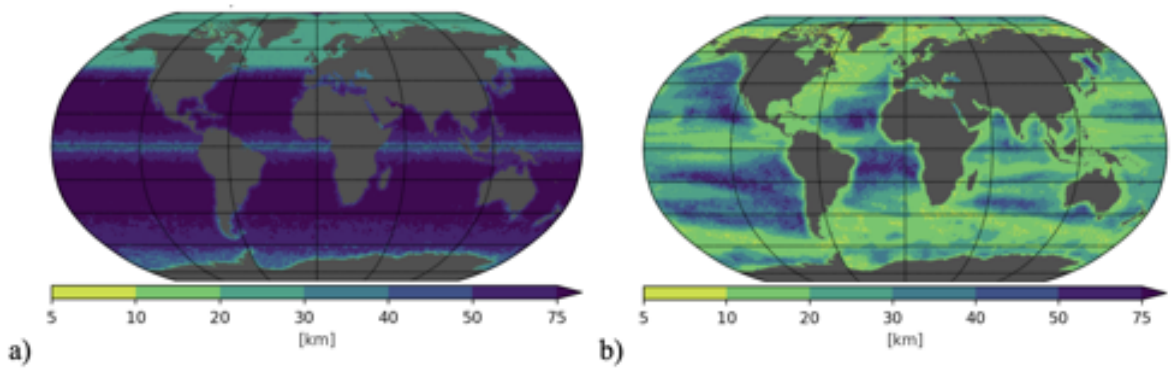


Figure S3. Horizontal resolution of the a) FESOM-LR and b) FESOM-HR models.

(Friedlingstein et al., 2020). The FESOM-HR configuration has a locally eddy-resolving mesh with the horizontal resolution varying according to the observed sea surface height (SSH) variability. The coarsest resolution is 60 km, and the finest is 8-10 km (Sein et al., 2018). This is equivalent to a $1/10^{\circ} - 1/4^{\circ}$ resolution. In particular, the high resolution is located along the pathways of the main currents, including the Gulf Stream. We performed a high-resolution physical ocean model spin-up run under JRA55 forcing. The spin-up spanned one full cycle from 1958-2017, and a second cycle 1958-1980 using FESOM-HR. We initialized our model from an existing simulation driven by CORE-II forcing (Large & Yeager, 2009). We branched off our simulations with coupled physics and biogeochemistry at the end of 1980 and ran the simulation from 1981 to 2019 using the HR mesh with an increasing atmospheric CO_2 concentration and interannual varying atmospheric forcing. The initial biogeochemical model fields for the year 1980 are taken from the FESOM-LR simulation and are interpolated to the FESOM-HR mesh.

IPSL

The IPSL ocean model uses the Nucleus for European Models of the Ocean (NEMO) Version 3.6 which includes three components, ocean physics from NEMO-OPA (Madec et al., 2017), the sea ice dynamics and thermodynamics from NEMO-LIM3 (Rousset et al., 2015), and the ocean biogeochemistry from NEMO-PISCES-v2 (Aumont et al., 2015). The global configuration used here is eORCA1L75, including a horizontal nominal resolution of 1° (with a latitudinal grid refinement of up to 0.3° in the equatorial region) and 75 levels on the vertical (with the partial step formulation of Barnier et al. (2006) and layer thicknesses increasing from 1m at the surface to 200m at the bottom). The simulation is forced at the surface by the atmospheric reanalysis product of JRA55-do-v1.4 (Tsujino et al., 2018) and global and annual mean values of atmospheric CO_2 as specified in the Global Carbon Budget protocol (Friedlingstein et al., 2022). Riverine inputs of carbon, alkalinity and nutrients are based on (Ludwig et al., 1996) and (Mayorga et al., 2010), and prescribed with a repeated seasonal cycle. Sediment burial of carbon, alkalinity and nutrients is simulated using the formulation of (Dunne et al., 2007) and (Middelburg et al., 1996).

MOM6-Princeton

The MOM6-Princeton model uses the Modular Ocean Model version 6 (MOM6), the Sea Ice Simulator version 2 (SIS2), and the Carbon Ocean Biogeochemistry and Lower Trophics version 2 (COBALT v2) developed by the NOAA Geophysical Fluid Dynamics Laboratory (GFDL). The specific version used here is available on Github (Git commit: 48536b downloaded in October 2018) and was used in Liao et al. (2020) and the global carbon budget 2020 (Friedlingstein et al., 2020). The physical and biogeochemical ocean configurations follow GFDL earth system model version 4 (ESM4) (Dunne et al., 2020)). The horizontal resolution is 0.5° in longitude and 0.25-0.5° in latitude. On the vertical, it includes 75 hybrid isopycnal $z^{\star}$ coordinate, including a $z^{\star}$ coordinate near the surface (about 2 m thick layers in the upper 20 m in the tropical Pacific Ocean) and a modified potential density coordinate below (Adcroft et al., 2019). COBALT2 includes 33 state variables, including nutrients (nitrate, phosphate, and iron), silicate, three phytoplankton groups, three zooplankton groups, three dissolved organic carbon pools, one particulate detritus pool, oxygen, and the carbonate system (Stock et al., 2020). The model was spun up from rest for 81 years by repeating the year 1959 of the JRA55-do v1.3 forcing. Temperature, salinity, nutrients (nitrate, phosphate, and silicate), and oxygen were initialized from World Ocean Atlas version 2013 (Garcia et al., 2014; Locarnini et al., 2014; Zweng et al., 2014). Initial dissolved inorganic carbon (DIC) and alkalinity (Alk) are from GLODAP v2 (Olsen et al., 2016). The initial DIC is corrected for the accumulation of anthropogenic carbon to match the level expected in 1959 using the data-based estimate of ocean anthropogenic carbon content (Khatiwala et al., 2013). Other COBALT tracer initial conditions (e.g., ammonium, calcium carbonate) are from a preindustrial GFDL-ESM2M-COBALT simulation (Stock et al., 2014). The simulation includes riverine nutrients from the Global-NEWS2 model (Mayorga et al., 2010) and riverine carbon inputs designed to roughly balance carbon burial in the model (here input of 0.11 of DIC and 0.07 of DOC). At the end of the 81-year spin-up, the model has reached a near-equilibrium between atmospheric pCO_2 and surface ocean pCO_2 , with a drift in global air-sea CO_2 flux ¡0.004 PgC/yr over the last 10 years of spin-up. The simulation was then performed from 1959 to 2018 using interannual forcing. In this version, the gas transfer coefficient was calculated using the parameterization of (Wanninkhof, 1992) but with the updated Schmidt number from (Wanninkhof, 2014).

MPIOM-HAMOCC

The Hamburg Ocean Carbon Cycle (HAMOCC) (Ilyina et al., 2013; Paulsen et al., 2017) model is a global ocean biogeochemical model embedded in the Max Planck Institute Ocean Model (MPIOM) (Jungclaus et al., 2013). The version used here is the same as used in the Global Carbon Budget 2021 (Friedlingstein et al., 2022). The nominal resolution here is 1.5 degree with 40 vertical levels.

The biogeochemical cycles of carbon, nutrients (nitrate, phosphate, iron), oxygen, silicate, phytoplankton (bulk and cyanobacteria), zooplankton, detritus, and organic matter in HAMOCC are computed in the water column and in the upper sediment. Biogeochemical tracers are transported with the ocean flow in the same way as temperature and salinity in MPIOM. The composition of organic matter follows a constant Redfield ratio of carbon (C:N:P:O2 = 122:16:1:-172). The sinking of organic matter follows the Martin curve, i.e. linearly increasing with depth. River inputs of carbon and nutrients are included (Lacroix et al., 2021). NCEP 6 hourly cyclic forcing (10 years starting from 1948) is used for the spin-up, transient NCEP forcing has been used during 1948- 2021.The air-sea gas exchange parameterization follows the OMIP protocol (Orr et al., 2017).

MRI-ESM2-1

MRI-ESM2-1 is a modified version for the ocean component of Meteorological Research Institute Earth System Model version 2 (MRI-ESM2) (Yukimoto et al., 2019). The source code is taken from Meteorological Research Institute Community Ocean Model version 4 (MRI.COMv4) (Tsujino et al., 2017), which is formulated on general orthogonal curvilinear coordinate in the horizontal and $z^\star$ coordinate in the vertical directions and is discretized on Arakawa B-grid frame. The horizontal resolution is 1.0° in the zonal and 0.3–0.5° in the meridional directions. There are 60 vertical levels with enhancement in the upper layer and an additional bottom boundary layer at the seafloor in the deep and bottom water formation regions such as the northern North Atlantic and in the Southern Ocean around Antarctica. The configuration and performance of this model in terms of physical fields are fully described and presented by Urakawa et al. (2020). The biogeochemical processes consist of a carbon cycle model with the carbonate chemistry and the surface gas exchange parameterization that follow the protocols of OMIP-BGC (Orr et al., 2017) and a simple NPZD (nutrient, phytoplankton, zooplankton, detritus) type ocean ecosystem model as used by (Nakano et al., 2011). Relative to the version used for CMIP6 (MRI-ESM2-0), the sinking velocity of detritus is changed from 7.0 m day-1 to 2.0 m day-1. Advection scheme for biogeochemical tracers is changed from MPDATA (Multi-dimensional Positive Definite Advection Tracer Algorism) to PPM (Piecewise Parabolic Method). The simulation was forced at the surface by the atmospheric state of JRA55-do v1.5.0 (Tsujino et al., 2018). Atmospheric CO_2 concentration is given as the spatially uniform, annual mean as specified by CMIP6 protocols and is linearly interpolated in time. No riverine inputs of nutrients or carbon and no burial are included. Instead, surface DIC and Alkalinity fluxes are added in proportion to surface salinity flux due to a restoring of the model sea surface salinity to that of World Ocean Atlas 2013 version 2 (WOA13v2).

NEMO-PlankTOM

The NEMO-PlankTOM model is based on the ORCA2 version of the NEMO physical model, which calculates vertical diffusion explicitly and includes a dynamic-thermodynamic sea-ice model. PlankTOM is the biogeochemical module that represents full cycles of carbon, oxygen, phosphorus, silica, calcite, and a simplified cycle for iron and nitrogen. PlankTOM12, used here for its estimate of CO_2 fluxes, represents twelve Plankton Functional Types, six phytoplankton, five zooplankton and archaea. The version used here is based on the work of (Wright et al., 2021) and integrates pteropods and the aragonite cycle from (Buitenhuis et al., 2019). This is the same version published in the Global Carbon Budget 2022 (Friedlingstein et al., 2022). The model is initialized in 1750 and run forward with constant atmospheric forcing up to 1948, then forced with daily weather conditions using the NCEP reanalysis data, and constant input of nutrient (N, P and Fe) and organic and inorganic carbon from rivers (see also Friedlingstein et al. 2022). NCEP winds are also used to calculate the gas exchange velocity using (Wanninkhof, 1992) formulation. PlankTOM5 is used to estimate N_2O fluxes. PlankTOM5 uses a simplified ecosystem composition with three phytoplankton and two zooplankton, and a full representation of N_2O production and loss processes (Buitenhuis et al., 2018).

NorESM-OC2.0

NorESM-OC2.0 is the ocean carbon-cycle stand-alone configuration of the Norwegian Earth System Model version 2 (NorESM2, (Seland et al., 2020; Tjiputra et al., 2020). The physical ocean component of NorESM2, the Bergen Layered Ocean Model (BLOM), is configured on a tripolar grid with a nominal resolution of 1° horizontally and 51 isopycnic layers in the vertical with 2 additional layers representing a bulk mixed layer on top. Ocean biogeochemistry is represented by the iHAMOCC model, which is derived from HAMOCC5 (Ilyina et al., 2013) and includes a 12-layer sediment scheme. The iHAMOCC model includes a NPZD ecosystem parameterization (Six & Maier-Reimer, 1996) and carbon chemistry follows the OCMIP protocols (Orr et al., 2015). The influx of carbon and nutrients from rivers to the coastal oceans has been implemented based on the Global-NEWS2 model (Mayorga et al., 2010) and work by (Hartmann et al., 2009) for DIC and alkalinity fluxes. Riverine fluxes are distributed as a function of river mouth distance (with an e-folding length scale of 1000 km and cutoff of 300 km) to the ocean grid and are assumed to be constant over time at year 2000 levels. The NorESM-OC2.0 simulation used here follows the CMIP6 omip2 protocol, which employs the JRA-55 atmospheric forcing data set. The gas exchange coefficient formulation is from (Wanninkhof, 2014).

ECCO2-Darwin and ECCO-Darwin

Global air-sea fluxes of N_2O were evaluated from two versions of the ECCO family: the ECCO2-Darwin and ECCO-Darwin models which include the same biogeochemical component Darwin but are embedded in two different ocean physical settings. ECCO2-Darwin model, is a global physical-biogeochemical ocean model with nominal horizontal grid of 1/6 of degree therefore eddy-permitting at lower latitudes. It is forced with ECMWF winds over the 2006-2008 period and JRA-55 winds over the 2009-2013 period, optimized with adjoint technique in order to realistically represent the observed physical ocean climate variability. ECCO-Darwin, a global physical-biogeochemical ocean model with nominal horizontal grid resolution of 1/3 of degree, and is forced with ERA-Interim winds (Carroll et al., 2020). Both models have 50 vertical levels and in the top 100 m the model is vertically resolved with 10-meter grid boxes. An extensive description of this model run of ECCO2-Darwin including the optimized atmospheric forcing spanning from 2004 to 2013 can be found in (Manizza et al., 2019) while for ECCO-Darwin a more detailed model description can be found in Carroll et al. (2020). The Darwin biogeochemical/ecological model used for this study explicitly represents the cycle of carbon, oxygen, phosphorus, silica, and iron in the global ocean. It also has an ecosystem component representing five groups of phytoplankton and two groups of zooplankton (Manizza et al., 2019; Carroll et al., 2020). For this particular version of the model we implemented a parameterization of the oceanic cycle of (Manizza et al., 2012) using the scheme of (Nevison et al., 2003) based on the oceanic oxygen cycle previously represented in ECCO2-Darwin model (Ganesan et al., 2020). The air-sea gas flux of N_2O was parameterized according to Wanninkhof (1992). In addition, a thermal-only N_2O

tracer (a tracer in which biogeochemical sources and sinks are suppressed but with the same solubility as N_2O) was also added to the model to isolate the process of ocean ventilation affecting the N_2O concentration in the ocean at seasonal time scales as done in (Manizza et al., 2012). The ventilation component of the air-sea N_2O fluxes is obtained by subtracting the solubility-only N_2O air-sea flux from the total N_2O air-sea flux. In the ECCO2-Darwin simulation the 2004-2005 period was discarded and we used the 2006-2013 period only for our analysis. However, the ECCO-Darwin numerical simulation was run for the 1992-2014 period but we discarded the inclusion of the output relative to the 1992-1996 period in our analysis due to the model adjustment in this initial part of our numerical simulation.

S1.d Regional ocean biogeochemical models

ACM-NWAtl

The model is based on the Rutgers version of the Regional Ocean Modelling System (ROMS) (Haidvogel et al., 2008), has 30 vertical levels and approximately 10 km horizontal resolution (240×120 horizontal grid cells). The model uses atmospheric surface forcing from the European Centre for Medium-Range Weather Forecasts (ECMWF) global atmospheric reanalysis (ERA-Interim) (Dee et al., 2011), and CO_2 fluxes are calculated following the Ho et al. (2006) parameterization. Within the ocean, it uses the GLS vertical mixing scheme (Umlauf & Burchard, 2003; Warner et al., 2005), and the "high-order spatial interpolation at the middle temporal level" (HSIMT) advection scheme for tracers (Wu & Zhu, 2010). Physical initial and boundary conditions are defined using the regional physical ocean model of the northwest North Atlantic by Urrego-Blanco and Sheng (2012). Climatological river discharge is imposed for 12 major rivers and uses observed long-term monthly means from the Water Survey of Canada. Full details on the physical model setup and its validation can be found in Brennan et al. (2016) and Rutherford and Fennel (2018). These studies have shown that the model simulates the vertical structure and seasonal variations of temperature and salinity on the shelf well. The model captures mesoscale features and coastal upwelling events and simulates the volume transport throughout the region in agreement with observation-based estimates.

The biogeochemical model is based on the nitrogen-cycle model with the inorganic carbon component of (Fennel et al., 2006) and Fennel and Wilkin (2009) but was recently expanded to include two phytoplankton and two zooplankton functional groups (Laurent et al., 2021). For a detailed description and validation of the biological model and the model's carbonate system parameters, we refer to Laurent et al. (2021) and Rutherford et al. (2021) respectively. Laurent et al. (2021) compared the model output with glider transects of temperature, salinity, and chlorophyll and in situ measurements of chlorophyll and nitrate. Rutherford et al. (2021) compared models results against a high-resolution pCO_2 time series and frequent cross-shelf transects of pCO_2 to ensure it faithfully represents both the seasonal cycle and cross-shelf gradients. Atmospheric pCO_2 is set to the seasonal cycle and secular trend derived from Sable Island monitoring data contributed by Environment Canada's Greenhouse Gas Measurement Program (Environment and Climate Change Canada: Canadian Greenhouse Gas Measurement Program). The long-term linear trend in the atmospheric pCO_2 is $\sim$2 uatm yr^{-1}. Further details of the biogeochemical model, including the carbonate chemistry equations, can be found in the supplementary information of (Laurent et al., 2017). Nitrate concentrations in rivers are prescribed from Global NEWS model output (Seitzinger et al., 2005). DIC and total alkalinity (TA) in rivers were calculated by fitting a linear relationship with salinity from Gulf of St. Lawrence bottle data and extrapolating to river water salinity.

ROMS-ETHZ-Atl and ROMS-ETHZ-Pac

The two regional models ETHZ-ROMS-Pac and ETHZ-ROMS-Atl rely on the coupling of the Regional Oceanic Modeling System (ROMS) (Shchepetkin & McWilliams, 2005) with the biogeochemical/ecological model BEC (Moore et al., 2013). Both setups rely on a telescopic grid that permits the model to resolve the mesoscale coastal processes in the region of interest, while covering at the same time nearly the entire ocean basin. In the ETHZ-ROMS-Pac setup, the telescopic grid is centered on the US West coast (resolution 4km), while in the ETHZ-ROMS-Atl setup, the telescopic grid has two poles, one centered in the Amazon outflow region (resolution 4km), and one on Western Africa. BEC simulates the cycling of carbon and 4 nutrients (N, P, Si, Fe) which govern, along with light and temperature, the growth of three phytoplankton types (Small Phytoplankton, Diatoms and Trichodesmium). The ETHZ-ROMS-Atl setup includes a fourth phytoplankton type representing a symbiosis between a diatom and a N2-fixer, i.e., Diatom-Diazotroph-Assemblages that have been shown to be regionally important for the cycling of carbon (Louchard et al., 2021). All phytoplankton are grazed by one zooplankton class. Particulate organic matter (POM) is produced as a result of non-grazing mortality, aggregation or grazing processes. POM is then exported and remineralized in an explicit manner (Frischknecht, 2018) in ETHZ-ROMS-Pac and following an implicit scheme in ETHZ-ROMS-Atl (Armstrong et al., 2001). The atmospheric forcing of surface short and long-wave radiations, wind stress, and surface freshwater fluxes is derived from the hourly ERA5 regridded product from 1979 to 2019 (Copernicus Climate Change Service [C3S], 2017; (Hersbach et al., 2020)). Additionally, the atmospheric forcing includes monthly varying atmospheric pCO_2 provided by (Landschützer et al., 2020), considering the dry air mixing ratio for the marine boundary layer from GLOBALVIEW-CO2 (2014), the atmospheric pressure and the water vapor contribution from Dickson et al. (2007). Also included in the atmospheric forcing are the input of iron from dust and nitrogen deposition, and only in the ETHZ-ROMS-Atl setup, phosphorus deposition, all derived from (Mahowald et al., 2009). The initial conditions and the boundary conditions are based on World Ocean Atlas for the main nutrients (Garcia et al., 2014). For DIC and Alkanity, GLODAP gridded products (Global Ocean Data Analysis Project version 2, (Lauvset et al., 2016)) are used as a climatology (centered on 2002) in ETHZ-ROMS-Alt and to create transiently evolving conditions in ETHZ-ROMS-Pac, following the procedures described by (Franco et al., 2018). Major rivers in the domain are represented as a surface flux of freshwater and nutrients (N,P) as described in (Frischknecht, 2018). One exception in the ETHZ-ROMS-Atl setup is the Amazon River that is represented by an inflow across an open lateral boundary condition and is delivering the whole suite of dissolved inorganic/organic nutrients and dissolved organic/inorganic carbon (estimates based on (Araujo et al., 2014)).

ROMS-NYUAD-Indian

The circulation model is based on the Regional Ocean Modeling System (ROMS) (Shchepetkin & McWilliams, 2005). Vertical mixing is represented using the non-local K-profile parameterization (KPP) scheme (Large et al., 1994). The model domain covers the Indian Ocean from 31.5S to 31N and 30E to 120E with a 1/10 degree horizontal resolution and 32 sigma-coordinate vertical layers with refined resolution near the surface. Coupled to the hydrodynamic model is a nitrogen-based nutrient, phytoplankton zooplankton, detritus (NPZD) model with two components for nutrients, nitrate and ammonium, one phytoplankton, one zooplankton, and two detrital classes (Gruber

et al., 2006). The model has a module describing the cycling of oxygen as well as a parameterization of water column and benthic denitrification (Lachkar et al., 2016, 2021). The model also includes a carbon module with three state variables: DIC, Total Alkalinity, and calcium carbonate (Gruber et al., 2012; Lachkar & Gruber, 2013; de Verneil et al., 2022). Organic carbon is linked to organic nitrogen through the Redfield ratio 106:16. Surface fluxes of DIC and Total Alkalinity driven by changes in sea surface salinity are included as virtual fluxes proportional to the sea surface salinity forcing. Carbonate chemistry is calculated using routines from the Ocean Carbon-Cycle Model Intercomparison Project (OCMIP) (Orr et al., 2005). The formulation of air-sea gas transfer uses a quadratic wind speed dependence following Wanninkhof (1992). Further details of the biogeochemical model are provided in (Lachkar et al., 2021; de Verneil et al., 2022). The hindcast simulation is forced with ECMWF ERA-Interim 6-hourly heat fluxes, air temperature, pressure, humidity, precipitation and winds over the period from January 1980 to December 2018. Initial and lateral boundary conditions for temperature, salinity, currents and sea surface height are based on the ECMWF Ocean Reanalysis System 5 (ORAS5). The initial and lateral boundary conditions for nitrate and oxygen are extracted from the World Ocean Atlas 2018. The initial and lateral boundary conditions for DIC and alkalinity are based on GLODAP. Atmospheric CO_2 concentrations are prescribed from monthly Mona Loa data (Keeling et al., 2005). Riverine inputs include nutrients (Krishna et al., 2016; Ramesh et al., 1995) but no carbon or alkalinity. To account for the accumulation of anthropogenic carbon at the lateral boundaries during the simulation period, we used decadally-varying DIC based on available estimates of anthropogenic CO_2 (Key et al., 2004; Gruber et al., 2019; Olsen et al., 2019) regressed to atmospheric CO_2 concentrations. Initial and boundary conditions for DIC and alkalinity are processed following de Verneil et al. (2022) to include a seasonal cycle in the upper ocean. The model is spun up for 30 years with a repeated normal year (1984) forcing. During the spin-up phase (1950-1979), time-varying atmospheric CO_2 concentrations and DIC are prescribed at the atmospheric and lateral boundaries, respectively. Atmospheric CO_2 data prior to 1958 is based on (Joos & Spahni, 2008).

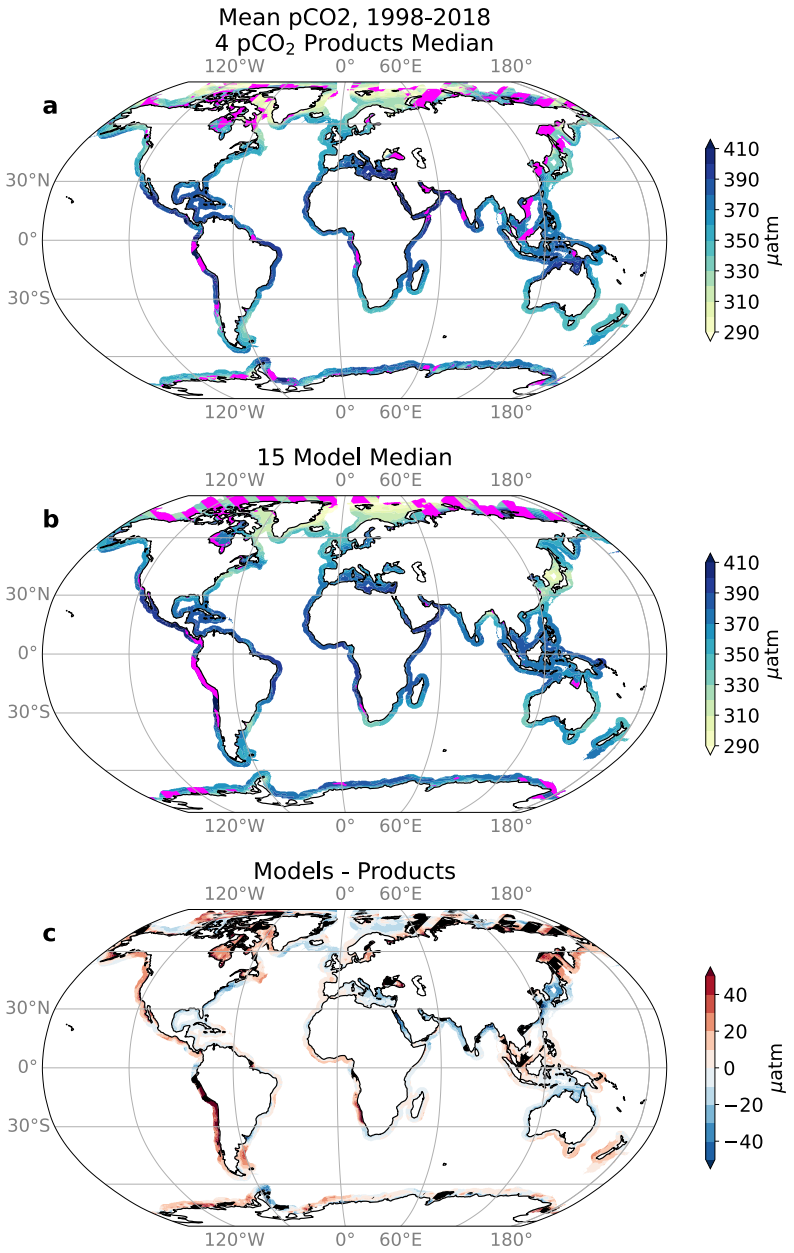


Figure S4. Annual mean coastal pCO_2 (in wide shelf waters) for a) the 4-product median, b) the 15-model median, and c) the difference between model and product medians. The model median in each point is calculated using the 11 global models and the 4 regional models. All are for 1998-2018 except coastal-SOM-FFN and merged-SOM-FFN pCO_2 products available for 1998-2015 only. Hatching indicates the coastal area with RMSD greater than 25 uatm across pCO_2 products (panels a and c) or 33 uatm across models (panel b) (20% of coastal area with highest RMSD in each case). Here pCO_2 is masked where sea ice on average covers 50% of the grid cell, to improve visual comparison with the flux.

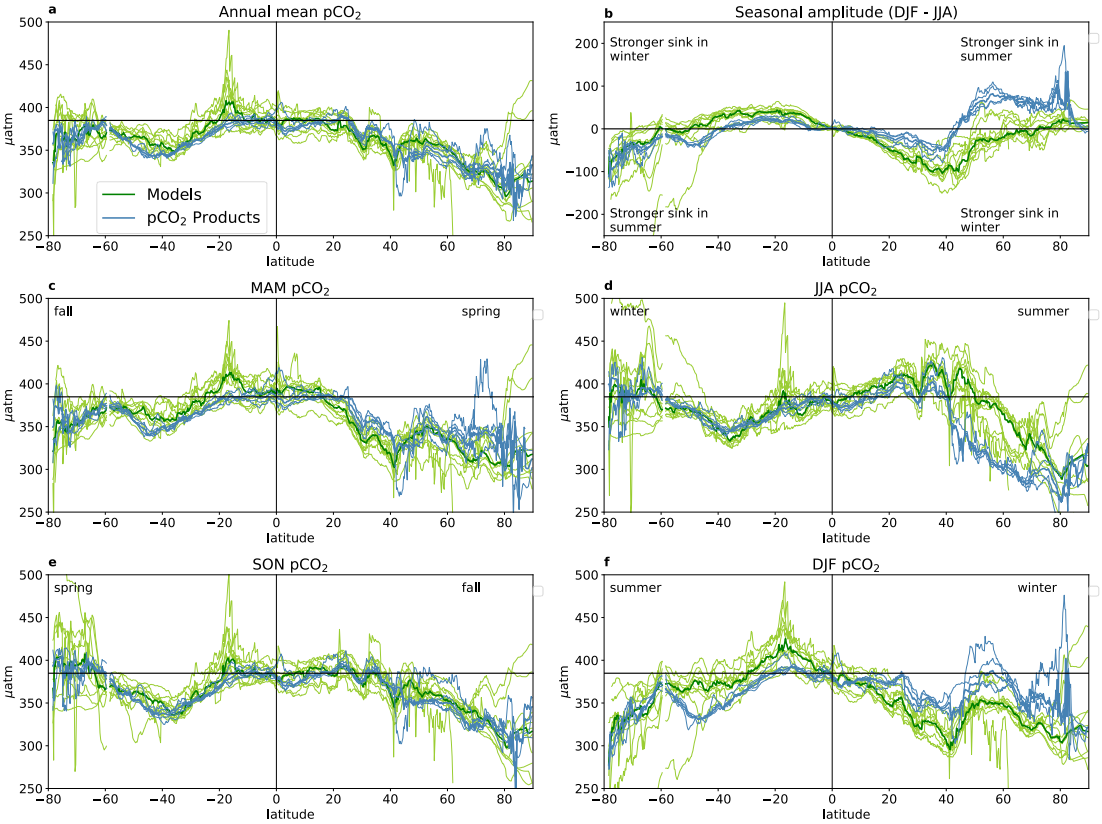


Figure S5. Latitudinal distribution of coastal ocean (wide shelf) a) annual mean pCO_2, b) pCO_2 seasonal amplitude computed as December-February minus June-August, c) March-May pCO_2, d) June-August pCO_2 , e) September-November pCO_2, and f) December-February pCO_2 for the product and model medians (thick lines). Thin lines indicate the mean pCO_2 in each of 11 global models (green) and the 4 products (blue).

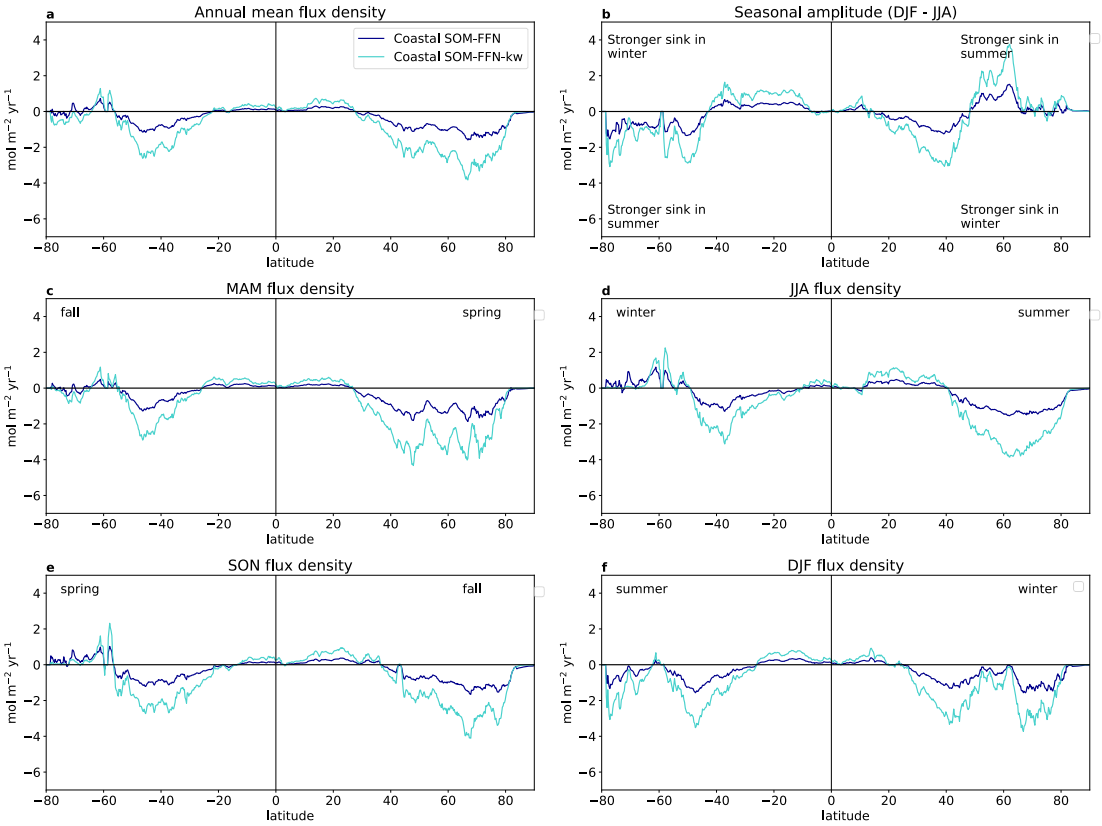


Figure S6. Influence of wind speed and gas exchange coefficient. Latitudinal distribution of coastal ocean (wide shelf) a) annual mean CO_2 flux, b) CO_2 flux seasonal amplitude computed as December-February minus June-August, c) March-May CO_2 flux, d) June-August CO_2 flux, e) September-November CO_2 flux, and f) December-February CO_2 flux in Coastal-SOM-FFN and Coastal SOM-FFN-kw (different wind product and gas exchange coefficient formulation, see Methods).

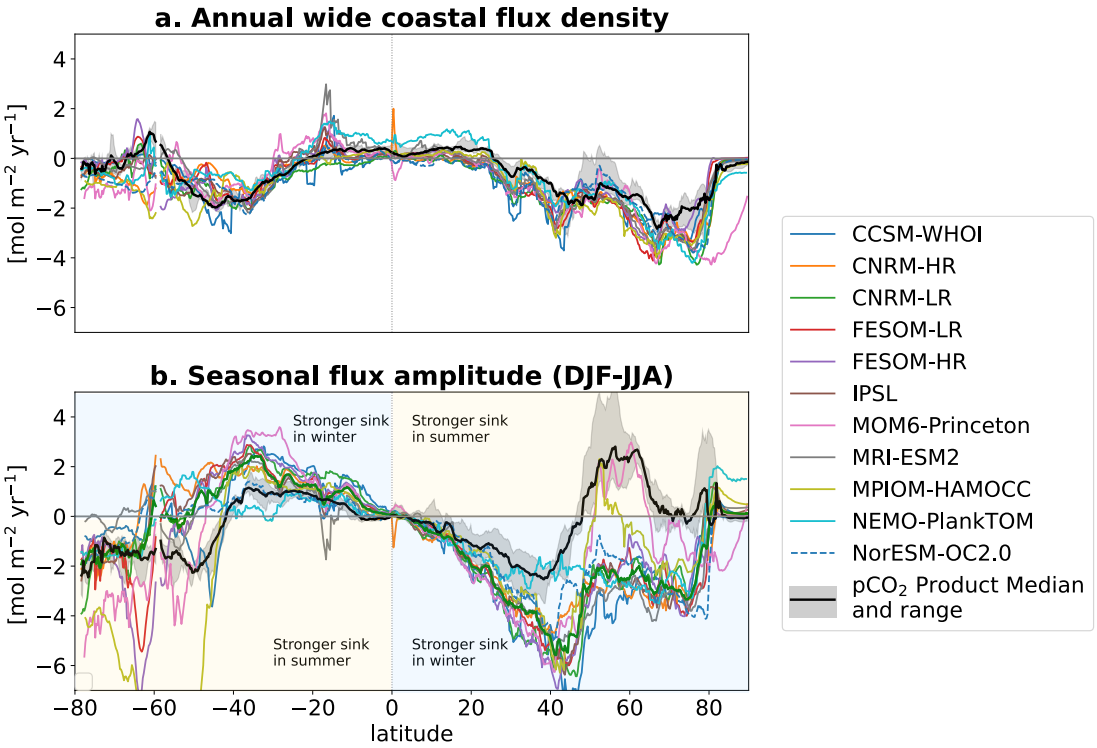


Figure S7. Latitudinal distribution of coastal ocean (wide shelf) a) annual mean CO_2 flux densities, b) CO_2 flux densities seasonal amplitude computed as December-February minus June-August, for the pCO_2 -product median and range (black line and grey shading) and each individual models (colored lines).

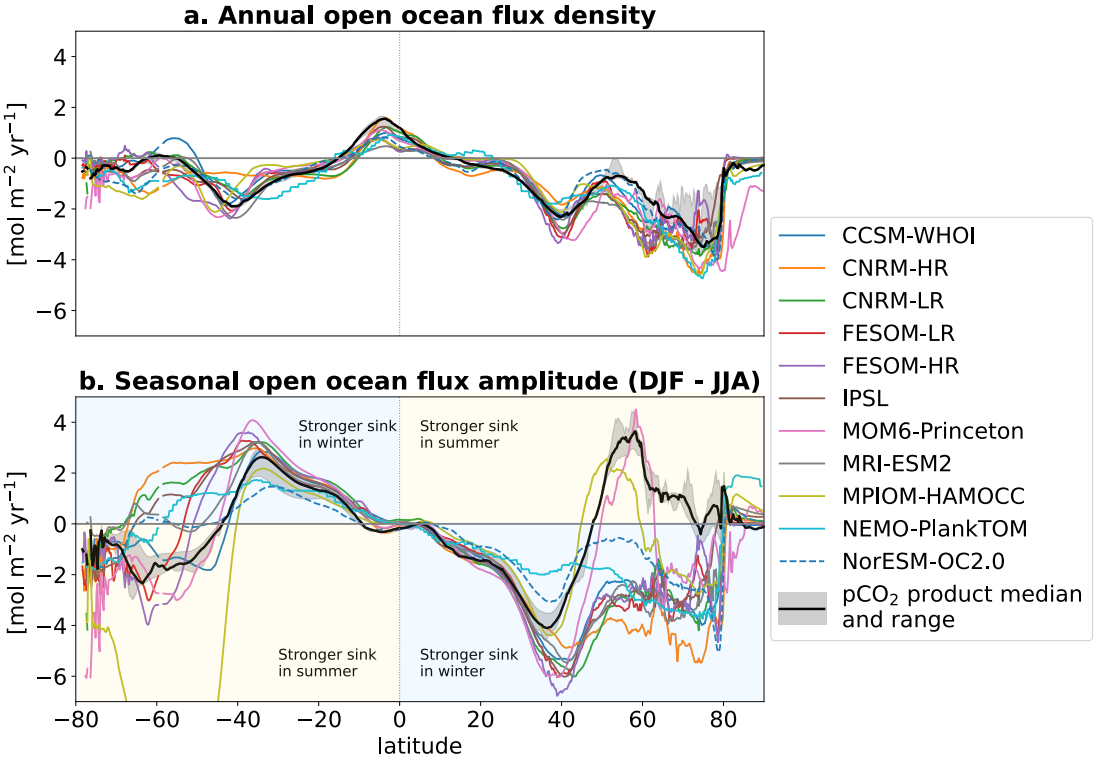


Figure S8. Latitudinal distribution of open ocean a) annual mean CO_2 flux densities, b) CO_2 flux densities seasonal amplitude computed as December-February minus June-August, for the pCO_2-product median (black line) and each individual models (colored lines). Note that the product median only includes the 3 (out of 4) products with open ocean values (CMEMS*, Carboscope-1 and Merged-SOM-FFN).

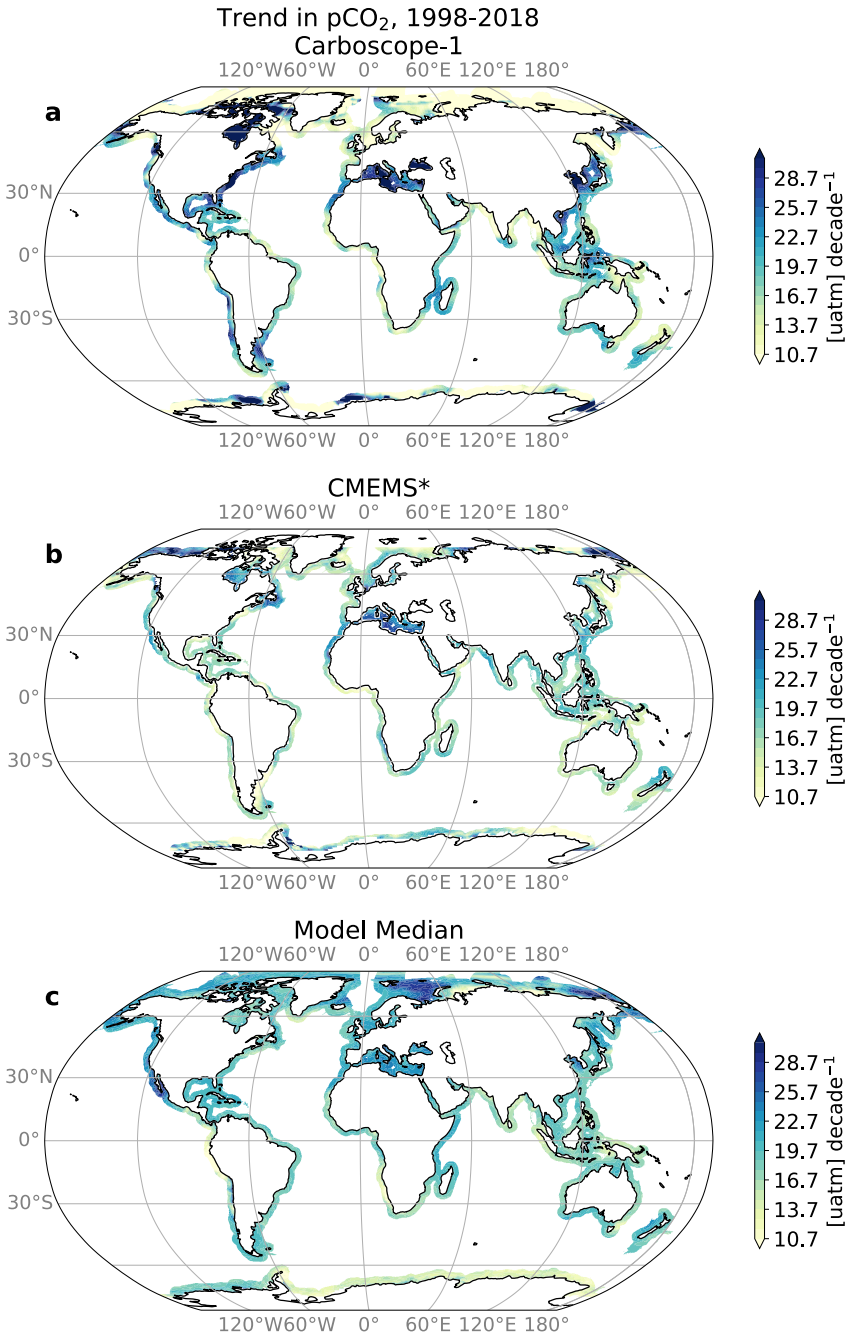


Figure S9. 1998-2018 trend in surface ocean pCO_2 in a) Carboscope-1 ; b) CMEMS* (area north of 75°N removed) c) multi-model median (global and regional models).

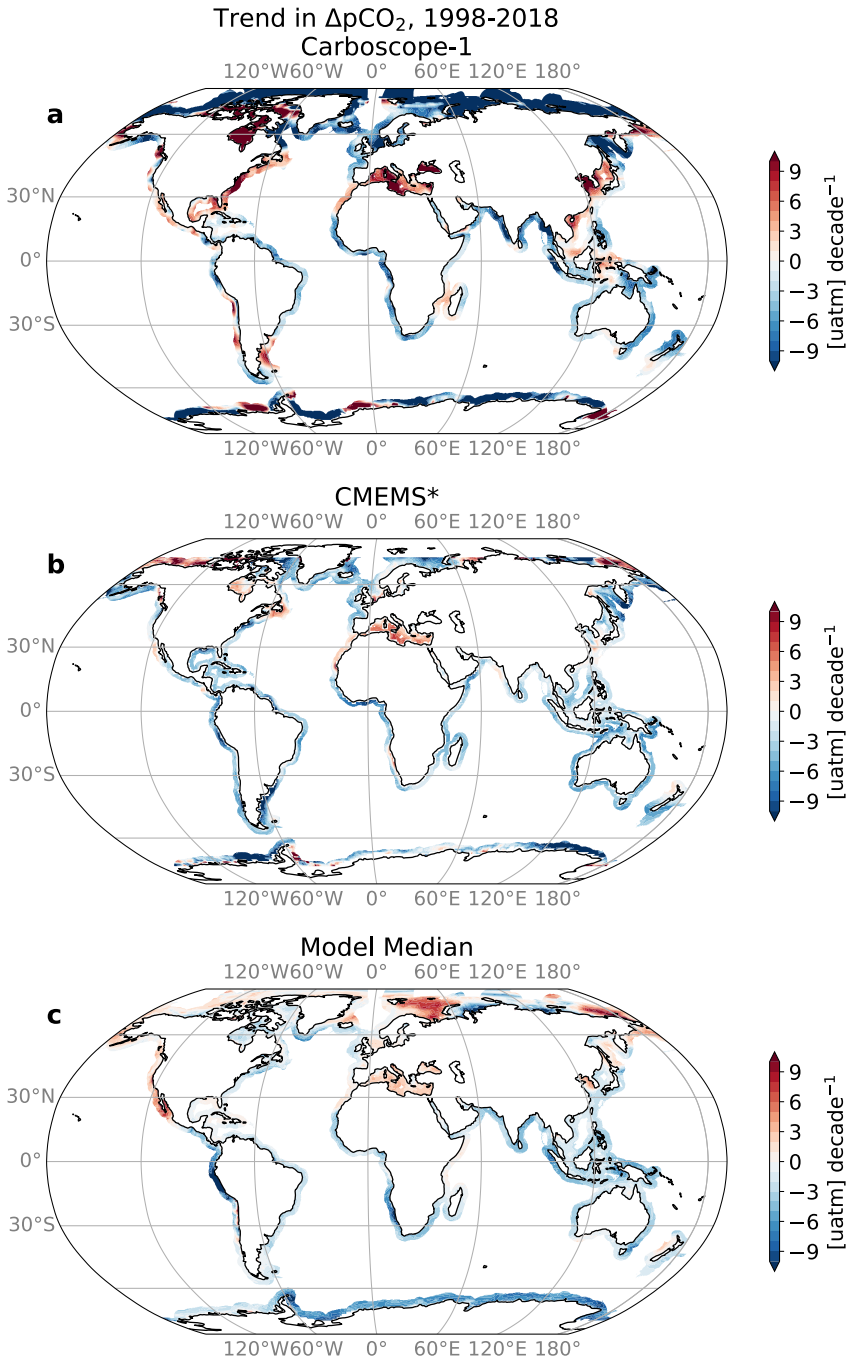


Figure S10. 1998-2018 trend in ΔpCO_2 (difference between coastal ocean surface ocean pCO_2 and atmospheric) for a) Carboscope-1; b) CMEMS* (area north of 75°N removed) c) multi-model median (global and regional models). Negative ΔpCO_2 trend values indicate that ocean pCO_2 increases at a lower rate than atmospheric and would therefore favor ocean uptake assuming constant wind and sea-ice coverage.

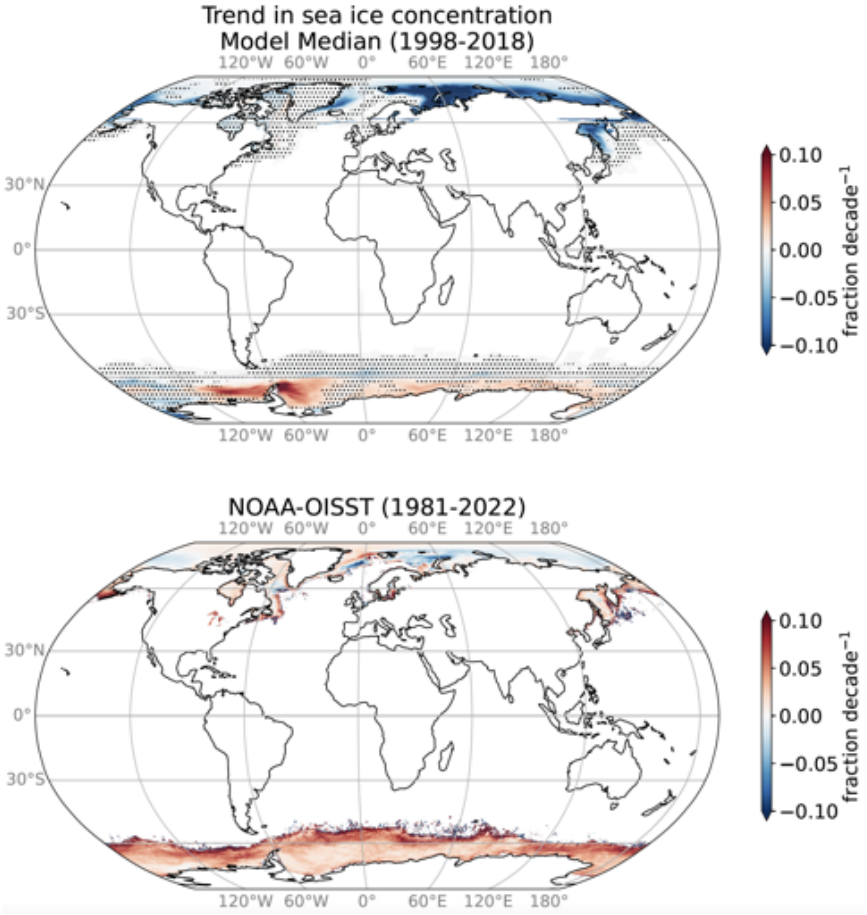


Figure S11. Linear trends in sea ice fraction from all 15 models median (top) and observation-based reference product NOAA-OISST (bottom). Stippling indicates where less than 6 out of the 11 global models agree on the sign of change.

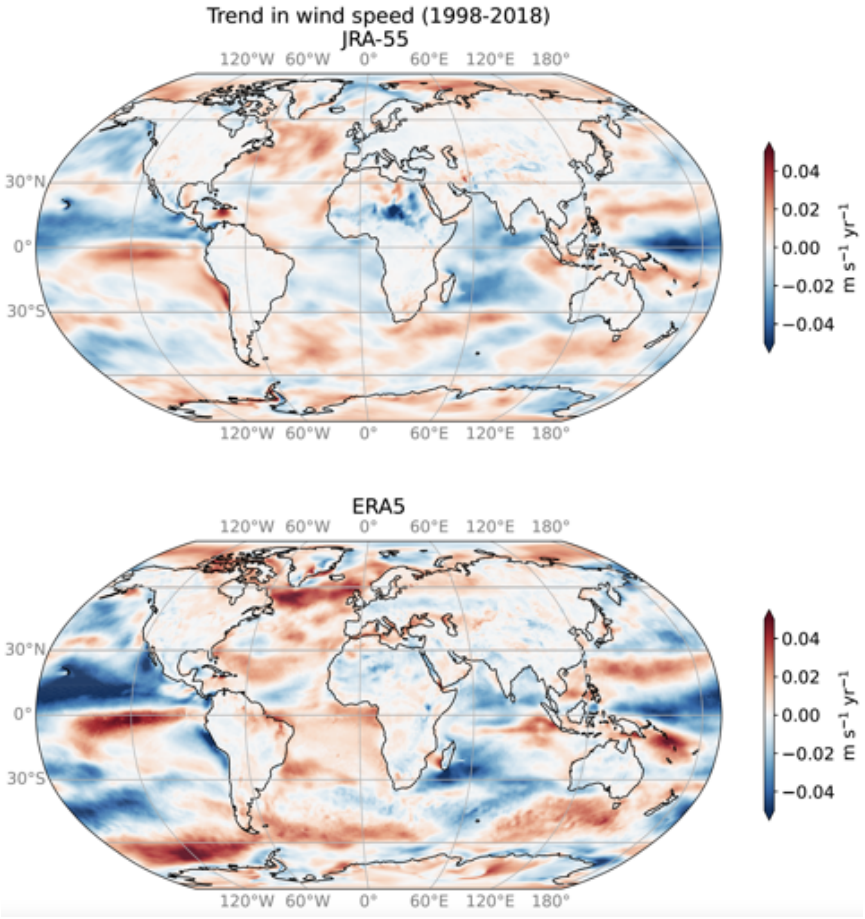


Figure S12. Linear trends in 10-meter wind speed from Japanese reanalysis JRA-55 (top) and ECMWF Reanalysis ERA-5 (bottom).

Table S2. Estimates of mean coastal ocean CO_2 flux densities, net CO_2 uptake and pCO_2 trends published since RECCAP-1 (Chen et al., 2013) and used in figures in the main text. Most prior estimates are given for coastal ocean areas similar to the area of the narrow coastal ocean used in this study (i.e. 28 million km^2).

Study	Mean coastal CO_2 flux density [mol m^{-2} yr^{-1}]	Net coastal CO_2 uptake [PgC yr^{-1}]	Coastal pCO_2 trends [uatm/decade]	Coastal area [million km^2]
Chen et al. (2013)	-1.09±2.9	-0.25±0.05	NA	30
Bauer et al. (2013)	NA	-0.25	NA	26
Laruelle et al. (2013)	-0.7	NA	NA	NA
Regnier et al. (2013)	NA	-0.2	NA	31
Laruelle et al. (2014)	-0.56 (global shelf) -0.7 (ice-free shelf)	-0.19±0.5 (1990-2011)	NA	28 22
Bourgeois et al. (2016)	NA	-0.1 (1993-2012)	NA	27
H. Wang et al. (2017)	NA	NA	+19.3±15.9 (from 10-30yr intervals in 1957-2014)	NA
Laruelle et al. (2018)	NA	-0.26 winter only	+13 [-6 to +32] winter only 1995-2006	30 (only 14 covered by obs. used)
Lacroix et al. (2021)	NA	-0.15 (1998-2015)	NA	24.5
Dai et al. (2022)	-0.68±0.14	-0.25±0.05 (1998-2021)	NA	30.32
Regnier et al. (2022)	NA	-0.32±0.08 (1990-2020)	NA	28

References

Adcroft, A., Anderson, W., Balaji, V., Blanton, C., Bushuk, M., Dufour, C. O., ... Zhang, R. (2019). The GFDL Global Ocean and Sea Ice Model OM4.0: Model Description and Simulation Features. *Journal of Advances in Modeling Earth Systems*, *11*(10), 3167–3211. Retrieved 2020-10-02, from https://agupubs.onlinelibrary.wiley.com/doi/abs/10.1029/2019MS001726 doi: 10.1029/2019MS001726

Araujo, M., Noriega, C., & Lefevre, N. (2014, May). Nutrients and carbon fluxes in the estuaries of major rivers flowing into the tropical Atlantic. *Frontiers in Marine Science*, *1*. Retrieved 2023-02-15, from http://journal.frontiersin.org/article/10.3389/fmars.2014.00010/abstract doi: 10.3389/fmars.2014.00010

Armstrong, R. A., Lee, C., Hedges, J. I., Honjo, S., & Wakeham, S. G. (2001, January). A new, mechanistic model for organic carbon fluxes in the ocean based on the quantitative association of POC with ballast minerals. *Deep Sea Research Part II: Topical Studies in Oceanography*, *49*(1-3), 219–236. Retrieved 2023-02-15, from https://linkinghub.elsevier.com/retrieve/pii/S0967064501001011 doi: 10.1016/S0967-0645(01)00101-1

Aumont, O., Ethé, C., Tagliabue, A., Bopp, L., & Gehlen, M. (2015, August). PISCES-v2: an ocean biogeochemical model for carbon and ecosystem studies. *Geoscientific Model Development*, *8*(8), 2465–2513. Retrieved 2023-02-15, from https://gmd.copernicus.org/articles/8/2465/2015/gmd-8-2465-2015.html (Publisher: Copernicus GmbH) doi: 10.5194/gmd-8-2465-2015

Bakker, D. C. E., Pfeil, B., Landa, C. S., Metzl, N., O'Brien, K. M., Olsen, A., ... Xu, S. (2016, September). A multi-decade record of high-quality fCO_2 data in version 3 of the Surface Ocean CO_2 Atlas (SOCAT). *Earth System Science Data*, *8*(2), 383–413. Retrieved from https://www.earth-syst-sci-data.net/8/383/2016/ doi: https://doi.org/10.5194/essd-8-383-2016

Barnier, B., Madec, G., Penduff, T., Molines, J., Treguier, A.-M., Le Sommer, J., ... de Cuevas, B. (2006, December). Impact of partial steps and momentum advection schemes in a global ocean circulation model at eddy-permitting resolution. *Ocean Dynamics*, *56*(5-6), 543–567. Retrieved 2023-02-15, from https://archimer.ifremer.fr/doc/00000/3514/ (Publisher: Springer) doi: 10.1007/s10236-006-0082-1

Bauer, J. E., Cai, W.-J., Raymond, P. A., Bianchi, T. S., Hopkinson, C. S., & Regnier, P. A. G. (2013, December). The changing carbon cycle of the coastal ocean. *Nature*, *504*(7478), 61–70. Retrieved 2016-01-12, from http://www.nature.com/nature/journal/v504/n7478/abs/nature12857.html doi: 10.1038/nature12857

Bernard, B., Madec, G., Penduff, T., Molines, J.-M., Treguier, A.-M., Le Sommer, J., ... De Cuevas, B. (2006, December). Impact of partial steps and momentum advection schemes in a global ocean circulation model at eddy-permitting resolution. *Ocean Dynamics*, *56*(5), 543–567. Retrieved 2023-02-15, from https://doi.org/10.1007/s10236-006-0082-1 doi: 10.1007/s10236-006-0082-1

Berthet, S., Jouanno, J., Séférian, R., Gehlen, M., & Llovel, W. (2022, August). How does the phytoplankton-light feedback affect marine N_2O inventory? *Earth Syst. Dynam. Discuss.*. Retrieved 2023-03-01, from https://esd.copernicus.org/preprints/

esd-2022-28/ doi: 10.5194/esd-2022-28

Berthet, S., Séférian, R., Bricaud, C., Chevallier, M., Voldoire, A., & Ethé, C. (2019, June). Evaluation of an Online Grid-Coarsening Algorithm in a Global Eddy-Admitting Ocean Biogeochemical Model. *Journal of Advances in Modeling Earth Systems*, *11*(6), 1759–1783. Retrieved 2023-03-01, from https://onlinelibrary.wiley.com/doi/abs/10.1029/2019MS001644 doi: 10.1029/2019MS001644

Bourgeois, T., Orr, J. C., Resplandy, L., Terhaar, J., Ethé, C., Gehlen, M., & Bopp, L. (2016, July). Coastal-ocean uptake of anthropogenic carbon. *Biogeosciences*, *13*(14), 4167–4185. Retrieved 2016-09-23, from http://www.biogeosciences.net/13/4167/2016/ doi: 10.5194/bg-13-4167-2016

Brennan, C. E., Bianucci, L., & Fennel, K. (2016, May). Sensitivity of Northwest North Atlantic Shelf Circulation to Surface and Boundary Forcing: A Regional Model Assessment. *Atmosphere-Ocean*, *54*(3), 230–247. Retrieved 2023-02-15, from https://www.tandfonline.com/doi/full/10.1080/07055900.2016.1147416 doi: 10.1080/07055900.2016.1147416

Buitenhuis, E. T., Le Quéré, C., Bednaršek, N., & Schiebel, R. (2019, March). Large Contribution of Pteropods to Shallow CaCO 3 Export. *Global Biogeochemical Cycles*, *33*(3), 458–468. Retrieved 2023-02-15, from https://onlinelibrary.wiley.com/doi/abs/10.1029/2018GB006110 doi: 10.1029/2018GB006110

Buitenhuis, E. T., Suntharalingam, P., & Le Quéré, C. (2018, April). Constraints on global oceanic emissions of N2O from observations and models. *Biogeosciences*, *15*(7), 2161–2175. Retrieved 2023-02-07, from https://bg.copernicus.org/articles/15/2161/2018/ (Publisher: Copernicus GmbH) doi: 10.5194/bg-15-2161-2018

Carroll, D., Menemenlis, D., Adkins, J. F., Bowman, K. W., Brix, H., Dutkiewicz, S., ... Zhang, H. (2020, October). The ECCO-Darwin Data-Assimilative Global Ocean Biogeochemistry Model: Estimates of Seasonal to Multidecadal Surface Ocean *p* CO 2 and Air-Sea CO 2 Flux. *Journal of Advances in Modeling Earth Systems*, *12*(10). Retrieved 2023-02-15, from https://onlinelibrary.wiley.com/doi/10.1029/2019MS001888 doi: 10.1029/2019MS001888

Chau, T. T. T., Gehlen, M., & Chevallier, F. (2022, February). A seamless ensemble-based reconstruction of surface ocean pCO2and air–sea CO2 fluxes over the global coastal and open oceans. *Biogeosciences*, *19*(4), 1087–1109. Retrieved 2023-02-15, from https://bg.copernicus.org/articles/19/1087/2022/ doi: 10.5194/bg-19-1087-2022

Chen, C.-T. A., Huang, T.-H., Chen, Y.-C., Bai, Y., He, X., & Kang, Y. (2013, October). Air–sea exchanges of CO2 in the world's coastal seas. *Biogeosciences*, *10*(10), 6509–6544. Retrieved 2021-09-03, from https://bg.copernicus.org/articles/10/6509/2013/ doi: 10.5194/bg-10-6509-2013

Dai, M., Su, J., Zhao, Y., Hofmann, E. E., Cao, Z., Cai, W.-J., ... Wang, Z. (2022). Carbon Fluxes in the Coastal Ocean: Synthesis, Boundary Processes, and Future Trends. *Annual Review of Earth and Planetary Sciences*, *50*(1), 593–626. Retrieved 2022-09-26, from https://doi.org/10.1146/annurev-earth-032320-090746 (_eprint: https://doi.org/10.1146/annurev-earth-032320-090746) doi: 10.1146/annurev-earth-032320-090746

Dee, D. P., Uppala, S. M., Simmons, A. J., Berrisford, P., Poli, P., Kobayashi, S., ... Vitart, F. (2011, April). The ERA-Interim reanalysis: configuration and performance of the data assimilation system. *Quarterly Journal of the Royal Meteorological Society*, *137*(656), 553–597. Retrieved 2023-02-15, from https://onlinelibrary.wiley.com/doi/10.1002/qj.828 doi: 10.1002/qj.828

de Verneil, A., Lachkar, Z., Smith, S., & Lévy, M. (2022, February). Evaluating the Arabian Sea as a regional source of atmospheric CO₂: seasonal variability and drivers. *Biogeosciences*, *19*(3), 907–929. Retrieved 2023-02-15, from https://bg.copernicus.org/articles/19/907/2022/ doi: 10.5194/bg-19-907-2022

Dickson, A. G., Sabine, C. L., Christian, J. R., Bargeron, C. P., & Organization, N. P. M. S. (Eds.). (2007). *Guide to best practices for ocean CO2 measurements* (No. no. 3). Sidney, BC: North Pacific Marine Science Organization.

Doney, S. C., Lima, I., Feely, R. A., Glover, D. M., Lindsay, K., Mahowald, N., ... Wanninkhof, R. (2009, April). Mechanisms governing interannual variability in upper-ocean inorganic carbon system and air–sea CO2 fluxes: Physical climate and atmospheric dust. *Deep Sea Research Part II: Topical Studies in Oceanography*, *56*(8-10), 640–655. Retrieved 2018-09-13, from http://linkinghub.elsevier.com/retrieve/pii/S096706450800427X doi: 10.1016/j.dsr2.2008.12.006

Dunne, J. P., Horowitz, L. W., Adcroft, A. J., Ginoux, P., Held, I. M., John, J. G., ... Zhao, M. (2020). The GFDL Earth System Model Version 4.1 (GFDL-ESM 4.1): Overall Coupled Model De-

scription and Simulation Characteristics. *Journal of Advances in Modeling Earth Systems*, *12*(11), e2019MS002015. Retrieved 2021-10-11, from https://onlinelibrary.wiley.com/doi/abs/10.1029/2019MS002015 doi: 10.1029/2019MS002015

Dunne, J. P., Sarmiento, J. L., & Gnanadesikan, A. (2007, December). A synthesis of global particle export from the surface ocean and cycling through the ocean interior and on the seafloor. *Global Biogeochemical Cycles*, *21*(4), GB4006. Retrieved 2016-02-08, from http://onlinelibrary.wiley.com/doi/10.1029/2006GB002907/abstract doi: 10.1029/2006GB002907

Fennel, K., & Wilkin, J. (2009, September). Quantifying biological carbon export for the northwest North Atlantic continental shelves. *Geophysical Research Letters*, *36*(18), L18605. Retrieved 2023-02-15, from http://doi.wiley.com/10.1029/2009GL039818 doi: 10.1029/2009GL039818

Fennel, K., Wilkin, J., Levin, J., Moisan, J., O'Reilly, J., & Haidvogel, D. (2006, September). Nitrogen cycling in the Middle Atlantic Bight: Results from a three-dimensional model and implications for the North Atlantic nitrogen budget: NITROGEN CYCLING IN THE MIDDLE ATLANTIC. *Global Biogeochemical Cycles*, *20*(3), n/a–n/a. Retrieved 2023-02-15, from http://doi.wiley.com/10.1029/2005GB002456 doi: 10.1029/2005GB002456

Franco, A. C., Gruber, N., Frölicher, T. L., & Kropuenske Artman, L. (2018, March). Contrasting Impact of Future CO_2 Emission Scenarios on the Extent of $CaCO_3$ Mineral Undersaturation in the Humboldt Current System. *Journal of Geophysical Research: Oceans*, *123*(3), 2018–2036. Retrieved 2023-02-15, from http://doi.wiley.com/10.1002/2018JC013857 doi: 10.1002/2018JC013857

Friedlingstein, P., O'Sullivan, M., Jones, M. W., Andrew, R. M., Gregor, L., Hauck, J., ... Zheng, B. (2022). Global Carbon Budget 2022. *Earth System Science Data*, *14*(11), 4811–4900. Retrieved from https://essd.copernicus.org/articles/14/4811/2022/ doi: 10.5194/essd-14-4811-2022

Friedlingstein, P., O'Sullivan, M., Jones, M. W., Andrew, R. M., Hauck, J., Olsen, A., ... Zaehle, S. (2020, December). Global Carbon Budget 2020. *Earth System Science Data*, *12*(4), 3269–3340. Retrieved 2021-08-31, from https://essd.copernicus.org/articles/12/3269/2020/ doi: 10.5194/essd-12-3269-2020

Frischknecht, M. (2018). *New Perspectives on the Three-Dimensional Cycling of Carbon and Nutrients in the California Current System and its Response to ENSO* (Doctoral dissertation, ETH Zurich). (Artwork Size: 254 p. Medium: application/pdf Pages: 254 p.) doi: 10.3929/ETHZ-B-000283522

Ganesan, A. L., Manizza, M., Morgan, E. J., Harth, C. M., Kozlova, E., Lueker, T., ... Rigby, M. (2020, July). Marine Nitrous Oxide Emissions From Three Eastern Boundary Upwelling Systems Inferred From Atmospheric Observations. *Geophysical Research Letters*, *47*(14). Retrieved 2023-02-15, from https://onlinelibrary.wiley.com/doi/10.1029/2020GL087822 doi: 10.1029/2020GL087822

Garcia, H. E., Locarnini, R. A., Boyer, T. P., Baranova, O. K., Zweng, M. M., Reagan, J. R., & Johnson, D. R. (2014). *World Ocean Atlas 2013, Volume 3: Dissolved Oxygen, Apparent Oxygen Utilization, and Oxygen Saturation.* (Tech. Rep.). S. Levitus, Ed., A. Mishonov Technical Ed.; NOAA Atlas NESDIS 75, 27 pp.

Good, S., Fiedler, E., Mao, C., Martin, M. J., Maycock, A., Reid, R., ... Worsfold, M. (2020, February). The Current Configuration of the OSTIA System for Operational Production of Foundation Sea Surface Temperature and Ice Concentration Analyses. *Remote Sensing*, *12*(4), 720. Retrieved 2023-02-14, from https://www.mdpi.com/2072-4292/12/4/720 doi: 10.3390/rs12040720

Good, S. A., Martin, M. J., & Rayner, N. A. (2013, December). EN4: Quality controlled ocean temperature and salinity profiles and monthly objective analyses with uncertainty estimates: THE EN4 DATA SET. *Journal of Geophysical Research: Oceans*, *118*(12), 6704–6716. Retrieved 2023-02-15, from http://doi.wiley.com/10.1002/2013JC009067 doi: 10.1002/2013JC009067

Gruber, N., Clement, D., Carter, B. R., Feely, R. A., Heuven, S. v., Hoppema, M., ... Wanninkhof, R. (2019, March). The oceanic sink for anthropogenic CO2 from 1994 to 2007. *Science*, *363*(6432), 1193–1199. Retrieved 2019-03-19, from http://science.sciencemag.org.ezproxy.princeton.edu/content/363/6432/1193 doi: 10.1126/science.aau5153

Gruber, N., Frenzel, H., Doney, S. C., Marchesiello, P., McWilliams, J. C., Moisan, J. R., ... Stolzenbach, K. D. (2006, September). Eddy-resolving simulation of plankton ecosystem dynamics in the California Current System. *Deep Sea Research Part I: Oceanographic Research Papers*, *53*(9), 1483–1516. Retrieved 2023-02-15, from https://www.sciencedirect.com/science/article/pii/S0967063706001713

doi: 10.1016/j.dsr.2006.06.005

Gruber, N., Hauri, C., Lachkar, Z., Loher, D., Frölicher, T. L., & Plattner, G.-K. (2012, July). Rapid Progression of Ocean Acidification in the California Current System. *Science*, *337*(6091), 220–223. Retrieved 2023-02-15, from https://www.science.org/doi/10.1126/science.1216773 doi: 10.1126/science.1216773

Haidvogel, D., Arango, H., Budgell, W., Cornuelle, B., Curchitser, E., Di Lorenzo, E., ... Wilkin, J. (2008, March). Ocean forecasting in terrain-following coordinates: Formulation and skill assessment of the Regional Ocean Modeling System. *Journal of Computational Physics*, *227*(7), 3595–3624. Retrieved 2023-02-15, from https://linkinghub.elsevier.com/retrieve/pii/S0021999107002549 doi: 10.1016/j.jcp.2007.06.016

Hartmann, J., Jansen, N., Dürr, H. H., Kempe, S., & Köhler, P. (2009, December). Global CO2-consumption by chemical weathering: What is the contribution of highly active weathering regions? *Global and Planetary Change*, *69*(4), 185–194. Retrieved 2020-01-30, from https://linkinghub.elsevier.com/retrieve/pii/S0921818109001349 doi: 10.1016/j.gloplacha.2009.07.007

Hauck, J., Völker, C., Wang, T., Hoppema, M., Losch, M., & Wolf-Gladrow, D. A. (2013, December). Seasonally different carbon flux changes in the Southern Ocean in response to the southern annular mode. *Global Biogeochemical Cycles*, *27*(4), 1236–1245. Retrieved 2023-02-15, from https://onlinelibrary.wiley.com/doi/10.1002/2013GB004600 doi: 10.1002/2013GB004600

Hauck, J., Zeising, M., Le Quéré, C., Gruber, N., Bakker, D. C. E., Bopp, L., ... Séférian, R. (2020). Consistency and Challenges in the Ocean Carbon Sink Estimate for the Global Carbon Budget. *Frontiers in Marine Science*, *7*. Retrieved 2020-12-18, from https://www.frontiersin.org/articles/10.3389/fmars.2020.571720/full (Publisher: Frontiers) doi: 10.3389/fmars.2020.571720

Hersbach, H., Bell, B., Berrisford, P., Hirahara, S., Horányi, A., Muñoz-Sabater, J., ... Thépaut, J.-N. (2020). The ERA5 global reanalysis. *Quarterly Journal of the Royal Meteorological Society*, *146*(730), 1999–2049. Retrieved 2023-02-14, from https://onlinelibrary.wiley.com/doi/abs/10.1002/qj.3803 doi: 10.1002/qj.3803

Ho, D. T., Law, C. S., Smith, M. J., Schlosser, P., Harvey, M., & Hill, P. (2006). Measurements of air-sea gas exchange at high wind speeds in the Southern Ocean: Implications for global parameterizations. *Geophysical Research Letters*, *33*(16). Retrieved 2019-06-25, from https://agupubs.onlinelibrary.wiley.com/doi/abs/10.1029/2006GL026817 doi: 10.1029/2006GL026817

Ho, D. T., Wanninkhof, R., Schlosser, P., Ullman, D. S., Hebert, D., & Sullivan, K. F. (2011, July). Toward a universal relationship between wind speed and gas exchange: Gas transfer velocities measured with ^{3}He/SF$_{6}$ during the Southern Ocean Gas Exchange Experiment. *Journal of Geophysical Research*, *116*, C00F04. Retrieved 2023-02-15, from http://doi.wiley.com/10.1029/2010JC006854 doi: 10.1029/2010JC006854

Hornafius, J. S., Quigley, D., & Luyendyk, B. P. (1999, September). The world's most spectacular marine hydrocarbon seeps (Coal Oil Point, Santa Barbara Channel, California): Quantification of emissions. *Journal of Geophysical Research: Oceans*, *104*(C9), 20703–20711. Retrieved 2023-02-23, from http://doi.wiley.com/10.1029/1999JC900148 doi: 10.1029/1999JC900148

Hovland, M., Judd, A., & Burke, R. (1993, January). The global flux of methane from shallow submarine sediments. *Chemosphere*, *26*(1-4), 559–578. Retrieved 2023-02-23, from https://linkinghub.elsevier.com/retrieve/pii/0045653593904428 doi: 10.1016/0045-6535(93)90442-8

Ilyina, T., Six, K. D., Segschneider, J., Maier-Reimer, E., Li, H., & Núñez-Riboni, I. (2013, June). Global ocean biogeochemistry model HAMOCC: Model architecture and performance as component of the MPI-Earth system model in different CMIP5 experimental realizations. *Journal of Advances in Modeling Earth Systems*, *5*(2), 287–315. Retrieved 2023-02-15, from https://onlinelibrary.wiley.com/doi/10.1029/2012MS000178 doi: 10.1029/2012MS000178

Joos, F., & Spahni, R. (2008, February). Rates of change in natural and anthropogenic radiative forcing over the past 20,000 years. *Proceedings of the National Academy of Sciences*, *105*(5), 1425–1430. Retrieved 2019-06-18, from https://www.pnas.org/content/105/5/1425 doi: 10.1073/pnas.0707386105

Jungclaus, J. H., Fischer, N., Haak, H., Lohmann, K., Marotzke, J., Matei, D., ... Storch, J. S. (2013, June). Characteristics of the ocean simulations in the Max Planck Institute Ocean Model (MPIOM) the ocean component of the MPI-Earth system model. *Journal of Advances in Modeling Earth Systems*, *5*(2), 422–446. Retrieved 2023-02-20, from https://onlinelibrary.wiley.com/doi/

10.1002/jame.20023 doi: 10.1002/jame.20023

Kanamitsu, M., Ebisuzaki, W., Woollen, J., Yang, S.-K., Hnilo, J. J., Fiorino, M., & Potter, G. L. (2002, November). NCEP–DOE AMIP-II Reanalysis (R-2). *Bulletin of the American Meteorological Society*, *83*(11), 1631–1644. Retrieved 2023-02-15, from https://journals.ametsoc.org/view/journals/bams/83/11/bams-83-11-1631.xml (Publisher: American Meteorological Society Section: Bulletin of the American Meteorological Society) doi: 10.1175/BAMS-83-11-1631

Keeling, C. D., Piper, S. C., Bacastow, R. B., Wahlen, M., Whorf, T. P., Heimann, M., & Meijer, H. A. (2005). Atmospheric CO_2 and $13CO_2$ Exchange with the Terrestrial Biosphere and Oceans from 1978 to 2000: Observations and Carbon Cycle Implications. In I. T. Baldwin et al. (Eds.), *A History of Atmospheric CO2 and Its Effects on Plants, Animals, and Ecosystems* (pp. 83–113). Springer New York. Retrieved 2016-09-16, from http://link.springer.com/chapter/10.1007/0-387-27048-5_5 doi: 10.1007/0-387-27048-5_5

Key, R. M., Kozyr, A., Sabine, C. L., Lee, K., Wanninkhof, R., Bullister, J. L., ... Peng, T.-H. (2004, December). A global ocean carbon climatology: Results from Global Data Analysis Project (GLODAP): GLOBAL OCEAN CARBON CLIMATOLOGY. *Global Biogeochemical Cycles*, *18*(4), n/a–n/a. Retrieved 2023-02-15, from http://doi.wiley.com/10.1029/2004GB002247 doi: 10.1029/2004GB002247

Khatiwala, S., Tanhua, T., Mikaloff Fletcher, S., Gerber, M., Doney, S. C., Graven, H. D., ... Sabine, C. L. (2013, April). Global ocean storage of anthropogenic carbon. *Biogeosciences*, *10*(4), 2169–2191. Retrieved 2016-01-19, from http://www.biogeosciences.net/10/2169/2013/ doi: 10.5194/bg-10-2169-2013

Kock, A., & Bange, H. (2015, February). Counting the Ocean's Greenhouse Gas Emissions. *Eos*, *96*. Retrieved 2023-02-14, from https://eos.org/project-updates/counting-oceans-greenhouse-gas-emissions doi: 10.1029/2015EO023665

Krishna, M., Prasad, M., Rao, D., Viswanadham, R., Sarma, V., & Reddy, N. (2016, January). Export of dissolved inorganic nutrients to the northern Indian Ocean from the Indian monsoonal rivers during discharge period. *Geochimica et Cosmochimica Acta*, *172*, 430–443. Retrieved 2023-02-23, from https://linkinghub.elsevier.com/retrieve/pii/S0016703715005955 doi: 10.1016/j.gca.2015.10.013

Lachkar, Z., & Gruber, N. (2013, January). Response of biological production and air–sea CO2 fluxes to upwelling intensification in the California and Canary Current Systems. *Journal of Marine Systems*, *109-110*, 149–160. Retrieved 2023-02-15, from https://www.sciencedirect.com/science/article/pii/S092479631200108X doi: 10.1016/j.jmarsys.2012.04.003

Lachkar, Z., Mehari, M., Al Azhar, M., Lévy, M., & Smith, S. (2021, October). Fast local warming is the main driver of recent deoxygenation in the northern Arabian Sea. *Biogeosciences*, *18*(20), 5831–5849. Retrieved 2023-02-15, from https://bg.copernicus.org/articles/18/5831/2021/ doi: 10.5194/bg-18-5831-2021

Lachkar, Z., Smith, S., Lévy, M., & Pauluis, O. (2016, September). Eddies reduce denitrification and compress habitats in the Arabian Sea. *Geophysical Research Letters*, *43*(17), 9148–9156. Retrieved 2018-01-16, from http://onlinelibrary.wiley.com/doi/10.1002/2016GL069876/full doi: 10.1002/2016GL069876

Lacroix, F., Ilyina, T., Laruelle, G. G., & Regnier, P. (2021). Reconstructing the Preindustrial Coastal Carbon Cycle Through a Global Ocean Circulation Model: Was the Global Continental Shelf Already Both Autotrophic and a CO2 Sink? *Global Biogeochemical Cycles*, *35*(2), e2020GB006603. Retrieved 2021-09-03, from https://agupubs.onlinelibrary.wiley.com/doi/abs/10.1029/2020GB006603 doi: 10.1029/2020GB006603

Landschützer, P., Gruber, N., Bakker, D. C. E., & Schuster, U. (2014, September). Recent variability of the global ocean carbon sink. *Global Biogeochemical Cycles*, *28*(9), 927–949. Retrieved 2015-08-11, from http://onlinelibrary.wiley.com/doi/10.1002/2014GB004853/abstract doi: 10.1002/2014GB004853

Landschützer, P., Gruber, N., Bakker, D. C. E., Schuster, U., Nakaoka, S., Payne, M. R., ... Zeng, J. (2013, November). A neural network-based estimate of the seasonal to inter-annual variability of the Atlantic Ocean carbon sink. *Biogeosciences*, *10*(11), 7793–7815. Retrieved 2023-02-15, from https://bg.copernicus.org/articles/10/7793/2013/ doi: 10.5194/bg-10-7793-2013

Landschützer, P., Laruelle, G. G., Roobaert, A., & Regnier, P. (2020, October). A uniform pCO2 climatology combining open and coastal oceans. *Earth System Science Data*, *12*(4), 2537–2553. Retrieved 2023-02-14, from https://essd.copernicus.org/articles/12/2537/2020/ doi: 10.5194/essd-12

-2537-2020

Large, W. G., McWilliams, J. C., & Doney, S. C. (1994). Oceanic vertical mixing: A review and a model with a nonlocal boundary layer parameterization. *Reviews of Geophysics*, *32*(4), 363–403. Retrieved 2023-02-15, from https://onlinelibrary.wiley.com/doi/abs/10.1029/94RG01872 doi: 10.1029/94RG01872

Large, W. G., & Yeager, S. G. (2009, August). The global climatology of an interannually varying air–sea flux data set. *Climate Dynamics*, *33*(2-3), 341–364. Retrieved 2015-04-02, from http://link.springer.com/10.1007/s00382-008-0441-3 doi: 10.1007/s00382-008-0441-3

Laruelle, G. G., Cai, W.-J., Hu, X., Gruber, N., Mackenzie, F. T., & Regnier, P. (2018, January). Continental shelves as a variable but increasing global sink for atmospheric carbon dioxide. *Nature Communications*, *9*, 454. Retrieved 2021-09-03, from https://www.ncbi.nlm.nih.gov/pmc/articles/PMC5792465/ doi: 10.1038/s41467-017-02738-z

Laruelle, G. G., Dürr, H. H., Lauerwald, R., Hartmann, J., Slomp, C. P., Goossens, N., & Regnier, P. A. G. (2013, May). Global multi-scale segmentation of continental and coastal waters from the watersheds to the continental margins. *Hydrology and Earth System Sciences*, *17*(5), 2029–2051. Retrieved 2020-03-27, from https://www.hydrol-earth-syst-sci.net/17/2029/2013/ doi: 10.5194/hess-17-2029-2013

Laruelle, G. G., Landschützer, P., Gruber, N., Tison, J.-L., Delille, B., & Regnier, P. (2017, October). Global high-resolution monthly pCO2 climatology for the coastal ocean derived from neural network interpolation. *Biogeosciences*, *14*(19), 4545–4561. Retrieved 2019-08-29, from https://www.biogeosciences.net/14/4545/2017/ doi: 10.5194/bg-14-4545-2017

Laruelle, G. G., Lauerwald, R., Pfeil, B., & Regnier, P. (2014). Regionalized global budget of the CO2 exchange at the air-water interface in continental shelf seas. *Global Biogeochemical Cycles*, *28*(11), 1199–1214. Retrieved 2021-09-03, from https://agupubs.onlinelibrary.wiley.com/doi/abs/10.1002/2014GB004832 doi: 10.1002/2014GB004832

Laurent, A., Fennel, K., Cai, W., Huang, W., Barbero, L., & Wanninkhof, R. (2017, January). Eutrophication-induced acidification of coastal waters in the northern Gulf of Mexico: Insights into origin and processes from a coupled physical-biogeochemical model. *Geophysical Research Letters*, *44*(2), 946–956. Retrieved 2023-02-15, from https://onlinelibrary.wiley.com/doi/abs/10.1002/2016GL071881 doi: 10.1002/2016GL071881

Laurent, A., Fennel, K., & Kuhn, A. (2021, March). An observation-based evaluation and ranking of historical Earth system model simulations in the northwest North Atlantic Ocean. *Biogeosciences*, *18*(5), 1803–1822. Retrieved 2023-02-15, from https://bg.copernicus.org/articles/18/1803/2021/ doi: 10.5194/bg-18-1803-2021

Lauvset, S. K., Key, R. M., Olsen, A., Heuven, S. v., Velo, A., Lin, X., ... Watelet, S. (2016, August). A new global interior ocean mapped climatology: the 1° × 1° GLODAP version 2. *Earth System Science Data*, *8*(2), 325–340. Retrieved 2016-11-07, from http://www.earth-syst-sci-data.net/8/325/2016/ doi: 10.5194/essd-8-325-2016

Liang, J.-H., Deutsch, C., McWilliams, J. C., Baschek, B., Sullivan, P. P., & Chiba, D. (2013). Parameterizing bubble-mediated air-sea gas exchange and its effect on ocean ventilation. *Global Biogeochemical Cycles*, *27*(3), 894–905. Retrieved 2023-02-14, from https://onlinelibrary.wiley.com/doi/abs/10.1002/gbc.20080 doi: 10.1002/gbc.20080

Liao, E., Resplandy, L., Liu, J., & Bowman, K. W. (2020). Amplification of the Ocean Carbon Sink During El Niños: Role of Poleward Ekman Transport and Influence on Atmospheric CO2. *Global Biogeochemical Cycles*, *34*(9), e2020GB006574. Retrieved 2020-10-15, from http://agupubs.onlinelibrary.wiley.com/doi/abs/10.1029/2020GB006574 doi: 10.1029/2020GB006574

Liss, P. S., & Merlivat, L. (1986). Air-Sea Gas Exchange Rates: Introduction and Synthesis. In P. Buat-Ménard (Ed.), *The Role of Air-Sea Exchange in Geochemical Cycling* (pp. 113–127). Dordrecht: Springer Netherlands. Retrieved 2023-02-23, from https://doi.org/10.1007/978-94-009-4738-2_5 doi: 10.1007/978-94-009-4738-2_5

Locarnini, R. A., Mishonov, A. V., Antonov, J. I., Boyer, T. P., Garcia, H. E., Baranova, O. K., ... Seidov, D. (2014). *World Ocean Atlas 2013, Volume 1: Temperature.* (Tech. Rep.). S. Levitus, Ed., A. Mishonov Technical Ed.; NOAA Atlas NESDIS 73, 40 pp.

Louchard, D., Gruber, N., & Münnich, M. (2021). The Impact of the Amazon on the Biological Pump and the Air-Sea CO2 Balance of the Western Tropical Atlantic. *Global Biogeochemical Cycles*, *35*(6), e2020GB006818. Retrieved 2021-09-22, from https://onlinelibrary.wiley.com/doi/abs/10.1029/2020GB006818 doi: 10.1029/

2020GB006818

Ludwig, W., Amiotte Suchet, P., & Probst, J.-L. (1996). River discharges of carbon to the world's oceans: determining local inputs of alkalinity and of dissolved and particulate organic carbon. *Sciences de la terre et des planètes (Comptes rendus de l'Académie des sciences)*, *t. 323*, 1007–1014. Retrieved 2023-02-15, from https://oatao.univ-toulouse.fr/3498/ (Publisher: Gauthier-Villars)

Madec, G., Bourdallé-Badie, R., Bouttier, P.-A., Bricaud, C., Bruciaferri, D., Calvert, D., ... Vancoppenolle, M. (2017). NEMO ocean engine. Retrieved 2023-02-15, from https://zenodo.org/record/1472492 doi: 10.5281/ZENODO.1472492

Mahowald, N. M., Engelstaedter, S., Luo, C., Sealy, A., Artaxo, P., Benitez-Nelson, C., ... Siefert, R. L. (2009). Atmospheric Iron Deposition: Global Distribution, Variability, and Human Perturbations. *Annual Review of Marine Science*, *1*(1), 245–278. Retrieved 2023-02-21, from https://doi.org/10.1146/annurev.marine.010908.163727 doi: 10.1146/annurev.marine.010908.163727

Manizza, M., Keeling, R. F., & Nevison, C. D. (2012, January). On the processes controlling the seasonal cycles of the air–sea fluxes of O_2 and N_2O: A modelling study. *Tellus B: Chemical and Physical Meteorology*, *64*(1), 18429. Retrieved 2023-02-15, from https://b.tellusjournals.se/article/10.3402/tellusb.v64i0.18429/ doi: 10.3402/tellusb.v64i0.18429

Manizza, M., Menemenlis, D., Zhang, H., & Miller, C. E. (2019). Modeling the Recent Changes in the Arctic Ocean CO_2 Sink (2006–2013). *Global Biogeochemical Cycles*, *33*(3), 420–438. Retrieved 2023-02-15, from https://onlinelibrary.wiley.com/doi/abs/10.1029/2018GB006070 doi: 10.1029/2018GB006070

Martinez-Rey, J., Bopp, L., Gehlen, M., Tagliabue, A., & Gruber, N. (2015, July). Projections of oceanic N2O emissions in the 21st century using the IPSL Earth system model. *Biogeosciences*, *12*(13), 4133–4148. Retrieved 2016-06-07, from http://www.biogeosciences.net/12/4133/2015/ doi: 10.5194/bg-12-4133-2015

Mayorga, E., Seitzinger, S. P., Harrison, J. A., Dumont, E., Beusen, A. H., Bouwman, A., ... Van Drecht, G. (2010, July). Global Nutrient Export from WaterSheds 2 (NEWS 2): Model development and implementation. *Environmental Modelling & Software*, *25*(7), 837–853. Retrieved 2023-02-23, from https://linkinghub.elsevier.com/retrieve/pii/S1364815210000186 doi: 10.1016/j.envsoft.2010.01.007

McGinnis, D. F., Greinert, J., Artemov, Y., Beaubien, S. E., & Wüest, A. (2006). Fate of rising methane bubbles in stratified waters: How much methane reaches the atmosphere? *Journal of Geophysical Research*, *111*(C9), C09007. Retrieved 2023-02-23, from http://doi.wiley.com/10.1029/2005JC003183 doi: 10.1029/2005JC003183

Middelburg, J. J., Soetaert, K., Herman, P. M. J., & Heip, C. H. R. (1996, December). Denitrification in marine sediments: A model study. *Global Biogeochemical Cycles*, *10*(4), 661–673. Retrieved 2023-02-15, from http://doi.wiley.com/10.1029/96GB02562 doi: 10.1029/96GB02562

Moore, J. K., Lindsay, K., Doney, S. C., Long, M. C., & Misumi, K. (2013, August). Marine Ecosystem Dynamics and Biogeochemical Cycling in the Community Earth System Model [CESM1(BGC)]: Comparison of the 1990s with the 2090s under the RCP4.5 and RCP8.5 Scenarios. *Journal of Climate*, *26*(23), 9291–9312. Retrieved 2016-06-16, from http://journals.ametsoc.org/doi/abs/10.1175/JCLI-D-12-00566.1 doi: 10.1175/JCLI-D-12-00566.1

Naegler, T. (2009, January). Reconciliation of excess 14C-constrained global CO2 piston velocity estimates. *Tellus B: Chemical and Physical Meteorology*, *61*(2), 372–384. Retrieved 2023-02-15, from https://doi.org/10.1111/j.1600-0889.2008.00408.x (Publisher: Taylor & Francis _eprint: https://doi.org/10.1111/j.1600-0889.2008.00408.x) doi: 10.1111/j.1600-0889.2008.00408.x

Nakano, H., Tsujino, H., Hirabara, M., Yasuda, T., Motoi, T., Ishii, M., & Yamanaka, G. (2011, December). Uptake mechanism of anthropogenic CO2 in the Kuroshio Extension region in an ocean general circulation model. *Journal of Oceanography*, *67*(6), 765–783. Retrieved 2019-09-25, from https://doi.org/10.1007/s10872-011-0075-7 doi: 10.1007/s10872-011-0075-7

Nevison, C., Butler, J. H., & Elkins, J. W. (2003, December). Global distribution of N_2O and the N_2O-AOU yield in the subsurface ocean. *Global Biogeochemical Cycles*, *17*(4), n/a–n/a. Retrieved 2023-02-15, from http://doi.wiley.com/10.1029/2003GB002068 doi: 10.1029/2003GB002068

Nightingale, P. D., Malin, G., Law, C. S., Watson, A. J., Liss, P. S., Liddicoat, M. I., ... Upstill-Goddard, R. C. (2000, March). In situ evaluation of air-sea gas exchange parameterizations using novel conservative and volatile tracers. *Global Biogeochemical Cycles*, *14*(1), 373–387. Retrieved 2023-02-15, from http://

doi.wiley.com/10.1029/1999GB900091 doi: 10.1029/1999GB900091

Olsen, A., Key, R. M., van Heuven, S., Lauvset, S. K., Velo, A., Lin, X., ... Suzuki, T. (2016, August). The Global Ocean Data Analysis Project version 2 (GLODAPv2) – an internally consistent data product for the world ocean. *Earth System Science Data*, *8*(2), 297–323. Retrieved 2023-02-15, from https://essd.copernicus.org/articles/8/297/2016/ (Publisher: Copernicus GmbH) doi: 10.5194/essd-8-297-2016

Olsen, A., Lange, N., Key, R. M., Tanhua, T., Álvarez, M., Becker, S., ... Wanninkhof, R. (2019, September). GLODAPv2.2019 – an update of GLODAPv2. *Earth System Science Data*, *11*(3), 1437–1461. Retrieved 2023-02-16, from https://essd.copernicus.org/articles/11/1437/2019/ (Publisher: Copernicus GmbH) doi: 10.5194/essd-11-1437-2019

Orr, J. C., Epitalon, J.-M., & Gattuso, J.-P. (2015, March). Comparison of ten packages that compute ocean carbonate chemistry. *Biogeosciences*, *12*(5), 1483–1510. Retrieved 2023-02-15, from https://bg.copernicus.org/articles/12/1483/2015/ (Publisher: Copernicus GmbH) doi: 10.5194/bg-12-1483-2015

Orr, J. C., Fabry, V. J., Aumont, O., Bopp, L., Doney, S. C., Feely, R. A., ... Yool, A. (2005, September). Anthropogenic ocean acidification over the twenty-first century and its impact on calcifying organisms. *Nature*, *437*(7059), 681–686. Retrieved 2023-02-15, from https://www.nature.com/articles/nature04095 (Number: 7059 Publisher: Nature Publishing Group) doi: 10.1038/nature04095

Orr, J. C., Najjar, R. G., Aumont, O., Bopp, L., Bullister, J. L., Danabasoglu, G., ... Yool, A. (2017, June). Biogeochemical protocols and diagnostics for the CMIP6 Ocean Model Intercomparison Project (OMIP). *Geoscientific Model Development*, *10*(6), 2169–2199. Retrieved 2020-02-20, from https://www.geosci-model-dev.net/10/2169/2017/ doi: https://doi.org/10.5194/gmd-10-2169-2017

Paulsen, H., Ilyina, T., Six, K. D., & Stemmler, I. (2017, March). Incorporating a prognostic representation of marine nitrogen fixers into the global ocean biogeochemical model HAMOCC: PROGNOSTIC NITROGEN FIXERS IN HAMOCC. *Journal of Advances in Modeling Earth Systems*, *9*(1), 438–464. Retrieved 2023-02-20, from http://doi.wiley.com/10.1002/2016MS000737 doi: 10.1002/2016MS000737

Ramesh, R., Purvaja, G. R., & Subramanian, V. (1995). Carbon and Phosphorus Transport by the Major Indian Rivers. *Journal of Biogeography*, *22*(2/3), 409–415. Retrieved 2023-02-23, from https://www.jstor.org/stable/2845937 (Publisher: Wiley) doi: 10.2307/2845937

Regnier, P., Friedlingstein, P., Ciais, P., Mackenzie, F. T., Gruber, N., Janssens, I. A., ... Thullner, M. (2013, June). Anthropogenic perturbation of the carbon fluxes from land to ocean. *Nature Geoscience*, *6*(8), 597–607. Retrieved 2015-06-25, from http://www.nature.com/doifinder/10.1038/ngeo1830 doi: 10.1038/ngeo1830

Regnier, P., Resplandy, L., Najjar, R. G., & Ciais, P. (2022, March). The land-to-ocean loops of the global carbon cycle. *Nature*, *603*(7901), 401–410. Retrieved 2022-04-18, from https://www.nature.com/articles/s41586-021-04339-9 doi: 10.1038/s41586-021-04339-9

Reynolds, R. W., Smith, T. M., Liu, C., Chelton, D. B., Casey, K. S., & Schlax, M. G. (2007, November). Daily High-Resolution-Blended Analyses for Sea Surface Temperature. *Journal of Climate*, *20*(22), 5473–5496. Retrieved 2023-02-15, from http://journals.ametsoc.org/doi/10.1175/2007JCLI1824.1 doi: 10.1175/2007JCLI1824.1

Rousset, C., Vancoppenolle, M., Madec, G., Fichefet, T., Flavoni, S., Barthélemy, A., ... Vivier, F. (2015, October). The Louvain-La-Neuve sea ice model LIM3.6: global and regional capabilities. *Geoscientific Model Development*, *8*(10), 2991–3005. Retrieved 2023-02-15, from https://gmd.copernicus.org/articles/8/2991/2015/ (Publisher: Copernicus GmbH) doi: 10.5194/gmd-8-2991-2015

Rutherford, K., & Fennel, K. (2018, October). Diagnosing transit times on the northwestern North Atlantic continental shelf. *Ocean Science*, *14*(5), 1207–1221. Retrieved 2023-02-15, from https://os.copernicus.org/articles/14/1207/2018/ doi: 10.5194/os-14-1207-2018

Rutherford, K., Fennel, K., Atamanchuk, D., Wallace, D., & Thomas, H. (2021, December). A modelling study of temporal and spatial pCO_2 variability on the biologically active and temperature-dominated Scotian Shelf. *Biogeosciences*, *18*(23), 6271–6286. Retrieved 2023-02-15, from https://bg.copernicus.org/articles/18/6271/2021/ (Publisher: Copernicus GmbH) doi: 10.5194/bg-18-6271-2021

Rödenbeck, C., Keeling, R. F., Bakker, D. C. E., Metzl, N., Olsen, A., Sabine, C., & Heimann, M. (2013, March). Global surface-ocean pCO_2 and sea–air CO_2 flux variability from an observation-driven ocean mixed-layer scheme. *Ocean Science*, *9*(2), 193–216. Retrieved 2015-05-12, from http://www.ocean-sci.net/9/193/2013/ doi: 10.5194/os-9-193-2013

Schourup-Kristensen, V., Sidorenko, D., Wolf-

Gladrow, D. A., & Völker, C. (2014, November). A skill assessment of the biogeochemical model REcoM2 coupled to the Finite Element Sea Ice–Ocean Model (FESOM 1.3). *Geoscientific Model Development*, *7*(6), 2769–2802. Retrieved 2023-02-15, from https://gmd.copernicus.org/articles/7/2769/2014/ doi: 10.5194/gmd-7-2769-2014

Sein, D. V., Koldunov, N. V., Danilov, S., Sidorenko, D., Wekerle, C., Cabos, W., ... Jung, T. (2018, August). The Relative Influence of Atmospheric and Oceanic Model Resolution on the Circulation of the North Atlantic Ocean in a Coupled Climate Model. *Journal of Advances in Modeling Earth Systems*, *10*(8), 2026–2041. Retrieved 2023-02-15, from http://doi.wiley.com/10.1029/2018MS001327 doi: 10.1029/2018MS001327

Seitzinger, S. P., Harrison, J. A., Dumont, E., Beusen, A. H. W., & Bouwman, A. F. (2005, December). Sources and delivery of carbon, nitrogen, and phosphorus to the coastal zone: An overview of Global Nutrient Export from Watersheds (NEWS) models and their application: GLOBAL EXPORT OF C, N, AND P TO COASTAL SYSTEMS. *Global Biogeochemical Cycles*, *19*(4), n/a–n/a. Retrieved 2023-02-15, from http://doi.wiley.com/10.1029/2005GB002606 doi: 10.1029/2005GB002606

Seland, O., Bentsen, M., Olivié, D., Toniazzo, T., Gjermundsen, A., Graff, L. S., ... Schulz, M. (2020, December). Overview of the Norwegian Earth System Model (NorESM2) and key climate response of CMIP6 DECK, historical, and scenario simulations. *Geoscientific Model Development*, *13*(12), 6165–6200. Retrieved 2023-02-15, from https://gmd.copernicus.org/articles/13/6165/2020/ doi: 10.5194/gmd-13-6165-2020

Shchepetkin, A. F., & McWilliams, J. C. (2005, January). The regional oceanic modeling system (ROMS): a split-explicit, free-surface, topography-following-coordinate oceanic model. *Ocean Modelling*, *9*(4), 347–404. Retrieved 2023-02-15, from https://www.sciencedirect.com/science/article/pii/S1463500304000484 doi: 10.1016/j.ocemod.2004.08.002

Six, K. D., & Maier-Reimer, E. (1996). Effects of plankton dynamics on seasonal carbon fluxes in an ocean general circulation model. *Global Biogeochemical Cycles*, *10*(4), 559–583. Retrieved 2023-02-15, from https://onlinelibrary.wiley.com/doi/abs/10.1029/96GB02561 doi: 10.1029/96GB02561

Stock, C. A., Dunne, J. P., Fan, S., Ginoux, P., John, J., Krasting, J. P., ... Zadeh, N. (2020). Ocean Biogeochemistry in GFDL's Earth System Model 4.1 and Its Response to Increasing Atmospheric CO2. *Journal of Advances in Modeling Earth Systems*, *12*(10), e2019MS002043. Retrieved 2021-10-11, from https://onlinelibrary.wiley.com/doi/abs/10.1029/2019MS002043 doi: 10.1029/2019MS002043

Stock, C. A., Dunne, J. P., & John, J. G. (2014, January). Global-scale carbon and energy flows through the marine planktonic food web: An analysis with a coupled physical–biological model. *Progress in Oceanography*, *120*, 1–28. Retrieved 2016-02-22, from http://www.sciencedirect.com/science/article/pii/S0079661113001079 doi: 10.1016/j.pocean.2013.07.001

Séférian, R., Nabat, P., Michou, M., Saint-Martin, D., Voldoire, A., Colin, J., ... Madec, G. (2019). Evaluation of CNRM Earth System Model, CNRM-ESM2-1: Role of Earth System Processes in Present-Day and Future Climate. *Journal of Advances in Modeling Earth Systems*, *11*(12), 4182–4227. Retrieved 2023-03-01, from https://onlinelibrary.wiley.com/doi/abs/10.1029/2019MS001791 (_eprint: https://onlinelibrary.wiley.com/doi/pdf/10.1029/2019MS doi: 10.1029/2019MS001791

Titchner, H. A., & Rayner, N. A. (2014, March). The Met Office Hadley Centre sea ice and sea surface temperature data set, version 2: 1. Sea ice concentrations: HADISST.2.1.0.0 SEA ICE CONCENTRATIONS. *Journal of Geophysical Research: Atmospheres*, *119*(6), 2864–2889. Retrieved 2023-02-17, from http://doi.wiley.com/10.1002/2013JD020316 doi: 10.1002/2013JD020316

Tjiputra, J. F., Schwinger, J., Bentsen, M., Morée, A. L., Gao, S., Bethke, I., ... Schulz, M. (2020, May). Ocean biogeochemistry in the Norwegian Earth System Model version 2 (NorESM2). *Geoscientific Model Development*, *13*(5), 2393–2431. Retrieved 2023-02-15, from https://gmd.copernicus.org/articles/13/2393/2020/ (Publisher: Copernicus GmbH) doi: 10.5194/gmd-13-2393-2020

Tsujino, H., Nakano, H., Sakamoto, K., Urakawa, S., Hirabara, M., Ishizaki, H., & Yamanaka, G. (2017). Reference Manual for the Meteorological Research Institute Community Ocean Model version 4(MRI.COMv4). *Technical Reports of the Meteorological Research Institute No. 80*. (10.11483/mritechrepo.80) doi: 10.11483/mritechrepo.80

Tsujino, H., Urakawa, S., Nakano, H., Small, R. J., Kim, W. M., Yeager, S. G., ... Yamazaki, D. (2018, October). JRA-55 based surface dataset for driving ocean–sea-ice models (JRA55-do). *Ocean Mod-*

elling, *130*, 79–139. Retrieved 2023-02-15, from https://linkinghub.elsevier.com/retrieve/pii/S146350031830235X doi: 10.1016/j.ocemod.2018.07.002

Umlauf, L., & Burchard, H. (2003, March). A generic length-scale equation for geophysical turbulence models. *Journal of Marine Research*, *61*(2), 235–265. Retrieved 2023-02-15, from http://www.ingentaselect.com/rpsv/cgi-bin/cgi?ini=xref&body=linker&reqdoi=10.1357/002224003322005087 doi: 10.1357/002224003322005087

Urakawa, L. S., Tsujino, H., Nakano, H., Sakamoto, K., Yamanaka, G., & Toyoda, T. (2020, October). The sensitivity of a depth-coordinate model to diapycnal mixing induced by practical implementations of the isopycnal tracer diffusion scheme. *Ocean Modelling*, *154*, 101693. Retrieved 2023-02-15, from https://linkinghub.elsevier.com/retrieve/pii/S1463500320301955 doi: 10.1016/j.ocemod.2020.101693

Urrego-Blanco, J., & Sheng, J. (2012, September). Interannual Variability of the Circulation over the Eastern Canadian Shelf. *Atmosphere-Ocean*, *50*(3), 277–300. Retrieved 2023-02-15, from http://www.tandfonline.com/doi/abs/10.1080/07055900.2012.680430 doi: 10.1080/07055900.2012.680430

Wang, C., Zhang, L., Lee, S.-K., Wu, L., & Mechoso, C. R. (2014, March). A global perspective on CMIP5 climate model biases. *Nature Climate Change*, *4*(3), 201–205. Retrieved 2015-09-23, from http://www.nature.com/nclimate/journal/v4/n3/full/nclimate2118.html doi: 10.1038/nclimate2118

Wang, H., Hu, X., Cai, W.-J., & Sterba-Boatwright, B. (2017). Decadal fCO2 trends in global ocean margins and adjacent boundary current-influenced areas. *Geophysical Research Letters*, *44*(17), 8962–8970. Retrieved 2022-04-15, from https://onlinelibrary.wiley.com/doi/abs/10.1002/2017GL074724 doi: 10.1002/2017GL074724

Wanninkhof, R. (1992, May). Relationship between wind speed and gas exchange over the ocean. *Journal of Geophysical Research: Oceans*, *97*(C5), 7373–7382. Retrieved 2015-06-22, from http://onlinelibrary.wiley.com/doi/10.1029/92JC00188/abstract doi: 10.1029/92JC00188

Wanninkhof, R. (2014, June). Relationship between wind speed and gas exchange over the ocean revisited. *Limnology and Oceanography: Methods*, *12*(6), 351–362. Retrieved 2015-06-22, from http://onlinelibrary.wiley.com/doi/10.4319/lom.2014.12.351/abstract doi: 10.4319/lom.2014.12.351

Warner, J. C., Sherwood, C. R., Arango, H. G., & Signell, R. P. (2005, January). Performance of four turbulence closure models implemented using a generic length scale method. *Ocean Modelling*, *8*(1-2), 81–113. Retrieved 2023-02-15, from https://linkinghub.elsevier.com/retrieve/pii/S1463500303000702 doi: 10.1016/j.ocemod.2003.12.003

Weber, T., Wiseman, N. A., & Kock, A. (2019, October). Global ocean methane emissions dominated by shallow coastal waters. *Nature Communications*, *10*(1), 4584. Retrieved 2020-10-21, from https://www.nature.com/articles/s41467-019-12541-7 (Number: 1 Publisher: Nature Publishing Group) doi: 10.1038/s41467-019-12541-7

Wright, R. M., Le Quéré, C., Buitenhuis, E., Pitois, S., & Gibbons, M. J. (2021, February). Role of jellyfish in the plankton ecosystem revealed using a global ocean biogeochemical model. *Biogeosciences*, *18*(4), 1291–1320. Retrieved 2023-03-27, from https://bg.copernicus.org/articles/18/1291/2021/ (Publisher: Copernicus GmbH) doi: 10.5194/bg-18-1291-2021

Wu, H., & Zhu, J. (2010, January). Advection scheme with 3rd high-order spatial interpolation at the middle temporal level and its application to salt-water intrusion in the Changjiang Estuary. *Ocean Modelling*, *33*(1-2), 33–51. Retrieved 2023-02-15, from https://linkinghub.elsevier.com/retrieve/pii/S1463500309002121 doi: 10.1016/j.ocemod.2009.12.001

Yang, S., Chang, B. X., Warner, M. J., Weber, T. S., Bourbonnais, A. M., Santoro, A. E., ... Bianchi, D. (2020, June). Global reconstruction reduces the uncertainty of oceanic nitrous oxide emissions and reveals a vigorous seasonal cycle. *Proceedings of the National Academy of Sciences*, *117*(22), 11954–11960. Retrieved 2022-05-12, from https://www.pnas.org/doi/10.1073/pnas.1921914117 (Publisher: Proceedings of the National Academy of Sciences) doi: 10.1073/pnas.1921914117

Yukimoto, S., Kawai, H., Koshiro, T., Oshima, N., Yoshida, K., Urakawa, S., ... Ishii, M. (2019). The Meteorological Research Institute Earth System Model Version 2.0, MRI-ESM2.0: Description and Basic Evaluation of the Physical Component. *Journal of the Meteorological Society of Japan. Ser. II*, *97*(5), 931–965. Retrieved 2023-02-15, from https://www.jstage.jst.go.jp/article/jmsj/97/5/97_2019-051/_article doi: 10.2151/jmsj.2019-051

Zweng, M. M., Reagan, J. R., Antonov, J. I., Locarnini, R. A., Mishonov, A. V., Boyer, T. P., ... Biddle, M. (2014). *World Ocean Atlas 2013, Vol-*

ume 2: Salinity. (Tech. Rep.). S. Levitus, Ed., A. Mishonov Technical Ed.; NOAA Atlas NESDIS 74, 39 pp.

Bibliography

[1] Corinne Le Quéré et al. "Impact of climate change and variability on the global oceanic sink of CO2". In: *Global Biogeochemical Cycles* 24.4 (2010).

[2] JG Canadell. "Global Carbon Project. Science framework and Implementation". In: *Earth System Science Partnership (IGBP, IHDP, WCRP, DIVERSITAS) Report No. 1; Global Carbon Project Report No. 1* (2003).

[3] Myles R Allen and William J Ingram. "Constraints on future changes in climate and the hydrologic cycle". In: *Nature* 419.6903 (2002), pp. 224–232.

[4] Nadir Jeevanjee and David M Romps. "Mean precipitation change from a deepening troposphere". In: *Proceedings of the National Academy of Sciences* 115.45 (2018), pp. 11465–11470.

[5] Jian Lu, Gabriel A Vecchi, and Thomas Reichler. "Expansion of the Hadley cell under global warming". In: *Geophysical Research Letters* 34.6 (2007).

[6] Isaac M Held and Brian J Soden. "Robust responses of the hydrological cycle to global warming". In: *Journal of climate* 19.21 (2006), pp. 5686–5699.

[7] Syukuro Manabe and Richard T Wetherald. "The effects of doubling the CO 2 concentration on the climate of a general circulation model". In: *Journal of Atmospheric Sciences* 32.1 (1975), pp. 3–15.

[8] Paul J Durack and Susan E Wijffels. "Fifty-year trends in global ocean salinities and their relationship to broad-scale warming". In: *Journal of Climate* 23.16 (2010), pp. 4342–4362.

[9] Paul J Durack, Susan E Wijffels, and Richard J Matear. "Ocean salinities reveal strong global water cycle intensification during 1950 to 2000". In: *science* 336.6080 (2012), pp. 455–458.

[10] Hu Yang et al. "Poleward shift of the major ocean gyres detected in a warming climate". In: *Geophysical Research Letters* 47.5 (2020), e2019GL085868.

[11] Jian Lu, Gang Chen, and Dargan MW Frierson. "Response of the zonal mean atmospheric circulation to El Niño versus global warming". In: *Journal of Climate* 21.22 (2008), pp. 5835–5851.

[12] Samuel J Levang and Raymond W Schmitt. "Intergyre Salt Transport in the Climate Warming Response". In: *Journal of Physical Oceanography* 50.1 (2020), pp. 255–268.

[13] Chenyu Zhu and Zhengyu Liu. "Weakening Atlantic overturning circulation causes South Atlantic salinity pile-up". In: *Nature Climate Change* 10.11 (2020), pp. 998–1003.

[14] Ben I McNeil and Richard J Matear. "Climate change feedbacks on future oceanic acidification". In: *Tellus B: Chemical and Physical Meteorology* 59.2 (2007), pp. 191–198.

[15] Sunke Schmidtko, Lothar Stramma, and Martin Visbeck. "Decline in global oceanic oxygen content during the past five decades". In: *Nature* 542.7641 (2017), pp. 335–339.

[16] Megumi O Chikamoto, Pedro DiNezio, and Nicole Lovenduski. "Long-Term Slowdown of Ocean Carbon Uptake by Alkalinity Dynamics". In: *Geophysical Research Letters* 50.4 (2023), e2022GL101954.

[17] S George H Philander. "El Nino southern oscillation phenomena". In: *Nature* 302.5906 (1983), pp. 295–301.

[18] Richard T Barber and Francisco P Chavez. "Biological consequences of el nino". In: *Science* 222.4629 (1983), pp. 1203–1210.

[19] NJ Burls and AV Fedorov. "What controls the mean east–west sea surface temperature gradient in the equatorial Pacific: The role of cloud albedo". In: *Journal of Climate* 27.7 (2014), pp. 2757–2778.

[20] Chunzai Wang et al. "El Niño and southern oscillation (ENSO): a review". In: *Coral reefs of the eastern tropical Pacific* (2017), pp. 85–106.

[21] Weimin Wang and Michael J McPhaden. "The surface-layer heat balance in the equatorial Pacific Ocean. Part II: Interannual variability". In: *Journal of Physical Oceanography* 30.11 (2000), pp. 2989–3008.

[22] Xuebin Zhang and Michael J. McPhaden. "Surface Layer Heat Balance in the Eastern Equatorial Pacific Ocean on Interannual Time Scales: Influence of Local versus Remote Wind Forcing*". In: *Journal of Climate* 23.16 (2010), pp. 4375–4394. ISSN: 1520-0442, 0894-8755. DOI: 10.1175/2010JCLI3469.1.

[23] Kevin E. Trenberth. "The Definition of El Niño". In: *Bulletin of the American Meteorological Society* 78.12 (1997), pp. 2771–2777. ISSN: 0003-0007, 1520-0477. DOI: 10.1175/1520-0477(1997)078<2771:TDOENO>2.0.CO;2.

[24] J David Neelin and Isaac M Held. "Modeling tropical convergence based on the moist static energy budget". In: *Monthly Weather Review* 115.1 (1987), pp. 3–12.

[25] Adam H Sobel, Isaac M Held, and Christopher S Bretherton. "The ENSO signal in tropical tropospheric temperature". In: *Journal of Climate* 15.18 (2002), pp. 2702–2706.

[26] Randy G. Brown and Christopher S. Bretherton. "A Test of the Strict Quasi-Equilibrium Theory on Long Time and Space Scales". In: *Journal of the Atmospheric Sciences* 54.5 (1997). ISSN: 0022-4928, 1520-0469. DOI: 10.1175/1520-0469(1997)054<0624:ATOTSQ>2.0.CO;2.

[27] Aiguo Dai. "Recent climatology, variability, and trends in global surface humidity". In: *Journal of Climate* 19.15 (2006), pp. 3589–3606.

[28] Laurent Bopp et al. "Multiple stressors of ocean ecosystems in the 21st century: projections with CMIP5 models". In: *Biogeosciences* 10.10 (2013), pp. 6225–6245.

[29] Lothar Stramma et al. "Expanding oxygen-minimum zones in the tropical oceans". In: *science* 320.5876 (2008), pp. 655–658.

[30] Lothar Stramma et al. "Expansion of oxygen minimum zones may reduce available habitat for tropical pelagic fishes". In: *Nature Climate Change* 2.1 (2012), pp. 33–37.

[31] Eric D Prince et al. "Ocean scale hypoxia-based habitat compression of Atlantic istiophorid billfishes". In: *Fisheries Oceanography* 19.6 (2010), pp. 448–462.

[32] Damian L Arevalo-Martínez et al. "Massive nitrous oxide emissions from the tropical South Pacific Ocean". In: *Nature Geoscience* 8.7 (2015), pp. 530–533.

[33] Andrew R Babbin et al. "Rapid nitrous oxide cycling in the suboxic ocean". In: *Science* 348.6239 (2015), pp. 1127–1129.

[34] Qixing Ji et al. "Global nitrous oxide production determined by oxygen sensitivity of nitrification and denitrification". In: *Global Biogeochemical Cycles* 32.12 (2018), pp. 1790–1802.

[35] Jackson WF Chu and Verena Tunnicliffe. "Oxygen limitations on marine animal distributions and the collapse of epibenthic community structure during shoaling hypoxia". In: *Global Change Biology* 21.8 (2015), pp. 2989–3004.

[36] Hans-Otto Pörtner et al. "The ocean and cryosphere in a changing climate". In: *IPCC Special Report on the Ocean and Cryosphere in a Changing Climate* (2019).

[37] Lester Kwiatkowski et al. "Twenty-first century ocean warming, acidification, deoxygenation, and upper-ocean nutrient and primary production decline from CMIP6 model projections". In: *Biogeosciences* 17.13 (2020), pp. 3439–3470.

[38] Marina Lévy et al. "The crucial contribution of mixing to present and future ocean oxygen distribution". In: *Ocean mixing*. Elsevier, 2022, pp. 329–344.

[39] Andreas Oschlies et al. "Drivers and mechanisms of ocean deoxygenation". In: *Nature Geoscience* 11.7 (2018), pp. 467–473.

[40] Jaime B Palter and David S Trossman. "The sensitivity of future ocean oxygen to changes in ocean circulation". In: *Global Biogeochemical Cycles* 32.5 (2018), pp. 738–751.

[41] I Stendardo and N Gruber. "Oxygen trends over five decades in the North Atlantic". In: *Journal of Geophysical Research: Oceans* 117.C11 (2012).

[42] Mariona Claret et al. "Rapid coastal deoxygenation due to ocean circulation shift in the northwest Atlantic". In: *Nature climate change* 8.10 (2018), pp. 868–872.

[43] Takamitsu Ito et al. "Upper ocean O2 trends: 1958–2015". In: *Geophysical Research Letters* 44.9 (2017), pp. 4214–4223.

[44] Kieran P Helm, Nathaniel L Bindoff, and John A Church. "Observed decreases in oxygen content of the global ocean". In: *Geophysical Research Letters* 38.23 (2011).

[45] HE Garcia et al. "World Ocean Atlas 2018, Volume 3: Dissolved Oxygen, Apparent Oxygen Utilization, and Dissolved Oxygen Saturation." In: (2019).

[46] Estrella Olmedo et al. "Increasing stratification as observed by satellite sea surface salinity measurements". In: *Scientific reports* 12.1 (2022), pp. 1–9.

[47] Nathaniel L Bindoff et al. "Changing ocean, marine ecosystems, and dependent communities". In: *IPCC special report on the ocean and cryosphere in a changing climate* (2019), pp. 477–587.

[48] Hao Zuo et al. "The ECMWF operational ensemble reanalysis–analysis system for ocean and sea ice: a description of the system and assessment". In: *Ocean science* 15.3 (2019), pp. 779–808.

[49] Maofeng Liu et al. "Enhanced hydrological cycle increases ocean heat uptake and moderates transient climate change". In: *Nature climate change* 11.10 (2021), pp. 848–853.

[50] PG Brewer et al. "A climatic freshening of the deep Atlantic north of 50 N over the past 20 years". In: *Science* 222.4629 (1983), pp. 1237–1239.

[51] Ruth Curry, Bob Dickson, and Igor Yashayaev. "A change in the freshwater balance of the Atlantic Ocean over the past four decades". In: *Nature* 426.6968 (2003), pp. 826–829.

[52] Igor Yashayaev. "Hydrographic changes in the Labrador Sea, 1960–2005". In: *Progress in Oceanography* 73.3-4 (2007), pp. 242–276.

[53] Jane F Read and W John Gould. "Cooling and freshening of the subpolar North Atlantic Ocean since the 1960s". In: *Nature* 360.6399 (1992), pp. 55–57.

[54] Bob Dickson et al. "Rapid freshening of the deep North Atlantic Ocean over the past four decades". In: *Nature* 416.6883 (2002), pp. 832–837.

[55] Sybren Drijfhout, Geert Jan Van Oldenborgh, and Andrea Cimatoribus. "Is a decline of AMOC causing the warming hole above the North Atlantic in observed and modeled warming patterns?" In: *Journal of Climate* 25.24 (2012), pp. 8373–8379.

[56] Wei Cheng, John CH Chiang, and Dongxiao Zhang. "Atlantic meridional overturning circulation (AMOC) in CMIP5 models: RCP and historical simulations". In: *Journal of Climate* 26.18 (2013), pp. 7187–7197.

[57] Yifei Fan, Jianhua Lu, and Laifang Li. "Mechanism of the Centennial Subpolar North Atlantic Cooling Trend in the FGOALS-g2 Historical Simulation". In: *Journal of Geophysical Research: Oceans* 126.9 (2021), e2021JC017511.

[58] Ronald J Stouffer et al. "Investigating the causes of the response of the thermohaline circulation to past and future climate changes". In: *Journal of climate* 19.8 (2006), pp. 1365–1387.

[59] John P Dunne et al. "GFDL's ESM2 global coupled climate–carbon earth system models. Part I: Physical formulation and baseline simulation characteristics". In: *Journal of climate* 25.19 (2012), pp. 6646–6665.

[60] John P Dunne et al. "GFDL's ESM2 global coupled climate–carbon earth system models. Part II: carbon system formulation and baseline simulation characteristics". In: *Journal of Climate* 26.7 (2013), pp. 2247–2267.

[61] Lynne D Talley. *Descriptive physical oceanography: an introduction*. Academic press, 2011.

[62] The international thermodynamic equation of seawater – 2010: Calculation and use of thermodynamic properties. "The international thermodynamic equation of seawater – 2010: Calculation and use of thermodynamic properties". In: *Intergovernmental Oceanographic Commission, Manuals and Guides* 56 (2010).

[63] Olaf Duteil et al. "A novel estimate of ocean oxygen utilisation points to a reduced rate of respiration in the ocean interior". In: *Biogeosciences* 10.11 (2013), pp. 7723–7738.

[64] Tim Boyer, ME Conkright, and Sydney Levitus. "Seasonal variability of dissolved oxygen, percent oxygen saturation, and apparent oxygen utilization in the Atlantic and Pacific Oceans". In: *Deep Sea Research Part I: Oceanographic Research Papers* 46.9 (1999), pp. 1593–1613.

[65] Dana R Kester and Ricardo M Pytkowicz. "Oxygen saturation in the surface waters of the Northeast Pacific Ocean". In: *Journal of Geophysical Research* 73.16 (1968), pp. 5421–5424.

[66] Kimberley L Drouin, M Susan Lozier, and William E Johns. "Variability and trends of the South Atlantic subtropical gyre". In: *Journal of Geophysical Research: Oceans* 126.1 (2021), e2020JC016405.

[67] Daniele Iudicone et al. "The formation of the ocean's anthropogenic carbon reservoir". In: *Scientific Reports* 6.1 (2016), pp. 1–16.

[68] Katja Lohmann and Mojib Latif. "Tropical Pacific decadal variability and the subtropical–tropical cells". In: *Journal of climate* 18.23 (2005), pp. 5163–5178.

[69] Syukuro Manabe and Ronald J Stouffer. "Simulation of abrupt climate change induced by freshwater input to the North Atlantic Ocean". In: *Nature* 378.6553 (1995), pp. 165–167.

[70] Paul D Williams et al. "A new feedback on climate change from the hydrological cycle". In: *Geophysical Research Letters* 34.8 (2007).

[71] Ralph F Keeling, Arne Körtzinger, Nicolas Gruber, et al. "Ocean deoxygenation in a warming world". In: *Annu. Rev. Mar. Sci* 2.1 (2010), pp. 199–229.

[72] Laurent Bopp et al. "Climate-induced oceanic oxygen fluxes: Implications for the contemporary carbon budget". In: *Global Biogeochemical Cycles* 16.2 (2002), pp. 6–1.

[73] Robert A Rohde and Zeke Hausfather. "The Berkeley Earth land/ocean temperature record". In: *Earth System Science Data* 12.4 (2020), pp. 3469–3479.

[74] Andrew G Pauling et al. "The response of the Southern Ocean and Antarctic sea ice to freshwater from ice shelves in an Earth system model". In: *Journal of Climate* 29.5 (2016), pp. 1655–1672.

[75] Ken Caldeira and Michael E Wickett. "Anthropogenic carbon and ocean pH". In: *Nature* 425.6956 (2003), pp. 365–365.

[76] Pierre Friedlingstein et al. "Global carbon budget 2021". In: *Earth System Science Data* 14.4 (2022), pp. 1917–2005.

[77] Joan A Kleypas et al. "Impacts of ocean acidification on coral reefs and other marine calcifiers: a guide for future research". In: *Report of a workshop held*. Vol. 18. 2005. 2005, p. 20.

[78] Vivek K Arora et al. "Carbon–concentration and carbon–climate feedbacks in CMIP5 Earth system models". In: *Journal of Climate* 26.15 (2013), pp. 5289–5314.

[79] P Friedlingstein and IC Prentice. "Carbon–climate feedbacks: a review of model and observation based estimates". In: *Current Opinion in Environmental Sustainability* 2.4 (2010), pp. 251–257.

[80] Richard G Williams, Anna Katavouta, and Philip Goodwin. "Carbon-cycle feedbacks operating in the climate system". In: *Current Climate Change Reports* 5.4 (2019), pp. 282–295.

[81] Nicole S Lovenduski, Nicolas Gruber, and Scott C Doney. "Toward a mechanistic understanding of the decadal trends in the Southern Ocean carbon sink". In: *Global Biogeochemical Cycles* 22.3 (2008).

[82] Anna Katavouta and Richard G Williams. "Ocean carbon cycle feedbacks in CMIP6 models: contributions from different basins". In: *Biogeosciences* 18.10 (2021), pp. 3189–3218.

[83] SA Siedlecki et al. "Projecting ocean acidification impacts for the Gulf of Maine to 2050: New tools and expectations". In: *Elem Sci Anth* 9.1 (2021), p. 00062.

[84] Darren J Pilcher et al. "Modeled effect of coastal biogeochemical processes, climate variability, and ocean acidification on aragonite saturation state in the Bering Sea". In: *Frontiers in Marine Science* (2019), p. 508.

[85] Vivek K Arora et al. "Carbon–concentration and carbon–climate feedbacks in CMIP6 models and their comparison to CMIP5 models". In: *Biogeosciences* 17.16 (2020), pp. 4173–4222.

[86] Wallace S Broecker and Tsung-Hung Peng. "Interhemispheric transport of carbon dioxide by ocean circulation". In: *Nature* 356.6370 (1992), pp. 587–589.

[87] Paul E Robbins. "Oceanic carbon transport carried by freshwater divergence: Are salinity normalizations useful?" In: *Journal of Geophysical Research: Oceans* 106.C12 (2001), pp. 30939–30946.

[88] Jorge Sarmiento and Nicholas Gruber. *Ocean biogeochemical dynamics*. Princeton University Press, 2006.

[89] Maribel I García-Ibáñez et al. "Ocean acidification in the subpolar North Atlantic: rates and mechanisms controlling pH changes". In: *Biogeosciences* 13.12 (2016), pp. 3701–3715.

[90] Matthew P Humphreys et al. "PyCO2SYS v1. 8: marine carbonate system calculations in Python". In: *Geoscientific Model Development* 15.1 (2022), pp. 15–43.

[91] Matthew B Menary and Richard A Wood. "An anatomy of the projected North Atlantic warming hole in CMIP5 models". In: *Climate Dynamics* 50.7-8 (2018), pp. 3063–3080.

[92] Kimio Hanawa and Lynne D Talley. "Mode waters". In: *International Geophysics*. Vol. 77. Elsevier, 2001, pp. 373–386.

[93] Tim DeVries. "The oceanic anthropogenic CO2 sink: Storage, air-sea fluxes, and transports over the industrial era". In: *Global Biogeochemical Cycles* 28.7 (2014), pp. 631–647.

[94] Michael Winton et al. "Connecting changing ocean circulation with changing climate". In: *Journal of climate* 26.7 (2013), pp. 2268–2278.

[95] Raffaele Ferrari et al. "Antarctic sea ice control on ocean circulation in present and glacial climates". In: *Proceedings of the National Academy of Sciences* 111.24 (2014), pp. 8753–8758.

[96] Qiuying Zhang et al. "Role of Sea-Surface Salinity in Simulating Historical Decadal Variations of Atlantic Meridional Overturning Circulation in a Coupled Climate Model". In: *Geophysical Research Letters* 49.4 (2022), e2021GL096922.

[97] Xinyue Wei and Rong Zhang. "A Simple Conceptual Model for the Self-Sustained Multidecadal AMOC Variability". In: *Geophysical Research Letters* 49.14 (2022), e2022GL099800.

[98] BB Cael and Malte F Jansen. "On freshwater fluxes and the Atlantic meridional overturning circulation". In: *Limnology and Oceanography Letters* 5.2 (2020), pp. 185–192.

[99] Anastasia Romanou et al. "Role of the ocean's AMOC in setting the uptake efficiency of transient tracers". In: *Geophysical research letters* 44.11 (2017), pp. 5590–5598.

[100] Julio T Bacmeister and Max J Suarez. "Wind stress simulations and the equatorial momentum budget in an AGCM". In: *Journal of the atmospheric sciences* 59.21 (2002), pp. 3051–3073.

[101] Adrian E Gill. "Some simple solutions for heat-induced tropical circulation". In: *Quarterly Journal of the Royal Meteorological Society* 106.449 (1980), pp. 447–462.

[102] Richard S Lindzen and Sumant Nigam. "On the role of sea surface temperature gradients in forcing low-level winds and convergence in the tropics". In: *Journal of Atmospheric Sciences* 44.17 (1987), pp. 2418–2436.

[103] Timothy M Merlis. "Direct weakening of tropical circulations from masked CO2 radiative forcing". In: *Proceedings of the National Academy of Sciences* 112.43 (2015), pp. 13167–13171.

[104] Jakob Bjerknes. "Atmospheric teleconnections from the equatorial Pacific". In: *Monthly weather review* 97.3 (1969), pp. 163–172.